Aix*Marseille université
Socialement engagée

NNT/NL :

THÈSE DE DOCTORAT

Soutenue à Aix-Marseille Université
le 14 mars 2024 par

Floriane SUDRE

Past and future variability of ocean fronts in the Mozambique Channel and influence on marine ecosystems

Discipline
Sciences de l'Environnement

Spécialité
Océanographie

École doctorale
ED 251 SCIENCES DE L'ENVIRONNEMENT

Laboratoire/Partenaires de recherche
Institut Méditerranéen d'Océanologie (MIO)
Institut de Recherche pour le Développement (IRD)

Composition du jury

Lionel RENAULT IRD-LEGOS, Directeur de recherche	Rapporteur
Michael ROBERTS Nelson Mandela University, Professeur	Rapporteur
Anne MOLCARD UTLN-MIO, Professeure	Présidente du jury
Marina LEVY CNRS-LOCEAN-IPSL, Directrice de Recherche	Examinatrice
Vincent ROSSI CNRS-MIO, Chargé de recherche	Directeur de thèse
Boris DEWITTE IRD-CECI, Directeur de recherche	Co-Directeur de thèse
Véronique GARÇON IPGP, Émérite	Invitée

IRD Institut de Recherche pour le Développement FRANCE

Institut Pythéas Observatoire des Sciences de l'Univers Aix*Marseille Université

mio Mediterranean Institute of Oceanography

Affidavit

Je soussignée, Floriane Sudre, déclare par la présente que le travail présenté dans ce manuscrit est mon propre travail, réalisé sous la direction scientifique de Vincent Rossi, Boris Dewitte et Véronique Garçon, dans le respect des principes d'honnêteté, d'intégrité et de responsabilité inhérents à la mission de recherche. Les travaux de recherche et la rédaction de ce manuscrit ont été réalisés dans le respect à la fois de la charte nationale de déontologie des métiers de la recherche et de la charte d'Aix-Marseille Université relative à la lutte contre le plagiat.

Ce travail n'a pas été précédemment soumis en France ou à l'étranger dans une version identique ou similaire à un organisme examinateur.

Fait à Marseille le 12 janvier 2024,



Cette œuvre est mise à disposition selon les termes de la Licence Creative Commons Attribution - Pas d'Utilisation Commerciale - Pas de Modification 4.0 International.

Liste de publications et participation aux conférences

1) Liste des publications réalisées dans le cadre du projet de thèse :

1. Spatial and seasonal variability of horizontal temperature fronts in the Mozambique Channel for both epipelagic and mesopelagic realms. **Sudre F.**, Dewitte B., Mazoyer C., Garçon V., Sudre J., Penven P. and Rossi V. **2023**. *Frontiers in marine science*, 9.
DOI : https://doi.org/10.3389/fmars.2022.1045136.

2. NOMAD: the ocean front dataset for the Mediterranean sea and southwest Indian ocean. **Sudre F.**, Hernández-Carrasco I., Mazoyer C., Sudre J., Dewitte B., Garçon V. and Rossi V. **2023**.
DOI : https://doi.org/10.12770/3ea321a1-d9d4-49e5-a592-605b80dec240.

3. An ocean front dataset for the Mediterranean sea and southwest Indian ocean. **Sudre F.**, Hernández-Carrasco I., Mazoyer C., Sudre J., Dewitte B., Garçon V. and Rossi V. **2023**. *Sci Data 10, 730.*
DOI : https://doi.org/10.1038/s41597-023-02615-z.

4. Changes in ocean eddy activity in the Mozambique Channel in a warming climate. **Sudre F.**, Rossi V., Pierrick P., Garçon V. and Dewitte B. **(in preparation)**.

5. Ocean fronts aggregates marine megafauna in the southwest Indian Ocean. Brito-Morales I., **Sudre F.**, Rossi V., Rohner C., Le Corre M., Jaeger A., Laran S., Bousquet O., Sequeira A., Scales K., Hazen E., Cerchio S., Davies T., Dunn D. and Hannah L. **(in preparation)**.

2) Participation aux conférences et écoles d'été au cours de la période de thèse :

1. Bornö Summer School 2021: Modelling the carbon cycle on continental shelves. **Summer school**. Organised by Copenhagen University. August 2021. Bornö Island, Sweden.

2. Spatio-temporal variability of sea-surface temperature fronts in the Mozambique Channel. F. Sudre, C. Mazoyer, P. Penven, I. Hernández-Carrasco, B. Dewitte, V.

Garçon, J. Sudre and V. Rossi. **Talk**. *OSM 2022 Ocean Sciences Virtual Meeting*, February 2022, Hawaii, USA.

3. **RESILIENCE Cruise** : participation on board of research vessel Marion Dufresne, April 19th - May 24th 2022, in the Mozambique Channel and east coast of South Africa. PIs: J-F. Ternon, M. Noyon, P. Penven and S. Herbette.
   DOI: http://dx.doi.org/10.17600/18001917.

4. Megafauna workshop 2022. **Workshop**. Organised by Conservation International. November 2022. Santa Barbara, USA.

5. NOMAD : The Ocean front database for the Mediterranean Sea and the South West Indian Ocean. Sudre, F., Hernández-Carrasco, I., Mazoyer, C., Sudre, J., Dewitte, B., Garçon, V. and Rossi, V. **Talk**. *ED251 PhD Congress 2023*, May 2023, Marseille, France.

6. NOMAD : The Ocean front database for the Mediterranean Sea and the South West Indian Ocean. **Poster**. *ASLO Aquatic science Meeting 2023*, June 2023, Palma de Mallorca, Spain.

7. Megafauna workshop 2023. **Workshop**. Organised by Conservation International and Nelson Mandela University. July 2023. Port Elizabeth, South Africa (remote).

8. CROCO Training 2023. **Summer school**. Organised by the Mediterranean Institute of Oceanography. September 2023. Barcelonnette, France.

9. Insights from a dynamically downscaled CROCO simulation and a repeat run on the thermal front variability in the Mozambique Channel. Sudre, F., Rossi, V., Penven, P., Garçon, V. and Dewitte, B. **Poster**. *CROCO User meeting 2023*, September 2023, Marseille, France.

10. Atelier enjeux benthiques, coralliens et océanographiques dans le cadre du projet de classement en RNN des îles Eparses. **Workshop**. Organised by the Terres Australes et Antarctic Françaises (TAAF). October 2023. Saint Pierre, La Réunion, France (remote).

11. Investigating fronts at depth in the Mozambique Channel: Are simulated subsurface fronts consistent with in-situ observations? Dutta A., Sudre F. and Rossi V. RESILIENCE cruise workshop 2023. **Talk**. Organised by J.F. Ternon and P. Penven. December 2023. Brest, France (remote).

Résumé

Les fronts sont des structures omniprésentes dans l'océan qui délimitent les transitions entre des eaux aux propriétés distinctes. Dans certains cas, les fronts peuvent être des acteurs majeurs de la variabilité climatique ainsi que des zones de biodiversité exceptionnelles, suscitant ainsi un grand intérêt interdisciplinaire. Les fronts de petite échelle, en particulier, qui durent de quelques jours à quelques semaines sur des échelles spatiales de dizaines à centaines de kilomètres, sont difficiles à étudier sur des échelles de temps multidécennales. Leur cycle de vie court et leur imprévisibilité les rendent difficiles à observer in situ, tandis que leur échelle spatiale fine implique des coûts importants en termes d'instruments et de calculs dans les études satellitaires et de modélisation. Le Canal du Mozambique (CM) est un laboratoire idéal pour étudier ces fronts de petite échelle en raison de sa turbulence et de sa biodiversité. Le CM est également de taille raisonnable, ce qui permet des analyses de modélisation multidécennales à haute résolution. Cette thèse a pour objectif d'évaluer la variabilité spatiale et temporelle des fronts dans le CM, ainsi que leur réponse au réchauffement climatique.

Nous analysons tout d'abord des données de température issues de satellites et de models pour décrire la variabilité saisonnière des fronts thermiques dans le CM au cours des dernières décennies. Les fronts sont identifiés par un seuil, correspondant à 30% de la distribution des gradients thermiques dans le CM. Nous montrons que les gradients thermiques sont maximum sous la couche de mélange, suggérant qu'ils sont largement associés à des dynamiques de subsurface. Nous suggérons que leur variabilité saisonnière dans le CM est modulée par l'activité des tourbillons de mésoéchelles et des cellules d'upwelling régionales.

Des tendances observationnelles montrent un changement significatif dans l'activité des tourbillons dans le CM dû au réchauffement climatique. Ainsi, et à la lumière des premiers résultats, nous émettons l'hypothèse qu'un réchauffement climatique entraînerait également des changements significatifs dans l'activité des fronts. Nous réalisons donc une expérience de downscaling dynamique à l'aide d'un modèle régional à haute résolution pour vérifier cette hypothèse. Nos résultats montrent que les activités des tourbillons et des fronts augmentent dans le nord du CM et diminuent au sud de 17°S. Les régions du CM les plus affectées par les projections de réchauffement climatique en termes de turbulence et de fronts chevauchent des habitats clés pour la mégafaune marine.

Bien que plusieurs études aient démontré que les fronts de petite échelle jouent un rôle structurant dans les écosystèmes planctoniques, les interactions entre ces fronts et la mégafaune marine demeurent largement méconnues. Nous proposons donc une base de données de fronts issues d'observations satellitaires, pour l'étude

des interactions entre la megafauna marine et les fronts dans le sud-ouest de l'Océan Indien. Cette base de données fournit deux diagnostics frontaux complémentaires : des gradients thermiques et des structures Lagrangiennes cohérentes convergentes. L'identification des fronts à partir de ces deux champs de données se fait à l'aide de seuils statistiques, qui sont inclus dans le dataset pour plusieurs écorégions.

L'examen de la variabilité passée et future des fronts océaniques à petite échelle, présenté dans cette thèse, apporte des éléments clés pour la compréhension des ecosystems marins et des flux biogéochimiques à fine échelle dans le CM, encore à déterminer. Les conclusions de cette étude pourraient fournir des éléments supplémentaires en faveur de l'établissement de zones de conservation dans le CM intégrant les caractéristiques des fronts océaniques et adaptées aux projections climatiques.

Mots clés: méso-échelle, fine échelle, tourbillons, fronts océaniques, océan indien, Canal du Mozambique

Abstract

Fronts are ubiquitous ocean structures delineating transitions between waters of distinct properties. Previous studies have shown how they can be major actors of climate variability as well as hotspots of biodiversity, thereby drawing a significant cross-disciplinary interest. Fine-scale fronts in particular, lasting for a few days to a few weeks over spatial scales of tens to hundreds of kilometers, are difficult to study on multidecadal timescales. Their short life-cycle and unpredictability makes them elusive to in-situ observations, while their fine spatial scale involves hefty instrumental and computational costs in satellite and modeling studies. The Mozambique Channel (MC) is an ideal laboratory to study those fine-scale fronts due to its energetic flow and rich biodiversity. The MC is also sensibly-sized which enables high-resolution multidecadal modeling analyses. This thesis thus aims to propose a description of where and when fronts are most frequent in the MC and how this variability responds to projected climate warming.

We first analyze satellite and modelled sea temperature data to describe the seasonal variability of thermal fronts in the MC over the past decades and up to 1000 m. Thermal fronts are identified via statistical thresholding as the top 30% of the thermal gradient distribution in the MC. We show that horizontal thermal gradients peak below the surface mixed layer, suggesting that they are largely associated to dynamics of the ocean interior rather than to mixed-layer processes. We also find that front dynamics are regionally dependent, and we argue that the seasonal variability of thermal fronts in the MC is driven by both the mesoscale eddy activity and regional upwelling cells.

Observational trends exhibit a significant change in the eddy activity within the MC in response to climate warming. Hence, and in light of the first results, we hypothesize that changes in eddy activity would result in significant changes in front activity as well. We thus perform a dynamical downscaling experiment using a high-resolution regional model to explore how eddy and front variability respond to projected warming in the MC. We find that both eddy and front activities are projected to increase in the northern MC and decrease south of 17°S, suggesting that the thermal fronts most affected by the warming perturbation are those forming on the edge of eddies. The regions of the MC most affected by the projected climate warming in turbulence and fronts overlap key habitats for marine megafauna.

While several studies have shown that fine-scale fronts structure plankton ecosystems, little is known about their interactions with highly mobile marine megafauna. Investigating the relationship between marine megafauna and ocean fronts involves both high-resolution front maps and animal tracking data. To this end, we propose a ready-to-use and publicly-available high-resolution observational front dataset focused on the Southwest Indian Ocean. This dataset provides two complementary

front diagnostics: thermal gradients (on a 1 km grid, over 2003-2020) and attracting Lagrangian Coherent Structures (on a 1.56 km grid, over 1994-2020). Fronts are then identified with statistical thresholds, which are included into the dataset for relevant ecoregions.

The comprehensive examination of past and future variability of fine-scale ocean fronts presented in this thesis leads to significant implications for marine ecosystems and fine-scale biogeochemical fluxes within the MC, which are yet to be determined. The findings brought by this research can contribute to developing conservation areas that are both aware of ocean fronts and adaptive to climate changes.

Keywords: mesoscale, fine scale, eddies, ocean fronts, Indian Ocean, Mozambique Channel

Remerciements

Even though my name has the biggest size on the title page, this thesis has been team work from beginning to end. I have only been very lucky to end up at the center of all of those contributions.

The forefront team players were my 3 supervisors: Vincent Rossi, Boris Dewitte and Véronique Garçon. I wish to thank them for designing such an exciting project and entrusting me with it. I am most grateful to Vincent's eagerness for Science, Boris' patience and vision and Véronique's sharp writing skills. I am grateful to the members of my thesis comity: Andrea Doglioli and Francis Marsac, for their interest in my thesis project and for their kindness. I also wish to thank Lionel Renault, Michael Roberts, Anne Molcard and Marina Levy for accepting to review this work.

The data analysis involved in this thesis would not have been possible without the invaluable help of Camille Mazoyer, who always knew how to stay calm and debug step by step. Beyond her technical assistance, Camille has been a model of kindness and patience, inspiring me throughout those 3 years. I also would like to thank Pierrick Penven for his generous modeling guidance and his encyclopedic knowledge of the Mozambique Channel. This thesis has also been possible thanks to Ismael Hernández-Carrasco, who introduced me very patiently to Lagrangian Coherent Structures, starting from zero, and shared his algorithms with us. I also wish to thank Lee Hannah for leading the Ocean Front Change project and Isaac Brito-Morales for organizing the two Megafauna Workshops and being such a supportive friend. Thanks also go to Joel Sudre, who helped us navigate the sea of satellite products. Finally, I am grateful for all the help I have received from Julien and Christophe, and from Amandine, Dominique and Estelle, tech and administrative heroes of the MIO.

I also wish to thank warmly the researchers at MIO who offered corridor smiles, pleasant breaks and interesting conversations: Jean-Luc Fuda, David Nerini, J.C. Poggiale, Andrea Doglioli, Nagib Bhairy, Cristèle Chevalier, Melika Baklouti, Magali Lescot, Elvira Pulido, Mar Benavides, Marion Fourquez, Caroline Lory, Stéphanie Barillon, Caroline Comby, Frédéric Menard and Valérie Michotey. I will keep a pleasant memory of the MIO thanks to you.

During these 3 years, I have also been kept sane and productive by Friends. First thanks go to Marine for the funniest dreams and unwavering emotional support, Thomas for our Gong Fu Cha ceremonies and the most beautiful butterflies, Akash for the best book suggestions and delightful cultural shocks, Nadège to win badminton games *en douceur*, Gustav for his cheerfulness and sense of humor and Térence for lending me his favorite book when I needed it. I wish to thank Alba, Thomas and

Witold for taking me climbing and conquer my deepest fears and Christopher for taking me running in the Calanques. Many thanks also go to the badminton team: Patrick for screaming, Jean-Marc's vicious drop shots, Mayan's Cantonese advice, Nico's patient training, Vince's teasing, Seb's motivational speeches and all the others. You made Mondays and Thursdays so much better. There is also the tennis team: Rabbah, Yann and Yirui. I owe you so many sore muscles, which I intend to give back. Finally, I wish to thank Anthony for the most memorable and cheesiest inspiring advice, shouted while trying to have me fall a bit later from the surfboard. That one sentence had me smile for months afterwards.

I am also most grateful to Markus Jochum and Julian Mak. I would have never even applied to this PhD without Markus tickling my curiosity with a slide on turbulence back in 2018. He was then the first to trust me with an oceanography project, despite me knowing nothing on the topic. Finally, I am glad that Julian has remained close to this PhD project, by offering regular advice and reliable friendship (and gelato) throughout those 3 years.

More intimately, I wish to thank my family: my parents but also Antonia, Leopoldo, Nicola and Giorgio who always welcomed me back with finocchi and anguria. I would also like to mention Angelo who let me eat all the figs three summers in a row, and plant all the flowers I wanted in his garden, significantly contributing to my well-being. Finally, I thank Titi and Axel, who have provided all the comfort, laughter, fancy teas and Thai green curry paste I needed during troubled times.

And last but not least, Luca is certainly the biggest (although hidden) team player in this PhD. Thank you for empowering me selflessly, giving me all the freedom (and bed space) I need to thrive, for enduring extreme temperature showers, bird stories and meditation propaganda. Most of all, thank you for cracking me up when I take things too seriously. I could not hope for a better friend and partner.

Contents

Affidavit 2

Liste de publications et participation aux conférences 3

Résumé 5

Abstract 7

Remerciements 9

Contents 11

List of Figures 14

List of Tables 18

Acronyms 19

1. Introduction 23

1.1. Prologue . . . 24
1.2. A multi-scale ocean . . . 25
1.3. Introducing ocean fronts . . . 27
1.3.1. Defining ocean fronts . . . 27
1.3.2. Frontal dynamics . . . 28
1.3.3. Typologies of ocean fronts . . . 29
1.4. Front detection methods . . . 33
1.4.1. Detecting ocean fronts from tracers . . . 33
1.4.2. Detecting ocean fronts from circulation . . . 34
1.4.3. Front detection methods based on tracers and circulation are complementary . . . 36
1.5. Why fronts are relevant in a changing climate . . . 38
1.5.1. Fronts feedbacks to climate . . . 38
1.5.2. Fronts and the carbon cycle . . . 38
1.5.3. Fronts and ecology . . . 40
1.6. The Mozambique Channel . . . 44
1.6.1. Circulation in the Mozambique Channel . . . 44
1.6.2. Biomass and biodiversity in the Mozambique Channel . . . 46
1.7. Gaps, objectives and plan . . . 50

2. Methods **51**
2.1. Prologue . . . 51
2.2. Satellite data . . . 52
2.2.1. Sea surface temperature . . . 52
2.2.2. Sea surface velocities . . . 52
2.3. Models . . . 52
2.3.1. The original MOZ36 . . . 53
2.3.2. The experiments: MOZ36_CR, MOZ36_F, MOZ36_repeat . . . 53
2.4. Numerical methods . . . 55
2.4.1. Eddy kinetic energy . . . 55
2.4.2. Front detection . . . 55

3. Seasonal thermal front variability in the Mozambique Channel **59**
3.1. Summary . . . 59
3.2. Résumé en français . . . 61
3.3. Article . . . 63
3.4. Supplementary Material . . . 84

4. Projected changes in thermal front variability in the Mozambique Channel **95**
4.1. Summary . . . 95
4.2. Résumé en français . . . 98
4.3. Introduction . . . 100
4.4. Method . . . 101
4.4.1. Regional simulations . . . 101
4.4.2. Numerical methods . . . 103
4.4.3. MOZ36_CR validation . . . 104
4.5. Results . . . 105
4.5.1. Changes in EKE . . . 105
4.5.2. Changes in mean thermal gradients . . . 106
4.5.3. Changes in thermal front frequency . . . 108
4.6. Discussion . . . 109
4.6.1. Changes in mean currents . . . 109
4.6.2. Changes in mean EKE . . . 110
4.6.3. Changes in thermal fronts . . . 111
4.7. Conclusion . . . 112
4.8. APPENDIX: Contrasting mean temperature and circulation between baseline and pseudo global warming experiments . . . 115

5. An ocean front dataset for the Mediterranean Sea and Southwest Indian Ocean **118**
5.1. Summary . . . 118
5.2. Résumé en français . . . 119
5.3. NOMAD dataset . . . 122

5.4. Data descriptor 122

6. Conclusion **138**
6.1. Summary 138
6.2. Key results 140

7. Discussion and perspectives **141**
7.1. Beyond surface front detection 141
7.2. On the relationship between thermal and dynamical front diagnostics 142
7.3. Modeling considerations 145
7.4. Beyond physical diagnostics 148

Bibliography **153**

A. Other collaborative works **187**

List of Figures

1.1. Meandering and eddying Gulf Stream: sea surface temperature (top) and chlorophyll concentration (bottom) acquired on April 18th, 2005 by NASA's MODIS AQUA satellite. Image credit: NASA Earth Observatory. 25
1.2. Typical spatial scales of ocean processes. Figure extracted from Taylor and Thompson, 2023. 26
1.3. Submesoscale structures as seen from satellite imagery. Left: Phytoplankton bloom in the Baltic sea, revealing a submesoscale eddy, acquired on August 15th, 2020 by NASA's Landsat 8 satellite. Right: phytoplankton blooms off the Alaskan coast, acquired on June 18th, 2018, by the Operational Land Imager (OLI) on NASA's Landsat 8. Image credits: NASA Earth Observatory. 27
1.4. Frontal dynamics for stable (a.) and unstable (b.) active fronts. Bold black circular arrows indicate the sign of vorticity generated on both sides of the fronts, while the grey contours are isopycnals. Figure extracted from Mahadevan, 2016. 28
1.5. Multi-scale ocean turbulence summarized in Taylor and Thompson, 2023. The colors correspond to idealized sea surface temperature. Cool dense water (deep purple) is upwelled at the core of a mesoscale eddy. Lighter warmer water (pale yellow) is pushed at the boundaries of the domain. Submesoscale fronts and filaments are generated at the border of the mesoscale eddies. Figure extracted from Taylor and Thompson, 2023. 30
1.6. Primary productivity is dependent on nutrient input in the sun-lit euphotic layer. Figure extracted from Williams and Follows, 2012. 39
1.7. Bathymetry and main surface currents in the Indian Ocean. The grey shading correspond to the bathymetry. The green shading marks the area influenced by the Monsoon. The current acronyms correspond to: **EACC** : East African Coastal Current; **EICC**: East Indian Coastal Current; **EGC**: Eastern Gyral Current; **LH**: Lakshwadeep high; **NEC**: Northeast Monsoon Current; **NEMC**: Northeast Madagascar Current; **SEMC**: Southeast Madagascar Current; **SICC**: South Indian Countercurrent ; **SJC**: South Java Current; **SMACC**: Southwest Madagascar Coastal Current; **WICC**: West Indian Coastal Current. Figure extracted from (Phillips et al., 2021). 44

1.8. Bathymetry and main currents in the Mozambique Channel and around Madagascar. The currents shown are the Northeast Madagascar Current and Southeast Madagascar Current (**NEMC** and **SEMC**, respectively), the South Indian Countercurrent (**SICC**), the Mozambique Current (**MZC**), the Mozambique Under Current (**MZUC**) and the Agulhas Current (**AC**). The background black contours represent isobaths at -200, -500, -1000, -2000, -3000 and -4000 m. The colormap is from cmocean (Thyng et al., 2016). 46

2.1. Climatic indices shown to have an impact on the Southwest Indian Ocean: El Niño-Southern Oscillation (ENSO) (Conejero et al., 2020), Indian Ocean Dipole (IOD) (Saji et al., 1999) and Southern Indian Ocean Dipole (SIOD) (Jo et al., 2022). The vertical dotted line mark the year 2001, where all indices are minimal. 55

4.1. Bathymetry from the ROMS 1/4° simulation detailed in (Sudre et al., 2023a) and MOZ12, MOZ36 subdomains. The background black contours represent isobaths at -200, -500, -1000, -2000, -3000 and -4000 m. The colormap is from cmocean (Thyng et al., 2016). 102
4.2. Mean temperature (a., b.) and salinity (c., d.) vertical sections at longitude 42.125°E from WOA2018 (a., c., Locarnini et al., 2018) and MOZ36_CR (b., d.). The colormaps are from cmocean (Thyng et al., 2016). . . . 104
4.3. Mean sea surface temperature from Multi-scale Ultra-high Resolution sea-surface temperature analysis (MUR SST) (left, Chin et al., 2017) and differences with MOZ36_CR (right). The colormaps are from cmocean (Thyng et al., 2016). 105
4.4. Mean intra-seasonal Eddy Kinetic Energy (EKE) derived from MOZ36_CR currents (left) and from COPERNICUS-GLOBCURRENT total currents (right, Rio et al., 2014. The colormaps are from cmocean (Thyng et al., 2016). 105
4.5. Changes in EKE (MOZ36_F - MOZ36_CR, left) and vertical profiles of the same EKE changes for four regions of interest, whose areas are represented in the left panel. The colormap is from cmocean (Thyng et al., 2016). 106
4.6. Hövmoller diagrams representing baselines (MOZ36_CR, top) and changes in (MOZ36_F minus MOZ36_CR, bottom) seasonal EKE variations as a function of depth for four regions of interest (same regions as in Fig. 4.5). The colormaps are from cmocean (Thyng et al., 2016). 107
4.7. Changes in Thermal Gradients (TG) (MOZ36_F minus MOZ36_CR) at surface (left panel) and subsurface (center panel) as well as vertical profiles of the same TG changes for four regions of interest, whose areas are represented in the left panel. The colormaps are from cmocean (Thyng et al., 2016). 108

4.8. Hövmoller diagrams representing baselines (MOZ36_CR, top) and changes in (MOZ36_F - MOZ36_CR, bottom) seasonal TG variations as a function of depth for four regions of interest (same regions as in Fig. 4.7). The colormaps are from cmocean (Thyng et al., 2016). 109
4.9. Maps of mean thermal front frequency changes (MOZ36_F minus MOZ36_-CR) at surface (a.) and subsurface (c.) and annual thermal front frequency boxplots at surface (b.) and subsurface (d.) for both experiments. The colormap is from cmocean (Thyng et al., 2016). 109
4.10. Vertical profiles of the spatial correlation coefficient between EKE and TG inside of the MC and East of Madagascar. The grey shading indicate where the correlation is significant. 112
4.11. Mean surface temperature from MOZ36_CR (a.), MOZ36_F (b.) and changes in mean surface temperature in the regional model (MOZ36_F - MOZ36_CR, c.) and in the global model (CESM_member$|_{2071\text{-}2100}$ minus CESM_member$|_{1993\text{-}2014}$, d.). The colormaps are from cmocean (Thyng et al., 2016). 116
4.12. Sections of mean temperature changes (projection minus baseline) in the regional (left column) and global (CESM_member$|_{2071\text{-}2100}$ minus CESM_member$|_{1993\text{-}2014}$, right column) models for several latitudes: 10°S (top row), 20°S (center row) and 30°S (bottom row). The colormaps are from cmocean (Thyng et al., 2016). 116
4.13. Mean current modulus from MOZ36_CR (1st column), changes in mean current modulus between MOZ36_F and MOZ36_CR (2nd column), mean current modulus from the global model (CESM_member$|_{1993\text{-}2014}$, 3rd column) and changes in mean current modulus in the global model (CESM_member$|_{2071\text{-}2100}$ minus CESM_member$|_{1993\text{-}2014}$, 4th column). The means and mean changes are shown for several depths: 0 m (1st row), -150 m (2nd row), -500 m (3rd row), -1000 m (last row). The colormaps are from cmocean (Thyng et al., 2016). 117

7.1. Probability of finding a thermal front at surface given one at -100 m (left) or at -500 m (right). 141
7.2. Seasonal Hovmöller diagrams in the zonally averaged Mozambique Channel (MC) open-ocean (bathymetry > 200 m) for oceaN frOnt dataset for the Mediterranean seA and southwest inDian ocean (NOMAD) TG (left, in °C.km^{-1}), EKE (center, in m^2.s^{-2}) and NOMAD Finite-Size Lyapunov Exponents (FSLE) (right, in day^{-1}). The y-axis corresponds to latitudes in degree north. The colormaps are from cmocean (Thyng et al., 2016). 143

7.3. Interannual Hovmöller diagrams in the zonally averaged MC open-ocean (bathymetry > 200 m) for anomalies of EKE (top, in $m^2.s^{-2}$) and NOMAD FSLE (2nd row, in day^{-1}) and TG (3rd row, in °C.km^{-1}). The y-axis corresponds to latitudes in degree north. The blank areas in the TG hovmöller diagram represent flagged pixels due to cloud cover. The bottom panel represents the time series of the IOD dipole mode indices following the method presented in Saji et al. (1999) and Cai et al. (2021) from HadISST 1.1 monthly average sea surface temperature (Rayner et al., 2003). Note that the indices derived from the method presented in Cai et al. (2021) only go up to 2015. The colormap is from cmocean (Thyng et al., 2016). 144
7.4. Correlation coefficients per latitude between TG (left), backward FSLE (center) and EKE (right) and IOD indices as per Saji et al. (1999) (in black) and Cai et al. (2021) (strong IOD in red and moderate IOD in blue). The interannual anomalies in TG, FSLE and EKE are the same as for the Hövmoller diagram in Fig. 7.3. Significant correlations (p-values<0.05) are marked by thicker shaded lines. 145
7.5. Key drivers of climate and ocean variability in the Indian Ocean region. This schematic is from CLIVAR's IndOOS-2 report (Indian Ocean Observing System, Beal et al., 2019). The schematic includes oxygen minimum zones (OMZs), upwelling and subduction zones, main heat flux components. On intraseasonal time scales: Madden–Julian Oscillations (MJO) and Monsoon Intra-Seasonal Oscillations (MISO). On interannual time scales: the Indian Ocean Dipole (IOD) and Indian Ocean Basin Mode (IOBM), the subtropical modes of Ningaloo Niño and subtropical IOD, cyclogenesis, and climate change. 146
7.6. Chlorophyll-a trend map (1997-2021) from Copernicus Marine Environment Monitoring Service (CMEMS) Observations Reprocessing. The trend comes from the 5th version of global climate-quality chlorophyll time series from the ESA Ocean Colour Climate Change Initiative (ESA OC-CCI, Sathyendranath et al., 2019) on a 4 km grid. Image credits: E.U. Copernicus Marine Service Information. 149
7.7. Evaluation of the vulnerability of Southwest Indian Ocean (SWIO) coral reefs and ecoregions following the Red List Ecosystem method from the International Union for Conservation of Nature (IUCN), figure extracted from Obura et al. (2021). 151
7.8. Preliminary figure of kernel density estimations between whale sharks (a, e), red-tailed tropic birds (b, f), wedge-tailed shearwater (c, g), turtles (d, h) and distance to high FSLE values (top) and thermal fronts (bottom) in blue. Orange kernel density estimations correspond to random walks. Figure extracted from Brito-Morales et al., in preparation. 152

List of Tables

2.1. Summary of simulation configurations. 58

Acronyms

AC

Agulhas Current. 45

ACC

Antarctic Circumpolar Current. 31

AVISO

Archiving, Validation, and Interpretation of Satellite Oceanographic. 52

BOA

Belkin and O'Reilly Algorithm. 33, 35, 37, 55, 56, 60, 61, 96, 98, 119, 120, 139, 148

CCA

Cayulla Cornillon Algorithm. 34

CESM-LENS

Community Earth System Model Large Ensemble. 54, 96, 98, 102, 103, 105, 109, 115, 147

CMEMS

Copernicus Marine Environment Monitoring Service. 17, 52, 56, 60, 61, 119, 120, 142, 143, 149

CMIP

Coupled Model Intercomparison Project. 100, 109, 113

CROCO

Coastal and Regional Ocean COmmunity model. 53, 139, 145

EACC

East African Coastal Current. 45

EBUS

Eastern Boundary Upwelling Systems. 31

EKE

Eddy Kinetic Energy. 15–17, 55, 60–62, 94, 96, 98, 99, 101, 103–106, 110–114, 139, 142–145, 148, 149

ENSO

El Niño-Southern Oscillation. 15, 54, 55, 144

ERA5

ECMWF Reanalysis v5. 52

FSLE

Finite-Size Lyapunov Exponents. 16, 17, 35–37, 51, 56, 57, 119, 121, 140, 142–145, 152

FTLE

Finite-Time Lyapunov Exponents. 36

GCM

Global Climate Models. 96, 98

IOD

Indian Ocean Dipole. 15, 17, 54, 55, 144, 145

IUCN

International Union for Conservation of Nature. 17, 151

LCS

Lagrangian Coherent Structures. 35, 119, 121, 140

MC

Mozambique Channel. 16, 17, 24, 44–51, 53–56, 59–61, 94–96, 98, 100, 101, 103–107, 109–115, 118, 120, 138, 139, 142–146, 148–150, 152

MUR SST

Multi-scale Ultra-high Resolution sea-surface temperature analysis. 15, 52, 56, 61, 104, 105, 119, 120

MZC

Mozambique Current. 45, 109, 115

MZUC

Mozambique Under Current. 45, 109, 115

NEMC

North East Madagascar Current. 45, 60, 61, 94, 106, 109–111, 115, 118, 120, 139, 141, 144

NOMAD

oceaN frOnt dataset for the Mediterranean seA and southwest inDian ocean. 16, 17, 119–121, 140, 142–144, 149, 150

OFC

Ocean Front Change. 24

RCP

Representative Concentration Pathway. 54, 96, 98, 102

ROMS

Regional Ocean Modeling System. 150

SEC

South Equatorial Current. 45, 109, 115, 143

SEMC

South East Madagascar Current. 45, 47, 60–62, 94, 96, 104–107, 109–112, 115, 118, 120, 139, 141, 144

SICC

Subtropical Indian Ocean Countercurrent. 45, 109–111, 115

SIOD

Southern Indian Ocean Dipole. 15, 54, 55

SSH

Sea Surface Height. 26, 36

SST

Sea Surface Temperature. 26, 33, 34, 36, 38, 47, 52, 103, 111, 141, 142

SWIO

Southwest Indian Ocean. 17, 119–121, 140, 150, 151

TG

Thermal Gradients. 15–17, 59, 60, 94, 96, 98, 99, 103, 106–112, 114, 142–145

WBC

Western Boundary Currents. 31, 38, 41, 45

1. Introduction

Content

1.1. Prologue . . . 24
1.2. A multi-scale ocean . . . 25
1.3. Introducing ocean fronts . . . 27
1.3.1. Defining ocean fronts . . . 27
1.3.2. Frontal dynamics . . . 28
1.3.3. Typologies of ocean fronts . . . 29
1.3.3.1. Persistent fronts . . . 30
1.3.3.2. Ephemeral fronts . . . 31
1.4. Front detection methods . . . 33
1.4.1. Detecting ocean fronts from tracers . . . 33
1.4.1.1. Gradient-based methods . . . 33
1.4.1.2. Population-based methods . . . 34
1.4.2. Detecting ocean fronts from circulation . . . 34
1.4.3. Front detection methods based on tracers and circulation are complementary . . . 36
1.5. Why fronts are relevant in a changing climate . . . 38
1.5.1. Fronts feedbacks to climate . . . 38
1.5.2. Fronts and the carbon cycle . . . 38
1.5.2.1. The biological pump . . . 39
1.5.2.2. Fronts, nutrients and light availability . . . 40
1.5.3. Fronts and ecology . . . 40
1.5.3.1. Fronts structure plankton communities . . . 41
1.5.3.2. Fronts aggregate pelagic fish and top predators . . . 41
1.6. The Mozambique Channel . . . 44
1.6.1. Circulation in the Mozambique Channel . . . 44
1.6.2. Biomass and biodiversity in the Mozambique Channel . . . 46
1.7. Gaps, objectives and plan . . . 50

1.1. Prologue

This thesis is part of the Ocean Front Change Project, financed by the Belmont Forum and implemented through the French National Research Agency (ANR-20-BFOC-0006-04).

Ocean Front Change (OFC) is an international and multidisciplinary project gathering scientists from the French National Research Institute for Sustainable Development (IRD, France), Conservation International (CI, US), Heidelberg University (HU, Germany) and Coastal Oceans Research and Development in the Indian Ocean - East Africa (CORDIO-EA, Kenya). The goal of OFC is to bring together scientists, fisheries and conservation stakeholders to design sustainable management solutions around front ecosystems in the MC.

This thesis is the product of a collaborative effort to map past and projected ocean front variability in the MC to inform marine biologists, ecologists and local conservation groups.

1.2. A multi-scale ocean

The ocean is a complex system operating on a wide range of spatial and temporal scales. Before the 1950s, oceanographers viewed the oceans as sluggish steady state systems operating mostly at the basin scale (Munk & Wunsch, 1982; Jochum & Murtugudde, 2006). Early theories about the *large scale* ocean circulation depict a quasi-stationary oceanic flow defined on spatial scales larger than thousands of kilometers (Sverdrup, 1947; Stommel, 1961). The development of satellite observations and buoy technologies in the 1960s lead to a very different picture of the oceans by revealing many smaller turbulent spiralling structures along large-scale currents (Fu, 1983; Munk et al., 2000).

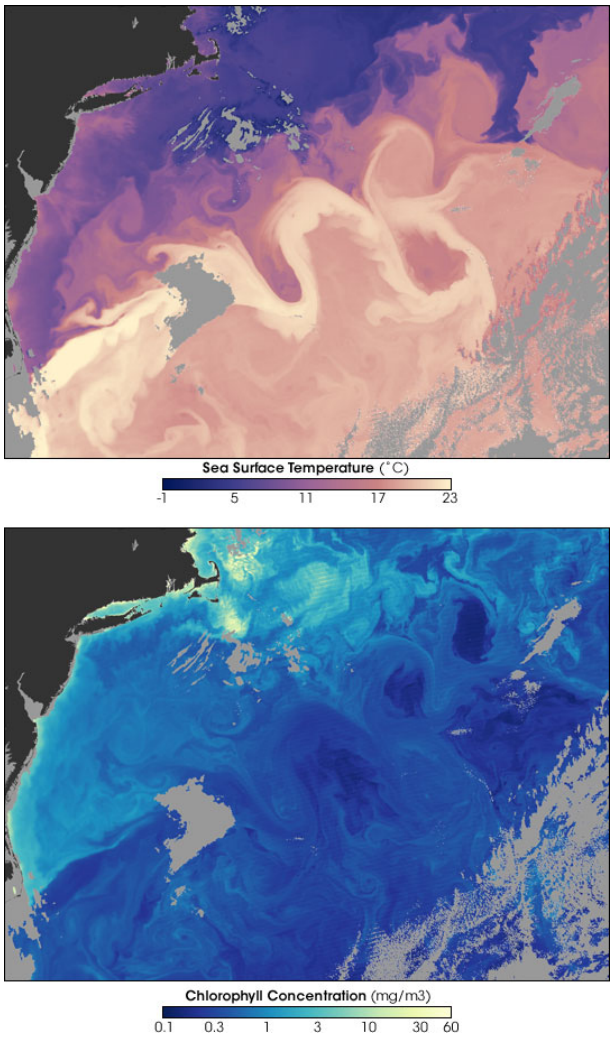

Figure 1.1.: Meandering and eddying Gulf Stream: sea surface temperature (top) and chlorophyll concentration (bottom) acquired on April 18th, 2005 by NASA's MODIS AQUA satellite. Image credit: NASA Earth Observatory.

For example, the meandering of the Gulf Stream is visible from satellite sea surface

temperature and chlorophyll concentration (Fig. 1.1). Warm waters (light pink in Fig. 1.1 top) from the tropics is advected northeast by the Gulf Stream across the Atlantic Ocean. Far from being straight and linear, the Gulf Stream form spirals spanning hundreds of kilometers in which cold or warm water remains trapped. The origin of the trapped water and its temperature can create suitable conditions for phytoplankton blooms, revealed by higher chlorophyll concentration (in light yellow in fig. 1.1 bottom) (Gower et al., 1980).

Those spirals or *eddies* span 10 to 200 kilometers in length and can last several weeks to several months, they belong to what is called the *mesoscale*. Mesoscale eddies are generated by the conversion of potential energy accumulated at tilted density surfaces along jets, a process referred to as baroclinic instability (Gill et al., 1974). Looking at even finer scales one can observe even smaller oceanic structures developing on the edge of mesoscale eddies; this is the *submesoscale* (Munk et al., 2000; Capet et al., 2008a, 2008b; Lévy et al., 2018; Taylor & Thompson, 2023). Submesoscale ocean motions operate on spatial scales finer than tens of kilometers and typically last for a few days to a few weeks (Fig. 1.2). They can be observed from satellite Sea Surface Height (SSH) and Sea Surface Temperature (SST) images (for example Fig. 1.1 top), but also from ocean color (for example Fig. 1.1 bottom and Fig. 1.3).

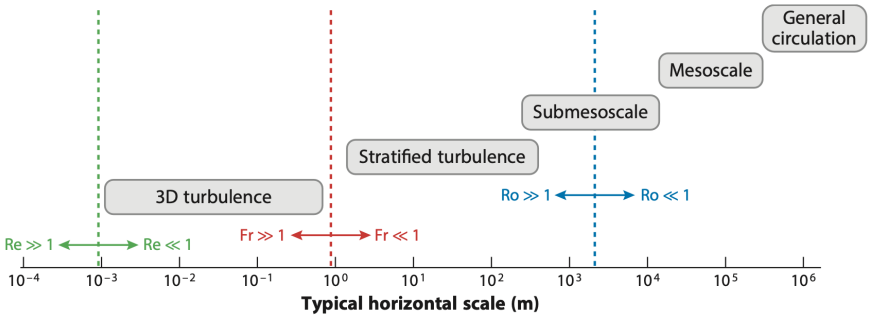

Figure 1.2.: Typical spatial scales of ocean processes. Figure extracted from Taylor and Thompson, 2023.

We can thus envision the ocean as a dynamic and multi-scale patchwork of swirling water masses each with its own thermohaline, chemical or biological signature. *Ocean fronts*, at the very center of this thesis, are transitory edges between those distinct water masses.

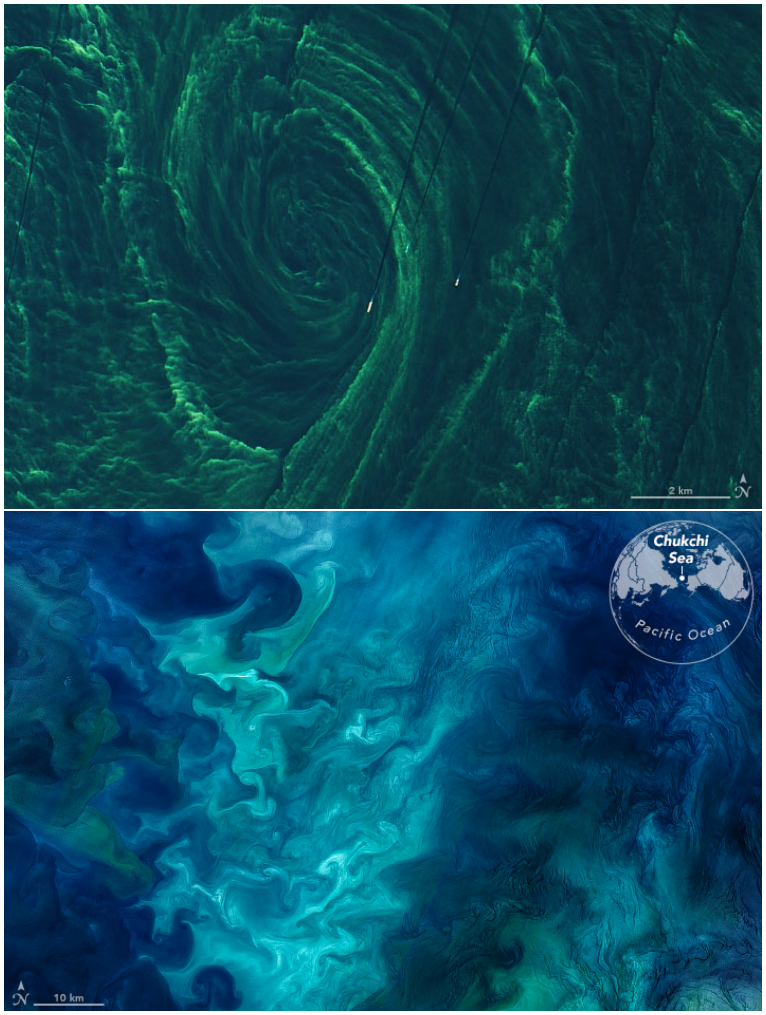

Figure 1.3.: Submesoscale structures as seen from satellite imagery. Left: Phytoplankton bloom in the Baltic sea, revealing a submesoscale eddy, acquired on August 15th, 2020 by NASA's Landsat 8 satellite. Right: phytoplankton blooms off the Alaskan coast, acquired on June 18th, 2018, by the Operational Land Imager (OLI) on NASA's Landsat 8. Image credits: NASA Earth Observatory.

1.3. Introducing ocean fronts

1.3.1. Defining ocean fronts

Far from being smooth and homogeneous, the ocean resembles a multi-scale swirling patchwork of water masses with different properties. Those properties can be of thermohaline nature (e.g. salinity, temperature, and thus density) but also of biogeochemical nature (e.g. concentration of nutrients, chlorophyll, sediments, etc.). Fronts delineate the sharp boundaries between those patches of dissimilar fluids. Fronts are thus defined by intense gradients contrasting a relatively homogeneous field.

Ocean fronts are said to be *passive* when no density gradient is involved in their formation, and they are marked by high gradients in other variables instead. For example, a passive front could develop between two water masses with different thermohaline properties but with similar density (e.g. warm and salty versus cold and fresh), or between two distinct plankton communities advected together. *Active* ocean fronts feature density gradients. They can result from persistent wind stress curl, instabilities, or from heterogeneous freshwater and heat surface fluxes (McWilliams, 2021).

1.3.2. Frontal dynamics

Active fronts emerging due to heterogeneous surface conditions in wind, freshwater and heat fluxes can be reinforced via *frontogenesis* (McWilliams, 2021).

On scales larger than tens of kilometers, active fronts can be considered in geostrophic and thermal wind balance. The Coriolis acceleration balances along-front velocities and cross-front pressure gradients (Fig. 1.4.a.). They feature a strong along-front jet and generate opposite-sign vorticity on either side. They are also places of higher horizontal flow shear and convergence (Pedlosky, 1979; Flament & Armi, 2000; Mahadevan, 2016). The density gradients are strengthened by frontogenesis, for example when the along-front jet intensifies due to thermal wind shear. The front then dissipates (i.e. their isopycnals are flattened out) when turbulent mixing processes interrupt the frontogenesis feedback, this is the *frontolysis* (Capet et al., 2008b; Taylor & Thompson, 2023).

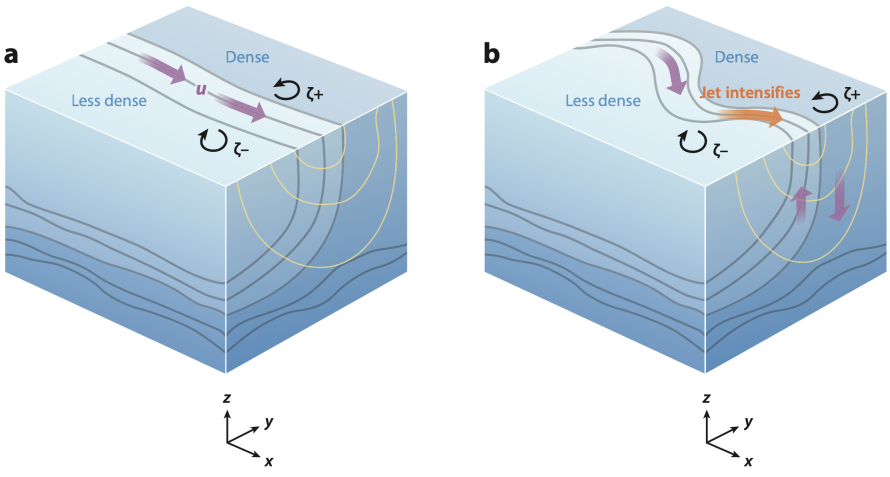

Figure 1.4.: Frontal dynamics for stable (a.) and unstable (b.) active fronts. Bold black circular arrows indicate the sign of vorticity generated on both sides of the fronts, while the grey contours are isopycnals. Figure extracted from Mahadevan, 2016.

At scales smaller than the Rossby deformation radius, front dynamics involve ageostrophic processes leading to a vertical overturning circulation. The Rossby

deformation radius is the length scale marking the threshold at which the effect of Earth rotation (the Coriolis force) and buoyancy are in dominant balance, also referred to as geostrophic balance. The radius of deformation R_D is expressed as a function of the Brünt-Vaisala frequency N (i.e. measure of buoyancy), the depth of the thermocline h (i.e. the depth at which the vertical temperature gradient is maximal) and the Coriolis parameter f:

$$R_D = \frac{Nh}{f} \tag{1.1}$$

The Rossby deformation radius is higher at the tropics, about several hundreds of kilometers, and smaller at high latitudes near the poles, about tens of kilometers (Chelton et al., 1998). Submesoscale ocean dynamics, by operating at scales shorter than the Rossby deformation radius, are not as constrained by geostrophic balance, and they involve an ageostrophic circulation (Mahadevan, 2016; Taylor & Thompson, 2023).

Indeed, tilted isopycnals[1] resulting from the sharpening of density gradients (grey lines in Fig. 1.4) can lead to baroclinic instabilities. At unstable active fronts (Fig. 1.4.b.), the horizontal jet starts meandering and a secondary ageostrophic vertical circulation is initiated to return to geostrophic balance. The horizontal density gradients are sharpened and elongated by the secondary overturning circulation in a positive feedback loop. The fronts remain until this feedback is interrupted by other processes (Nagai et al., 2006; Capet et al., 2008b; Thomas & Ferrari, 2008; Klein & Lapeyre, 2009; Gula et al., 2014; McWilliams, 2016; Lévy et al., 2018; McWilliams, 2021; Taylor & Thompson, 2023).

Submesoscale density gradients can form in-between mesoscale eddies for example, when the water between them is strained, squeezing the isopycnals together, further intensifying the gradient and the along-front jet (Fig. 1.5). This ageostrophic overturning circulation occurring at submesoscale ocean fronts is key to biological processes because it modulates the availability of nutrients in the sun-lit ocean layer (Mahadevan, 2016; Lévy et al., 2018).

1.3.3. Typologies of ocean fronts

Fronts are found everywhere in the oceans, they are generated by a variety and combination of complex processes and therefore cover a wide range of temporal and spatial scales (Lévy et al., 2018; Belkin, 2021; McWilliams, 2021). Some last barely a few days (e.g. Baudena et al., 2021) while others are quasi-stationary (e.g. Mauzole, 2022). Their width can cover a few (e.g. Mangolte et al., 2023) or thousands of kilometers (e.g. Belkin et al., 2009). Vertically, some fronts remain in the surface mixed layer (e.g. Pingree et al., 1975), while others reach several hundreds meters below sea level (e.g. Siegelman et al., 2019).

There are many ways to classify ocean fronts based on their characteristics and on the processes involved in their generation and dissipation. Various typologies have

[1] lines of constant density

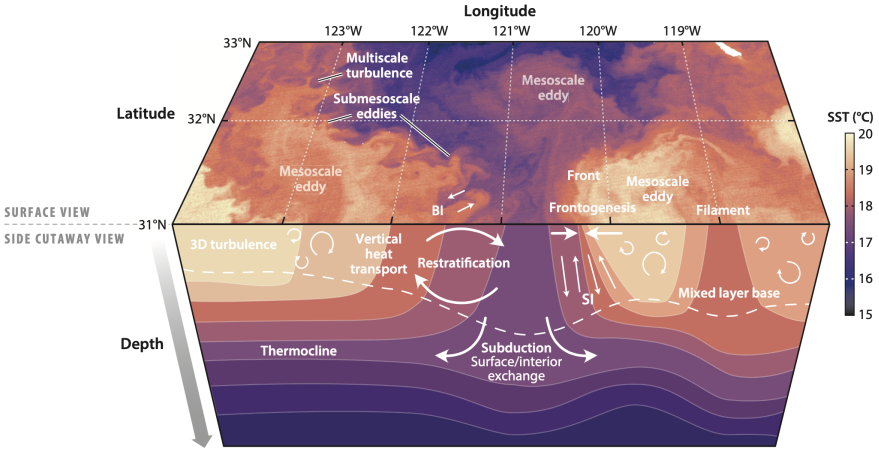

Figure 1.5.: Multi-scale ocean turbulence summarized in Taylor and Thompson, 2023. The colors correspond to idealized sea surface temperature. Cool dense water (deep purple) is upwelled at the core of a mesoscale eddy. Lighter warmer water (pale yellow) is pushed at the boundaries of the domain. Submesoscale fronts and filaments are generated at the border of the mesoscale eddies. Figure extracted from Taylor and Thompson, 2023.

been proposed before, for example in Scales et al., 2014b, Belkin, 2021, McWilliams, 2021, and more recently in Mauzole, 2022. Front typologies help us apprehend their possible drivers, subsequent variability and biological responses. However, real-world fronts are likely to be driven by a unique combination of complex processes under favorable conditions. Those front typologies are thus not exhaustive or exclusive in any way. We give here a few examples of the most common ocean fronts and of their related driving forces. We first make a distinction between persistent and ephemeral fronts.

1.3.3.1. Persistent fronts

Persistent fronts are quasi-permanent, highly energetic structures that tend to operate on larger spatial scales and extend deeper in the water column than their ephemeral counterparts.

Shelf-break fronts form along continental shelves due to sharp changes in bathymetry (Lozier & Reed, 2005) and they are considered to be quasi-permanent since the bathymetry driving them usually remains constant (Gawarkiewicz & Chapman, 1992; Acha et al., 2004; Belkin et al., 2009). **River plume and tidal fronts** are found at estuaries, they are driven by tidal mixing and by the addition of buoyancy from freshwater discharge (Garvine & Monk, 1974; Pingree et al., 1975; Pingree & Griffiths, 1978; Yanagi & Tamaru, 1990; Akan et al., 2018). They are not stationary per se but their variability is usually easily predictable and follows those of their associated astronomical tides and rivers.

In the open ocean, **planetary-scale fronts** are those driven by large-scale atmospheric forcings (such as mid-latitude westerlies) and constrained by the bathymetry. Their mean position is rather fixed but might show some seasonal variability (Mauzole, 2022). Their spatial scale is in the order of hundreds of kilometers. Within this category, one can distinguish between planetary fronts caused by powerful jets such as Western Boundary Currents (WBC) and those occurring at Eastern Boundary Upwelling Systems (EBUS). Planetary fronts related to strong ocean currents are observed in the Southern Ocean, along the Antarctic Circumpolar Current (ACC) (Orsi et al., 1995) and at WBC: along the Gulf Stream (Bower et al., 1985), the Kuroshio (Nagata et al., 1986) and the Agulhas currents (Tozuka & Cronin, 2014). EBUS stage **along-shore upwelling fronts** (Letelier et al., 2009; Landry et al., 2012), sometimes also related to shelf-break fronts (Rossi et al., 2010).

Along persistent fronts, the potential energy caused by tilted isopycnals is then converted, via baroclinic instabilities, into whirling meso-to-submesoscale meanders and eddies (McWilliams, 2016).

1.3.3.2. Ephemeral fronts

Ephemeral fronts feature smaller space and time scales than the aforementioned persistent fronts, they are mobile and involve more stochastic processes, which also makes them less predictable.

Dynamical instabilities causes powerful ocean currents such as the aforementioned WBC and the ACC to meander, thereby forming mesoscale eddies and finer scale **deformation fronts** and filaments (Capet et al., 2008b; Gula et al., 2014; Tedesco et al., 2019; Siegelman et al., 2020a; McWilliams, 2021; Xi et al., 2022). Ephemeral fronts can also appear in EBUS, when they are associated with their offshore jets and filaments (Lutjeharms & Stockton, 1987; Castelao et al., 2005; Capet et al., 2008b; Calil et al., 2021).

These fronts are related to the background eddy field and associated interactions between eddies and topography (Roden, 1991; Roberts et al., 2014; De Falco et al., 2022) and between eddies and mean flow (Strub et al., 1991; Qiu & Chen, 2010). They usually last a few days to a few months and cover spatial scales ranging from a few kilometers to tens of kilometers (McWilliams, 2016).

There are different ways to characterize ocean fronts and this lead to a variety of methods being developed to detect them.

KEY POINTS

. Ocean fronts are defined by sharp tracer (e.g. temperature, density) gradients contrasting a homogeneous background.

. Dynamically, they are characterized by an along-front jet, strong horizontal velocity shear and convergence.

. Submesoscale fronts also feature a vertical ageostrophic overturning circulation.

. Fronts are driven by a variety of processes involving a wide range of spatial and temporal scales.

To the interested reader

The complex fluid dynamics occurring at ocean fronts are covered in the following review papers: Mahadevan, 2016, McWilliams, 2016, 2021, Lévy et al., 2018 and Taylor and Thompson, 2023.

1.4. Front detection methods

A variety of front detection methods has been developed over the years. Each method is designed around specific front definitions, limits and availability of datasets and tailored to relevant research questions.

Historically, ocean fronts were detected manually from cruises (e.g. Yoder et al., 1994), or satellite images (e.g. in Legeckis, 1978; Munk et al., 2000). Subsequently, the wealth of images resulting from improvement of satellite technologies and computing capabilities fostered the need for automated feature detection. Automated edge detection methods tailored to oceanographic features allowed for faster and more consistent front detection at finer scales and over longer time periods. Today, most methods of front detection are tracer-based, which means that front positions are inferred from studying the distribution of temperature (or chlorophyll concentration) in a Eulerian framework. Another significant branch of front detection adopts a Lagrangian perspective to map frontal edges from velocities. These two perspectives on ocean fronts are complementary because they tackle different aspects of front dynamics: tracer-based methods focus on the strong horizontal gradients, while dynamic-based methods focus on the along-front horizontal flow convergence.

1.4.1. Detecting ocean fronts from tracers

Tracer-based front detection methods take advantage of the high gradients defining fronts and are thus akin to edge detection methods in image processing. Most of the methods described in the following paragraphs are applied on satellite SST or ocean color images.

1.4.1.1. Gradient-based methods

To identify frontal edges in any tracer field, one could compute a simple horizontal gradient, a Sobel operator gradient (e.g. Gao et al., 2010) or approximate second derivatives with a Laplacian operator (e.g. Kazmin and Rienecker, 1996 or Moore et al., 1997). Beside their simplicity, the advantage of gradient operations is that the output is a field of gradient magnitudes, which can then be used to discriminate fronts by the intensity of their gradient via thresholding. However, gradient methods typically tend to amplify the noise of the initial field during the differentiation process and even more so for finer scale edge detection (Holyer & Peckinpaugh, 1989). The Canny algorithm (Canny, 1986) reduces the noise of the tracer field by adding a Gaussian filter to the traditional gradient operations. However, filtering also tends to smooth the frontal edges. The Belkin and O'Reilly Algorithm (BOA) further improves the signal to noise ratio while keeping the tracer ridges intact by using a contextual median filter with a Sobel operator (Belkin & O'Reilly, 2009). The BOA is originally designed to detect chlorophyll-a fronts but can be applied to other tracers as well, for example with temperature front detection in the South China Sea (Wang et al., 2001) and the East China Sea (Liu et al., 2018; Lin et al., 2019).

1.4.1.2. Population-based methods

Population-based methods do not estimate tracer gradients, instead they leverage the fact that fronts essentially separate two fluids with statistically different properties. The first histogram-based front detection algorithm was developed by Cayula and Cornillon. The Cayulla Cornillon Algorithm (CCA) considers a histogram of tracer values and tests whether there are two statistically different populations (i.e. two peaks) in the histogram with unsupervised machine learning methods. If the histogram features two distinct populations then a front is marked between them (Cayula & Cornillon, 1992, 1995). This operation is performed at three stages: at the picture, window, and local/pixel levels. The CCA has been widely validated and used by the scientific community and the interested reader can see a list of the numerous applications of the CCA in the review compiled by Belkin (2021). An improved version of the CCA has been developed by Nieto et al. by applying multiple sliding windows to correct front spatial continuity and increase edge detection efficiency (Nieto et al., 2012). Applications of the Nieto Algorithm include the Canary upwelling system (Nieto et al., 2012), southeast Indian Ocean (Nieblas et al., 2014), northeast Pacific Ocean (Nieto et al., 2017). Others have built on the CCA to adapt it to their research needs. For example, Miller et al. used the CCA on both temperature and chlorophyll satellite images to produce composite front maps around Scotland and the Iberian peninsula (Miller, 2009; Miller et al., 2015). Additionally, Vázquez et al. and then Shimada et al. adapted the CCA to the study of finer scales fronts by using an entropic criterion to test the bi-modality of tracer histograms. They demonstrated an improved performance on mesoscale front detection near the shore of the Iberian Peninsula (Vázquez et al., 1999) and Japan (Shimada et al., 2005). Later Kirches et al. designed a method including both the Canny Algorithm and the CCA and tailored it to North Sea satellite observations (Kirches et al., 2016). More recently, Liu and Levine (2016) and Haëck et al. (2023) used the CCA in combination with a heterogeneity index to study chlorophyll patchiness at large-to-submesoscale. The combination allowed them to classify the detected fronts based on the bi-modality of the tracer population (Cayula & Cornillon, 1992) but also on the variance and skewness of the distribution (Liu & Levine, 2016; Haëck et al., 2023).

The main shortcoming of high resolution satellite SST and ocean color images is that they are sensitive to cloud cover. Satellite altimetry is not affected by cloud cover but its resolution is not as high. Lagrangian methods such as Lyapunov exponents combine both spatial and temporal variability of the velocity field to estimate finer-scale structures like ocean fronts, independently of cloud cover. Velocity-based front detection methods are thus complementary tools to tracer-based edge detection.

1.4.2. Detecting ocean fronts from circulation

In addition to Eulerian tracer-based front detection methods, one can map ocean fronts from the ocean circulation.

Since fronts are areas of horizontal flow convergence, one can estimate their location by adopting a Lagrangian perspective and advecting artificial particles in a modelled or remotely-sensed velocity field. In this framework, we expect our artificial particles to reveal lines where the flow converge, also highlighting transport barriers. Those lines are referred to as attracting Lagrangian Coherent Structures (LCS). Attracting LCS are useful tools to visualize the boundaries between water masses with distinct flow dynamics, for e.g. eddies, filaments and fronts (Beron-Vera et al., 2008; Prants, 2023). Amongst Lagrangian diagnostics, Finite-Size Lyapunov Exponents (FSLE) are one of the most popular tools to map attracting LCS and thus ocean fronts (Aurell et al., 1997; Boffetta et al., 2001; Haller, 2015; Prants, 2023). This is the Lagrangian tool we chose to complement the BOA algorithm for ocean front detection.

To understand the definition of FSLE, we can picture two particles, initially separated by a distance δ_0. Then let those two particles being advected by a known velocity field until the distance separating them reaches δ_f. The time it takes for the two particles to reach the distance δ_f between them is τ. In practice, the artificial particles cannot be advected indefinitely, and so one also needs to set a maximum time of integration. After advecting the artificial particles for the maximum time of integration, the FSLE are defined as:

$$\lambda(x,t,\delta_0,\delta_f) = \frac{1}{\tau} log(\frac{\delta_f}{\delta_0}) \tag{1.2}$$

FSLE can be tuned to study specific spatial and temporal scales of interest by choosing adequate δ_0, δ_f and maximum time of integration. First, the initial distance δ_0 is usually set equal to the distance between two neighbouring grid points in the FSLE grid. The spatial resolution of the final FSLE grid can be higher than the resolution of the initial velocity grid, to some extent. A balance must be found between too low spatial resolutions to map oceanic features of interest and too high resolutions resulting in spurious numerical results (Hernández-Carrasco et al., 2011). Second, the final distance between advecting particles δ_f should reflect the spatial scale of interest. For example, to study mesoscale structures, one would set δ_f so that $\delta_f - \delta_0$ is of the order of 100 km (e.g. Tew Kai et al., 2009). Third, the value of maximum integration time should allow enough time for the relevant Lagrangian structures to develop. In practice, when τ values exceed the maximum integration time, meaning when the particles have not reached the final distance δ_f at the maximum integration time, λ is set to zero.

The resulting FSLE maps thus show the inverse time scale necessary to the mixing of water masses at the spatial scale defined by $\delta_f - \delta_0$ (Aurell et al., 1997; Haller, 2015). To go back to ocean fronts, ridges of elevated FSLE values delineate transport barriers, also referred to as hyperbolic LCS, useful to detect eddies, filaments and fronts (Haller, 2015; Lehahn et al., 2018). More specifically, if the particles are advected forward in time, the resulting FSLE ridges will reveal lines of locally high divergence. If they are advected backward in time, the FSLE ridges correspond to lines of local convergence. In this case, ridges of high backward FSLE values thus identify *dynamical fronts* also referred to as *Lagrangian fronts* (Baudena et al., 2021; Prants, 2023).

Other Lagrangian methods exist to map dynamical fronts (Haller, 2015; Prants, 2023). The most popular alternatives are Finite-Time Lyapunov Exponents (FTLE). FTLE are similar to FSLE, but instead of advecting artificial particles until their reach a specific distance δ_f, they are advected until a specific time is attained. FTLE give information about the inverse space scale necessary to the mixing of water masses within the specified time scale of interest. Examples of front detection using FTLE include Gough et al., 2016 and Bakhoday-Paskyabi, 2020.

Backward in time FSLE are particularly well suited to study ocean fronts for several reasons. First, they are derived from velocity fields which can easily be obtained via satellite altimetry and independently of cloud cover. Second, they can robustly estimate flow structures at a smaller spatial resolution than the initial velocity field (Hernández-Carrasco et al., 2011). And third, they integrate both spatial and temporal variability of the flow (Aurell et al., 1997; Haller, 2015).

1.4.3. Front detection methods based on tracers and circulation are complementary

Finally, backward FSLE complement tracer-based methods of front detection. Indeed they often coincide with high tracer gradients (Bettencourt et al., 2017; Rousselet et al., 2018) and they have been extensively used to investigate the transport of tracers such as temperature and chlorophyll (e.g. d'Ovidio et al., 2004; Lehahn et al., 2018; Hernández-Carrasco et al., 2018, 2020; Hernández-Carrasco et al., 2023). Moreover, tracer-based and circulation-based methods offer different effective spatial coverage for the same area of interest. On one hand SST datasets are impacted by cloud cover while satellite altimetry is not. On the other hand, backward FSLE algorithms do not perform well on the border of the computing domain and near the coastal boundaries, while tracer-based methods are not affected by border artefacts as much. Additionally, while remotely-sensed SST concerns only the near-surface layer of the water column, SSH from satellite altimetry incorporates the effects of both surface and subsurface thermohaline processes. Circulation-based methods derived from altimetry thus also offer robust estimates of flow properties at depth (Bettencourt et al., 2012, 2017; Siegelman et al., 2020b).

KEY POINTS

- Front detection methods can be divided in two categories, each tackling a different aspect of the front definition.
- Eulerian tracer-based methods highlight sharp tracer gradients, they include gradient-based and population-based algorithms.
- Lagrangian circulation-based methods reveal Lagrangian Coherent Structures and thus dynamical fronts.
- In this thesis, we leverage the complementary aspects of the 2 different approaches and use both the Belkin and O'Reilly Algorithm (BOA) and backward Finite-Size Lyapunov Exponents (FSLE) to map ocean front positions.

To the interested reader

Tracer-based methods of front detection are reviewed and presented with numerous applications in Belkin, 2021. The Lagrangian techniques mentioned in this section are evaluated in greater detail in Boffetta et al., 2001; Hernández-Carrasco et al., 2011; Haller, 2015; Lehahn et al., 2018; Prants, 2023.

1.5. Why fronts are relevant in a changing climate

The interest in frontal systems spans multiple disciplines. Ocean front variability has consequences for the Earth's climate, chemistry, biology, ecology and across the whole range of spatial scales. In this section, we try to highlight the complexity and inter-dependence of processes occurring at oceans fronts.

1.5.1. Fronts feedbacks to climate

The local dynamics happening at ocean fronts are not isolated from the broader climate system: frontal zones are major actors of ocean and climate variability.

The ocean at large is directly affected by the atmosphere, through changes in buoyancy and momentum fluxes (Sverdrup, 1947; Pedlosky, 1979). On smaller scales, wind stress impacts the development of mesoscale activity (Hogg et al., 2009; Backeberg et al., 2012; Munday & Zhai, 2015; Hogg et al., 2015) and frontogenesis (Thomas & Lee, 2005; Thomas & Ferrari, 2008). Indeed, ocean models reproduce mesoscale activity better when they are forced by realistic winds (Renault et al., 2016a). In turn, mesoscale eddies and fronts respond to the atmospheric circulation by modulating surface flux anomalies. Not only do these mesoscale flux anomalies have a regional impact in the marine atmospheric boundary layer but also a broader influence on the climate system.

Eddies and fronts interact with the atmospheric boundary layer via *thermal feedbacks* (Small et al., 2008; Renault et al., 2019). This was first shown through positive correlations between SST and wind stress anomalies over regions of rich mesoscale activity: e.g. in the tropics (Small et al., 2005), at midlatitudes (Gaube et al., 2015), along WBC (O'Neill et al., 2012) and in the southern ocean (Frenger et al., 2013). This thermal feedback was shown to impact the strength of large scale ocean circulation (Hogg et al., 2009) and the position of planetary scale fronts associated with WBC (Ma et al., 2016) in eddy-resolving simulations. Eddies and fronts also interact with the atmospheric boundary layer via *current feedbacks* (Renault et al., 2019), which was shown to dampen local eddy kinetic energy in the Gulf Stream (Renault et al., 2016b) and California Current System (Seo et al., 2016; Renault et al., 2018). At larger scales, air-sea interactions happening in frontal zones such as the Gulf Stream and Kuroshio extensions are strong enough to nudge storm tracks (Nakamura et al., 2013; Small et al., 2014; O'Reilly & Czaja, 2015; Kuwano-Yoshida & Minobe, 2017) and large-scale climate variability (Seo et al., 2006; Minobe et al., 2008; Frankignoul et al., 2011; Frenger et al., 2013; Ma et al., 2015).

1.5.2. Fronts and the carbon cycle

Another way in which ocean fronts contribute to climate variability is through the carbon cycle. Carbon is the backbone of life. It is found in sediments, in the atmosphere, in the oceans and in living organisms. We speak about the carbon *cycle* because

carbon flows between reservoirs: from the atmosphere to the ocean, from phytoplankton to zooplankton all the way up to higher trophic levels, then to decomposers, to sediments in the ocean floor and back to the atmosphere we breathe (Williams & Follows, 2012). Since the industrial revolution, anthropogenic activities have released significant amounts of carbon dioxide in the atmosphere, affecting the natural carbon cycle and unequivocally causing global warming (Hansen et al., 1981; IPCC, 2023). Understanding ocean fronts variability and their related biogeochemical processes is important in a changing climate to improve the performance of Earth System Models and refine estimates of carbon sequestration in the ocean .

1.5.2.1. The biological pump

Fronts can modulate the rate at which carbon is sequestrated in the ocean via subduction processes (e.g. Omand et al., 2015; Dall'Olmo et al., 2016; Stukel et al., 2017; Boyd et al., 2019) but also via the *biological pump*.

Organic carbon enters the ocean via photosynthesis from plant-like phytoplankton organisms. During photosynthesis, carbon dioxide is converted into sugars to build organic matter as soft or hard tissues. Phytoplankton is then eaten by zooplankton, which marks the base of the trophic chain. Marine organisms are then either eaten by higher trophic level individuals or sink towards the ocean floor at the end of their life cycle. Some of the carbon contained in their bodies is dissolved back into the deep ocean via remineralization while the rest lands on the ocean floor sediments. This combination of complex processes, shortly summarized here, is referred to as the biological pump (Williams & Follows, 2012).

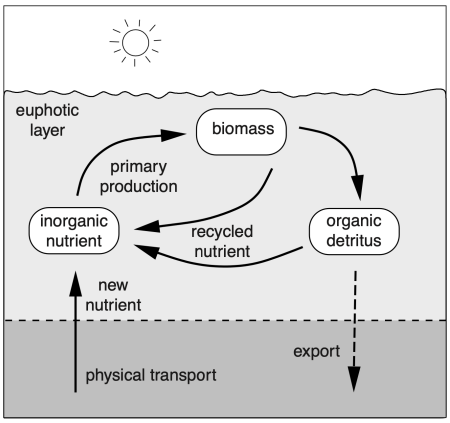

Figure 1.6.: Primary productivity is dependent on nutrient input in the sun-lit euphotic layer. Figure extracted from Williams and Follows, 2012.

Phytoplankton ability to photosynthesize, or *primary productivity*, and with it the productivity of the biological pump, is limited by light and nutrient availability (Fig. 1.6). Light is available in the top layer of the water column, the euphotic layer, which is usually defined as the depth at which light reaches 1% of its surface value (Fig. 1.6 in light grey). The euphotic layer rarely exceeds 150 m in the clearest ocean

regions. Inorganic nutrients such as phosphates, nitrates but also iron and silicates are consumed by phytoplankton in the presence of light, in the euphotic layer. However, below the euphotic layer, in the dark deep ocean (Fig. 1.6 in darker grey), nutrients remain more abundant because they are not consumed. This simplified view of the biological pump (Fig. 1.6) thus opposes a nutrient-poor euphotic layer to a nutrient-dense ocean interior. Marine primary productivity would end if not for nutrient input into the euphotic layer. Such input can happen either via atmospheric depositions and river discharge, or via ocean horizontal and vertical mixing processes (Williams & Follows, 2003, 2012).

Ocean fronts are particularly relevant to the carbon cycle, via the biological pump, because their associated vertical velocities can alter the availability of nutrients in the euphotic layer.

1.5.2.2. Fronts, nutrients and light availability

The overturning circulation occurring at active fronts (Fig. 1.4 b.) brings nutrient-rich deep waters into the euphotic layer and sink nutrient-poor surface waters below the euphotic layer. This frontal process contributes to the vertical nutrient exchange necessary to maintain biological production in the well-lit upper ocean. (Klein & Lapeyre, 2009; Mahadevan, 2016).

One can see the effect of meso-to-submesoscale structures, i.e. eddies and fronts, nutrient fluxes by contrasting two biogeochemical simulations, one resolving mesoscale (or submesoscale) processes and one that does not (Oschlies & Garçon, 1998). Numerical experiments in which the spatial resolution is progressively increased could thus quantify the effect of mesoscale (Mahadevan & Archer, 2000) and submesoscale (Lévy et al., 2001) dynamics on nutrient exchanges. Those enhanced vertical biogeochemical fluxes have also been studied specifically in several large front-rich areas, including at the Southern Ocean fronts (Pollard et al., 2002; Wang et al., 2003; Freeman et al., 2018), the Gulf Stream front (Wenegrat et al., 2020; McKee et al., 2023), Kuroshio Extension front (Nagai & Clayton, 2017) and in the California Current system (Li et al., 2012), all exhibiting significant impacts on regional primary productivity. Furthermore, submesoscale nutrient injections were found particularly strong during extreme weather events such as storms (Whitt et al., 2019; Barrillon et al., 2023). At high latitude, in nutrient-rich but light-limited regions, ocean fronts also alter the primary productivity by modifying mixed-layer stratification and increasing light availability (Sverdrup, 1953; Taylor & Ferrari, 2011a; Taylor & Ferrari, 2011b).

Ocean fronts are thus key physical structures modulating nutrient and light availability in the upper ocean, thereby affecting primary productivity and carbon storage into the ocean.

1.5.3. Fronts and ecology

By boosting primary productivity locally, ocean fronts create ecological niches, favored by marine organisms from all trophic levels: from plankton to pelagic fish and all

the way up to top predators. Understanding the variability of ocean fronts is critical to improve ecological models and predictions, tackle contemporary challenges of fishery sustainability (Scales et al., 2023) and design effective marine spatial planning (Maxwell et al., 2015; Bates et al., 2018).

1.5.3.1. Fronts structure plankton communities

Ocean fronts impact plankton biomass. Higher plankton biomass at ocean fronts has been observed in models (Franks, 1992; Abraham, 1998; Lima et al., 2002), satellite observations (Hernández-Carrasco et al., 2020; Haëck et al., 2023) and in-situ observations: e.g. in the Mediterranean Sea (Thibault et al., 1994; Hernández-Carrasco et al., 2018; Tzortzis et al., 2021), in the California Current System (Ohman et al., 2012; Luo et al., 2014), and in the Pacific Ocean (Bertrand et al., 2014; Liu & Levine, 2016; Benavides et al., 2021). Several processes are involved in the increase of plankton biomass at fronts (Lévy et al., 2018; Mangolte et al., 2023). The vertical velocities associated with ocean fronts directly drive plankton biomass increases due to nutrient injection in the well-lit upper ocean (Allen et al., 2005; Mahadevan, 2016; Mangolte et al., 2022). However, the vertical overturning circulation happening at fronts can also remove plankton and/or nutrients from the euphotic zone by subducting them to deeper layers (Lévy et al., 2001; McGillicuddy et al., 2003). Plankton is also more abundant at fronts because of the along-front horizontal convergence of the flow. However this process was shown to have a much lesser impact than nutrient injection from an ocean-ecosystem model focusing on a WBC (Mangolte et al., 2022).

Fronts also impact plankton biodiversity. In persistent fronts, such as those formed by powerful WBC, frontal structures act as a barrier separating two water masses and therefore two distinct plankton communities (Bower et al., 1985; Hunt & Hosie, 2005; d'Ovidio et al., 2010; Clayton et al., 2014; Lévy et al., 2015). Tzortzis et al. (2021) also showed from in-situ data that less energetic fronts can segregate plankton communities. Furthermore, the variability and patchiness of plankton communities have also recently been shown to operate at scales finer than those of their related fronts (Benavides et al., 2021; Mangolte et al., 2023). This suggests that trophic interactions at ocean fronts are not only driven by fluid dynamics and that not all types of plankton benefit from the frontal nutrient injections to the same extent. For example Mangolte et al. (2022) demonstrated in a WBC frontal zone that some types of phytoplankton can modify the optical properties of the upper euphotic layer, thereby limiting light availability for deeper communities.

The increased plankton biomass and biodiversity at ocean fronts then impact the distribution and behaviour of higher trophic level marine species.

1.5.3.2. Fronts aggregate pelagic fish and top predators

Because frontal zones are convergent areas of higher productivity they attract foraging fish and top-predators.

Although fishermen have been seeking out ocean fronts for decades, recent studies

have indeed demonstrated the higher abundance of pelagic fish in frontal zones (Bertrand et al., 2014; Prants et al., 2014; Tseng et al., 2014; Woodson & Litvin, 2015; Morato et al., 2016; Baudena et al., 2021) and subsequent greater fishing effort at fronts (Alemany et al., 2014; Oh et al., 2020). Some fronts have been found to form favourable conditions for fish spawning (Mariani et al., 2010; Nieblas et al., 2014; Nieto et al., 2017; Netburn & Koslow, 2018) and foraging (Polovina et al., 2001). Fronts also appear to affect fish connectivity and biodiversity by acting as dynamical barriers (Alemany et al., 2009; Galarza et al., 2009; Hernández-Carrasco & Orfila, 2018; Sato et al., 2018; Ser-Giacomi et al., 2021).

Additionally, numerous studies have documented higher occurrences of top-predators at ocean fronts. At the mesoscale, frontal zones offer transient habitats to tunas (Fiedler & Bernard, 1987; Xu et al., 2017; Snyder et al., 2017), sharks (Queiroz et al., 2012, 2016; Ryan et al., 2017), turtles (Polovina et al., 2000, 2001), marine mammals (Doniol-Valcroze et al., 2007; Bost et al., 2009; Murase et al., 2014; Cotté et al., 2015; Fonvieille et al., 2023) and sea-birds (Weimerskirch et al., 2004; Tew Kai et al., 2009; Schneider, 1990; Scheffer et al., 2010; Scheffer et al., 2012; Scales et al., 2014a; Sabarros et al., 2014). The importance of submesoscale fronts in particular has been highlighted for sharks (Sims & Quayle, 1998) and marine mammals (Cotte et al., 2011; Scales et al., 2018; Siegelman et al., 2019).

The aggregation of higher trophic level taxa at ocean fronts could be linked to several non-exclusive processes. First, predators may gather at ocean fronts because of the locally enhanced primary productivity, in turn sustaining the supply of prey from aggregating zooplankton to foraging fish. Second, the along-front horizontal flow convergence may increase the encounter rate between preys and predators. Third, ocean fronts could procure predators with a physiological edge over their preys (Sims & Quayle, 1998; Kirby et al., 2000; Snyder et al., 2017).

Subsequently, ocean fronts enhance bycatch and depredation risks by attracting both fisheries and marine megafauna (Scales et al., 2018; Tixier et al., 2021). They are thus becoming dynamical hotspots of vulnerability (Scales et al., 2014b) and calling for more dynamical marine protected areas (Maxwell et al., 2015; Brito-Morales et al., 2022). A holistic understanding of ocean fronts and their interactions with marine life is thus key to balance the conflicting needs of fisheries and biodiversity conservation.

Because ocean fronts impact so many key processes across a variety of disciplines, one needs a holistic and multidisciplinary approach to improve understanding of frontal systems and their variability in a changing climate. The Mozambique Channel is an ideal laboratory to study ocean front variability and their interactions with marine ecosystems.

KEY POINTS

Ocean fronts are relevant to study in a changing climate because they:

- impact climate variability by modulating heat, carbon and momentum fluxes between ocean and atmosphere
- feature a vertical overturning circulation facilitating light and nutrient availability in the euphotic layer
- enhance primary productivity and thus impact the rate of carbon sequestration
- appear to aggregate zooplankton, pelagic fish and top-predators

To the interested reader

This section is meant to provide a succinct overview of the cross-disciplinary and complex processes happening at ocean fronts. In-depth reviews of ocean front physical, biogeochemical and ecological processes are presented in Small et al., 2008, Klein and Lapeyre, 2009, Scales et al., 2014b, McWilliams, 2016, Mahadevan, 2016, McGillicuddy, 2016, Lévy et al., 2018, McWilliams, 2021 and Seo et al., 2023.

1.6. The Mozambique Channel

1.6.1. Circulation in the Mozambique Channel

The Mozambique Channel (MC) is located in the southwest Indian Ocean between Madagascar Island and the African mainland, and is considered part of the greater Agulhas system (Fig. 1.7). The Channel is characterized by a turbulent flow which makes it ideal to study ocean fronts (Schott & McCreary, 2001; Lutjeharms, 2006; Phillips et al., 2021).

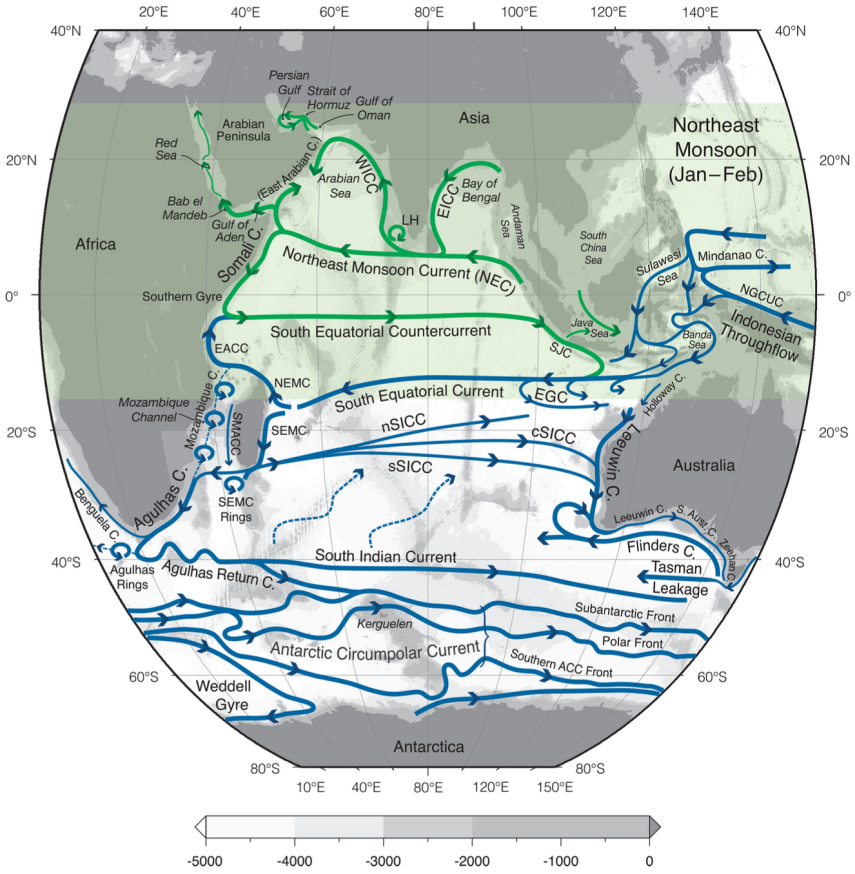

Figure 1.7.: Bathymetry and main surface currents in the Indian Ocean. The grey shading correspond to the bathymetry. The green shading marks the area influenced by the Monsoon. The current acronyms correspond to: **EACC** : East African Coastal Current; **EICC**: East Indian Coastal Current; **EGC**: Eastern Gyral Current; **LH**: Lakshwadeep high; **NEC**: Northeast Monsoon Current; **NEMC**: Northeast Madagascar Current; **SEMC**: Southeast Madagascar Current; **SICC**: South Indian Countercurrent ; **SJC**: South Java Current; **SMACC**: Southwest Madagascar Coastal Current; **WICC**: West Indian Coastal Current. Figure extracted from (Phillips et al., 2021).

The circulation of the northern MC is influenced by biannual monsoons wind

reversals. Winds blow from the northwest during the Northeast Monsoon (January to February), and from the southeast during the Southwest Monsoon (July to August). South of 20°S, winds blow from the southeast all year round (Schott & McCreary, 2001; Schott et al., 2009; Obura et al., 2019; Phillips et al., 2021).

The circulation in the MC is driven by the South Equatorial Current (SEC) (Sætre & Da Silva, 1984). East of Madagascar the SEC divides itself into the North East Madagascar Current (NEMC) and the South East Madagascar Current (SEMC). The NEMC flows northwestwards from the northern tip of Madagascar towards the Mozambican coast and join the East African Coastal Current (EACC). The SEMC flows south along the eastern Madagascar shelf, then part of it flows southwestwards to join the Agulhas Current (AC) while the remaining part retroflects eastward to form the Subtropical Indian Ocean Countercurrent (SICC). The NEMC transports around 30-40 Sv at the northern tip of Madagascar. The SEMC transports around 20 Sv southward along Madagascar east coast (Schott & McCreary, 2001; DiMarco et al., 2002; Siedler et al., 2006; Collins et al., 2014; Ramanantsoa et al., 2021).

Being located west of the southern Indian Ocean subtropical gyre, one could expect a western boundary current (WBC) to form within the MC (Pedlosky, 1979). However, the MC features a rather weak and intermittent flow along the Mozambican shelf, also referred to as the Mozambique Current (MZC) (poleward, near surface) and the Mozambique Under Current (MZUC) (equatorward, deep) (de Ruijter et al., 2002; Biastoch et al., 2009; Lutjeharms et al., 2012). Indeed, the absence of a typical WBC in the MC has then been attributed to the presence of Madagascar Island (Penven et al., 2006). The transport through the Channel is carried instead by successive trains of eddies propagating poleward, they combine with the SEMC eddies and feed the Agulhas current (de Ruijter et al., 2002; Schouten et al., 2003; Ridderinkhof & de Ruijter, 2003; Quartly et al., 2006; Ridderinkhof et al., 2010; Ramanantsoa et al., 2021).

The MC eddies have a typical spatial scale of several hundreds of kilometers. The largest anti-cyclonic eddies in the MC are often referred to as *Mozambique rings* when their radius exceeds 100 km. They usually form south of the Comoros Basin and their tracks follow closely the Mozambique shelf break (Fig. 1.8). The rings propagate southwest at a speed of 3 to 10 kilometers per day and at a rate of about 4 to 7 per year. Smaller anti-cyclonic eddies usually form south of 16°S, their life cycle is much shorter and is proportional to their size (de Ruijter et al., 2002; Schouten et al., 2003; Halo et al., 2014). Cyclonic eddies are more numerous yet smaller than their anti-cyclonic counter-parts, they can form *dipoles* when developing on the side of an anti-cyclonic eddy. They appear everywhere in the Channel but are particularly numerous on its eastern and southeastern boundaries (Siedler et al., 2009; Halo et al., 2014; Roberts et al., 2014).

The turbulent circulation and narrow topography of the MC provide the ideal test-bed to study both persistent and ephemeral ocean fronts. The turbulent dynamics of the MC are responsible for significant transport of nutrient-rich coastal and deeper waters to the euphotic layer, sustaining high biomass and biodiversity in the Channel.

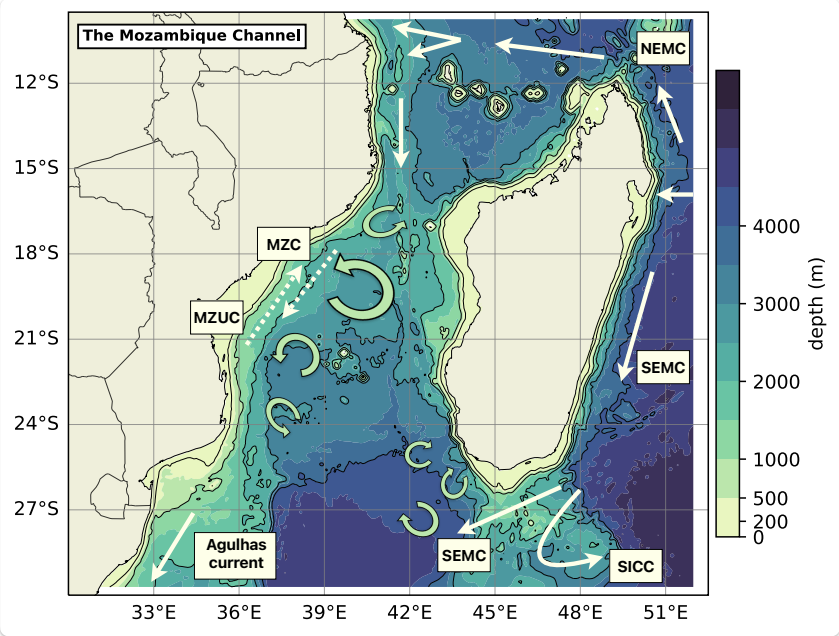

Figure 1.8.: Bathymetry and main currents in the Mozambique Channel and around Madagascar. The currents shown are the Northeast Madagascar Current and Southeast Madagascar Current (**NEMC** and **SEMC**, respectively), the South Indian Countercurrent (**SICC**), the Mozambique Current (**MZC**), the Mozambique Under Current (**MZUC**) and the Agulhas Current (**AC**). The background black contours represent isobaths at -200, -500, -1000, -2000, -3000 and -4000 m. The colormap is from cmocean (Thyng et al., 2016).

1.6.2. Biomass and biodiversity in the Mozambique Channel

The turbulent circulation and particular topography of the MC (Fig. 1.8) result in higher biological productivity by facilitating eddy-shelf interactions. The enhanced primary productivity fostered by mesoscale activity in the Channel sustains high biodiversity in higher trophic levels. The MC is thus ideal to study interactions between marine organisms and ocean fronts.

Mozambique rings and eddy dipoles can transport nutrient-rich waters from the continental shelves to the open ocean. Subsequently, ocean fronts forming in the strained corridors between dipole eddies or at the radial edge of lone eddies near shelves can form long filaments carrying enriched waters to the open ocean and enhance primary productivity offshore (Tew-Kai & Marsac, 2009; Marsac et al., 2014; Roberts et al., 2014). For example, Roberts et al. (2014) used in-situ and satellite observations to investigate shelf-eddy processes. They found that the interaction between the Mozambique shelf and a dipole resulted in horizontal divergence, leading to upwelling at the shelf, thereby enhancing primary productivity locally. They documented

the formation of a long chlorophyll filament developing between the dipole eddies, extending further offshore and traveling southward with the dipole (Roberts et al., 2014). The eddy circulation also boosts primary productivity in the Channel via the transient upwelling observed within cyclonic eddies (Tew-Kai & Marsac, 2009). This enhancement is intensified when the eddy is formed near continental shelves and the subsequently advected nutrient-rich water remains trapped in the cyclone (José et al., 2014; Barlow et al., 2014; Huggett, 2014). Similarly, anti-cyclonic eddies can also present higher productivity if the water trapped in their core is advected from the shelf (José et al., 2014; Béhagle et al., 2014).

Upwelling cells near the MC continental shelves also facilitate biological production in the region (Vinayachandran et al., 2021). A seasonally intermittent upwelling cell was identified near Angoche (Mozambique), between 15°S and 18°S. Malauene et al. 2014 demonstrated that the Angoche upwelling events occur between August and March, while April to July showed a much reduced SST variability. They attributed these events to upwelling-favourable winds occurring during the Northeast Monsoon. The cool nutrient-rich upwelled waters are then transported offshore and southward with passing eddies coming near the shelf (Malauene et al., 2014). Pripp et al. (2014) surveyed the opposite side of the Channel, along the Madagascar shelf. They analyzed in-situ cruise CTD[2] measurements, current profiles, acoustic and trawl biomass estimates as well as whale observations. They identified three additional upwelling zones: Nosy Be Island at 13°S, Cap St. André at 16°S and another one at the southern tip of Madagascar Island around 26°S. The first two upwelling regions were associated to passing eddies, the third one was linked to favourable winds. The upwelling zone situated south of Madagascar was also reported from satellite observations first from ocean color (Ho et al., 2004) and then from SST, chlorophyll-a, and altimetry (Ramanantsoa et al., 2018). Ramanantsoa et al. (2018) complemented satellite observations with in-situ data and a numerical model to study the variability of the upwelling region. They found that the South Madagascar upwelling originates from two cells, located on opposite sides of the island's southern tip, and with distinct drivers, seasonal variability and intensity. The southeast upwelling cell is mostly driven by variation in the SEMC and intensified by upwelling-favourable winds. The southwest upwelling cell is mostly driven by upwelling favourable winds (Ramanantsoa et al., 2018). All four upwelling regions were associated with higher biological activity than what is normally expected in tropical waters (Pripp et al., 2014; Malauene et al., 2014; Ramanantsoa et al., 2018).

The MC exhibits high biodiversity across all levels of the trophic chain thanks to extensive and diverse tropical habitats such as coral reefs, mangrove forests, seagrass beds, and a turbulent pelagic zone (Tittensor et al., 2010; Obura, 2012; Unep-Nairobi Convention, 2015; Obura et al., 2019).

In-situ cruise observations have demonstrated the diversity in plankton (Barlow et al., 2014; Huggett, 2014), micronekton (Béhagle et al., 2014; Annasawmy et al., 2018)

[2] conductivity, temperature and depth

and especially along the fronts in-between eddies (Sabarros et al., 2009). Further up the food chain, the MC is an important spawning site for tropical tuna species and at the center of their migration routes (Hallier & Fonteneau, 2015; Obura et al., 2019). The southwest Indian Ocean is indeed characterized by intense tropical tuna fisheries (Sequeira et al., 2012; Kaplan et al., 2014; Chassot et al., 2019; Nataniel et al., 2022).

The Channel is also a hotspot of megafauna species (Laran et al., 2017; Mannocci et al., 2014; Obura et al., 2019) and bycatch (Lewison et al., 2014). The Scattered Islands in the southern MC are key breeding and foraging grounds for numerous species of seabirds (Le Corre et al., 2012). And several studies have investigated the relationship between Great Frigatebirds and mesoscale activity in the Channel, and found that they forage preferentially along the edge of eddies (Weimerskirch et al., 2004; Tew Kai et al., 2009; Tew Kai & Marsac, 2010; Weimerskirch et al., 2010). Green turtles nest in the Northern part of the Channel (Bourjea et al., 2007; Benhamou et al., 2011), while loggerhead turtles have been found to forage and remain in the shallow waters of the MC (Robinson et al., 2016). Populations of large elasmobranchs such as whale sharks and manta rays have been studied on the Mozambique and Madagascar shelves (Rohner et al., 2013; Rohner et al., 2018; Diamant et al., 2018; Venables et al., 2020) and predicted to be abundant in the Channel from fisheries sightings (Sequeira et al., 2012; Sequeira et al., 2013; Sequeira et al., 2014). Significant cetacean diversity and abundance was reported around the island of Mayotte, in the northern MC (Kiszka & Ridoux, 2007; Gross et al., 2009; Kiszka et al., 2009) and across the entire Channel (Fossette et al., 2014; Mannocci et al., 2014; Findlay et al., 2020).

KEY POINTS

The Mozambique Channel (MC) is characterised by:

. a turbulent flow made of successive trains of mesoscale eddies propagating southward

. higher primary productivity than what is normally expected of an oligotrophic system, boosted by the eddy circulation and upwelling cells

. high biodiversity at all levels of the trophic chain

To the interested reader

This section is meant to provide a quick overview of the characteristic circulation, turbulence and biodiversity of the MC. Interested readers might also be interested in the reviews by Schott and McCreary, 2001, Marsac et al., 2014, Obura et al., 2019 and Phillips et al., 2021.

1.7. Gaps, objectives and plan

Fronts are meeting place in the ocean where marine organisms congregate across all trophic levels. The presence of marine top predators at fronts has been widely documented, and especially so since the availability of animal tracking devices (e.g. Siegelman et al., 2019 and Fonvieille et al., 2023). However a holistic understanding of marine ecosystem interactions with fronts remain largely speculative, particularly so with ephemeral fronts (Lévy et al., 2018). Predictable frontal ecosystems, such as those associated with persistent or mesoscale fronts lasting for several months are easier to study than the transitory ecosystems forming at submesoscale fronts. The main difficulty in sampling or modeling marine ecosystem interactions with ephemeral fronts resides in their associated fine scales. On the one hand, cruise measurements are challenged by the unpredictability of both physical structures and mobile organisms. On the other hand, high-resolution numerical models are computationally expensive. A direct consequence of the computational cost is that contemporary climate projections from global earth system models do not have a spatial resolution fine enough to resolve submesoscale structures such as ephemeral fronts. This means that little is known about ephemeral fronts variability in response to climate change.

The focus of this work is on ocean front variability at fine spatial (a few kilometers to a few hundreds of kilometers) and temporal (a few days to a few years) scales. Geographically, we focus on the Mozambique Channel (MC), because of its unique turbulent flow and high biodiversity. The objectives of this thesis is to contribute to a better understanding of present and future variability of fine-scale ocean fronts in the MC to inform future marine conservation initiatives in the Channel. We aim to fill the current knowledge gaps related to ocean front variability in the MC by focusing on the following research questions:

1. where are ocean fronts more frequent in the MC?
2. how deep do they extend in the water column?
3. what is driving their seasonal variability in the MC?
4. how will fronts change in response to global warming?

Following the present Introduction, the data and methods used in the thesis are summarized in Chapter 2. Chapter 3 offers a description of spatial and seasonal variabilities of mesoscale eddy activity and thermal fronts in the MC from a hindcast simulation and satellite observations. Chapter 4 investigates the changes in mesoscale eddy activity and thermal fronts in a pseudo global warming experiment of the MC. Chapter 5 describes the multidecadal high-resolution front dataset that we designed to study interactions between fronts and marine megafauna in the Southwest Indian Ocean. The comparison between fronts and megafauna in the Southwest Indian Ocean is an ongoing collaborative work with Isaac Brito-Morales (Conservation International) illustrating the value in the present work for multidisciplinary applications.

2. Methods

Content

2.1. Prologue . . . 51
2.2. Satellite data . . . 52
2.2.1. Sea surface temperature . . . 52
2.2.2. Sea surface velocities . . . 52
2.3. Models . . . 52
2.3.1. The original MOZ36 . . . 53
2.3.2. The experiments: MOZ36_CR, MOZ36_F, MOZ36_repeat . . . 53
2.3.2.1. The control run: MOZ36_CR . . . 54
2.3.2.2. The pseudo global warming run: MOZ36_F . . . 54
2.3.2.3. The repeat run: MOZ36_repeat . . . 54
2.4. Numerical methods . . . 55
2.4.1. Eddy kinetic energy . . . 55
2.4.2. Front detection . . . 55
2.4.2.1. Thermal front detection . . . 55
2.4.2.2. Dynamical front detection . . . 56

2.1. Prologue

In this Chapter 2, I provide a succinct overview of the datasets and methods used for the thesis as well as my contribution to each data processes. The interested reader may refer to the associated publications in Chapters 3, 4 (in preparation) and 5 for detailed accounts of methods and datasets.

We investigate ocean fronts in the MC from both Eulerian and Lagrangian perspectives, for which we need sea temperatures and velocities. Temperatures are needed to estimate thermal gradients and thus *thermal fronts*, while velocities are needed to estimate turbulence in the Channel and to compute backward FSLE and thus *dynamical fronts*. We use temperature and velocity fields from satellite observations and high-resolution ocean models.

2.2. Satellite data

2.2.1. Sea surface temperature

We analyze sea surface temperature (SST) from the MUR SST. The dataset is provided daily on a 1/100° (approximately 1 km) grid. The MUR SST dataset integrates several satellite and in-situ products, whose spatial resolution range from 1 to 25 km. Infrared products have higher spatial resolution (1 to 9 km in MUR SST) but they are sensitive to clouds thereby limiting their effective coverage. Microwave products are much less sensitive to clouds which improves their effective coverage but at the cost of their spatial resolution (25 km in MUR SST). MUR SST integrates and interpolates those different satellite products and point-wise in-situ observations by the so-called Multi-Resolution Variational Analysis method, which employs scale-dependent time windows to adjust for various spatial resolutions (Chin et al., 2017). We chose the MUR SST dataset to compromise between high spatial resolution and reduced impact from cloud cover.

2.2.2. Sea surface velocities

Total currents are taken from the Altimetric absolute geostrophic velocities and Modeled Ekman Current Reprocessing from the CMEMS. This product was previously referred to as MULTIOBS_GLO_PHY_REP_015_004, and is now included in MULTIOBS_GLO_PHY_MYNRT_015_003. The dataset is provided daily on a 1/4° (about 25 km) grid. Geostrophic velocities are taken from Ssalto/Duacs delayed-time multimission maps of altimeter height and geostrophic velocity anomalies distributed by Archiving, Validation, and Interpretation of Satellite Oceanographic (AVISO) and the Ekman velocity components are computed from ECMWF Reanalysis v5 (ERA5) wind stress (Rio et al., 2014).

2.3. Models

Satellite observations provide a realistic estimate of the surface ocean state, but are limited to a few variables and to the top ocean layers. Numerical ocean models are useful to investigate fine-scale dynamical ocean processes when in-situ data is too sparse and satellite observations do not suffice. However, care should be taken when using ocean models to study ephemeral ocean processes. While ocean models are helpful to highlight statistics on time scales larger than several years, the stochastic nature of those processes implies that models cannot reproduce the exact same real-world ocean turbulence without adequate data-assimilation procedures.

Models also allow us to investigate the ocean response to global warming by adjusting atmospheric and boundary forcings to fit likely future scenarii. However, future projections from contemporary global earth systems models are computationally expensive. This means that their spatial resolution is rarely high enough to resolve

fine-scale ocean fronts. Dynamical downscaling procedures bridge the gap between low-resolution global ocean projections and high-resolution regional models.

We use high-resolution nested regional configurations of the Coastal and Regional Ocean COmmunity model (CROCO) (Shchepetkin & McWilliams, 2005; Auclair et al., 2022). The configurations are all centered on the MC and last for 22 years, they are summarized in Table 2.1. Based on this model platform, we performed various types of simulations consisting in hindcast runs, pseudo-global-warming experiments built with a dynamical downscaling procedure, and repeat experiments.

2.3.1. The original MOZ36

In Chapter 3, I use the output of a realistic CROCO simulation of the MC developed by Pierrick Penven to investigate the seasonal variability of ocean fronts.

This configuration integrates three nested grids of increasing spatial resolutions: 1/4° (MOZ4), 1/12° (MOZ12) and 1/36° (MOZ36). All simulations have 60 sigma layers and the bathymetry is taken from GEBCO 2014 (Weatherall et al., 2015), without rivers. The simulations were forced at the surface from ERA-interim Reanalysis daily mean atmospheric fields (Dee et al., 2011) and at boundaries with the GLORYS reanalysis (1/4°) from Mercator Ocean integrated in the two-way nesting feedback procedure (Marchesiello et al., 2001; Debreu et al., 2012). I analyze 22 years of daily output (e.g. temperature, velocity), from 1993 to 2014, on the 1/36° (about 3 km) child grid, referred to as MOZ36. The setup of these simulations is summarized in the first column of Table 2.1.

2.3.2. The experiments: MOZ36_CR, MOZ36_F, MOZ36_repeat

For Chapter 4, new grids at 1/12° and 1/36° were developed that resemble the original domains of MOZ12 and MOZ36. We built those new grids in order to reduce computational cost and carry out downscaling experiments with a global warming scenario without the need to run the model over extended domains. Those new grids are used in the simulations detailed in the last 3 columns of Table 2.1. With guidance from Pierrick Penven and Boris Dewitte, I designed three CROCO types of experiments with these new CROCO grids: one hindcast run and two experimental runs. Each experiment includes both a parent simulation on the new 1/12° grid and a child simulation on the new 1/36° grid. The nesting was done offline. All configurations have the same bathymetry taken from GEBCO 2014 (Weatherall et al., 2015), without tides nor river input. They all have 60 topography-following sigma layers in the vertical and the vertical grid is stretched for increased resolution at the surface (hcline = 10m and with a stretching parameter of $\theta_s = 5$), but not at the bottom. They were all run for 22 years after 3 years of spin-up. The three configurations only differ in their atmospheric and boundary forcings.

2.3.2.1. The control run: MOZ36_CR

The control run is a hindcast covering the period 1993 to 2014. At the surface, both parent and child are forced by ERA-interim Reanalysis daily mean atmospheric fields (Dee et al., 2011). At the boundaries, the parent simulation (MOZ12_CR) is forced by the original MOZ4 described in section 2.3.1. The boundaries of the child (MOZ36_CR) are forced offline by the parent (MOZ12_CR). A model assessment is included in Chapter 4 to demonstrate the ability of the control run (MOZ36_CR) to reproduce the mean state of the MC well enough to use it as a baseline.

2.3.2.2. The pseudo global warming run: MOZ36_F

The objective of this experiment is to investigate front and mesoscale eddy activity response to global warming in the MC with a dynamical downscaling procedure. We design the pseudo global warming experiment by altering the surface atmospheric and boundary forcings of the control run following the delta method. Essentially, the delta method consists in adding monthly deltas (or anomalies) to baseline forcings (Schär et al., 1996; Sato et al., 2018). The monthly deltas are given by the difference between a mean future state and a mean historical one. In this case, the mean historical state corresponds to the period that we used for the control run: 1993-2014. The mean future state is computed from the "business as usual" Representative Concentration Pathway (RCP) 8.5 scenario of one member of the Community Earth System Model Large Ensemble (CESM-LENS) over the period 2071-2100 (Kay et al., 2015). At the surface, both parent and child simulations are thus forced with the ERA-interim Reanalysis daily mean atmospheric fields (Dee et al., 2011) but with added monthly deltas. Similarly, at the open boundaries of the domain, the parent simulation (MOZ12_F) is forced by the original MOZ4 simulation upon which we added the deltas. The boundaries of the child (MOZ36_F) are forced offline by the parent (MOZ12_F).

2.3.2.3. The repeat run: MOZ36_repeat

The third experiment is a so-called repeat experiment, which means that the model is forced by the same year on a loop. The purpose of this repeat experiment is to isolate the chaotic intrinsic variability of the historical run, since this simulation will only experience forcing conditions filtered out from interannual variability. The boundary forcings are similar to those of the control experiment except that only the year 2001 is used. This particular year is selected since it is a “neutral” year. It was identified by considering climatic indices shown to have an impact on the Southwest Indian Ocean: the IOD (Saji et al., 1999; Webster et al., 1999; Cai et al., 2021)), the SIOD (Jo et al., 2022) and ENSO (Yang et al., 2015; Marathe et al., 2021). The IOD (Saji et al., 1999) and SIOD (Jo et al., 2022) indices were computed with HadISST 1.1 monthly average sea surface temperature (Rayner et al., 2003) for 1993-2014. The ENSO indices are from Conejero et al., 2020, following the methods detailed in Takahashi et al., 2011. The chosen year 2001 is the most neutral year in the aforementioned indices for the period 1993-2014 (Fig. 2.1).

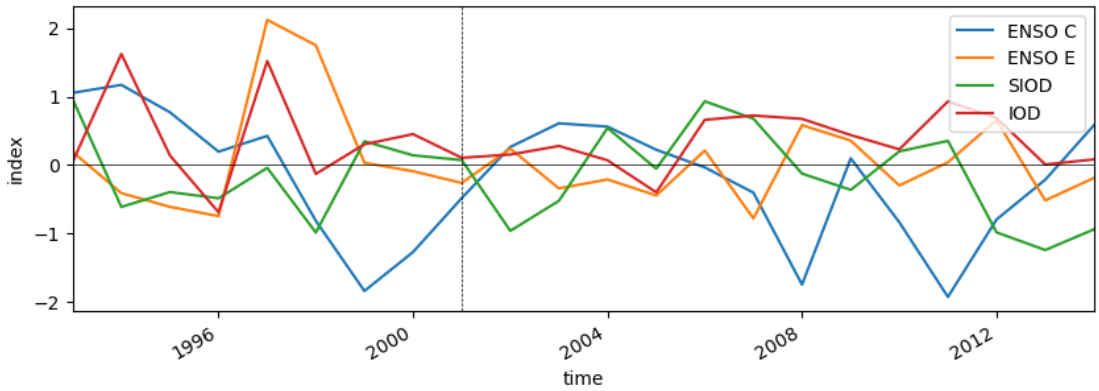

Figure 2.1.: Climatic indices shown to have an impact on the Southwest Indian Ocean: ENSO (Conejero et al., 2020), IOD (Saji et al., 1999) and SIOD (Jo et al., 2022). The vertical dotted line mark the year 2001, where all indices are minimal.

Note that the interpretation of the results derived from the repeat experiment are still ongoing and are thus not presented in this manuscript.

2.4. Numerical methods

2.4.1. Eddy kinetic energy

In Chapter 3 and 4, I examine the mesoscale variability in the MC due to eddies by quantifying the eddy kinetic energy (EKE), defined as:

$$EKE = \frac{1}{2}(u'^2 + v'^2) \tag{2.1}$$

where u' and v' are deviations from mean total velocities. To make sure that the computed EKE is only associated with the propagating eddies of the MC and excludes the interannual variability of the mean circulation, I compute the velocity anomalies from the 3-month running mean of total currents. We call it the *intra-seasonal* EKE. To compute the *inter-annual* EKE, velocity anomalies are computed from their climatologies.

2.4.2. Front detection

2.4.2.1. Thermal front detection

In Chapters 3, 4 and 5, I apply the Belkin and O'Reilly Algorithm BOA to compute thermal gradients from daily horizontal temperature slices. The BOA allows us not only to map the position of fronts in space and time, but also gives a direct quantitative

estimate of frontal intensity, which is why we preferred this method over population based algorithms.

The BOA build on existing gradient-based front detection methods (see section 1.4.1.1) to improve the signal to noise ratio while keeping the tracer ridges intact (Belkin & O'Reilly, 2009). More specifically, the BOA involves two processing steps. First, the original two-dimensional tracer field goes through a contextual median filter. Median filters are common image processing steps to remove noise. Median filters operate on moving 1-D slices of odd number of pixels (in this case 3 pixels) to replace the center value of the slice by the median value of the (3) pixels within that slice. In order to remove noise *while* preserving the sharpness of frontal edges, the BOA does not uses a conventional median filter but a *contextual* median filter. This means that each 3-pixel-long slice is also evaluated within a larger 5-pixel-long slice. The contextual median filter is applied recursively to decide whether to replace each center value by a median value or to keep it intact. The contextual median filter is thus applied until convergence, when each pixel value is set. In the second step, the BOA estimates the tracer gradient, or front intensity, with a Sobel operator. For each pixel in the contextually filtered field, the Sobel operator approximates both latitudinal and longitudinal gradients on two 3-by-3 convolution masks and then combine both to estimate the gradient magnitude at the center pixel. This second step highlights the frontal edges from the filtered image background (Belkin & O'Reilly, 2009).

I use the BOA from Benjamin Galuardi's publicly available R package. This gives us a field of daily thermal gradient magnitude. I then use a thresholding procedure to evaluate thermal front frequency from daily thermal gradient magnitudes. I consider that the pixels with the highest horizontal thermal gradients mark thermal fronts. More specifically, for each satellite or simulated daily temperature field, I apply the BOA, and I retain only the top 30% of the thermal gradient magnitude distribution. The resulting thermal front frequency maps reveal the proportion of days in a (thermal) front state.

In Chapters 3 and 4 I thus apply the BOA on the remotely-sensed MUR SST and on modelled temperature fields in the MC. As one of the objectives of this thesis is also to provide an observational front database to investigate relationships between megafauna and fronts in the greater Southwest Indian Ocean, I also apply the BOA and the aforementioned thresholding procedure on MUR SST to generate a multi-decadal database of thermal gradients in the Southwest Indian Ocean (and the Mediterranean Sea), described in Chapter 5.

2.4.2.2. Dynamical front detection

To complement the Southwest Indian Ocean thermal gradient database detailed in Chapter 5, I provide backward FSLE computed from total currents (geostrophic currents with added Ekman component, from CMEMS), which gives us a multi-decadal dynamical front database.

The backward FSLE are computed with Ismael Hernandez-Carrasco's algorithm, described by Hernández-Carrasco et al. 2011. The parametrization of the backward

FSLE algorithm reflects our interest in fine scale ephemeral fronts. The maximum time of integration is set at 90 days. The initial separation distance δ_0 between paired fluid particles correspond to the spatial resolution of the FSLE grid, at 1/64°, which is about 1.56 km. The final distance δ_f between the same fluid particles is set so that $\delta_f = 10\delta_0$.

I computed the backward FSLE in the Southwest Indian Ocean, while Ismael Hernandez-Carrasco provided the same for the Mediterranean Sea. During this process, I was also helped by Camille Mazoyer to optimize the algorithm execution on the regional cluster.

	MOZ*	MOZ*_CR	MOZ*_F	MOZ*_repeat
Purpose	Hindcast v1 (P. Penven)	Hindcast v2	Pseudo global warming experiment	Estimation of intrinsic variability
Model	CROCO (Auclair et al., 2022)			
Bathymetry	GEBCO 2014			
Vertical levels	60 sigma layers			
Atmospheric forcings	ERA-Interim Reanalysis (daily means)	ERA-Interim Reanalysis (daily means)	same as MOZ*_CR + monthly deltas derived from a member of the CESM-LENS RCP8.5 scenario	same as MOZ*_CR but only with the forcings of the year 2001 on repeat
Open boundary forcings	GLORYS reanalysis (1/4°)	from MOZ4	same as MOZ*_CR + monthly deltas derived from a member of the CESM-LENS RCP8.5 scenario	same as MOZ*_CR but only with the forcings of the year 2001 on repeat
Nesting	online (two-way)	offline		
Spatial resolution	MOZ4 : 1/4° MOZ12 : 1/12° MOZ36 : 1/36°	MOZ12_CR : 1/12° MOZ36_CR : 1/36°	MOZ12_F : 1/12° MOZ36_F : 1/36°	MOZ12_repeat : 1/12° MOZ36_repeat : 1/36°
Temporal resolution	daily			
Temporal length	22 years (1993-2014)		22 years	
Spin-up duration	3 years			

Table 2.1.: Summary of simulation configurations.

3. Seasonal thermal front variability in the Mozambique Channel

Content

3.1. Summary 59
3.2. Résumé en français 61
3.3. Article 63
3.4. Supplementary Material 84

3.1. Summary

As evoked in Chapter 1, fronts are key dynamical structures in the world oceans. Their variability has been studied extensively on long time scales (e.g. Legeckis, 1978; Belkin et al., 2009; Mauzole, 2022), but only a few studies explore the variability of finer scale ephemeral fronts (e.g. Mathur et al., 2019; Amos and Castelao, 2022; Haëck et al., 2023), despite their ecological importance (Scales et al., 2014b; Lévy et al., 2018). One difficulty of studying fine-scale front variability is related to their unpredictability, which makes them difficult to track from cruises for example. Another difficulty resides in the high resolution that they require in both space and time. This implies a hefty computational cost for any statistically-robust long-term analysis, making it even harder to go beyond the surface to investigate the ocean interior.

In the southwest Indian Ocean, the Mozambique Channel (MC) provides an ideal sensibly-sized test-bed to investigate ocean front variability. The Channel is characterized by a turbulent flow and a particular topography facilitating the generation of both persistent and ephemeral fronts (Marsac et al., 2014; Phillips et al., 2021). The MC is also particularly relevant to study because of its high biodiversity (Sabarros et al., 2009; Laran et al., 2017; Obura et al., 2019), fishing pressures (Sequeira et al., 2012; Chassot et al., 2019; Nataniel et al., 2022) and recent conservation projects (Unep-Nairobi Convention, 2015; Obura et al., 2019). In this context, mapping seasonal front variability in the MC is essential to identify key front-rich areas, both at the ocean surface and interior, in order to inform regional conservation initiatives.

In this chapter 3, we thus explore the seasonal variability of thermal fronts in the MC. We analyze two decades of temperature fields from a hindcast simulation (the original MOZ36, as described in Section 2.3.1) and satellite observations (MUR SST, as described in Section 2.2) at respective spatial resolution of 3 and 1 km. Thermal fronts are identified by estimating thermal gradients (TG) with the Belkin and O'Reilly

Algorithm (BOA) described in Section 1.4.1.1. We also use modelled (from the original MOZ36) and remotely-sensed (from CMEMS, as described in Section 2.2) velocities on 3 and 25 km grids (respectively) to estimate mesoscale eddy activity via intra-seasonal eddy kinetic energy (EKE). Both thermal fronts and EKE are computed at surface and in the ocean interior up to -1000 m, since marine life exploits the entire water column.

Persistent thermal fronts are present along the Mozambique and Madagascar shelf-breaks year-round and in the wake of the Northeast and Southeast Madagascar Currents (NEMC and SEMC). Ephemeral fronts are mostly generated via the interactions between the Comoros archipelago and meanders from the NEMC (approx. 11 to 14°S), at the border of the MC mesoscale eddies propagating southwest along the Mozambican shelf (approx. 15 to 24°S), and South of Madagascar from meanders of the SEMC (approx. 25 to 30°S). Modelled and remotely-sensed thermal fronts have shown the same spatial distribution in intensity and frequency. Vertically, modelled TG peak at around -80 to -120 m which is consistent with stratification profiles from the same hindcast simulation.

Given that most ephemeral fronts in the Channel occur at the edge of eddies, it is sensible to hypothesize that the seasonality of the EKE explains most of the thermal front seasonal variability. However, comparing the climatologies of TG and EKE reveals that the EKE does not explain fully the seasonal variability of thermal fronts in the Channel. The EKE peaks between May and July in the Comoros Basin (approx. 11°S to 14°S) and between November and January within the Channel (approx. 15°S to 24°S) while it remains fairly constant south of 25°S. TG show peaks that are concomitant to the EKE seasonal maxima, especially at -100 m and deeper. However surface TG climatologies also show peaks apparently distinct from the local mesoscale eddy activity. Such TG local maxima occur between November and January in the Comoros Basin (approx. 11°S to 14°S), between July and August within the Channel (approx. 15°S to 24°S), and between June and August south of 25°S. We hypothesize that coastal upwelling cells could modulate the seasonal variability of thermal fronts in the Channel. For example, upwelling along the northern Mozambican coast (11-16°S) during the North East monsoon (November-March) could lead to cooler water being advected southwest in the Channel by passing eddies, thereby enhancing thermal gradients locally.

This Chapter 3 provides the first detailed description of the spatial and seasonal variability of persistent and ephemeral thermal fronts in the MC, from the surface all the way down to -1000 m, covering ecologically-relevant layers. We distinguish several subregions behaving differently and we propose several mechanisms linking the variability of thermal fronts to regional ocean dynamics. This descriptive analysis provides clues as to where, when and how thermal fronts appear in the MC and can thus be used to determine suitable areas for marine conservation initiatives or bio-physical surveys.

3.2. Résumé en français

Les fronts sont des structures dynamiques clés de l'océan. Leur variabilité a été largement étudiée à long terme (par exemple, Legeckis, 1978; Belkin et al., 2009; Mauzole, 2022), mais seulement quelques études ont exploré la variabilité des fronts éphémères à fines echelles spatiales (par example Mathur et al., 2019; Amos and Castelao, 2022; Haëck et al., 2023), et ce malgré leur importance écologique (Scales et al., 2014b; Lévy et al., 2018). Une des difficultés principales de l'étude de la variabilité des fronts à fine échelle réside dans leur imprévisibilité, ce qui les rend difficiles à échantilloner, par exemple, lors de campagnes océanographiques. Une autre difficulté réside dans la haute résolution spatiale et temporelle nécéssaires à leur étude, impliquant un coût informatique élevé pour toute analyse statistique à long terme, et rendant encore plus difficile l'exploration des fronts au-delà de la surface dans l'interieur de l'océan.

Dans le sud-ouest de l'Océan Indien, le Canal du Mozambique (MC) offre un laboratoire idéal, et aux dimensions raisonnables, pour étudier la variabilité des fronts océaniques à fines échelles. Le Canal est caractérisé par une circulation turbulente et une topographie particulière facilitant la génération de fronts persistants et éphémères (Marsac et al., 2014; Phillips et al., 2021). Il est également intéressant d'étudier le Canal en raison de sa biodiversité (Sabarros et al., 2009; Laran et al., 2017; Obura et al., 2019), des pressions de pêche (Sequeira et al., 2012; Chassot et al., 2019; Nataniel et al., 2022) et de projets recents de conservation (Unep-Nairobi Convention, 2015; Obura et al., 2019). Dans ce contexte, cartographier la variabilité saisonnière des fronts dans le Canal du Mozambique est essentiel pour identifier les zones clés riches en fronts, tant à la surface qu'à l'intérieur de l'océan, et afin d'informer les initiatives de conservation régionales.

Dans ce Chapitre 3, nous explorons donc la variabilité saisonnière des fronts thermiques dans le Canal du Mozambique. Nous analysons deux décennies de champs de température à partir d'une simulation de réanalyse (le MOZ36 d'origine, cf. Section 2.3.1) et d'observations satellitaires (MUR SST, cf. Section 2.2) à des résolutions spatiales respectives de 3 et 1 km. Les fronts thermiques sont identifiés en estimant les gradients de température avec l'algorithme de Belkin et O'Reilly (BOA) détaillé dans la Section 1.4.1.1. Nous utilisons également des vitesses modélisées (à partir du MOZ36 d'origine) et issues de courantologie satellitaire (du CMEMS, cf. Section 2.2) sur des grilles de 3 et 25 km (respectivement) pour estimer l'activité tourbillonaire mésoéchelle dans le Canal par un calcul d'énergie cinétique des tourbillons (EKE). Les fronts thermiques et l'EKE sont calculés en surface et à l'intérieur de l'océan, jusqu'à -1000 m, Les fronts thermiques et EKE sont calculés à la surface et à l'intérieur de l'océan jusqu'à -1000 m, car la vie marine exploite toute la colonne d'eau.

Les fronts thermiques persistants apparaissent le long des plateaux continentaux du Mozambique et de Madagascar tout au long de l'année et dans le sillage des courants du nord-est et du sud-est de Madagascar (NEMC et SEMC). Les fronts éphémères, quant à eux, sont générés: par les interactions entre l'archipel des Comores et les méandres du NEMC (environ 11°S à 14°S) ; à la frontière des tourbillons mésoéchelle du MC se propageant vers le sud le long de la côte mozambicaine (environ 15°S à 24°S)

; et au sud de Madagascar à partir des méandres du SEMC (environ 25°S à 30°S). Les fronts thermiques issus du model MOZ36 et des données satelitaires présentent la même distribution spatiale en intensité et fréquence. Verticalement, les gradients thermiques modélisés atteignent leur maximum à d'environ -80 à -120 m, ce qui est cohérent avec les profils de stratification de MOZ36.

Étant donné que la plupart des fronts thermiques éphémères dans le canal se produisent à la lisière des tourbillons, nous avons emis l'hypothèse que la saisonnalité de l'EKE explique la majorité de la variabilité saisonnière des fronts thermiques. Cependant, la comparaison des climatologies des gradients thermiques et d'EKE révèle que l'EKE n'explique pas entièrement la variabilité saisonnière des fronts thermiques dans le Canal. L'EKE atteint son maximum entre mai et juillet dans le bassin des Comores (environ 11°S à 14°S) et entre novembre et janvier dans le Canal (environ 15°S à 24°S), tout en restant constante au sud de 25°S. Les gradient thermiques montrent bien des pics concomitants aux maxima saisonniers de l'EKE, surtout à -100 m et plus profond. Cependant, les climatologies de gradients thermiques en surface montrent également des pics apparemment distincts de l'activité mésoéchelle locale. De tels maxima locaux de gradients thermiques se produisent entre novembre et janvier dans le bassin des Comores (environ 11°S à 14°S), entre juillet et août dans le canal (environ 15°S à 24°S), et entre juin et août au sud de 25°S. Nous émettons alors l'hypothèse que les cellules d'upwelling côtières influencent aussi la variabilité saisonnière des fronts thermiques dans le Canal. Par exemple, des upwellings le long de la côte nord du Mozambique (11-16°S) pendant la mousson du nord-est (novembre-mars) pourrait entraîner des masses d'eau plus fraîche en surface et vers le sud-ouest dans le Canal par le passage de tourbillons, renforçant ainsi les gradients thermiques associés.

Ce Chapitre 3 propose une première description détaillée de la variabilité spatiale et saisonnière des fronts thermiques persistants et éphémères dans le Canal, en surface et jusqu'à -1000 m. Nous distinguons plusieurs sous-régions se comportant différemment et proposons plusieurs mécanismes liant la variabilité des fronts thermiques à la dynamique océanique régionale. Cette analyse descriptive informe sur où, quand et comment les fronts thermiques apparaissent dans le Canal du Mozambique et peut donc être utilisée pour déterminer des zones intéressantes pour des project de conservation ou des campagnes d'observations biophysiques.

3.3. Article

Sudre, F., Dewitte, B., Mazoyer, C., Garçon, V., Sudre, J., Penven, P., & Rossi, V. (2023a). Spatial and seasonal variability of horizontal temperature fronts in the mozambique channel for both epipelagic and mesopelagic realms. *Frontiers in Marine Science*, *9*. https://doi.org/10.3389/fmars.2022.1045136

frontiers | Frontiers in Marine Science

TYPE Original Research
PUBLISHED 04 January 2023
DOI 10.3389/fmars.2022.1045136

Check for updates

OPEN ACCESS

EDITED BY
Francisco Machín,
University of Las Palmas de Gran Canaria, Spain

REVIEWED BY
Li Yineng,
South China Sea Institute of Oceanology (CAS), China
Chibuike Ibebuchi,
Kent State University, United States

*CORRESPONDENCE
Floriane Sudre
Floriane.sudre@mio.osupytheas.fr

SPECIALTY SECTION
This article was submitted to Physical Oceanography, a section of the journal Frontiers in Marine Science

RECEIVED 15 September 2022
ACCEPTED 05 December 2022
PUBLISHED 04 January 2023

CITATION
Sudre F, Dewitte B, Mazoyer C, Garçon V, Sudre J, Penven P and Rossi V (2023) Spatial and seasonal variability of horizontal temperature fronts in the Mozambique Channel for both epipelagic and mesopelagic realms.
Front. Mar. Sci. 9:1045136.
doi: 10.3389/fmars.2022.1045136

COPYRIGHT
© 2023 Sudre, Dewitte, Mazoyer, Garçon, Sudre, Penven and Rossi. This is an open-access article distributed under the terms of the Creative Commons Attribution License (CC BY). The use, distribution or reproduction in other forums is permitted, provided the original author(s) and the copyright owner(s) are credited and that the original publication in this journal is cited, in accordance with accepted academic practice. No use, distribution or reproduction is permitted which does not comply with these terms.

Spatial and seasonal variability of horizontal temperature fronts in the Mozambique Channel for both epipelagic and mesopelagic realms

Floriane Sudre[1]*, Boris Dewitte[2,3,4,5], Camille Mazoyer[1], Véronique Garçon[6], Joel Sudre[7], Pierrick Penven[8] and Vincent Rossi[1]

[1]Aix Marseille Univ, Université de Toulon, French National Centre for Scientific Research (CNRS), French National Research Institute for Sustainable Development (IRD), Mediterranean Institute of Oceanography (MIO), French National Research Institute for Sustainable Development (IRD), Mediterranean Institute of Oceanography (MIO), Marseille, France, [2]Centro de Estudios Avanzados en Zonas Áridas, Facultad de Ciencias del Mar, Universidad Católica del Norte, Coquimbo, Chile, [3]Departamento de Biología Marina, Universidad Católica del Norte, Coquimbo, Coquimbo, Chile, [4]Millennium Nucleus of Ecology and Sustainable Management of Oceanic Islands, Faculty of Marine Sciences, Catholic University of the North, Coquimbo, Chile, [5]UMR5318 Climat, Environnement, Couplages et Incertitudes (CECI), Toulouse, France, [6]UMR5566 Laboratoire d'études en géophysique et océanographie spatiales (LEGOS), Toulouse, France, [7]UAR 2013 CPST, IR DATA TERRA, La Seyne sur Mer, France, [8]UMR6523 Laboratoire d'Oceanographie Physique et Spatiale (LOPS), Plouzane, France

Introduction: Ocean fronts are moving ephemeral biological hotspots forming at the interface of cooler and warmer waters. In the open ocean, this is where marine organisms, ranging from plankton to mesopelagic fish up to megafauna, gather and where most fishing activities concentrate. Fronts are critical ecosystems so that understanding their spatio-temporal variability is essential not only for conservation goals but also to ensure sustainable fisheries. The Mozambique Channel (MC) is an ideal laboratory to study ocean front variability due to its energetic flow at sub-to-mesoscales, its high biodiversity and the currently debated conservation initiatives. Meanwhile, fronts detection relying solely on remotely-sensed Sea Surface Temperature (SST) cannot access aspects of the subsurface frontal activity that may be relevant for understanding ecosystem dynamics.

Method: In this study, we used the Belkin and O'Reilly Algorithm on remotely-sensed SST and hindcasts of a high-resolution nested ocean model to investigate the spatial and seasonal variability of temperature fronts at different depths in the MC.

Results: We find that the seasonally varying spatial patterns of frontal activity can be interpreted as resulting from main features of the mean circulation in the MC region. In particular, horizontally, temperature fronts are intense and frequent along continental shelves, in islands' wakes, at the edge of eddies, and in the pathways of both North-East Madagascar Current (NEMC) and South-

East Madagascar Current (SEMC). In austral summer, thermal fronts in the MC are mainly associated with the Angoche upwelling and seasonal variability of the Mozambique current. In austral winter, thermal fronts in the MC are more intense when the NEMC and the Seychelles-Chagos and South Madagascar upwelling cells intensify. Vertically, the intensity of temperature fronts peaks in the vicinity of the mean thermocline.

Discussion: Considering the marked seasonality of frontal activity evidenced here and the dynamical connections of the MC circulation with equatorial variability, our study calls for addressing longer timescales of variability to investigate how ocean ecosystem/front interactions will evolve with climate change.

KEYWORDS

fronts, temperature fronts, seasonal variability, mozambique channel, ROMS-CROCO, Belkin and O'Reilly algorithm, submesoscale, indian ocean

1 Introduction

Ocean fronts are ubiquitous discrete features in the ocean which are now more readily available thanks to the ever-increasing spatial resolution of satellite data (Belkin et al., 2009; Kartushinsky and Sidorenko, 2013; Belkin, 2021). Fronts are defined as a sharp transition between waters of different properties (temperature, salinity, chlorophyll-a, nutrients, etc.) and are usually detected by high local horizontal gradients in those same properties (Largier, 1993; Cayula and Cornillon, 1995; Shimada et al., 2005). Frontal phenomena encompass a wide range of space and time scales, from submesoscale structures to thousands of kilometers and from hours to hundreds of years (McWilliams, 2021; Belkin, 2021). More specifically, some fronts are seasonally persistent (Acha et al., 2004; Vinayachandran et al., 2021; McWilliams, 2021), while others display clear seasonal patterns (Park and Chu, 2006; Castelao et al., 2006; Bosse and Fer, 2019).

In the open ocean, fronts are dynamic biological hotspots, offering rich habitats to numerous marine species across all trophic levels for migration, reproduction and foraging (Largier, 1993; Acha et al., 2004; Bakun, 2006; Tew Kai et al., 2009; Tew Kai and Marsac, 2010; Rossi et al., 2013; Sabarros et al., 2014; Lévy et al., 2018). Additionally, species of all trophic levels exploit the whole water column around those dynamical structures (Bakun, 2006), from phytoplankton communities (Barlow et al., 2014), to micronekton (Annasawmy et al., 2018), and megafauna (Brunnschweiler et al., 2009), thus increasing the interest for ecological and conservation studies with a vertical component.

Indeed, submesoscale fronts were previously thought to be confined in the mixed layer (Fox-Kemper et al., 2008) but recent studies show that fronts could penetrate much deeper than the mixed layer, and reach depths up to 1000m (Bettencourt et al., 2012; Yu et al., 2019; Siegelman et al., 2020b). There is thus an opportunity to infer deep circulation as well as vertically-integrated biological hotspots from surface mesoscale activity. This is essential for understanding the spatio-temporal variability of these critical ecosystems, at both ocean surface and interior, in order to design conservation management strategies and ensure sustainable resources (Alemany et al., 2009; Nieblas et al., 2014; Watson et al., 2018; Scales et al., 2018).

In this study, we investigate the temperature fronts in the Mozambique Channel (MC). The MC is part of the greater Agulhas system (Lutjeharms, 2006) starting North of Madagascar and reaching south all the way to South Africa (Figure 1). The circulation in the Mozambique Channel is highly energetic and unstable. The South Equatorial Current (SEC) parts in two at around 17°S east of Madagascar forming the Northeast and Southeast Madagascar currents (SEMC and NEMC, respectively). The MC is characterized by a highly variable Mozambique Current flowing southward along the Mozambican shelf (DiMarco et al., 2002; Lutjeharms et al., 2012) and a succession of mesoscale eddies propagating southward at a speed of about 3 to 6 km/day (de Ruijter et al., 2002; Halo et al., 2014). Eddies in the MC have a typical scale of several hundreds of kilometers (de Ruijter et al., 2002; Halo et al., 2014; Ternon et al., 2014), and a frequency of occurrence of 4 to 7 per year (Schouten et al., 2003). Those eddies display a strong barotropic component and some are felt all the way to the bottom of the channel (i.e., over -2000m) (de Ruijter et al., 2002; Ridderinkhof and de Ruijter, 2003; Schouten et al., 2003; Halo et al., 2014). The most intense eddies are anticyclonic eddies (AE), also referred to as Mozambique Rings. They form at the

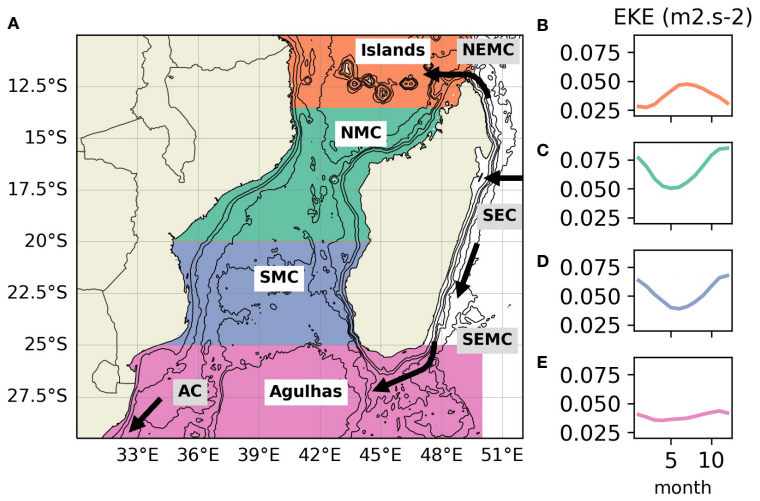

FIGURE 1
Major currents in the Mozambique Channel, its 4 subregions **(A)**, and their respective EKE climatology **(B–E)**. The subregions are defined in the text as "Islands" (10°S- 13.5°S), "North Mozambique Channel" (NMC: 13.5°S- 20°S), "South Mozambique Channel" (SMC: 20°S-25°S) and "Agulhas" (25°S-30°S). The major currents, South Equatorial Current (SEC), North East Madagascar Current (NEMC), South East Madagascar Current (SEMC) and the Agulhas Current (AC) are indicated by arrows. The background contours represent isobaths at -200, -1000, -2000, -3000 and -4000 m.

narrowest part of the MC around 12-16°S and travel southward along the Mozambican shelf (Halo et al., 2014), where the flow is most intense (de Ruijter et al., 2002) and where eddy kinetic energy (EKE) is the highest (Biastoch and Krauss, 1999). Cyclonic eddies (CE) are more numerous, yet smaller than AE in the channel (Halo et al., 2014). They usually form at the edge of bigger AE on the eastern side of the channel and south of 20°S, to then travel to the southwest (Halo et al., 2014; Roberts et al., 2014). The formation of submesoscale filaments and fronts at the edge of mesoscale eddies is a common feature in turbulent regions and has been extensively documented from satellite imagery (Munk et al., 2000; Zhang and Qiu, 2020) and from observations (Read et al., 2007; Roberts et al., 2014; Adams et al., 2017; Siegelman et al., 2020a; Tarry et al., 2021). The highly energetic flow at sub-to-mesoscale of the MC makes it thus ideal to study fronts.

The MC also exhibits a strong seasonal cycle and experiences biannual monsoons north of 20°S (Schott et al., 2009). During the northeast monsoon, from December to March, winds blow from the northwest, while winds blow from the southeast during the southwest monsoon, from June to November. South of 20°S, winds blow from the southeast all year round (Obura et al., 2019). The monsoon reversals of the north MC also modulate currents intensity (Ridderinkhof et al., 2010; Obura et al., 2019) and create a distinct seasonal pattern, which affects the large anticyclonic eddies forming at 12-16°S (Donguy and Piton, 1991). Finally, altimetry-derived EKE climatology for different parts of the MC (Figure 1) shows a strong seasonal variability, especially north of 25°S. The MC energetic turbulent flow, seasonal cycle and exceptional biodiversity (Obura et al., 2019) thus motivate the investigation of temperature front seasonal variability.

Historically, fronts have mostly been detected from satellite imagery. Originally, fronts were simply identified manually from SST images (Legeckis, 1978), but more sophisticated automatic front detection algorithms have been developed since then. Front detection algorithms are usually based on SST gradients, even though some also use entropy (Shimada et al., 2005), neural networks (Torres Arriaza et al., 2003) or singularity exponents (Turiel and del Pozo, 2002; Turiel et al., 2008; Tamim et al., 2015). The Canny algorithm (Canny, 1986) is often referred to as the original "gradient method" and is based on the high gradient property of fronts. However, this method often results in enhanced noise from the differentiation (Belkin and O'Reilly, 2009). The Cayulla-Cornillon Algorithm (CCA) addresses this shortcoming by operating with histograms to detect the edge between two water masses (Cayula and Cornillon, 1995). This method requires fine-tuning to find the appropriate threshold distinguishing fronts from background noise, but has been successfully used in many different systems: in the Baltic Sea (Kahru et al., 1995), in the Atlantic Ocean (Mantas et al., 2019) or in the South China Sea (Wang et al., 2001). The performance of the CCA was further improved by adding multiple sliding windows (Nieto et al., 2012) and then applied in the Indian (Nieblas et al., 2014) and Pacific (Nieto et al., 2017) Oceans. As opposed to histogram-based methods, the algorithm proposed by Belkin and O'Reilly is based on SST gradients and effectively

remove the noise generally produced by other gradient methods, while preserving the shape of the detected front (Belkin and O'Reilly, 2009). The Belkin and O'Reilly algorithm (BOA) produced fronts dataset in the South China Sea (Wang et al., 2001), East China Sea (Lin et al., 2019) and the Kuroshio current (Liu et al., 2018).

Fronts can originate from the interaction between strong currents and topography anomalies, such as shelf-breaks, islands and seamounts (Heywood et al., 1990; Condie, 1993; McWilliams, 2021); at the edge of eddies in turbulent areas (Munk et al., 2000; Read et al., 2007; Siegelman et al., 2020a) and in upwelling zones (Bettencourt et al., 2012; Rossi et al., 2013; Sabarros et al., 2014; Calil et al., 2021). The Island Mass Effect (Doty and Oguri, 1956) in particular plays an important role in frontogenesis, as it has been shown to be associated with the generation of vortices in the lee of islands (De Falco et al., 2022). Although it is very rare to attribute clearly a single driver to frontogenesis, it is instead often a complex combination of favorable conditions (McWilliams, 2021).

The complex dynamic of processes behind frontogenesis (McWilliams, 2021) suggests that fronts detection relying solely on remotely sensed SST might miss important front features and variability at depth, and estimates of the magnitude of SST gradients in satellite products is highly sensitive to resolution and interpolation technique (Vazquez-Cuervo et al., 2013). In this study, we use remotely-sensed SST and outputs of a high-resolution realistic ocean model to investigate the spatial and seasonal variability of thermal fronts at different depths in the Mozambique Channel. The paper is organized as follows: we first introduce our material and methods for front detection and we follow with a description of front variability in the Mozambique Channel. The article ends by a discussion and a few concluding remark

2 Material and methods

2.1 Domain subregions

Before studying thermal front variability, we divided our domain into 4 subregions, as seen in Figure 1. The rationale for this meridional subdivision is based on a literature review about drivers of oceanic variability (i.e. bathymetry effects, monsoon forcing) in the channel and relies on the dependence of eddy characteristics and therefore fronts to the Coriolis force. The "Islands" subregion (10-13.5°S, 38-49.5°E) starts just above the Comoros archipelago and extends to 13.5°S at the entrance of the Angoche Basin. The "Northern Mozambique Channel" (NMC) subregion (13.5-20°S, 34-48°E) ends at 20°S where the influence of monsoons weakens substantially (Schott et al., 2009). The "South Mozambique Channel" (SMC) subregion (20-25°S, 33-45°E) goes as far south as 25°S, which corresponds to the southern tip of Madagascar island. Finally, the "Agulhas" subregion (25-30°S, 31-50°E) covers the southernmost part of our domain from 25°S to 30°S.

2.2 Model configuration

In this study, temperature fronts are derived from a ROMS-CROCO (Regional Ocean Modeling System and Coastal and Regional Ocean COmmunity model) configuration of the MC (Shchepetkin and McWilliams, 2005). ROMS-CROCO solves the primitive hydrostatic equations for momentum and tracer variables and successfully resolves regional and coastal oceanic processes at high resolution, as well as mesoscale eddies (Halo et al., 2014). The model configuration consists in 3 nested grids (two-way nesting) with the child domain at the highest resolution of 1/36° used here. 60 vertical sigma (topography following) layers are used. The bathymetry used in the model is from GEBCO 2014 (Weatherall et al., 2015). A bulk formulation (Fairall et al., 1996) is used to compute surface turbulent heat to force the model, based on ERA-Interim Reanalysis daily mean atmospheric fields (2 m air temperature, relative humidity, surface wind speed, net shortwave and downwelling longwave fluxes, and precipitations). Wind stress forcing is also from the ERA-Interim Reanalysis. At the lateral open boundaries, mixed active-passive conditions are used (Marchesiello et al., 2001) with forcing data from GLORYS reanalysis at 1/4° resolution. The generated daily output covers 22 years, from 1993 to 2014. This 1/36° ROMS-CROCO configuration of the Mozambique Channel, referred to as MOZ36, was first used by Miramontes et al. (Miramontes et al., 2019) to document the deep oceanic circulation in the Zambezi turbidite system (SMC subregion in Figure 1)

2.3 Climatological and satellite datasets

We used climatological seawater properties from CARS2009 (Ridgway et al., 2002) generated from compiled *in-situ* observations spanning from January 1941 to May 2009, on a 1/2° grid. We also retrieved World Ocean Atlas 2018 annual mean temperature (Locarnini et al., 2018) and salinity (Zweng et al., 2018). Remotely-sensed Sea Surface Height (SSH) was taken from Global Total Surface and 15 m Current (Rio et al., 2014, COPERNICUS-GLOBCURRENT) from Altimetric Geostrophic Current and Modeled Ekman Current Reprocessing, on a 1/4° grid. Finally, Sea Surface Temperature (SST) was provided by GHRSST Level 4 Multi-scale Ultra-high Resolution (MUR) 1/10° Global Foundation Sea Surface Temperature Analysis v4.1 (SST MUR) (Chin et al., 2017). In this work, we use the full MUR dataset from January 2003 to December 2020, for the MC. SST MUR data comes with 2 data quality flags. Flag 1 corresponds to the estimated error standard deviation of the SST data and flag 2 is the time lag to most recent 1 km data. Flag 1 is available for the entire dataset while flag 2 is only included after July 2016.

2.4 Numerical methods

We use the Brunt-Väisälä frequency N as a proxy for stratification. N is given by:

$$N^2 = \frac{-g}{\rho_0}\frac{\partial \rho}{\partial z} \quad (1)$$

Where g is the gravitational constant, ρ_0 is a reference density set at 1025 kg.m^{-3} ρ is the seawater density and z its depth.

Intra-seasonal and inter-annual eddy kinetic energy (EKE) were computed following a similar method to Dewitte et al. (Dewitte et al., 2021). First, intra-seasonal current anomalies (u_{IS} and v_{IS}) were estimated by subtracting monthly mean currents to the daily velocity dataset. Then, the mean intra-seasonal EKE was computed as:

$$\langle EKE_{IS} \rangle = \langle \frac{(u_{IS}^2 + v_{IS}^2)}{2} \rangle \quad (2)$$

Second, inter-annual current anomalies (u_{IA} and v_{IA}) were computed by subtracting the climatology to the daily velocity dataset. Then, the mean inter-annual EKE was computed as:

$$\langle EKE_{IA} \rangle = \langle \frac{(u_{IA}^2 + v_{IA}^2)}{2} \rangle \quad (3)$$

Following the same methodology, MOZ36 intra-seasonal EKE was also computed at -100 m, -500 m and -1000 m.

We chose the Belkin and O'Reilly algorithm (Belkin and O'Reilly, 2009) to detect the location and intensity of temperature fronts in the MC. More specifically, we use Ben Galuardi's BOA pseudo-code written in R and publicly available on https://github.com/galuardi/boaR (accessed on 19 May 2022). BOA first applies a contextual median filter until convergence to reduce noise originating from natural variability and artifacts. The algorithm then uses 3x3 kernel Sobel operator to compute the gradient magnitude (Belkin and O'Reilly, 2009). BOA temperature gradients were computed on MUR SST but also on MOZ36 temperatures between 0 and -1000 m, leveraging the fact that the model is not limited to the surface, as would be satellite datasets. From the surface to -300 m, the model outputs were interpolated on a 10 m vertical resolution grid, while below -300 m we use a resolution of 50 m.

We derive several statistics to characterize temperature fronts and to evaluate their variability. BOA being a gradient-based method of front detection, the algorithm produces a continuous field of *temperature gradient magnitude*, or *front intensity* in °C/km. As such, a threshold must be determined to define what is considered a front. Choosing a high threshold might prevent weak fronts from being recorded, while a weak threshold might blur any meaningful signal into noise. We thus define *front* pixels as pixels whose temperature gradient magnitude is equal or above the chosen threshold. We finally define the *probability of front occurrence* per month for each ocean pixel as the percentage of days when the gradient value qualifies as "front", i.e. when the pixel gradient magnitude is over the threshold, over the total number of days for each month of simulation.

Finally, we computed sea level anomalies (SLA) from the mean MOZ36 sea-surface heights in order to link frontal activity with (sub)-mesoscale features in the MC. And dominant time-frequencies were studied based on 1-D discrete fast Fourier transforms (FFT) computed with the scipy.fft package.

2.5 Model validation

2.5.1 EKE

To validate MOZ36 (sub-)mesoscale structures on intra-seasonal and inter-annual time scales, we evaluated the mean eddy kinetic energy (EKE) derived from the model and remotely-sensed currents (see supplementary material Figure S1). The spatial EKE patterns are similar in both model and satellite data: the EKE is most intense on the western part of the MC and in its southern part, in the wake of the SEMC. Note that, the slightly higher EKE from the model could be well-explained by its higher resolution.

2.5.2 Hydrography

When comparing the SST variability in the MC from MOZ36 and from MUR SST (Figure S2), both datasets exhibit comparable seasonal and spatial SST patterns. Additionally, and to further validate seawater properties of MOZ36, we compared World Ocean Atlas 2018 temperature (Locarnini et al., 2018) and salinity (Zweng et al., 2018) annually-averaged vertical profiles on a meridional section at 42.125°E, in the center of the channel (Figure S3). Observed and modelled vertical profiles show good consistency, confirming that MOZ36 is suitable to study temperature fronts in the MC.

2.5.3 Stratification

We used CARS2009 (Ridgway et al., 2002) temperature and salinity profiles to evaluate the realism of the modelled vertical stratification thanks to the Brunt-Väisälä frequency from the surface to -1000 m. The comparison between the mean model and CARS2009 squared Brunt-Väisälä frequencies for the 4 MC subregions (Figure S4) reveals that MOZ36 is able to reproduce a range of values similar to observations, with a maximum N^2 of about $0.2*10^{-3}s^{-2}$. For both datasets, N^2 in the Agulhas region is markedly smaller than the other 3 subregions and peaks at -60 m. The Islands, NMC and SMC subregions peaks between -60 and -100 m in the model and between -80 and -125 m in CARS2009. Overall the model reproduces a rather realistic mean thermocline structure, providing high confidence in its ability to simulate well the main aspects of ocean dynamics.

3 Results

3.1 Front threshold definition

We define a single temperature front threshold for all depths using statistical distribution and quantiles of MOZ36 temperature front intensity for all ocean pixels across the 22 years of simulation and 4 depth levels: surface, -100 m, -500 m, and -1000 m (Figure S5). Surface temperature gradients go up to 2.3°C/km, and 70% of those are below 0.05°C/km. We subsequently define *front pixels* as pixels whose temperature gradient magnitude is equal or above 0.05°C/km, and the *probability of front occurrence* per month for each ocean pixel as the percentage of days when the pixel gradient magnitude is over 0.05°C/km, over the total number of days for each month of simulation.

3.2 Spatial variability

3.2.1 Surface

The mean surface temperature front intensity and probability maps (Figures 2A, B) reveals that SST fronts derived from the model are more intense and more likely to appear along the continental shelves, in the wake of both Northeast and Southeast Madagascar currents (NEMC and SEMC) and more generally southward of 25°S.

The equivalent mean maps of temperature front intensity and probability derived from the MUR dataset exhibit a spatial distribution similar to that of the modelled fronts (Figures 2C, D), despite a slightly lower range of values.

3.2.2 Ocean interior

Figure 3 represents the mean vertical profiles of front intensity in °C/km from MOZ36, the shading around the mean corresponds to the seasonal standard variation. The vertical profiles reveal three distinct regimes, similar in all 4 subregions of the MC:

1. From the surface to about -100 m, the frontal activity increases abruptly to reach its maximum to 0.75-0.9°C/km at -100 to -200 m, in the vicinity of the mean thermocline.
2. From -200 m to -500 m, the front intensity decreases sharply to reach 0.35°C/km in the NMC region and around 0.05°C/km in the Islands, NMC and Agulhas regions.
3. From -500 m and deeper, frontal intensities decrease at a slower rate with depth. At -1000 m the NMC region exhibits the lowest frontal activity, followed by the Islands regions. The SMC and the Agulhas region show less of a vertical difference between surface and depth, than the NMC and the Islands regions.

The vertical distribution of temperature front intensity is very similar to MOZ36 and CARS2009 stratification profiles (Figure S4). Indeed, the Islands (Agulhas) subregion has the

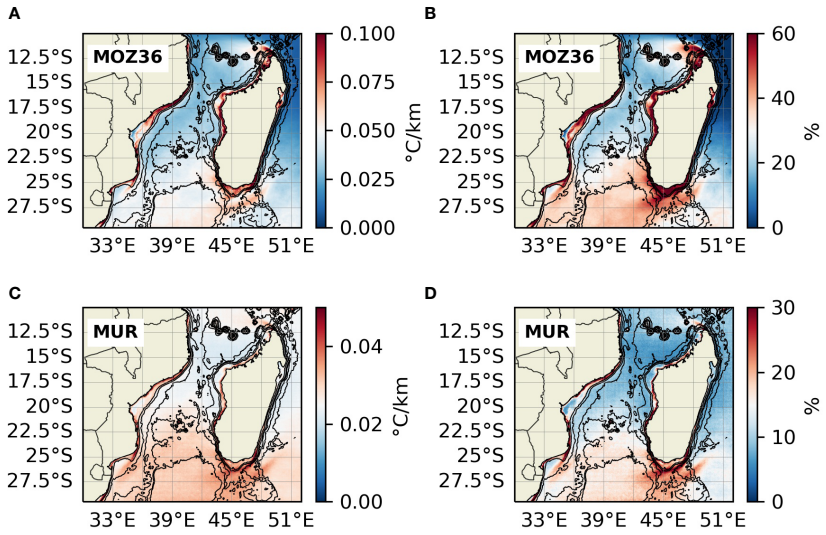

FIGURE 2
Mean surface temperature front intensity **(A, C)** and probability **(B, D)** for MOZ36 **(A, B)** and MUR SST **(C, D)**.

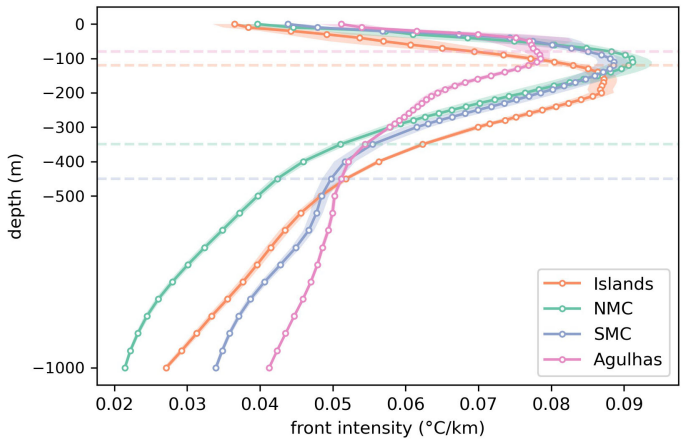

FIGURE 3
Mean temperature front intensity for each MOZ36 subregion in °C/km. The shading shows the seasonal standard deviation from the mean. The dashed horizontal lines mark the depth below which the seasonal standard deviation of temperature front intensity is lower than 5% of its mean.

deepest (shallowest) thermocline and frontal intensity peak, at about -200 m (-80 m).

Seasonal variability ceases to be significant, i.e. it amounts to less than 5% of the front intensity mean, below -150 m for the Islands region, below -350 m and -450 m for the NMC and SMC regions (respectively) and below -70 m in the Agulhas region.

Frontal activity peaks at around -100 m, in the vicinity of the mean thermocline (Figure 3). The resulting 22-year map of mean front intensity at -100 m (Figure 4C) indicates stronger frontal activity than at the surface, as expected from the front intensity distribution (Figure S5). The frontal activity is specifically stronger along the continental shelves, in the wake of the NEMC and SEMC and in the central part of the MC, in between Bassas da India and Juan de Nova islands across the Angoche Basin.

-500 m and -1000 m temperature fronts are most intense along the Mozambican shelf, near Maputo and in the path of the NEMC and SEMC (Figure 4).

3.2.3 Front typology

Selected snapshots of temperature front intensity at different depth and time of the year allowed us to distinguish three types of temperature fronts based on their signature behaviors (Figure 5).

- *Topographic fronts*, as defined by McWilliams McWilliams, (2021) are formed where currents encounter land masses or other sharp topographic changes such as seamounts. In this study, topographic fronts are found along Mozambique and Madagascar shelves and around islands (French Scattered Islands, Comoros Archipelago), they reach maximum intensity at -100 m. NEMC and SEMC paths can clearly be identified from the front intensity patterns at the north and south tips of Madagascar Island (Figure 4).
- The next two types of fronts correspond to the "deformation fronts" in McWilliams's typology. They form at the edge of eddies.
  - *Anticyclonic deformation fronts* (ADF) are located at the edge of anticyclonic eddies (AE) in the MC. AE usually form at the entrance of the Angoche Valley at 15° S and travel southward close to the Mozambican shelf to then merge or dissipate around 22°S and feed the Agulhas Current. ADF reach their maximum intensity at around -100 m and then weaken substantially at -500 m, to disappear completely by -1000 m.
  - *Cyclonic deformation fronts* (CDF) form at the edge of cyclonic eddies (CE), generally south of 23°S. Most of those CE are driven by the SEMC: some go slightly northward up the southern tip of the Madagascar shelf, but most go southwest following the SEMC track towards the Agulhas current. CDF reach their maximum intensity at -500 m and can still be detected at -1000 m.

A summary of the front typology and locations can be found in Table 1.

3.3 Seasonal variability

3.3.1 Islands and NMC subregions

In the Islands (10°S-13°S) and NMC (13°S-20°S) regions, SST fronts are strongest in the wake of the NEMC between the

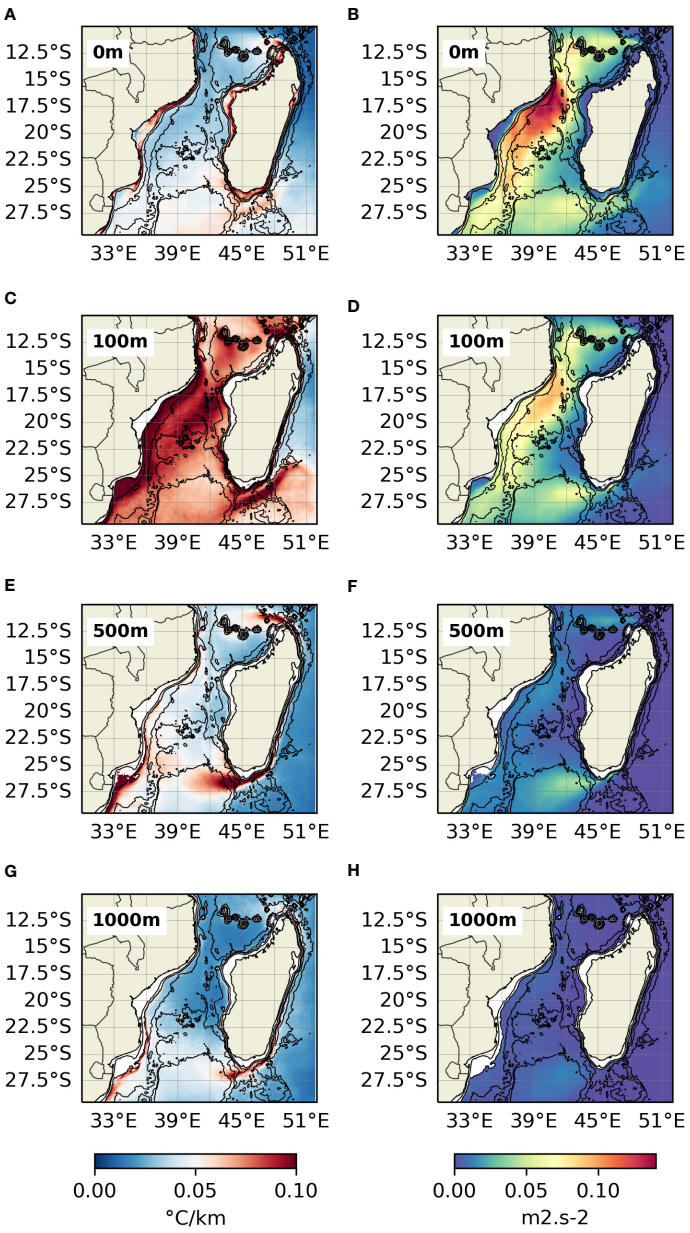

FIGURE 4
Mean temperature front intensity **(A, C, E, G)** and EKE **(B, D, F, H)** from MOZ36 at the surface **(A, B)**, -100 m **(C, D)**, -500 m **(E, F)** and -1000 m **(G, H)**.

northwestern tip of Madagascar and the Comoros archipelago (Figure 4) and along the Madagascar and Mozambican continental shelves. Most of the fronts in the Islands region are identified as topographic fronts, generated by the interaction between NEMC and the local topography, while fronts in the NMC are mostly topographic fronts and ADF. The FFT analysis of the 22-year daily time series of surface temperature front intensity from MOZ36 in the Island and NMC regions reveals a predominant 6-month and a moderate 1-year periods (Figure 6, additional depths are provided in supplementary material (Figure S6). Indeed, SST front intensity climatology shows two peaks: a moderate one in May and a greater one in November (Figure 7).

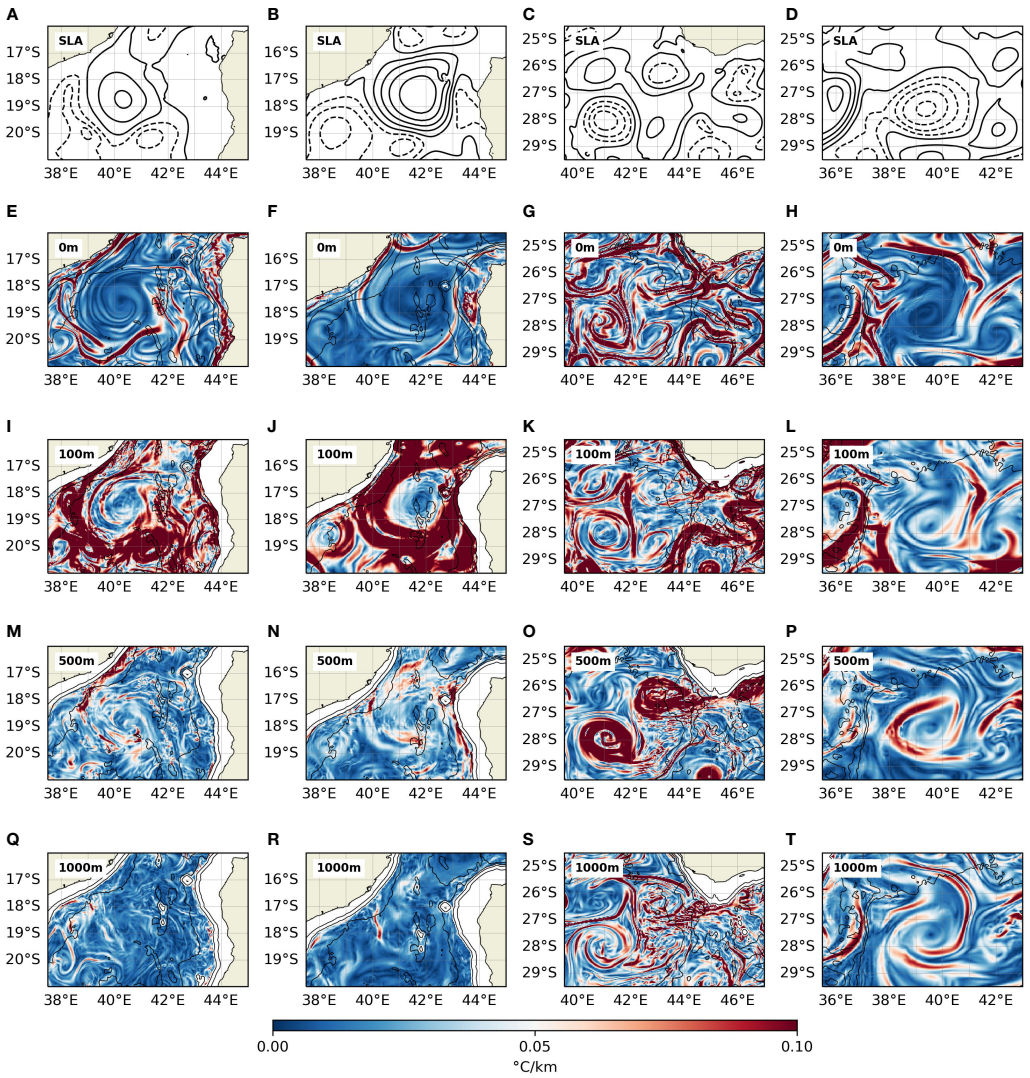

FIGURE 5
Selected snapshots comparing the vertical structures of anticyclonic (first 2 columns: **A, B, E, F, I, J, M, N, Q, R**) and cyclonic (last 2 columns: **C, D, G, H, K, L, O, P, S, T**) eddies from MOZ36. Each column represents a different eddy structure. The first row corresponds to sea-levels anomalies relative to mean sea-surface height, full (dashed) lines are positive (negative) anomalies. Rows 2, 3, 4 and 5 are temperature front intensities in °C/km, at surface, -100 m, -500 m, -1000 m respectively.

TABLE 1 **Front typology based on behavior and depth signatures.**

	General location	Subregion	Surface	-100m	-500m	-1000m
Topographic fronts	Along continental shelves and lee of islands (Scattered Islands, Comoros Archipelago)	Islands, NMC, SMC, Agulhas	yes	max	yes	n/a
***Anticyclonic deformation fronts* (ADF)**	15°S-22°S, western MC	NMC, SMC, Agulhas	yes	max	weak	very weak
***Cyclonic deformation fronts* (CDF)**	22°S-30°S, eastern MC	SMC, Agulhas	yes	yes	max	strong

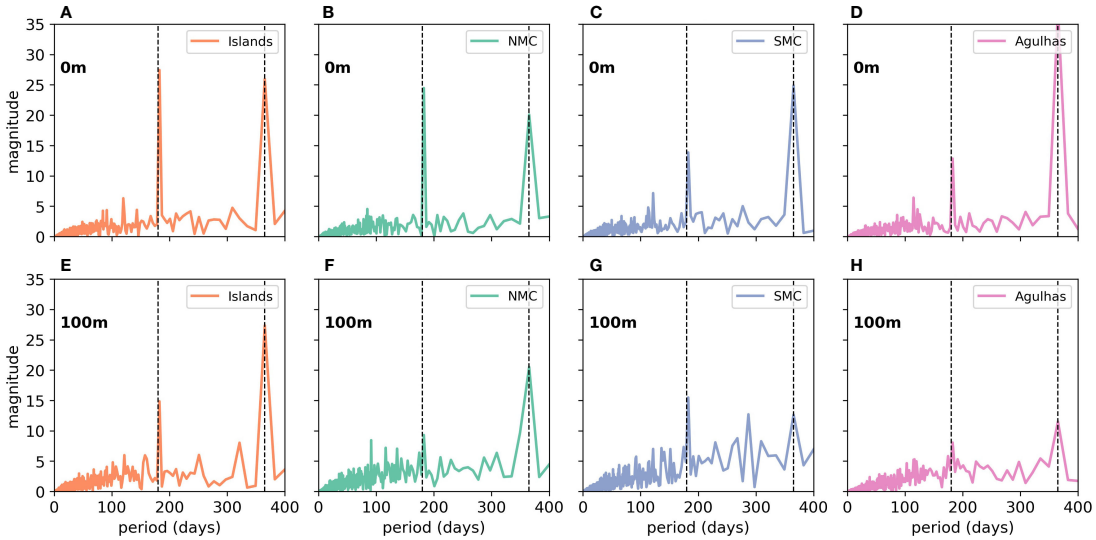

FIGURE 6
Fast Fourier Transform analysis periodograms of MOZ36 front intensity in the 4 subregions: Islands **(A, E)**, NMC **(B, F)**, SMC **(C, G)**, Agulhas **(D, H)** and at two depths: surface **(A-D)**, -100 m **(E-H)**. The dashed vertical lines represent periods of 6 and 12 months. -500 m and -1000 m periodograms are not shown here because they did not show any significant magnitude peak, they are available as Supplementary Material, Figure S6.

Note that the surface climatology of front intensity from MUR SST (Figure 7) shows little seasonal variability compared to the model. This aspect is explored later in the discussion part, where quality flags explain well why the seasonal cycle is significantly dampened compared to the model.

In the Islands subregion, the -100 m front intensity is greater than at the surface and peaks in late austral autumn (June). The signature 2-peak of the surface signal seems to have disappeared entirely, leaving only one clear maximum in winter. In the NMC area, the -100 m front intensity is higher than at the surface and peaks in austral summer, with a second local maximum in austral winter. At -500 m and -1000 m, there is not much seasonal variation anymore (Figure 7).

3.3.2 SMC and Agulhas subregions

In the SMC (20°S-25°S) and in the Agulhas (25°S-30°S) subregions, surface temperature fronts are more intense along the continental shelves and in the wake of the SEMC. The FFT analysis of the 22-year daily time series of SST front intensity from MOZ36 in the two southernmost regions reveals both 6-month and 1-year periods, but this time the yearly signal exhibits stronger magnitude than the biannual one (Figure 6). The climatology of surface temperature front intensity (Figure 7) shows stronger frontal activity during austral winter and spring, with a slight increase in December in the SMC.

Similarly to the NMC, the -100 m temperature front climatology in the SMC is stronger than at the surface and reveals two local maxima with comparable range, in austral summer and winter (Figure 7). In the Agulhas region, the -100 m front climatology (Figure 7) shows a much weaker seasonal variation, also seen on the FFT analysis (Figure 6), with a slight maximum in austral winter.

At -500 m and -1000 m, little seasonal variation is seen in frontal activity (Figure 7). However, even though the fronts become less intense with depth, -500 m and -1000 m fronts in the SMC and Agulhas subregions are still more intense than in the Islands and NMC regions. Indeed, the interaction between the SEMC and local topography fosters the formation of cyclonic eddies and thus of CDF, which have shown to have a strong deep signature in the model (Figure 5).

4 Discussion

4.1 Data and method

The extended MOZ36 validation process conducted in this work and in Miramontes et al. (2019) has confirmed its suitability in depicting realistic basin-scale and regional dynamics of the MC. Yet, the temperature front seasonal

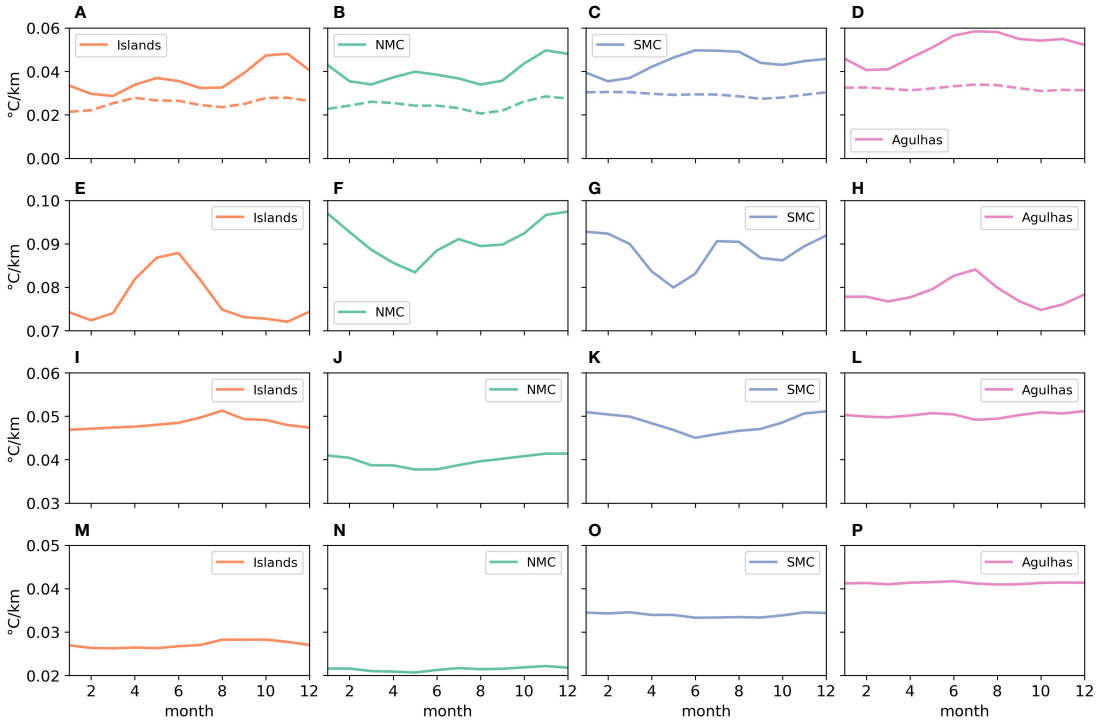

FIGURE 7
Temperature front intensity climatology for each subregion at surface **(A-D)**, -100 m **(E-H)**, -500 m **(I-L)**, -1000 m **(M-P)**. At surface **(A-D)**, data from MOZ36 (full line) and from SST MUR (dashed line) are represented. Please note the different y axis range.

variability exhibited by MUR SST data does not match perfectly MOZ36 results, despite consistent spatial patterns. This disparity can be explained by MUR SST cloud cover adjustments. A preliminary comparative study between MUR SST flags values and corresponding BOA temperature front intensity revealed that periods with higher cloud cover (mostly during austral summer) resulted in dampened frontal activity: the frontal structures are less sharp or non-existent, and the gradient magnitudes much less intense. These higher cloud cover areas correspond to flag 1 values being above 0.39°C and flag 2 values being above 20 hours. For example, Figure 8 shows snapshots of front intensity (C, D) and corresponding flag 1 (E, F) and flag 2 (G, H) for the first day of February and July 2020. One can distinctively see a difference in Figure 8C between the Mozambique shelf north of 17°S where fronts are dimmed, and the center of the MC at around 20°S, where the structures are much sharper. The top panels of Figure 8 show the climatology of monthly percentage of ocean pixels having acceptable flag values to study frontal activity, based on flag 1 for 2003-2020 (Figure 8A) and on both flags for 2017-2020 (Figure 8B). If we only take flag 1 into account, 50-90% of the dataset is acceptable, while if we consider both flags then only 10-50% of the dataset is suitable to study seasonal variability of submesoscale fronts in the MC. Regardless of how many flags are considered, a bigger proportion of pixels are not suitable in austral summer, compared to austral winter, providing a good explanation as to why so little seasonality is seen from MUR SST front intensity in Figure 7. Indeed, the difference between seasons in frontal activity could be significantly dampened by the cloud cover. Additionally, the seasonality in mean EKE is comparable between observations (altimetry) and the model (not shown), which also suggests the limitations of the MUR dataset.

Other tracer-based front detection algorithms, such as the objective Cayulla Cornillon Algorithm (Cayula and Cornillon, 1995) and the Nieto method (Nieto et al., 2012), could have been used to detect temperature fronts in the MC, but they do not provide gradient magnitudes. Moreover, we did find a temperature front intensity threshold and spatial variability similar to what is documented in Nieblas et al. (2014), despite using a different front detection algorithm.

Finally, it would be interesting to use Lyapunov Exponents as in Hernández-Carrasco et al. (2012); Bettencourt et al. (2012) and Siegelman et al. (2020b; 2020a) to bring a dynamic-based approach to our multidecadal tracer-based front database.

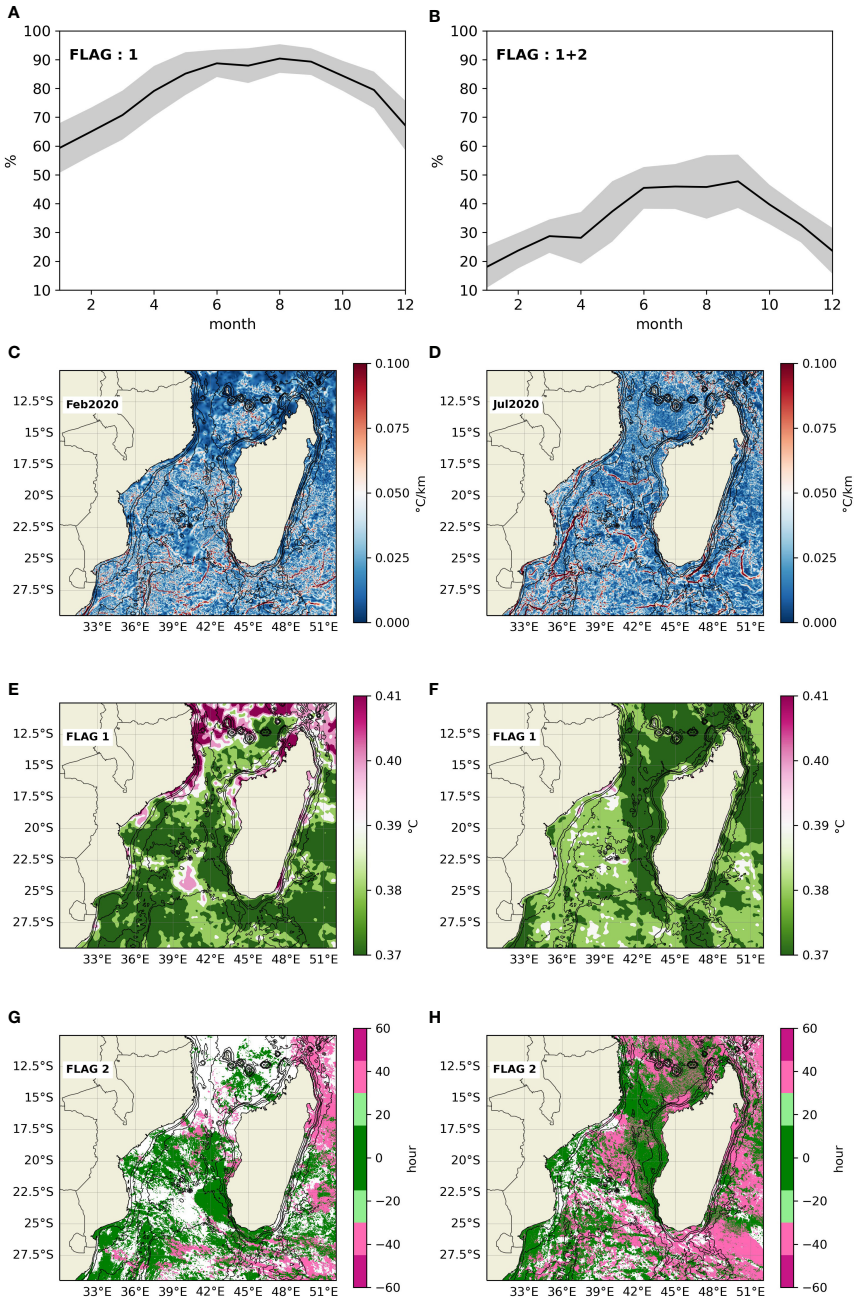

FIGURE 8
The first row represents the climatology of the percentage of pixel deemed of a sufficient quality for frontal analysis based on: flag 1 for 2003-2020 **(A)**; or flag 1 and flag 2 for 2017-2020 **(B)**. The grey shaded area is the standard deviation from the climatology mean. The 2nd row shows temperature front intensity snapshots for February **(C)** and July **(D)** 1st, 2020. The 3rd and 4th row correspond to the same dates as the 1st row and show the corresponding flag values: flag 1 **(E, F)** and flag2 **(G, H)**.

4.2 Spatial variability

We have leveraged the 3D component of the well-validated MOZ36 to go beyond the surface and explore temperature front activity in the MC ocean interior as well. To our knowledge, this is the first temperature front spatial and seasonal variability analysis extending to the ocean interior in the MC.

The mean maps of frontal intensity and probability (Figure 2) from MOZ36 and MUR SST present similar spatial patterns to what is shown in Nieblas et al. (2014). Additionally, the vertical distribution of temperature front intensity is consistent with the stratification profiles from MOZ36 and CARS2009 (Figure S4). Indeed, the Islands (resp. Agulhas) region has the deepest (resp. shallowest) thermocline and frontal intensity peak, at about -200 m (-80 m). It is worth noting that as MOZ36 does not consider the run-off from the Zambeze river, we expect thermal shelfs fronts over the SofalaBank to be underestimated. In all 4 regions, front intensity is maximum at around -100 m, in the vicinity of the mean thermocline. The maximum intensity fronts at around -100 m may be explained by strain-induced vertical velocities at the edge of eddies, which intensify below the mixed layer and up to -400 m below it (Keppler et al., 2018; Siegelman et al., 2020a).

ADF develop at the border of large anticyclonic eddies, or Mozambique Rings, on the western side of the MC, as observed by Biastoch and Krauss (1999) and Schouten et al. (2003). On the other side of the channel, CDF form at the edge of smaller cyclonic eddies, mostly on the southeastern side of the channel and driven by the SMEC, as seen in Gründlingh's work (Gründlingh, 1995). In MOZ36, the temperature front signature of the anticyclonic Mozambique Rings seems to be limited to the upper layers of the water column. However, some discrete observations (de Ruijter et al., 2002) and MOZ36 modelled current (Miramontes et al., 2019) have shown that the dynamics of the Mozambique Rings could indeed reach the bottom. It is still unclear why the temperature front signature of these anticyclonic rings remains weak below 500 m while their associated currents have been previously reported at much deeper levels in the model.

4.3 Seasonal variability

Our EKE mean maps (Figure 4) and seasonal variability analysis (Figure 9) in the MC are consistent with Martínez-Moreno et al. (2022) work on EKE seasonality in the Southern Hemisphere.

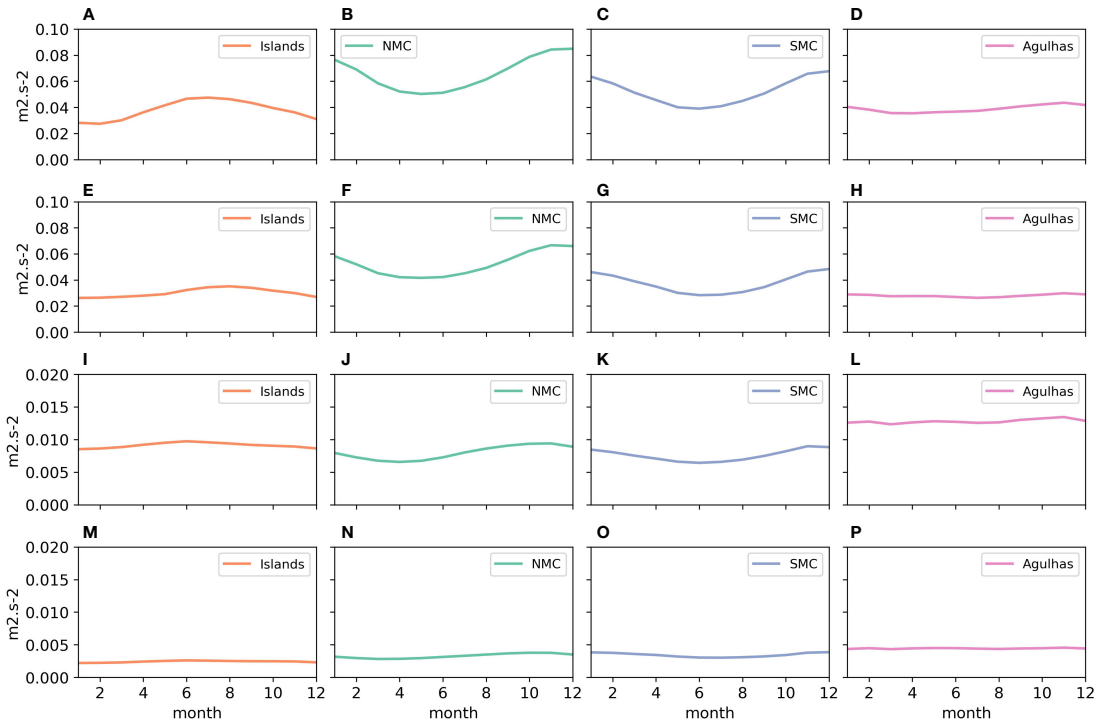

FIGURE 9
MOZ36 EKE climatology for each subregion at surface **(A-D)**, -100 m **(E-H)**, -500 m **(I-L)**, -1000 m **(M-P)**. Please note the different y-axis range.

Seasonal variability in the MC ceases to be significant below -150 m for the Islands subregion, below -350 m and -450 m for the NMC and SMC subregions (respectively) and below -70 m in the Agulhas subregion (Figure 3). This is aligned with the types of fronts that characterize each subregion, as summarized in Table 1. The NMC and SMC subregions are eddy-rich subregions generating mostly ADF and CDF fronts which are more likely to reach deeper in the water column than topographic fronts, and thus propagate surface seasonal signals at depth. We suspect this explains why the seasonal variability in the NMC and SMC subregions reaches deeper layers in the water column. Potential drivers of the seasonal variability for each region are summarized in Table 2.

4.3.1 Islands and NMC subregions

In the Islands and NMC regions, SST front intensity climatology shows two local maxima: a moderate one in May and a greater one in November (Figure 7). A similar semi-annual cycle at the Seychelles Chagos thermocline ridge (Hermes and Reason, 2008) suggests that the Seychelle-Chagos upwelled waters might be one of the possible drivers of temperature front seasonal variability at the surface of both northernmost regions. Additionally, the presence of "cool water" events near Angoche during August to March (Malauene et al., 2014), and upwelling along the Mozambican coast at 11-16°S during the North East monsoon (November-March) (Sætre and Da Silva, 1984) could explain the higher intensity of the second peak in austral spring and summer, especially in the NMC. Another driver behind the local winter maximum could be the elevated EKE in this area responding to the seasonal increase of the NEMC (Figure 9) (Obura et al., 2019).

In the Islands subregion, the -100 m front intensity is greater than at the surface and peaks in late austral autumn. The signature 2-peak of the surface signal has disappeared entirely, leaving only one clear maximum in May-June (Figure 7). This suggests that the -100 m fronts may not be driven by the same processes than the surface ones. Since most fronts in the Islands region belong to the topographic class, and since the NEMC peaks in austral winter (Obura et al., 2019), -100 m temperature fronts in the Islands region seem to be driven solely by seasonal variations of the NEMC and its subsequent interactions with the local topography.

In the NMC area, the -100m front intensity is higher than at the surface and peaks in austral summer, with a second local maximum in austral winter (Figure 7). Those two peaks can be explained by the types of front predominantly found in this region: topographic fronts, and especially ADF (Table 1). On the first hand, as seen in the Islands subregion, topographic fronts follow the variability of the NEMC, which is stronger in austral winter (Obura et al., 2019), explaining the winter peak of frontal activity. On the other hand, ADF are shaped at the edge of anticyclonic eddies forming in this region (Schouten et al., 2003; Halo et al., 2014) and are thus likely linked to variations of EKE, which would explain the frontal activity maximum in austral summer, coinciding with peaks of EKE (Figure 9)

At -500 m and -1000 m, there is not much seasonal variation anymore and frontal activity weakens with depth (Figure 9). This is consistent with our preliminary front typology since ADF and topographic fronts, which represent the majority of fronts in Islands and NMC regions, have been found to present a weak deep signature.

4.3.2 SMC and Agulhas subregions

The FFT periodograms of the two southernmost subregions show that the yearly signal is stronger than the biannual one (Figure 6). The weaker biannual signal can be explained by the lesser influence of the monsoon below 20°S (Schott et al., 2009). The climatology of surface temperature front intensity in the

TABLE 2 Summary of the main drivers of thermal front seasonal variability in the Mozambique Channel, at surface and -100 m.

	Surface	
	Summer	**Winter**
Islands	Angoche upwelling + Mozambique Current + EKE (western MC)	Seychelles-Chagos upwelling + NEMC + EKE (Comoros basin)
NMC	Angoche upwelling + Mozambique Current + EKE (western MC)	Seychelles-Chagos upwelling + NEMC + EKE (Comoros basin)
SMC	Angoche upwelling + Mozambique Current + EKE (western MC)	Seychelles-Chagos upwelling + South Madagascar upwelling
Agulhas	Angoche upwelling + Mozambique Current + EKE (western MC)	SEMC + EKE (SW madagascar) + South Madagascar upwelling
	100m	
	Summer	**Winter**
Islands	n/a	Seychelles-Chagos upwelling + NEMC + EKE (Comoros basin)
NMC	Angoche upwelling + Mozambique Current + EKE (western MC)	Seychelles-Chagos upwelling + NEMC + EKE (Comoros basin)
SMC	Angoche upwelling + Mozambique Current + EKE (western MC)	Seychelles-Chagos upwelling + South Madagascar upwelling
Agulhas	Mozambique Current + EKE (western MC)	South Madagascar upwelling

SMC and Agulhas regions (Figure 7) shows stronger frontal activity during austral winter and spring which coincides with upwelling cells at the southern tip of Madagascar driven by the SEMC (Ho et al., 2004; Ramanantsoa et al., 2018) and the local winds (Lutjeharms and Machu, 2000; DiMarco et al., 2000). Frontal activity in the SMC and Agulhas regions also show a slight increase around December (Figure 7). One possible explanation is the Angoche upwelling cell, which brings cooler water to the surface in austral summer (Malauene et al., 2014). Another possible driver could be the eddy activity, which peaks in austral summer in these regions. Indeed, since the SMC and Agulhas regions seems to host mostly CDF and topographic fronts, it is likely that the temperature front variability in these regions depends on EKE variability.

In the SMC at -100m depth, the first local maximum in austral summer (Figure 7) coincides with a -100 m EKE peak (Figure 9), which suggests that frontal activity there is driven by MC eddies. The second peak in austral winter can be attributed to the local upwelling cells south of Madagascar island (Ramanantsoa et al., 2018), which was also the main driver of surface frontal activity in this region. In the Agulhas region, the -100 m front climatology (Figure 7) shows much weaker seasonal variation, also seen on the FFT analysis (Figure 6), with a slight maximum in austral winter, when the South Madagascar upwelling cells are most active (Ramanantsoa et al., 2018). The absence of austral summer peak, like it is observed in NMC and SMC, can be explained by the comparably weaker EKE seasonal variations in the Agulhas region (Figure 9). It is worth noting that the FFT analysis (Figure 6, and Figure S6) does not show a clear annual or bi-annual period for the SMC and Agulhas regions from -100 m depth and below, which could be linked to the higher inter-annual variability observed in this region (Palastanga et al., 2006).

-500 m and -1000 m fronts in the SMC and Agulhas subregions are more intense than in the Islands and NMC at the same depth, possibly due to the specific typology of fronts most often encountered in the south MC (Table 1). In the SMC and Agulhas, the majority of fronts belong to the CDF category, which have a stronger depth signature, hence the greater -500 and -1000 m front intensity compared to regions where ADF dominate.

Finally, a modest peak at about 4-month can be identified in the FFT analysis periodograms (Figure 6), especially at the surface of the Islands, SMC and Agulhas subregions. This could be attributed to Indian Ocean basin resonance characterized by 120-day period, as detected by both idealized and realistic models (Han et al., 2011).

4.4 Main drivers of frontogenesis in the MC

We have thus documented thermal front seasonal variability in the MC. The next section addresses the relative importance of the main drivers of frontogenesis in the region. A clear distinction between those physical processes would require carrying dynamical diagnostics such as eddy kinetic budgets [e.g., Conejero et al. (2020)], eddy kinetic energy decompositions [e.g., Martínez-Moreno et al. (2019; 2022] or frontogenesis function decompositions [e.g., Koseki et al. (2019)] based on the model outputs, which would fall beyond the scope of this work. We nonetheless argue that thermal fronts in the MC depends on mean and seasonal circulation, seasonal upwellings and variations of EKE. To do so, we first define our seasonal division: In the Mozambique Channel monsoon reversals occur first in April to June and then in October to November, marking the separation between winter and summer (Collins, 2013; Obura et al., 2019). We thus define winter as the period from April to September, and summer as the period from October to March.

4.4.1 Mean circulation

We can infer the role of the mean circulation on thermal front intensity (especially on the quasi-permanent fronts since no seasonal variability is involved here) from mean maps of surface current (northward and eastward velocities) and SST generated by the MOZ36 configuration (Figure S7). From the mean SST map (Figure S7.B), we can observe a strong thermal front at the northern tip of Madagascar, following the path of the North East Madagascar Current (NEMC), also visible in the mean current map (Figure S7.A) and the mean thermal front intensity (Figure 2). Similarly at the southwestern tip of Madagascar, a strong thermal front follows the path of the South East Madagascar Current (SEMC) toward the Agulhas current. Additionally, we can identify along-shelf thermal gradients of moderate intensity at the southeastern tip of Madagascar and off Maputo (Delagoa Bay), which are probably due to quasi-permanent coastal upwelling cells (Ramanantsoa et al., 2018), as well as a colder tongue extending along the outer parts of the Sofala Bank, which could be indicating the presence of a quasi-permanent shelf-break upwelling there, as documented by Hill and Johnson (1974); Gibbs et al. (2000) and Rossi et al. (2010).

4.4.2 Seasonal upwellings

Seasonal upwelling cells such as the Seychelles-Chagos upwelling (Hermes and Reason, 2008), the Angoche upwelling (Malauene et al., 2014) and, to a lesser extent, the South Madagascar upwelling cells (Ramanantsoa et al., 2018) mentioned in this work are strongly localized in space and time. The Seychelles-Chagos upwelling turns on in austral winter (Hermes and Reason, 2008), while the Angoche upwelling is active during the August-March period (Malauene et al., 2014). The first upwelling core south of Madagascar is present all year round but reaches its maximum at the end of austral winter, while the second (much weaker) core is most

active from October to January (Ramanantsoa et al., 2018). In the Islands and NMC regions, the mean thermal front intensity peaks first in May-June (Figure 7), which corresponds to the first active period of the Seychelles-Chagos upwelling system. This front intensity peak is mostly felt in the Islands subregion which is closest to the Seychelles-Chagos upwelling cell. We thus postulate that this first front intensity peak at surface and -100 m depth in both Islands and NMC subregions depends on the Seychelles-Chagos upwelling system. The second peak of frontal intensity in the same two northern subregions happens in November-December (Figure 7), and especially in the NMC region. We argue that this second peak is driven first by the Angoche upwelling and to a lesser extent by the Seychelles-Chagos upwelling. The seasonality of this second peak coincides with the Angoche most active period, which is located in the NMC, and the second (weaker) upwelling maximum in the Seychelles-Chagos located further upstream. The South Madagascar upwelling cells reach their maximum in winter, when the thermal front intensity peaks in both NMC and Agulhas subregions Figure 7). It thus suggests that the South Madagascar upwelling cells play an important role in the increased front intensity documented in the southernmost subregion during winter.

4.4.3 Seasonal current and EKE variability

Some quasi-permanent thermal fronts are found in the path of the NEMC, the SEMC and the Mozambique Current. The seasonal variability of these currents induces in turn variability of instabilities. We suggest that these instabilities, in turn, produce the sub to mesoscale activity that affects the intensity of those thermal fronts. The NEMC, and the EKE associated to its instabilities, are both stronger in winter (Figure S8 and S9), which also corresponds to a higher thermal front intensity in the northern Islands subregion, especially at -100 m (Figure S10 and S11). The Mozambique Current and the EKE in the western MC are stronger in summer (Figure S8 and S9), which also corresponds to higher thermal front intensity in the western half of the MC, especially in NMC and SMC subregions (Figure S10 and S11).

Finally, the suspected main drivers of seasonal variability of thermal front intensity, for each season and each subregion, and at both surface and -100 m, are summarized in Tables 2 and Table S1.

5 Conclusion and perspectives

We presented here the first thermal front seasonality analysis in the Mozambique Channel from the surface down to -1000 m depth. This work demonstrates that front dynamics in the MC are complex, and we suggest several possibilities to link temperature front seasonal variability to regional and remote ocean dynamics. Temperature fronts are generally more intense and more likely to occur over continental shelves, in the wake of the NEMC and SEMC, on the lee of islands, and at the edge of eddies. We show that temperature front intensity peaks below the mixed layer, between -100 and -200 m depth, which indicates that they are largely associated to aspects of the ocean dynamics rather than to mixed-layer processes. This consistent with the energetic mesoscale dynamics in this region.

Seasonal variations are felt down to -150 m in the Islands subregion, -350 m and -450 m in the NMC and SMC subregions (respectively) and -70 m in the Agulhas subregion. We argue that the main drivers of thermal front seasonal variability in the MC are upwelling cells (Angoche, South Madagascar, Seychelles-Chagos), current seasonal variability (NEMC, SEMC, and the Mozambique Current) and variations in EKE.

Since the MC circulation is connected to equatorial circulation in the Indian ocean, it is expected that temperature fronts experience fluctuations at interannual timescales. The Indian Ocean Dipole (IOD) seems to affect the variability of the transport (Ridderinkhof et al., 2010) and the SSH in the channel (Palastanga et al., 2006) through planetary wave propagation. A positive (negative) IOD event is linked to a weaker (stronger) NEMC (Ridderinkhof et al., 2010) which could potentially affect the intensity of fronts in the Islands and NMC subregions through fluctuations in current instabilities. Additionally, a change in SSH would also modulate the interactions between currents at the entrance or within the MC, which affects not only the EKE in the MC (Palastanga et al., 2006) but also the production of temperature front at the edge of eddies.

Another relevant path of investigation is suggested by Martínez-Moreno et al. (2021) in their global multidecadal study on altimetry and SST satellite-based observations. Their analysis shows that, even though SST gradients in the northern part of the MC have generally weakened between 1993 and 2020, the EKE has significantly increased during the same period in the northern MC and decreased in the southwest MC. This multidecadal trend suggests that climate change could have a significant impact on eddy-driven frontogenesis in the channel, as temperature fronts could be weaker but more numerous. Li et al. (2020) have also demonstrated a significant increase of stratification over the past half-century in the MC, especially in the Islands and NMC subregions. This suggests a possible enhancing of frontal activity due to climate change, especially in the two northernmost subregions, yet to be studied.

Thermal fronts, within and below the mixed layer, are thought to create transitory biodiverse hotspots across all trophic levels. Our analyses of their variability sheds light on where and when they are the strongest, with each subregion behaving differently. Altogether, it provides critical insights about where, horizontally and vertically, it is more relevant to survey bio-physical interactions and to consider protection initiatives in the MC. Conservation stakeholders could indeed use our synthetic analyses of front spatial and seasonal variability

to elaborate rules for an adaptive and dynamic management of both epipelagic and mesopelagic realms, as also suggested in Brito-Morales et al. (2020) work on climate velocities. More research is needed to better apprehend climate change implications for front variability and their associated biological impacts to design an effective and climate-resilient network of pelagic and coastal marine reserves in the MC.

Data availability statement

The raw data supporting the conclusions of this article will be made available by the authors, without undue reservation.

Author contributions

FS with VR, BD, and VG designed the study. PP provided MOZ36 model output, and guidance for model analyses. JS retrieved the remotely sensed MUR SST data. FS produced the front database and subsequent analysis of the results. CM assisted with the High Performance Computing. VR, BD, and VG supervised the findings of this work and provided critical feedbacks. FS produced the figures and wrote the manuscript with input from all authors. All authors contributed to the article and approved the submitted version.

Funding

The authors acknowledge funding from the "Ocean Front Change" project, funded by the Belmont Forum and implemented through the French National Research Agency (ANR-20-BFOC-0006-04).

Acknowledgments

This work was supported by the Mediterranean Institute of Oceanography (MIO) and the French National Institute for Sustainable Development (IRD). The authors wish to thank J. Lecubin and C. Yohia for technical assistance with the local high performance computers and two reviewers for their helpful and constructive comments.

Conflict of interest

The authors declare that the research was conducted in the absence of any commercial or financial relationships that could be construed as a potential conflict of interest.

Publisher's note

All claims expressed in this article are solely those of the authors and do not necessarily represent those of their affiliated organizations, or those of the publisher, the editors and the reviewers. Any product that may be evaluated in this article, or claim that may be made by its manufacturer, is not guaranteed or endorsed by the publisher.

Supplementary material

The Supplementary Material for this article can be found online at: https://www.frontiersin.org/articles/10.3389/fmars.2022.1045136/full#supplementary-material

References

Acha, E. M., Mianzan, H. W., Guerrero, R. A., Favero, M., and Bava, J. (2004). Marine fronts at the continental shelves of austral south america. *J. Mar. Syst.* 44, 83–105. doi: 10.1016/j.jmarsys.2003.09.005

Adams, K. A., Hosegood, P., Taylor, J. R., Sallée, J. B., Bachman, S., Torres, R., et al. (2017). Frontal circulation and submesoscale variability during the formation of a southern ocean mesoscale eddy. *J. Phys. Oceanogr.* 47, 1737–1753. doi: 10.1175/jpo-d-16-0266.1

Alemany, D., Acha, E. M., and Iribarne, O. (2009). The relationship between marine fronts and fish diversity in the patagonian shelf large marine ecosystem. *J. Biogeogr.* 36, 2111–2124. doi: 10.1111/j.1365-2699.2009.02148.x

Annasawmy, P., Ternon, J. F., Marsac, F., Cherel, Y., Béhagle, N., Roudaut, G., et al. (2018). Micronekton diel migration, community composition and trophic position within two biogeochemical provinces of the south west indian ocean: Insight from acoustics and stable isotopes. *Deep-sea. Res. Part I. Oceanogr. Res. Papers.* 138, 85–97. doi: 10.1016/j.dsr.2018.07.002

Bakun, A. (2006). Fronts and eddies as key structures in the habitat of marine fish larvae: opportunity, adaptive response and competitive advantage. *Sci. Marina.* 70S2, 105–122. doi: 10.3989/scimar.2006.70s2105

Barlow, R., Lamont, T., Morris, T., Sessions, H., and van den Berg, M. (2014). Adaptation of phytoplankton communities to mesoscale eddies in the mozambique channel. *Deep-sea. Res. Part II. Topical. Stud. Oceanogr.* 100, 106–118. doi: 10.1016/j.dsr2.2013.10.020

Belkin, I. M. (2021). Remote sensing of ocean fronts in marine ecology and fisheries. *Remote Sens.* 12, 883. doi: 10.3390/rs13050883

Belkin, I. M., Cornillon, P. C., and Sherman, K. (2009). Fronts in large marine ecosystems. *Prog. Oceanogr.* 81, 223–236. doi: 10.1016/j.pocean.2009.04.015

Belkin, I. M., and O'Reilly, J. E. (2009). An algorithm for oceanic front detection in chlorophyll and sst satellite imagery. *J. Mar. Syst.* 78, 319–326. doi: 10.1016/j.jmarsys.2008.11.018

Bettencourt, J. H., López, C., and Hernández-García, E. (2012). Oceanic three-dimensional lagrangian coherent structures: A study of a mesoscale eddy in the benguela upwelling region. *Ocean. Model.* 51, 73–83. doi: 10.1016/j.ocemod.2012.04.004

Biastoch, A., and Krauss, W. (1999). The role of mesoscale eddies in the source regions of the agulhas current. *J. Phys. Oceanogr.* 29, 2303–2317. doi: 10.1175/1520-0485(1999)029<2303:tromei>2.0.co;2

Bosse, A., and Fer, I. (2019). Mean structure and seasonality of the norwegian atlantic front current along the mohn ridge from repeated glider transects. *Geophys. Res. Lett.* 46, 13170–13179. doi: 10.1029/2019gl084723

Brito-Morales, I., Schoeman, D. S., Molinos, J. G., Burrows, M. T., Klein, C. J., Arafeh-Dalmau, N., et al. (2020). Climate velocity reveals increasing exposure of deep-ocean biodiversity to future warming. *Nat. Climate Change* 10, 576–581. doi: 10.1038/s41558-020-0773-5

Brunnschweiler, J. M., Baensch, H., Pierce, S. J., and Sims, D. W. (2009). Deep-diving behaviour of a whale shark rhincodon typus during long-distance movement in the western indian ocean. *J. Fish. Biol.* 74, 706–714. doi: 10.1111/j.1095-8649.2008.02155.x

Calil, P. H. R., Suzuki, N., Baschek, B., and da Silveira, I. C. A. (2021). Filaments, fronts and eddies in the cabo frio coastal upwelling system, brazil. *Fluids* 6, 54. doi: 10.3390/fluids6020054

Canny, J. (1986). A computational approach to edge detection. *IEEE Trans. Pattern Anal. Mach. Intell.* 8, 679–698. doi: 10.1109/TPAMI.1986.4767851

Castelao, R. M., Mavor, T. P., Barth, J. A., and Breaker, L. C. (2006). Sea surface temperature fronts in the California Current System from geostationary satellite observations. *J. Geophys. Res.* 111, C09026. doi: 10.1029/2006jc003541

Cayula, J. F., and Cornillon, P. (1995). Multi-image edge detection for sst images. *J. Atmospheric. Oceanic. Technol.* 12, 821–829. doi: 10.1175/1520-0426(1995)012<0821:miedfs>2.0.co;2

Chin, T. M., Vazquez-Cuervo, J., and Armstrong, E. M. (2017). A multi-scale high-resolution analysis of global sea surface temperature. *Remote Sens. Environ.* 200, 154–169. doi: 10.1016/j.rse.2017.07.029

Collins, C. (2013). *The dynamics and physical processes of the Comoros basin* (University of Cape Town). pp 8–44

Condie, S. A. (1993). Formation and stability of shelf break fronts. *J. Geophys. Res.* 98, 12405–12416. doi: 10.1029/93jc00624

Conejero, C., Dewitte, B., Garçon, V., Sudre, J., and Montes, I. (2020). Enso diversity driving low-frequency change in mesoscale activity off peru and chile. *Sci. Rep.* 10, 17902. doi: 10.1038/s41598-020-74762-x

De Falco, C., Desbiolles, F., Bracco, A., and Pasquero, C. (2022). Island mass effect: A review of oceanic physical processes. *Front. Mar. Sci.* 9. doi: 10.3389/fmars.2022.894860

de Ruijter, W. P. M., Ridderinkhof, H., Lutjeharms, J. R. E., Schouten, M. W., and Veth, C. (2002). Observations of the flow in the mozambique channel: Observations in the mozambique channel. *Geophys. Res. Lett.* 29, 140–1–140–3. doi: 10.1029/2001gl013714

Dewitte, B., Conejero, C., Ramos, M., Bravo, L., Garçon, V., Parada, C., et al. (2021). Understanding the impact of climate change on the oceanic circulation in the chilean island ecoregions. *Aquat. Conservation.: Mar. Freshw. Ecosyst.* 31, 232–252. doi: 10.1002/aqc.3506

DiMarco, S. F., Chapman, P., and Nowlin J Worth, D. (2000). Satellite observations of upwelling on the continental shelf south of madagascar. *Geophys. Res. Lett.* 27,3965–3968. doi: 10.1029/2000gl012012

DiMarco, S. F., Chapman, P., Nowlin J Worth, D., Hacker, P., Donohue, K., Luther, M., et al. (2002). Volume transport and property distributions of the mozambique channel. *Deep-sea. Res. Part II. Topical. Stud. Oceanogr.* 49, 1481–1511. doi: 10.1016/s0967-0645(01)00159-x

Donguy, J., and Piton, B. (1991). The mozambique channel revisited. *Oceanol. Acta* (1991) 14, 549–558. Available at: https://archimer.ifremer.fr/doc/00101/21275/18884.pdf

Doty, M. S., and Oguri, M. (1956). The island mass effect. *ICES. J. Mar. Sci.: J. du. Conseil.* 22, 33–37. doi: 10.1093/icesjms/22.1.33

Fairall, C. W., Bradley, E. F., Rogers, D. P., Edson, J. B., and Young, G. S. (1996). Bulk parameterization of air-sea fluxes for tropical ocean-global atmosphere coupled-ocean atmosphere response experiment. *J. Geophys. Res.* 101, 3747–3764. doi: 10.1029/95jc03205

Fox-Kemper, B., Ferrari, R., and Hallberg, R. (2008). Parameterization of mixed layer eddies. part i: Theory and diagnosis. *J. Phys. Oceanogr.* 38, 1145–1165. doi: 10.1175/2007jpo3792.1

Gibbs, M. T., Marchesiello, P., and Middleton, J. H. (2000). Observations and simulations of a transient shelfbreak front over the narrow shelf at sydney, southeastern australia. *Continental. Shelf. Res.* 20, 763–784. doi: 10.1016/s0278-4343(99)00090-4

Gründlingh, M. L. (1995). Tracking eddies in the southeast atlantic and southwest indian oceans with topex/poseidon. *J. Geophys. Res.* 100 (C12), 24977–24986. doi: 10.1029/95jc01985

Halo, I., Backeberg, B., Penven, P., Ansorge, I., Reason, C., and Ullgren, J. E. (2014). Eddy properties in the mozambique channel: A comparison between observations and two numerical ocean circulation models. *Deep-sea. Res. Part II. Topical. Stud. Oceanogr.* 100, 38–53. doi: 10.1016/j.dsr2.2013.10.015

Han, W., McCreary, J. P., Masumoto, Y., Vialard, J., and Duncan, B. (2011). Basin resonances in the equatorial indian ocean. *J. Phys. Oceanogr.* 41, 1252–1270. doi: 10.1175/2011jpo4591.1

Hermes, J. C., and Reason, C. J. C. (2008). Annual cycle of the South Indian Ocean (Seychelles-Chagos) thermocline ridge in a regional ocean model. *J. Geophys. Res.* 113, C04035. doi: 10.1029/2007jc004363

Hernández-Carrasco, I., López, C., Hernández-García, E., and Turiel, A. (2012). Seasonal and regional characterization of horizontal stirring in the global ocean. *J. Geophys. Res.* 117, C10007. doi: 10.1029/2012jc008222

Heywood, K. J., Barton, E. D., and Simpson, J. H. (1990). The effects of flow disturbance by an oceanic island. *J. Mar. Res.* 48, 55–73. doi: 10.1357/002224090784984623

Hill, R. B., and Johnson, J. A. (1974). A theory of upwelling over the shelf break. *J. Phys. Oceanogr.* 4, 19–26. doi: 10.1175/1520-0485(1974)004<0019:atouot>2.0.co;2

Ho, C. R., Zheng, Q., and Kuo, N. J. (2004). Seawifs observations of upwelling south of madagascar: long-term variability and interaction with east madagascar current. *Deep-sea. Res. Part II. Topical. Stud. Oceanogr.* 51, 59–67. doi: 10.1016/j.dsr2.2003.05.001

Kahru, M., Håkansson, B., and Rud, O. (1995). Distributions of the sea-surface temperature fronts in the baltic sea as derived from satellite imagery. *Continental. Shelf. Res.* 15, 663–679. doi: 10.1016/0278-4343(94)e0030-p

Kartushinsky, A. V., and Sidorenko, A. Y. (2013). Analysis of the variability of temperature gradient in the ocean frontal zones based on satellite data. *Adv. Space. Res.* 52, 1467–1475. doi: 10.1016/j.asr.2013.07.023

Keppler, L., Cravatte, S., Chaigneau, A., Pegliasco, C., Gourdeau, L., and Singh, A. (2018). Observed characteristics and vertical structure of mesoscale eddies in the southwest tropical pacific. *J. Geophys. Res. Oceans.* 123, 2731–2756. doi: 10.1002/2017jc013712

Koseki, S., Giordani, H., and Goubanova, K. (2019). Frontogenesis of the angola–benguela frontal zone. *Ocean. Sci.* 15, 83–96. doi: 10.5194/os-15-83-2019

Largier, J. L. (1993). Estuarine fronts: How important are they? *Estuaries* 16, 1–11. doi: 10.2307/1352760

Legeckis, R. A. (1978). A survey of worldwide sea surface temperature fronts detected by environmental satellites. *J. Geophys. Res.* 83, 4501–4522. doi: 10.1029/jc083ic09p04501

Lévy, M., Franks, P. J. S., and Smith, K. S. (2018). The role of submesoscale currents in structuring marine ecosystems. *Nat. Commun.* 9, 4758. doi: 10.1038/s41467-018-07059-3

Li, G., Cheng, L., Zhu, J., Trenberth, K. E., Mann, M. E., and Abraham, J. P. (2020). Increasing ocean stratification over the past half-century. *Nat. Climate Change* 10, 1116–1123. doi: 10.1038/s41558-020-00918-2

Lin, L., Liu, D., Luo, C., and Xie, L. (2019). Double fronts in the yellow sea in summertime identified using sea surface temperature data of multi-scale ultra-high resolution analysis. *Continental. Shelf. Res.* 175, 76–86. doi: 10.1016/j.csr.2019.02.004

Liu, D., Wang, Y., Wang, Y., and Keesing, J. K. (2018). Ocean fronts construct spatial zonation in microfossil assemblages. *Global Ecol. Biogeogr.: J. Macroecol.* 27, 1225–1237. doi: 10.1111/geb.12779

Locarnini, R. A., Mishonov, A. V., Baranova, O. K., Boyer, T. P., Zweng, M. M., Garcia, H. E., et al. (2018). World ocean atlas 2018, Volume 1. *Temperature. A. Mishonov. Tech. Editor. NOAA. Atlas. NESDIS.* 81, 52 pp.

Lutjeharms, J. R. E. (2006). Three decades of research on the greater Agulhas Current. *Ocean Science* (2006) 3, 129–147.

Lutjeharms, J. R. E., Biastoch, A., van der Werf, P. M., Ridderinkhof, H., and De Ruijter, W. P. M. (2012). On the discontinuous nature of the mozambique current. *South Afr. J. Sci.* 108 (1/2), 428. doi: 10.4102/sajs.v108i1/2.428

Lutjeharms, J. R. E., and Machu, E. (2000). An upwelling cell inshore of the east madagascar current. *Deep-sea. Res. Part I. Oceanogr. Res. Papers.* 47, 2405–2411. doi: 10.1016/s0967-0637(00)00026-1

Malauene, B. S., Shillington, F. A., Roberts, M. J., and Moloney, C. L. (2014). Cool, elevated chlorophyll-a waters off northern mozambique. *Deep-sea. Res. Part II. Topical. Stud. Oceanogr.* 100, 68–78. doi: 10.1016/j.dsr2.2013.10.017

Mantas, V. M., Pereira, A. J. S. C., and Marques, J. C. (2019). Partitioning the ocean using dense time series of earth observation data. regions and natural boundaries in the western iberian peninsula. *Ecol. Indic.* 103, 9–21. doi: 10.1016/j.ecolind.2019.03.045

Marchesiello, P., McWilliams, J. C., and Shchepetkin, A. (2001). Open boundary conditions for long-term integration of regional oceanic models. *Ocean. Model.* 3, 1–20. doi: 10.1016/s1463-5003(00)00013-5

Martínez-Moreno, J., Hogg, A. M., and England, M. H. (2022). Climatology, seasonality, and trends of spatially coherent ocean eddies. *J. Geophys. Res. Oceans.* 127, e2021JC017453. doi: 10.1029/2021jc017453

Martínez-Moreno, J., Hogg, A. M., England, M. H., Constantinou, N. C., Kiss, A. E., and Morrison, A. K. (2021). Global changes in oceanic mesoscale currents over the satellite altimetry record. *Nat. Climate Change* 11, 397–403. doi: 10.1038/s41558-021-01006-9

Martínez-Moreno, J., Hogg, A. M., Kiss, A. E., Constantinou, N. C., and Morrison, A. K. (2019). Kinetic energy of eddy-like features from sea surface altimetry. *J. Adv. Modeling. Earth Syst.* 11, 3090–3105. doi: 10.1029/2019ms001769

McWilliams, J. C. (2021). Oceanic frontogenesis. *Annu. Rev. Mar. Sci.* 13, 227–253. doi: 10.1146/annurev-marine-032320-120725

Miramontes, E., Penven, P., Fierens, R., Droz, L., Toucanne, S., Jorry, S. J., et al. (2019). The influence of bottom currents on the zambezi valley morphology (mozambique channel, sw indian ocean): In situ current observations and hydrodynamic modelling. *Mar. Geol.* 410, 42–55. doi: 10.1016/j.margeo.2019.01.002

Munk, W., Armi, L., Fischer, K., and Zachariasen, F. (2000). Spirals on the sea. *Proc. Math. Phys. Eng. Sci.* 457, 1217–1280. doi: 10.1098/rspa.2000.0560

Nieblas, A. E., Demarcq, H., Drushka, K., Sloyan, B., and Bonhommeau, S. (2014). Front variability and surface ocean features of the presumed southern bluefin tuna spawning grounds in the tropical southeast indian ocean. *Deep-sea. Res. Part II. Topical. Stud. Oceanogr.* 107, 64–76. doi: 10.1016/j.dsr2.2013.11.007

Nieto, K., Demarcq, H., and McClatchie, S. (2012). Mesoscale frontal structures in the canary upwelling system: New front and filament detection algorithms applied to spatial and temporal patterns. *Remote Sens. Environ.* 123, 339–346. doi: 10.1016/j.rse.2012.03.028

Nieto, K., Xu, Y., Teo, S. L. H., McClatchie, S., and Holmes, J. (2017). How important are coastal fronts to albacore tuna (thunnus alalunga) habitat in the northeast pacific ocean? *Prog. Oceanogr.* 150, 62–71. doi: 10.1016/j.pocean.2015.05.004

Obura, D. O., Bandeira, S. O., Bodin, N., Burgener, V., Braulik, G., Chassot, E., et al. (2019). *Chapter 4 - The Northern Mozambique Channel, World Seas: an Environmental Evaluation* (*Second* Edition), Academic Press, 2019, 75–99. doi: 10.1016/B978-0-08-100853-9.00003-8.

Palastanga, V., van Leeuwen, P. J., and de Ruijter, W. P. M. (2006). A link between low-frequency mesoscale eddy variability around madagascar and the large-scale indian ocean variability. *J. Geophys. Res.* 111, C09029. doi: 10.1029/2005jc003081

Park, S., and Chu, P. C. (2006). Thermal and haline fronts in the yellow/east china seas: Surface and subsurface seasonality comparison. *J. Oceanogr.* 62, 617–638. doi: 10.1007/s10872-006-0081-3

Ramanantsoa, J. D., Krug, M., Penven, P., Rouault, M., and Gula, J. (2018). Coastal upwelling south of madagascar: Temporal and spatial variability. *J. Mar. Syst.* 178, 29–37. doi: 10.1016/j.jmarsys.2017.10.005

Read, J. F., Pollard, R. T., and Allen, J. T. (2007). Sub-Mesoscale structure and the development of an eddy in the subantarctic front north of the crozet islands. *Deep-sea. Res. Part II. Topical. Stud. Oceanogr.* 54, 1930–1948. doi: 10.1016/j.dsr2.2007.06.013

Ridderinkhof, H., and de Ruijter, W. P. M. (2003). Moored current observations in the mozambique channel. *Deep-sea. Res. Part II. Topical. Stud. Oceanogr.* 50, 1933–1955. doi: 10.1016/s0967-0645(03)00041-9

Ridderinkhof, H., van der Werf, P. M., Ullgren, J. E., van Aken, H. M., van Leeuwen, P. J., and de Ruijter, W. P. M. (2010). Seasonal and interannual variability in the mozambique channel from moored current observations. *J. Geophys. Res.* 115, C06010. doi: 10.1029/2009jc005619

Ridgway, K., Dunn, J., and Wilkin, J. (2002). Ocean interpolation by four-dimensional least squares -application to the waters around australia. *J. Atmos. Ocean. Tech.* 19, 1357–1375. doi: 10.1175/1520-0426(2002)019<1357:OIBFDW>2.0.CO;2

Rio, M. H., Mulet, S., and Picot, N. (2014). Beyond goce for the ocean circulation estimate: Synergetic use of altimetry, gravimetry, and in situ data provides new insight into geostrophic and ekman currents: Ocean circulation beyond goce. *Geophys. Res. Lett.* 41, 8918–8925. doi: 10.1002/2014gl061773

Roberts, M. J., Ternon, J. F., and Morris, T. (2014). Interaction of dipole eddies with the western continental slope of the mozambique channel. *Deep-sea. Res. Part II. Topical. Stud. Oceanogr.* 100, 54–67. doi: 10.1016/j.dsr2.2013.10.016

Rossi, V., Garçon, V., Tassel, J., Romagnan, J. B., Stemmann, L., Jourdin, F., et al. (2013). Cross-shelf variability in the iberian peninsula upwelling system: Impact of a mesoscale filament. *Continental. Shelf. Res.* 59, 97–114. doi: 10.1016/j.csr.2013.04.008

Rossi, V., Morel, Y., and Garçon, V. (2010). Effect of the wind on the shelf dynamics: Formation of a secondary upwelling along the continental margin. *Ocean. Model.* 31, 51–79. doi: 10.1016/j.ocemod.2009.10.002

Sabarros, P. S., Grémillet, D., Demarcq, H., Moseley, C., Pichegru, L., Mullers, R. H. E., et al. (2014). Fine-scale recognition and use of mesoscale fronts by foraging cape gannets in the benguela upwelling region. *Deep-sea. Res. Part II. Topical. Stud. Oceanogr.* 10, 77–84. doi: 10.1016/j.dsr2.2013.06.023

Sætre, R., and Da Silva, A. J. (1984). The circulation of the mozambique channel. *Deep-sea. Res. Part A. Oceanogr. Res. Papers.* 31 (5), 485–508. doi: 10.1016/0198-0149(84)90098-0

Scales, K. L., Hazen, E. L., Jacox, M. G., Castruccio, F., Maxwell, S. M., Lewison, R. L., et al. (2018). Fisheries bycatch risk to marine megafauna is intensified in lagrangian coherent structures. *Proc. Natl. Acad. Sci. United. States America* 115, 7362–7367. doi: 10.1073/pnas.1801270115

Schott, F. A., Xie, S. P., McCreary, J., and Julian, P. (2009). Indian Ocean circulation and climate variability. *Rev. Geophys.* 47, RG1002. doi: 10.1029/2007rg000245

Schouten, M. W., de Ruijter, W. P. M., van Leeuwen, P. J., and Ridderinkhof, H. (2003). Eddies and variability in the mozambique channel. *Deep-sea. Res. Part II. Topical. Stud. Oceanogr.* 50, 1987–2003. doi: 10.1016/s0967-0645(03)00042-0

Shchepetkin, A. F., and McWilliams, J. C. (2005). The regional oceanic modeling system (roms): a split-explicit, free-surface, topography-following-coordinate oceanic model. *Ocean. Model.* 9, 347–404. doi: 10.1016/j.ocemod.2004.08.002

Shimada, T., Sakaida, F., Kawamura, H., and Okumura, T. (2005). Application of an edge detection method to satellite images for distinguishing sea surface temperature fronts near the japanese coast. *Remote Sens. Environ.* 98, 21–34. doi: 10.1016/j.rse.2005.05.018

Siegelman, L., Klein, P., Rivière, P., Thompson, A. F., Torres, H. S., Flexas, M., et al. (2020b). Enhanced upward heat transport at deep submesoscale ocean fronts. *Nat. Geosci.* 13, 50–55. doi: 10.1038/s41561-019-0489-1

Siegelman, L., Klein, P., Thompson, A. F., Torres, H. S., and Menemenlis, D. (2020a). Altimetry-based diagnosis of deep-reaching sub-mesoscale ocean fronts. *Fluids* 5, 145. doi: 10.3390/fluids5030145

Tamim, A., Yahia, H., Daoudi, K., Minaoui, K., Atillah, A., Aboutajdine, D., et al. (2015). Detection of moroccan coastal upwelling fronts in sst images using the microcanonical multiscale formalism. *Pattern Recognit. Lett.* 55, 28–33. doi: 10.1016/j.patrec.2014.12.006

Tarry, D. R., Essink, S., Pascual, A., Ruiz, S., Poulain, P. M., Özgökmen, T., et al. (2021). Frontal convergence and vertical velocity measured by drifters in the alboran sea. *J. Geophys. Res. Oceans.* 126, e2020JC016614. doi: 10.1029/2020jc016614

Ternon, J. F., Roberts, M. J., Morris, T., Hancke, L., and Backeberg, B. (2014). *In situ* measured current structures of the eddy field in the mozambique channel. *Deep-sea. Res. Part II. Topical. Stud. Oceanogr.* 100, 10–26. doi: 10.1016/j.dsr2.2013.10.013

Tew Kai, E., and Marsac, F. (2010). Influence of mesoscale eddies on spatial structuring of top predators' communities in the mozambique channel. *Prog. Oceanogr.* 100, 214–223. doi: 10.1016/j.pocean.2010.04.010

Tew Kai, E., Rossi, V., Sudre, J., Weimerskirch, H., Lopez, C., Hernandez-Garcia, E., et al. (2009). Top marine predators track lagrangian coherent structures. *Proc. Natl. Acad. Sci. United. States America* 86, 8245–8250. doi: 10.1073/pnas.0811034106

Torres Arriaza, J. A., Guindos Rojas, F., Peralta Lopez, M., and Canton, M. (2003). Competitive neural-net-based system for the automatic detection of oceanic mesoscalar structures on avhrr scenes. *IEEE Trans. Geosci. Remote Sensing.: Publ. IEEE Geosci. Remote Sens. Soc.* 41, 845–852. doi: 10.1109/tgrs.2003.809929

Turiel, A., and del Pozo, A. (2002). Reconstructing images from their most singular fractal manifold. *IEEE Trans. Image. Processing.: Publ. IEEE Signal Process. Soc.* 11, 345–350. doi: 10.1109/TIP.2002.999668

Turiel, A., Solé, J., Nieves, V., Ballabrera-Poy, J., and García-Ladona, E. (2008). Tracking oceanic currents by singularity analysis of microwave sea surface temperature images. *Remote Sens. Environ.* 112, 2246–2260. doi: 10.1016/j.rse.2007.10.007

Vazquez-Cuervo, J., Dewitte, B., Chin, T. M., Armstrong, E. M., Purca, S., and Alburqueque, E. (2013). An analysis of sst gradients off the peruvian coast: The impact of going to higher resolution. *Remote Sens. Environ.* 131, 76–84. doi: 10.1016/j.rse.2012.12.010

Vinayachandran, P. N. M., Masumoto, Y., Roberts, M. J., Huggett, J. A., Halo, I., Chatterjee, A., et al. (2021). Reviews and syntheses: Physical and biogeochemical processes associated with upwelling in the indian ocean. *Biogeosciences* 18, 5967–6029. doi: 10.5194/bg-18-5967-2021

Wang, D., Liu, Y., Qi, Y., and Shi, P. (2001). Seasonal variability of thermal fronts in the northern south china sea from satellite data. *Geophys. Res. Lett.* 28, 3963–3966. doi: 10.1029/2001gl013306

Watson, J. R., Fuller, E. C., Castruccio, F. S., and Samhouri, J. F. (2018). Fishermen follow fine-scale physical ocean features for finance. *Front. Mar. Sci.* 5. doi: 10.3389/fmars.2018.00046

Weatherall, P., Marks, K. M., Jakobsson, M., Schmitt, T., Tani, S., Arndt, J. E., et al. (2015). A new digital bathymetric model of the world's oceans: New digital bathymetric model. *Earth Space. Sci. (Hoboken N.J.)* 2, 331–345. doi: 10.1002/2015ea000107

Yu, X., Naveira Gabarato, A. C., Martin, A. P., Buckingham, C. E., Brannigan, L., and Su, Z. (2019). An annual cycle of submesoscale vertical flow and restratification in the upper ocean. *J. Phys. Oceanogr.* 49 (6), 1439–1461. doi: 10.1175/jpo-d-18-0253.1

Zhang, Z., and Qiu, B. (2020). Surface chlorophyll enhancement in mesoscale eddies by submesoscale spiral bands. *Geophys. Res. Lett.* 47, e2020GL088820. doi: 10.1029/2020gl088820

Zweng, M. M., Reagan, J. R., Seidov, D., Boyer, T. P., Locarnini, R. A., Garcia, H. E., et al. (2018). *World Ocean Atlas 2018*, Volume 2: Salinity. A. Mishonov Technical Ed.; NOAA Atlas NESDIS 82, 50pp. (World Ocean Atlas)

3.4. Supplementary Material

frontiers

Supplementary Material

1 SUPPLEMENTARY FIGURES

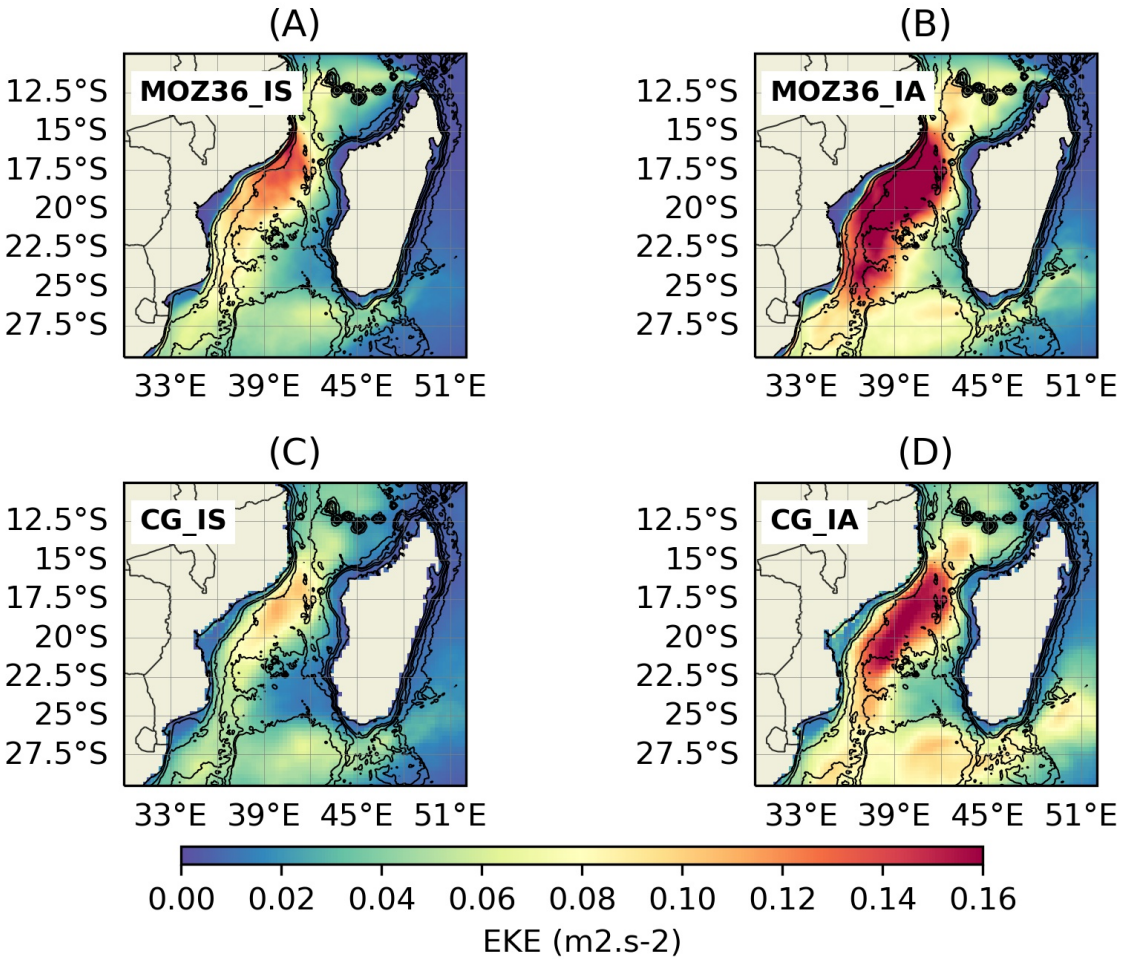

Figure S1. Intra-seasonal (A, C) and inter-annual (B, D) EKE from COPERNICUS GLOBCURRENT (A, B) and MOZ36 (C, D)

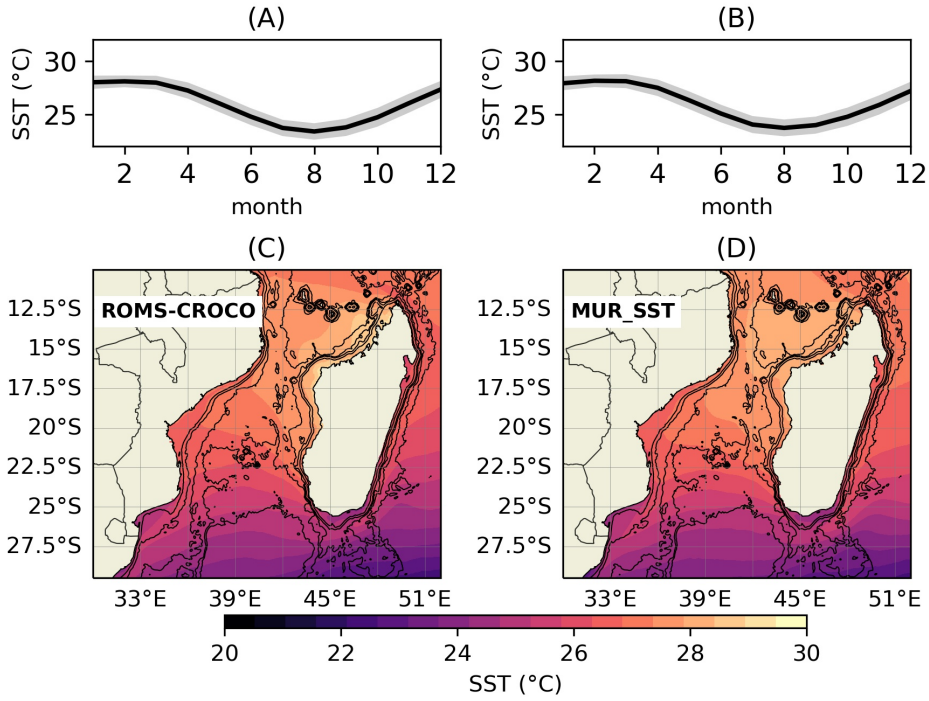

Figure S2. Climatological and mean SST for the CROCO model (left panels) and the observations (right panels): (A, B) climatology of the spatial mean, (C, D) temporal mean. The shading in grey in (A,B) represents the standard deviation of the climatological value amongst each grid cells of the domain.

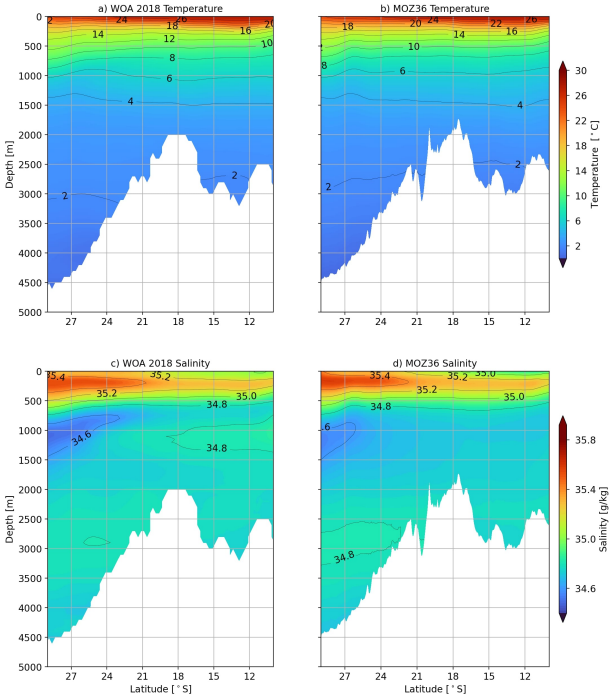

Figure S3. Comparison between MOZ36 (b, d) and World Ocean Atlas 2018 (a, c) annual mean temperature (a, b) and salinity (c, d) on a meridional section at 42.125°E.

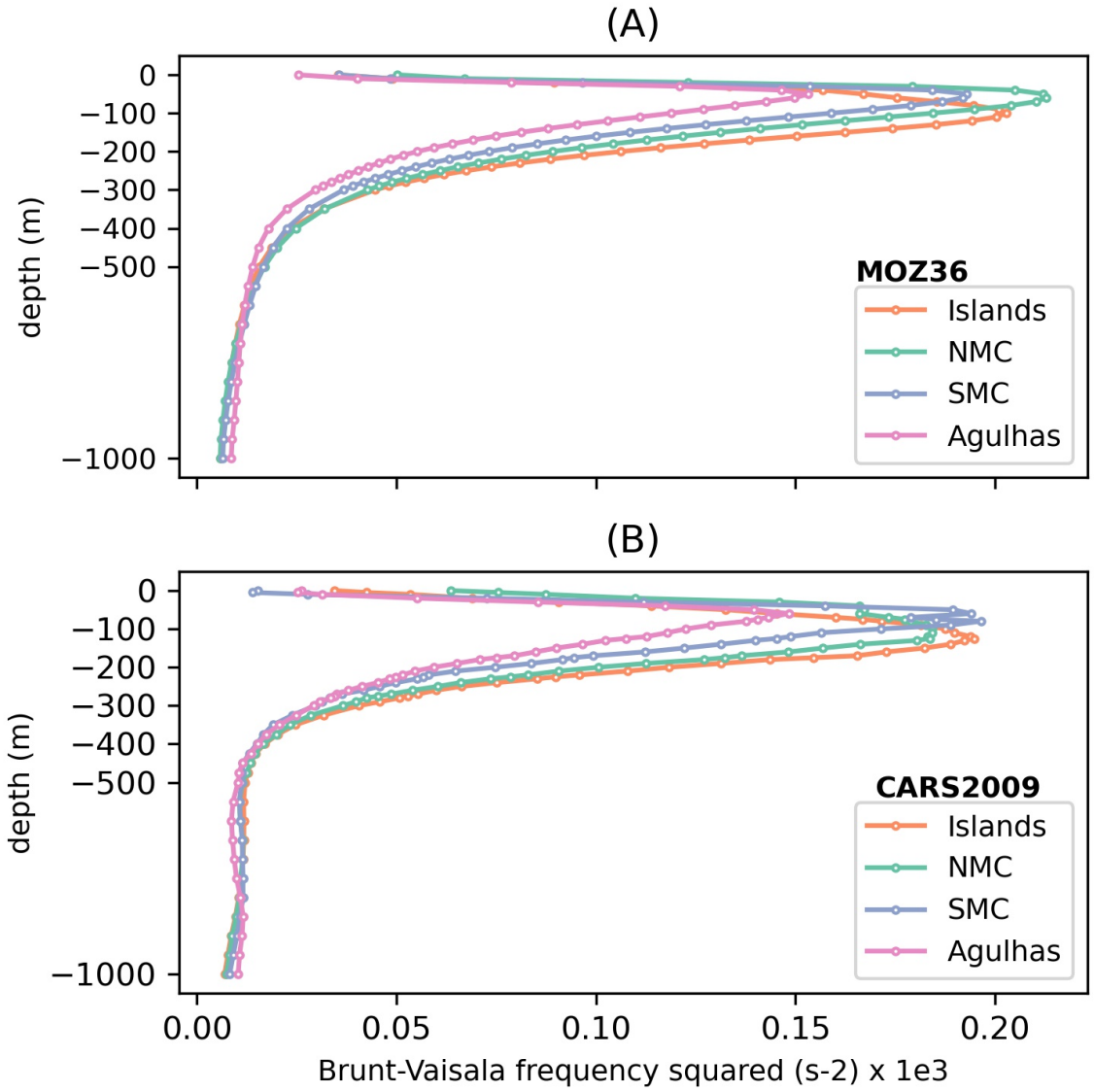

Figure S4. Mean vertical profiles of the Brunt-Vaisälä frequency derived from MOZ36 (A) and CARS2009 (B) for the 4 subregions.

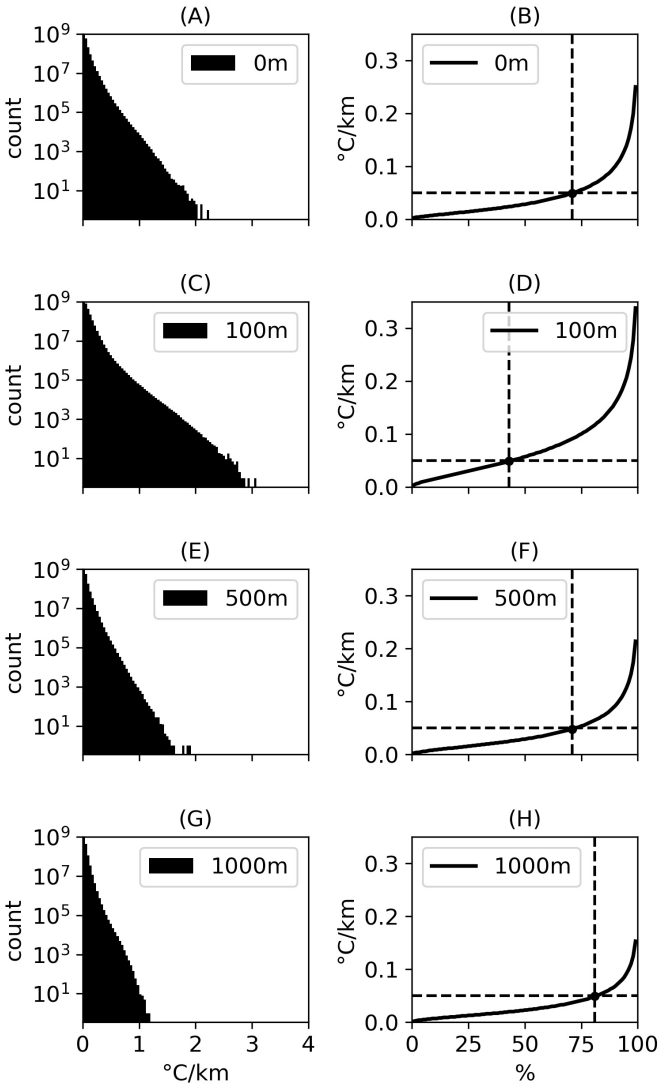

Figure S5. MOZ36 temperature front intensity distribution histograms (A, C, E, G) and percentiles (B, D, F, H) at surface (A, B), -100m (C, D), -500m (E, F) and -1000m (G, H).

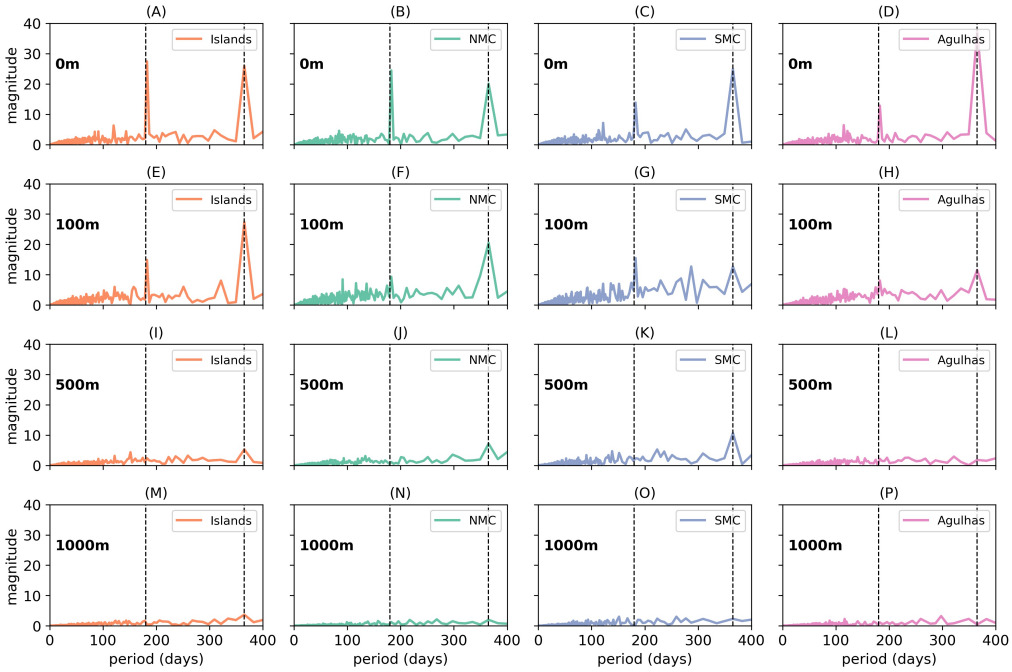

Figure S6. Fast Fourrier Transform analysis periodograms for the subregions: Islands (A, E, I, M), NMC (B, F, J, N), SMC (C, G, K, O), Agulhas (D, H, L, P) and at 4 depths: surface (A, B, C, D), 100m (E, F, G, H), -500m (I, J, K, L) and -1000m (M, N, O, P). The vertical dashed lines represent periods of 6 and 12 months.

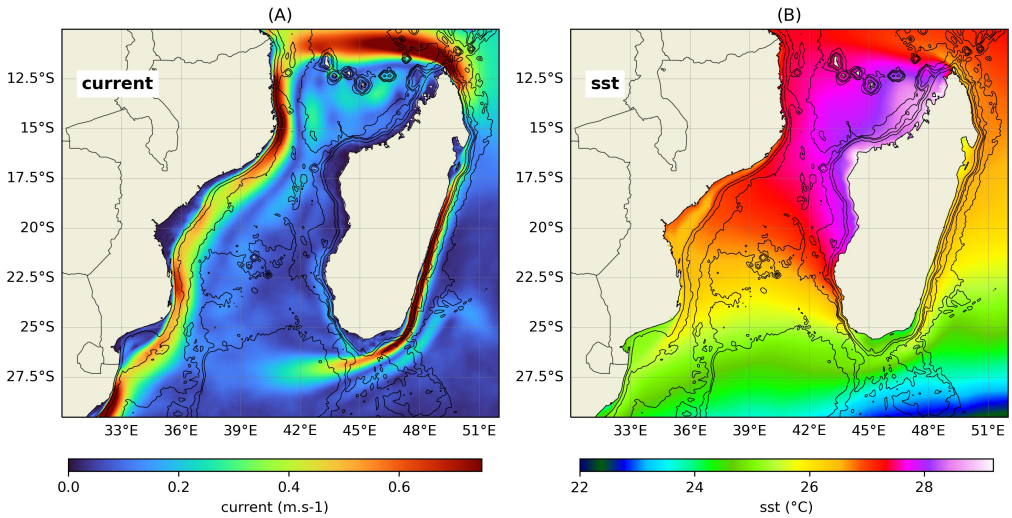

Figure S7. A) surface current modulus (sqrt(u2+v2)) averaged over 1993-2014 and B) corresponding mean SST map derived from MOZ36. Black contours represent the -200, -1000, -2000, -3000 and -4000m isobaths.

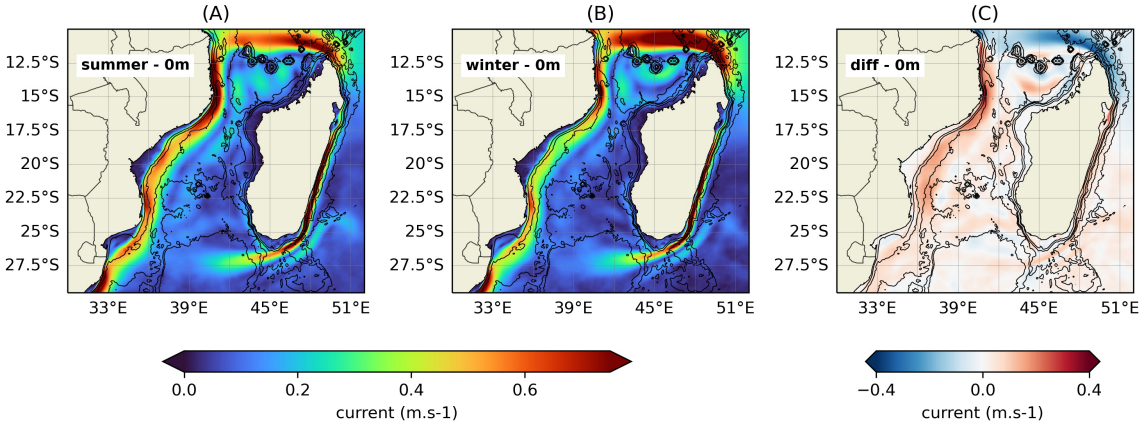

Figure S8. A) and B) represent the seasonal means and C) the seasonal difference between summer (Oct-Mar) and winter (Apr-Sep) for MOZ36 surface current modulus (sqrt(u2+v2))

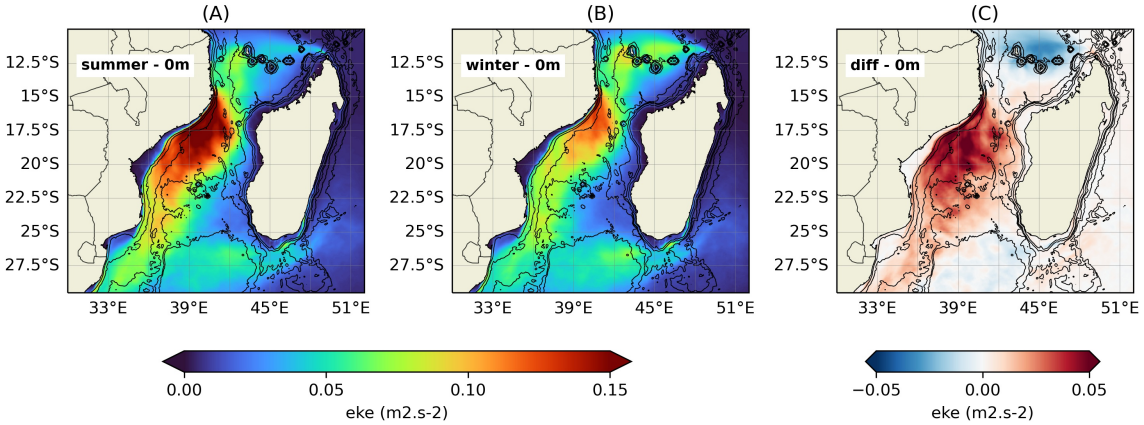

Figure S9. A) and B) represent the seasonal means and C) the seasonal difference between summer (Oct-Mar) and winter (Apr-Sep) for MOZ36 surface intra-seasonal EKE

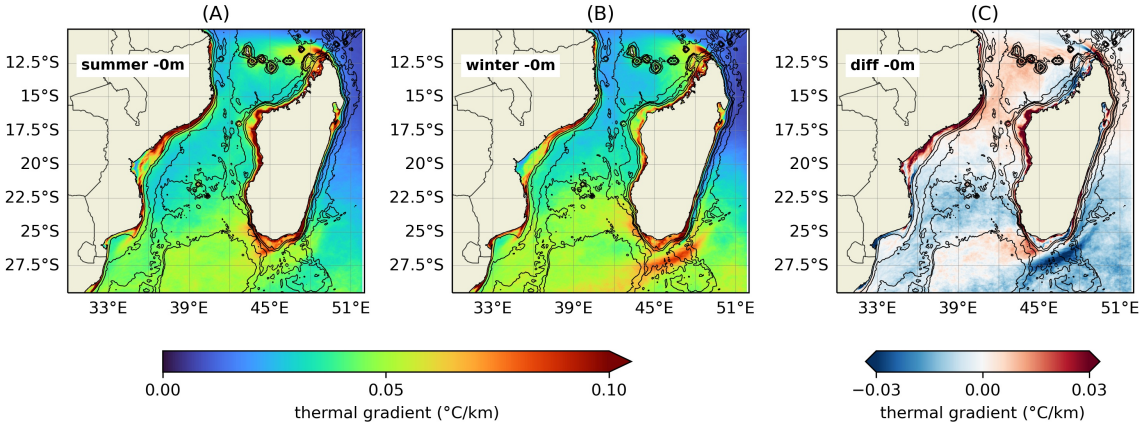

Figure S10. A) and B) represent the seasonal means and C) the seasonal difference between summer (Oct-Mar) and winter (Apr-Sep) for MOZ36 surface thermal front intensity

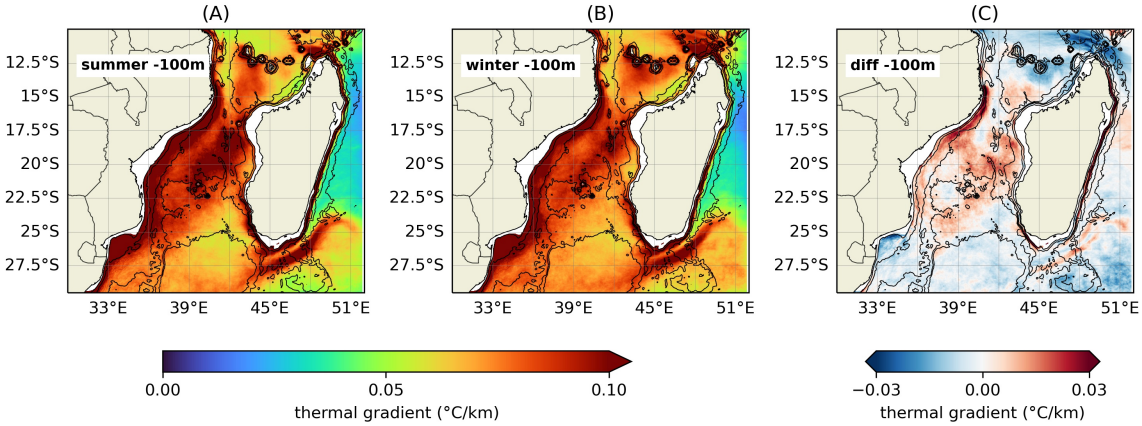

Figure S11. A) and B) represent the seasonal means and C) the seasonal difference between summer (Oct-Mar) and winter (Apr-Sep) for MOZ36 thermal front intensity at -100 m

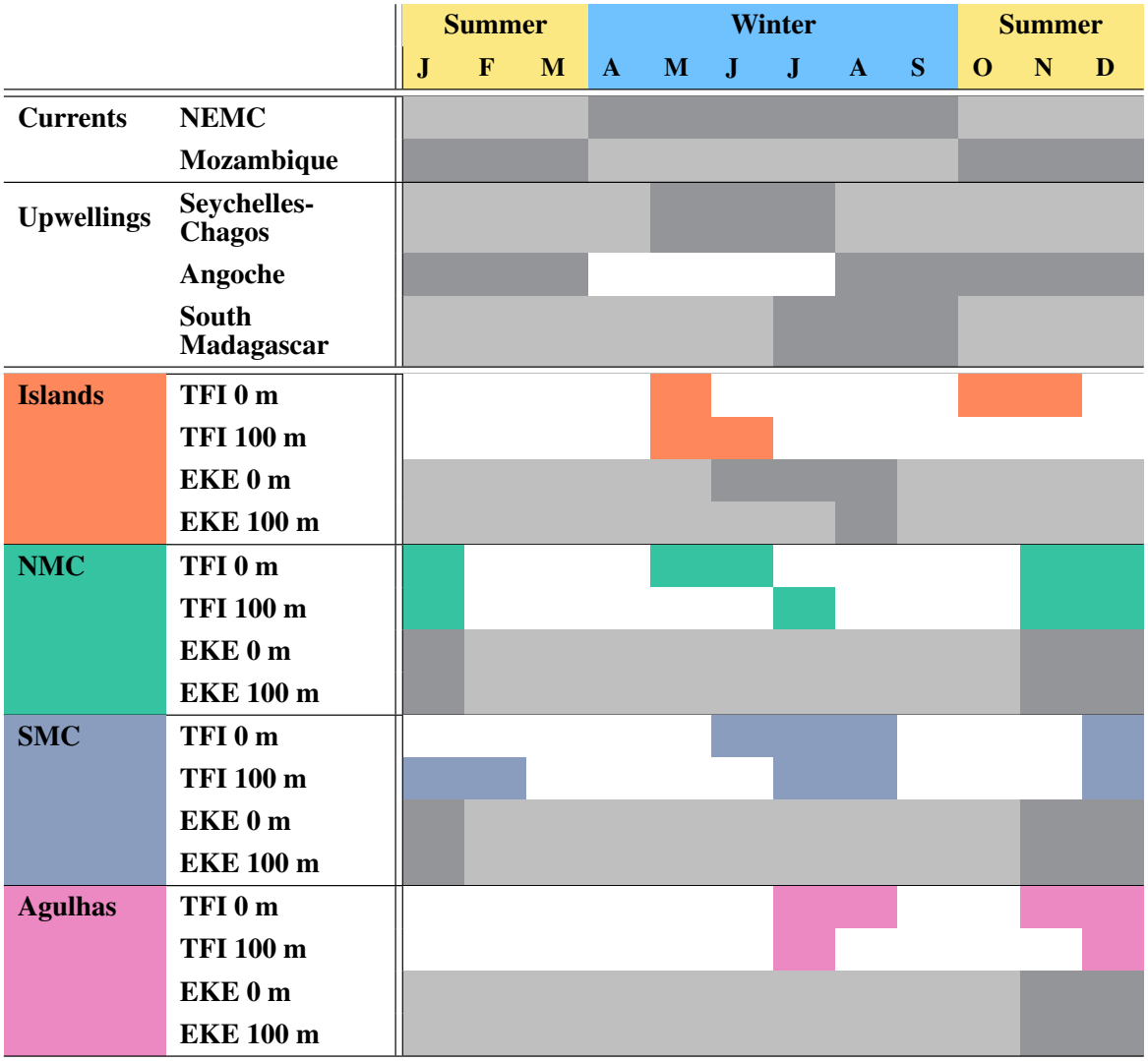

Table S1. Seasonal peaks of thermal front intensity (TFI) and main drivers (currents, upwellings, EKE) at surface and 100 m. For drivers, dark (resp. light) grey cells correspond to higher (resp. lower) influence, while white cells refer to non-existent drivers. For thermal front intensity, shaded values correspond to seasonal peak values, while white cells correspond to lower values.

KEY POINTS

- Persistent fronts in the MC are located along the Mozambique and Madagascar shelf-breaks and along the NEMC and SEMC.
- Ephemeral fronts form at the edge of eddies propagating southwest within the Channel (between 16°S and 25°S) and along meanders associated with the NEMC and SEMC.
- Vertically, TG are found to be significant in the whole mesopelagic realm, and peak at around -100 m depth, where stratification is also maximum.
- We have identified four subregions characterized by distinct EKE and thermal front seasonal regimes.
- Seasonal variations of the EKE field do not suffice to explain the seasonal variability of thermal fronts in the Channel. We argue that regional upwelling cells also affect the variability of thermal fronts in the MC.

4. Projected changes in thermal front variability in the Mozambique Channel

Content

4.1. Summary . . . 95
4.2. Résumé en français . . . 98
4.3. Introduction . . . 100
4.4. Method . . . 101
4.4.1. Regional simulations . . . 101
4.4.2. Numerical methods . . . 103
4.4.3. MOZ36_CR validation . . . 104
4.5. Results . . . 105
4.5.1. Changes in EKE . . . 105
4.5.2. Changes in mean thermal gradients . . . 106
4.5.3. Changes in thermal front frequency . . . 108
4.6. Discussion . . . 109
4.6.1. Changes in mean currents . . . 109
4.6.2. Changes in mean EKE . . . 110
4.6.3. Changes in thermal fronts . . . 111
4.7. Conclusion . . . 112
4.8. APPENDIX: Contrasting mean temperature and circulation between baseline and pseudo global warming experiments . . . 115

4.1. Summary

In Chapter 3, we propose the first descriptive analysis of fine-scale thermal fronts in the MC for the last decades. We suggest that the thermal front variability in the MC is modulated by both the mesoscale eddy activity and regional upwelling cells. However, observational trends show that the mesoscale eddy activity in the Channel is evolving in response to changes in the climate system (Backeberg et al., 2012; Martínez-Moreno et al., 2021). We thus hypothesize that by altering the eddy regime in the Channel, global warming would also impact the variability of ocean fronts.

Because ephemeral fronts and filaments in the MC have a spatial scale smaller than hundreds of kilometers, they require a finer spatial resolution than what is

currently available in contemporary Global Climate Models (GCM) projections due to computational and storage costs. We also know that GCM projections are sensitive to spatial resolution and possess regional biases (Saba et al., 2016; Drenkard et al., 2021). To map ocean front changes in the MC, we thus require a high-resolution regional model incorporating global warming conditions. Downscaling methods bridge the gap between high-resolution – but regional – simulations and global – but coarse – projections. Downscaling procedures allow us to resolve smaller-scale features, like ephemeral ocean fronts, from larger-scale GCM information via statistical or dynamical tools.

In Chapter 4, we use a dynamical downscaling procedure centered on the MC to infer changes in ocean fronts due to global warming. We compare a hindcast (1993-2014) and a pseudo global warming experiment and detail the changes in mesoscale eddy activity and thermal fronts. The regional pseudo global warming experiment is built with the delta method (Sato et al., 2007), applied on a member of the CESM-LENS ensemble (Kay et al., 2015) for the RCP 8.5 ("business-as-usual") scenario at the end of the century (2071-2100). Mesoscale eddy activity is evaluated by computing intra-seasonal eddy kinetic energy (EKE). And we identify thermal fronts by thresholding a thermal gradient (TG) field, estimated with the BOA.

The pseudo global warming experiment reveals a remarkable increase of EKE in the Northern MC and southwest of Madagascar in the wake of the SEMC. The projected EKE is reduced in the southern part of the MC and southeast of Madagascar. The divide between positive and negative EKE anomalies within the MC is also found in observational trends (Backeberg et al., 2012; Martínez-Moreno et al., 2021) although its position varies slightly between studies. Vertically, the mean changes in EKE are confined to the top 400 m of the water column.

Similar to the changes observed in EKE, TG are anticipated to rise in the Comoros Basin and southwest of Madagascar, while decreasing within the southern MC and southeast of Madagascar. The close alignment between the changes in TG, in thermal front frequency and those in EKE implies that the ocean fronts most impacted by the climate warming perturbation are likely ephemeral fronts forming on the edge of eddies. Vertically, modelled thermal fronts appear shallower in the pseudo global warming experiment, and TG changes between the two experiments can reach as deep as 1000 m. While changes in the annual frequency of thermal fronts, averaged across the entire domain, do not exhibit a significant difference in median values between experiments, there seems to be an increase in interannual variability in the pseudo-global warming experiment.

The results of Chapter 4 reveal significant changes in ocean front distribution for an end-of-century "business-as-usual" scenario. Those changes are most pronounced in the Comoros Basin, along the Mozambican shelf and South of Madagascar, and concern mostly ephemeral fronts forming on the edge of eddies. Previous studies have reported that seabirds populations in the MC forage preferentially at ephemeral fronts (e.g. Tew Kai et al., 2009) and that the MC and South of Madagascar are key habitats for megafauna (Tew Kai & Marsac, 2010; Rohner et al., 2013; Laran et al., 2017; Diamant et al., 2018; Rohner et al., 2018), including seabirds (Weimerskirch et al., 2004;

Le Corre et al., 2012). Hence, the present study calls for further research to identify how those ocean front changes will impact regional ecosystems. Looking at lower trophic levels, the use of a biogeochemical model coupled to our pseudo global warming experiment would provide insights on projected primary productivity changes. At higher trophic levels, marine megafauna and top-predators act as sentinels informing on ecosystem response to ocean changes (Hazen et al., 2019). Combined to this work, a multi-species, long-term statistical survey on how marine megafauna exploit ocean fronts would also shed light on future ecosystem trends in the region.

4.2. Résumé en français

Dans le Chapitre 3, nous présentons la première analyse descriptive des fronts thermiques à fine échelle dans le Canal du Mozambique (MC) au cours des dernières décennies. Nous suggérons que la variabilité des fronts thermiques dans le Canal est modulée à la fois par l'activité tourbillonaire méso-échelle et par des cellules d'upwelling régionales. Cependant, des observations de courantologie à large échelle spatiale indiquent que l'activité tourbillonaire dans le canal est en train d'évoluer en réponse au changements climatiques (Backeberg et al., 2012; Martínez-Moreno et al., 2021). Nous émettons donc l'hypothèse qu'en altérant le régime des tourbillons dans le Canal, le réchauffement climatique global aurait également un impact sur la variabilité des fronts océaniques.

Étant donné que les fronts éphémères dans le Canal ont une échelle spatiale plus petite que des centaines de kilomètres, ils nécessitent une résolution spatiale plus fine que celle qui est actuellement utilisée par les projections futures des modèles climatiques globaux (GCM). Ceci est dû aux coûts informatiques et de stockage liés aux GCM. Nous savons également que les projections des GCM sont sensibles à la résolution spatiale utilisée et introduisent des biais régionaux (Saba et al., 2016; Drenkard et al., 2021). Pour cartographier les changements des fronts océaniques à fine échelle dans le Canal du Mozambique, nous avons donc besoin d'un modèle régional, à haute résolution, intégrant des conditions de réchauffement climatique. Les méthodes de downscaling comblent le fossé entre les simulations à haute résolution - mais régionales - et les projections mondiales - mais à resolution spatiale insuffisante. Les procédures de downscaling nous permettent de modéliser des structures à fine échelle, comme les fronts océaniques éphémères, à partir d'informations à plus grande échelle à partir des GCM via des outils statistiques ou dynamiques.

Dans le Chapitre 4, nous utilisons une procédure de downscaling dynamique centrée sur le Canal du Mozambique pour déduire les changements des fronts océaniques dus au réchauffement climatique global. Nous comparons une simulation de référence (1993-2014) et une simulation de pseudo réchauffement climatique, détaillant les changements de l'activité tourbillonaire et des fronts thermiques. La simulation régionale de pseudo réchauffement climatique est construite avec la méthode des deltas (Sato et al., 2007), appliquée à un membre de l'ensemble CESM-LENS (Kay et al., 2015) avec un scénario RCP8.5 "business-as-usual" pour la fin du 21e siècle (2071-2100). L'activité tourbillonaire est évaluée en calculant l'énergie cinétique des tourbillons intra-saisonnière (EKE). Et nous identifions les fronts thermiques en appliquant un seuil aux champs de gradients thermiques (TG) estimés avec le BOA.

La simulation de pseudo réchauffement climatique révèle une augmentation remarquable de l'EKE dans le nord du Canal et au sud-ouest de Madagascar. L'EKE est réduite dans la partie sud du Canal et sud-est Madagascar (Siedler et al., 2009). La ligne de démarcation entre les anomalies positives (au nord) et négatives (au sud) de l'EKE dans le Canal se retrouve également dans la tendance des données de courantologie satellitaires (Backeberg et al., 2012; Martínez-Moreno et al., 2021), bien que sa position varie légèrement entre les études. Verticalement, les changements de l'EKE

sont confinés aux 400 premiers mètres de la colonne d'eau.

De manière similaire aux changements observés pour l'EKE, on prévoit une hausse des TG dans le bassin des Comores et sud-ouest de Madagascar, tout en diminuant dans le sud du Canal et sud-est de Madagascar. La concordance étroite entre les changements de fronts thermiques et ceux de l'EKE implique que les fronts océaniques les plus impactés par la perturbation de réchauffement climatique sont les fronts éphémères se formant à la lisière des tourbillons. Verticalement, les fronts thermiques modélisés apparaissent moins profonds dans la simulation de pseudo réchauffement climatique. Et les variations entre les valeurs de TG entre les deux simulations peuvent atteindre une profondeur pouvant aller jusqu'à 1000 mètres. Enfin, bien que les changements dans la fréquence annuelle des fronts thermiques, moyennés sur l'ensemble du domaine, ne montrent pas de différence significative dans les valeurs médianes entre les deux simulations régionales, il semble y avoir une augmentation de la variabilité interannuelle dans la simulation de pseudo réchauffement climatique.

Les résultats du Chapitre 4 révèlent des changements significatifs dans la distribution des fronts océaniques pour un scénario "business-as-usual" correspondant à la fin du 21e siècle. Ces changements sont particulièrement prononcés dans le bassin des Comores, le long du plateau continental du Mozambique et au sud de Madagascar, et concernent principalement les fronts éphémères se formant à la lisière des tourbillons. Des études antérieures ont montré que les populations d'oiseaux de mer du Canal se nourrissent préférentiellement le long des fronts éphémères (Tew Kai et al., 2009) et que le Canal du Mozambique et le sud de Madagascar sont des habitats clés pour la mégafaune (Tew Kai & Marsac, 2010; Rohner et al., 2013; Laran et al., 2017; Diamant et al., 2018; Rohner et al., 2018) dont les oiseaux de mer (Weimerskirch et al., 2004; Le Corre et al., 2012). Cette étude souligne la nécessité d'approfondir nos connaissances sur la manière et les modalités dont les fronts océaniques influencent les écosystèmes régionaux. Au niveaux trophiques inférieurs, l'utilisation d'un modèle biogéochimique couplé à notre simulation de pseudo réchauffement climatique pourrait fournir des informations sur les changements futurs de productivité primaire. Aux niveaux trophiques supérieurs, les prédateurs marins et la mégafaune agissent comme des sentinelles, informant sur la réponse de l'écosystème aux changements océaniques (Hazen et al., 2019). Combiner les résultats de ce Chapitre avec une enquête statistique à long terme et multi-espèces sur la manière dont les prédateurs marins exploitent les fronts à fine échelle éclairerait sur les changements futurs des écosystèmes regionaux.

4.3. Introduction

The Mozambique Channel (MC) is of particular interest to the scientific community because of its turbulent flow dominated by southward eddy trains along the Mozambican shelf (Lutjeharms et al., 2012; Backeberg & Reason, 2010; Halo et al., 2014; Ternon et al., 2014b), its ocean fronts (Sudre et al., 2023a, 2023b) and its role in the Greater Agulhas System (Penven et al., 2006). The Channel is also characterised by a rich biodiversity (Sabarros et al., 2009; Béhagle et al., 2014; Ternon et al., 2014a; Laran et al., 2017; Diamant et al., 2018), intense fishing pressures (Chassot et al., 2019; Nataniel et al., 2022) and numerous conservation initiatives (Unep-Nairobi Convention, 2015; Obura et al., 2019). Looking into the next decades, the MC has been projected to be a warming hotspot from observations and large ensemble climate models (Roxy et al., 2014; Zhang et al., 2018; Tittensor et al., 2021). We also expect that increased temperatures in the channel lead to higher stratification and reduced vertical mixing (Capotondi et al., 2012; Li et al., 2020). Finally, the currents modulating the MC transport east and south of Madagascar Island (Fig. 1.8) have all been reported to slow down in future scenarios from Coupled Model Intercomparison Project (CMIP). (Sen Gupta et al., 2021), potentially contributing to reduced heat transport (Mecking & Drijfhout, 2023) as well as changes in mesoscale eddy activity regimes (Martínez-Moreno et al., 2021, 2022).

Recent studies indicated that mesoscale activity is a key component of the ocean energy budget, which currently limits the interpretation of climate projections by models that do not resolve horizontal scales of O(1–10) km nor time scales of O(1) day, as this is the case for the current-generation CMIP-class models. Recent efforts have been dedicated to increasing the resolution in global climate systems to address this issue with a focus on reducing mean state biases (Delworth et al., 2012) and investigating many aspects of the sensitivity of the climate dynamics to mean state change in these eddy-populated systems (Wengel et al., 2021; Wang et al., 2022; Chang et al., 2023). However, even in eddy-rich simulations, the resolution may remain too large to resolve scales of the order to the local Rossby radius, like in the mid-to-high latitudes (Moreton et al., 2020). Regional modeling remains a powerful tool for producing climate change projections at resolutions not yet accessible by global systems (Howard et al., 2020), especially given that the response to climate change perturbations can be highly sensitive to model spatial resolution (Saba et al., 2016; Drenkard et al., 2021; Chang et al., 2023). This approach also makes it possible to avoid systematic biases in the mean state of global models.

Furthermore, there is numerous evidence demonstrating how sub-to-mesoscale fronts and filaments structure entire ephemeral ecosystems (Bakun, 2006; Lévy et al., 2012; Scales et al., 2014b, 2018; Chapman et al., 2020; Mangolte et al., 2023) and especially in the MC: from primary productivity (Tew-Kai & Marsac, 2009; José et al., 2014), to micronekton (Potier et al., 2014; Annasawmy et al., 2018) and up the food chain to top predators (Tew Kai et al., 2009; Tew Kai & Marsac, 2010; Weimerskirch et al., 2010). Yet, despite the aforementioned ecological pressures and scientific interests, there has been no study to date evaluating the impact of global warming on ocean

fronts and filaments.

Our motivation is thus to document changes in mesoscale circulation in the MC associated with warming conditions representative of the future climate. We rely here on a dynamical downscaling experiment using a high-resolution regional model to investigate how thermal front and EKE variability responds to projected warming in the MC. Our model experiment is designed to simulate mean oceanic circulation corresponding to a stabilised warm state corresponding to conditions of the late 21st century (2071-2100), and as such does not address the transient climate response. While our approach follows previous studies that tackled ecological impacts (e.g. Sun et al., 2012; Alexander et al., 2020; Pozo Buil et al., 2021; Drenkard et al., 2021), we focus here on changes in the oceanic circulation relevant for understanding ecological metrics, that is, changes in mesoscale activity and thermal fronts.

Following this introduction, Section 4.4 details the regional experiments and numerical diagnostics that were used in this chapter and a short assessment of the baseline experiment. In Section 4.5 we describe the changes in mesoscale eddy activity and thermal fronts in the pseudo global warming experiment relative to the baseline. We then discuss those changes in Section 4.6. Section 4.7 provides concluding remarks with implications of our results.

4.4. Method

4.4.1. Regional simulations

In this work, we use the Coastal and Regional Ocean COmmunity model (CROCO, Auclair et al., 2022; Marchesiello et al., 2001) built upon the Regional Ocean Modeling System (ROMS) (Shchepetkin & McWilliams, 2005). The model configuration consists in two embedded domains in a one-way nesting setup: a parent domain at a 1/12° horizontal resolution consisting in a rectangular basin over the region (27.1°E–54.2°E, 7.5°S–33.1°S), and an inner child domain at higher-resolution (1/36°) over the region (30.6°E–51.9°E, 9.8°S-29.7°S) (Fig. 4.1). The model used 60 sigma layers in the vertical for both configurations and the vertical grid is stretched for increased resolution at the surface boundary layer.

The bathymetry is from GEBCO 2014 (Weatherall et al., 2015) for consistency with the background lateral boundary conditions that are derived from the outputs of a ROMS simulation at 1/4° (see Table 2.1). For consistency, atmospheric forcings are also derived from ERA interim (Dee et al., 2011). Daily-mean outputs consist in 3-D mean temperature, salinity, sea level, and current fields. A mixed radiation-nudging scheme (Marchesiello et al., 2001) is used for avoiding numerical inconsistencies at the open boundaries. Unresolved scales are parametrized with a K-Profile vertical mixing scheme (Large et al., 1994) at the surface and bottom, including shear instability interior mixing, convection interior mixing, and a Smagorinsky scheme for turbulent viscosity.

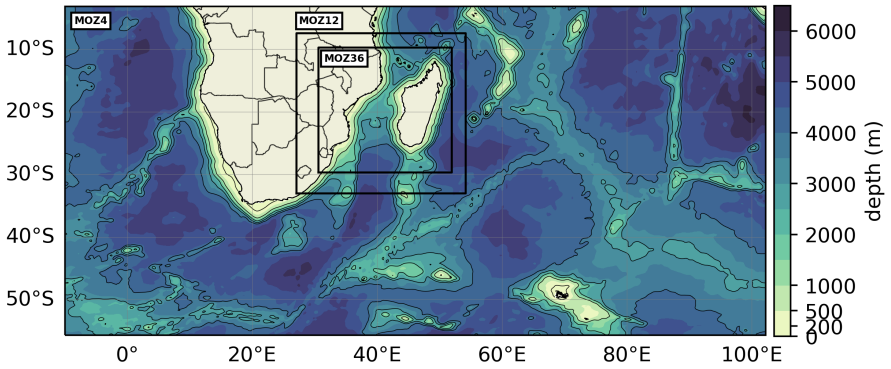

Figure 4.1.: Bathymetry from the ROMS 1/4° simulation detailed in (Sudre et al., 2023a) and MOZ12, MOZ36 subdomains. The background black contours represent isobaths at -200, -500, -1000, -2000, -3000 and -4000 m. The colormap is from cmocean (Thyng et al., 2016).

The control experiments – MOZ12_CR and MOZ36_CR

Baseline simulations consist in running the model using unaltered boundary forcings from the hindcast experiment at 1/4° detailed by Miramontes et al. (2019) and Sudre et al. (2023a) over the period 1993-2014. Atmospheric forcings are based on bulk formulations (Fairall et al., 1996) applied to ERA-Interim Reanalysis daily mean temperature, relative humidity, surface wind speed, radiative fluxes and precipitation. The child control run open boundaries are forced by the parent control run. The resulting child simulation, thereafter referred to as MOZ36_CR, covers the period 1993-2014 (for a total of 22 years) on a 1/36° grid. A 3-year spin-up is considered for both simulations.

The pseudo global warming experiments – MOZ12_F and MOZ36_F

The second set of simulations is a so-called pseudo global warming experiment. In this experiment, we introduce a climate warming perturbation to both atmospheric and boundary forcings of the hindcast control run with the "delta method" (Schär et al., 1996; Sato et al., 2007). The delta method consists in adding to the boundary conditions the difference between the future and present climates for each prognostic variable. The deltas are computed from the first member of the Community Earth System Model Large Ensemble (CESM-LENS) choosing the Representative Concentration Pathway (RCP)8.5 (high emission scenario for "business as usual", (Kay et al., 2015)) scenario for the period 2071-2100 and compared to the historical period 1993-2014. More specifically, for a forcing variable $F(x,y,z)$, the delta is given by:

$$\Delta F_{\text{month}}(x,y,z) = \overline{F_{\text{month}}(x,y,z)}|_{\text{2071-2100}} - \overline{F_{\text{month}}(x,y,z)}|_{\text{1993-2014}} \tag{4.1}$$

where the overlines indicate seasonal averages for the future (2071-2100) and historical (1993-2014) periods. We chose to compute the deltas from one CESM-LENS member only instead of taking the ensemble (as in Pozo Buil et al., 2021) to avoid a potential loss of variability as suggested by Trapp et al. (2021). Note that this particular member sits within the upper bound of the ensemble in terms of the trend in mean SST over the MC, which is akin to the CMIP ensemble mean. The resulting forcing variable follows:

$$F(x,y,z,t)|_{\text{pseudo global warming}} = F(x,y,z,t)|_{\text{historical}} + \Delta F_{\text{month}}(x,y,z) \tag{4.2}$$

This procedure is applied for running the simulation for the parent domain (MOZ12_-F) and thereafter the outputs are used to run the simulation for the child domain, thereafter referred to as MOZ36_F. Both simulations cover 22 years with a 3-years spin-up.

The configuration of each experiment is summarised in Table 2.1. Hereafter we will focus on the analysis of the simulations of the child domain, unless stated otherwise.

4.4.2. Numerical methods

We estimate daily intra-seasonal eddy kinetic energy (EKE) following the method described in Dewitte et al. (2021) with:

$$EKE = \frac{1}{2}(u'^2 + v'^2) \tag{4.3}$$

Where the daily turbulent eastward and northward velocities u' and v' (respectively) are defined as deviations from the 3-month running mean of total currents. We then take a 3-month running mean of the resulting daily EKE and resample it with a weighted monthly average.

Horizontal thermal gradients (TG) are computed with the Belkin and O'Reilly algorithm (Belkin & O'Reilly, 2009) which associates a contextual median filter to a Sobel operator (as in Gao et al., 2010) to estimate spatial gradients of the temperature field. Thermal fronts are obtained by applying a statistical threshold to those thermal gradients. Following the method in Sudre et al. (2023a, 2023b), only the top 30% of the thermal gradient distribution qualifies as thermal front. The thermal front frequency corresponds to the percentage of days in which a pixel is in a front state. Yearly thermal front frequencies averaged over the entire domain are also computed to evaluate interannual differences in front occurrences.

Both TG and EKE are then computed on 45 horizontal slices for all child simulations, ranging from the surface to -1000 m depth. From the surface to -300 m slices were taken every 10 m. Below -300 m, slices were taken every 50 m.

4.4.3. MOZ36_CR validation

In this subsection we validate some aspects of MOZ36_CR considering that this simulation has slight differences with the one used in Sudre et al. (2023a), which includes the use of a different version of the model. The control run (hereafter MOZ36_CR) mean temperature and salinity profiles were found in good agreement with those of the World Ocean Atlas 2018 (WOA2018) annual mean temperature (Locarnini et al., 2018) and salinity (Zweng et al., 2018) in the top 1000 m (Fig. 4.2), despite a slight warm bias in the subsurface.

Similarly, MOZ36_CR sea surface temperature and GHRSST Level 4 Multi-scale Ultra-high Resolution 1/10° Global Foundation Sea Surface Temperature Analysis v4.1 (MUR SST) (Chin et al., 2017) show very similar spatial distributions, despite a slight warm bias south of the domain (Fig. 4.3).

Finally, we evaluated the EKE from MOZ36_CR and from the remotely-sensed Altimetric Geostrophic Current and Modeled Ekman Current Reprocessing product (COPERNICUS-GLOBCURRENT) (Rio et al., 2014) (Fig. 4.4). Both maps show enhanced EKE in the MC, especially along the Mozambique continental shelf, and on the wake the the SEMC. The higher EKE values in MOZ36_CR could be explained first by the higher spatial resolution of the model compared to the satellite product, and second by the fact that the satellite product only provides geostrophic velocities while the modelled EKE is derived from total velocities (thus including both geostrophic velocities and the Ekman component).

We conclude that MOZ36_CR accounts realistically enough for the mean circulation of the Mozambique Channel and can then be used confidently as a benchmark to evaluate the impact of global warming in the region, given the limitations associated to the "pseudo-global warming" methodology (Dixon et al., 2016; Trapp et al., 2021).

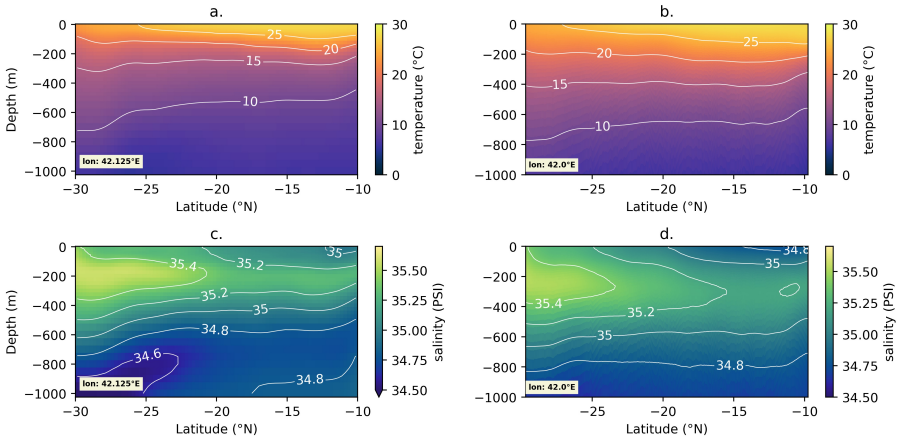

Figure 4.2.: Mean temperature (a., b.) and salinity (c., d.) vertical sections at longitude 42.125°E from WOA2018 (a., c., Locarnini et al., 2018) and MOZ36_CR (b., d.). The colormaps are from cmocean (Thyng et al., 2016).

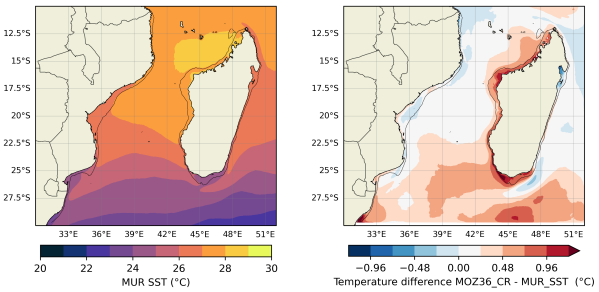

Figure 4.3.: Mean sea surface temperature from MUR SST (left, Chin et al., 2017) and differences with MOZ36_CR (right). The colormaps are from cmocean (Thyng et al., 2016).

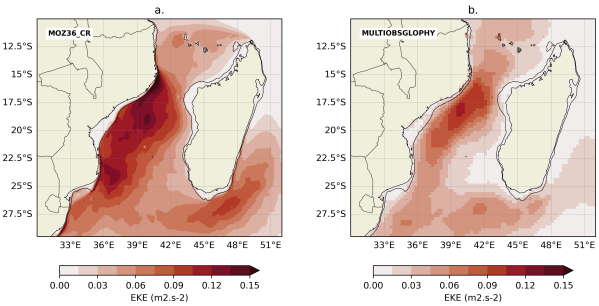

Figure 4.4.: Mean intra-seasonal EKE derived from MOZ36_CR currents (left) and from COPERNICUS-GLOBCURRENT total currents (right, Rio et al., 2014. The colormaps are from cmocean (Thyng et al., 2016).

4.5. Results

A description of mean changes in modelled temperature and circulation between baseline and pseudo global warming experiments is attached as supplementary material in Section 4.8. Those results are also contrasted to mean changes in the global CESM-LENS model.

4.5.1. Changes in EKE

The mean EKE in the MC has a characteristic pattern consisting in a peak amplitude along the Mozambican continental shelf and to the southeast of Madagascar (Fig. 4.4). In the pseudo global warming experiment, we find that it is projected to increase the most in the Comoros Basin while decreasing along the Mozambican shelf, where it is usually maximum 4.5, left). South of Madagascar, the projected changes in mean EKE (i.e. difference in mean state between MOZ36_F and MOZ36_CR) are collocated with the changes of the SEMC (Fig. 4.13): changes in mean EKE are positive southwest of the Madagascar shelf and negative southeast of the shelf, at the SEMC retroflection (Fig. 4.5, left).

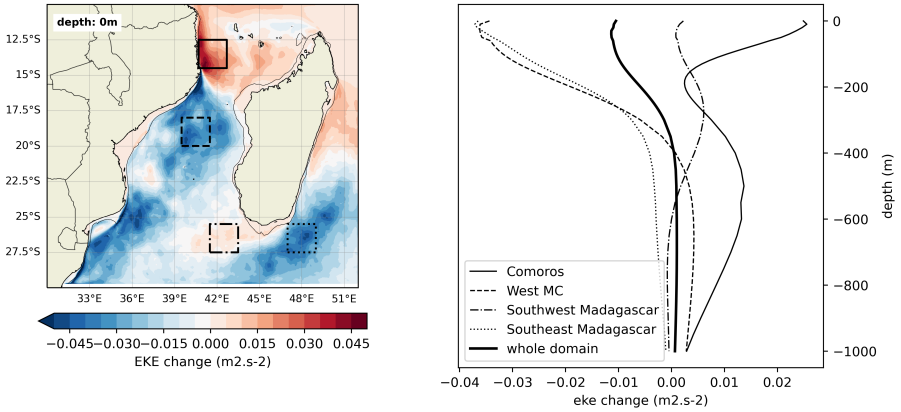

Figure 4.5.: Changes in EKE (MOZ36_F - MOZ36_CR, left) and vertical profiles of the same EKE changes for four regions of interest, whose areas are represented in the left panel. The colormap is from cmocean (Thyng et al., 2016).

On average over the whole MOZ36 domain, EKE changes (MOZ6_F minus MOZ36_-CR) are negative. However there are marked regional discrepancies, which we illustrate by considering mean EKE changes within 4 small regions (squares in Fig. 4.5, left). The right panel of Figure 4.5 displays the EKE changes in these regions as a function of depth, evidencing a rich baroclinic structure that is distinct between regions. In the Comoros Basin, positive EKE changes peak at surface, reach above 0.02 $m^2.s^{-2}$ and then taper down to approximately 200 m. A second local maxima is reached at about 500 m, peaking at 0.015 $m^2.s^{-2}$. Within the Channel, EKE changes are most intense in the surface mixed layer, at about -0.04 $m^2.s^{-2}$ and felt all the way to 400 m. The negative changes in mean EKE southeast of Madagascar are similar to those within the MC, with a surface maximum at around -0.04 $m^2.s^{-2}$. Southwest of Madagascar, the mean EKE changes are less intense, less than 0.01 $m^2.s^{-2}$, but with a deeper peak around 300 m.

Baseline EKE seasonal variations are most pronounced within the MC between 17°S and 25°S and for the top 400 m (Fig. 4.6, top row) (also see Sudre et al., 2023a in Chapter 3). Changes in EKE seasonal variations concern mainly the top 400 m of the water column (Fig. 4.6, bottom row). EKE changes are rather seasonally uniform at around 0.03 $m^2.s^{-2}$ in the Comoros Basin. Notably there are hardly any changes in the depth ranges between 100 m and 300 m. Within the MC, EKE changes are greater during austral summers, with negative anomalies reaching down to -0.05 $m^2.s^{-2}$. South of Madagascar, EKE changes are fairly homogeneous throughout the year. The negative changes southeast of Madagascar are contained in the top 200 m and reach down to -0.04 $m^2.s^{-2}$.

4.5.2. Changes in mean thermal gradients

Baseline mean TG are elevated along continental shelves, at the edge between eddies, and in the wake of strong geostrophic currents and their meanders (NEMC, SEMC)

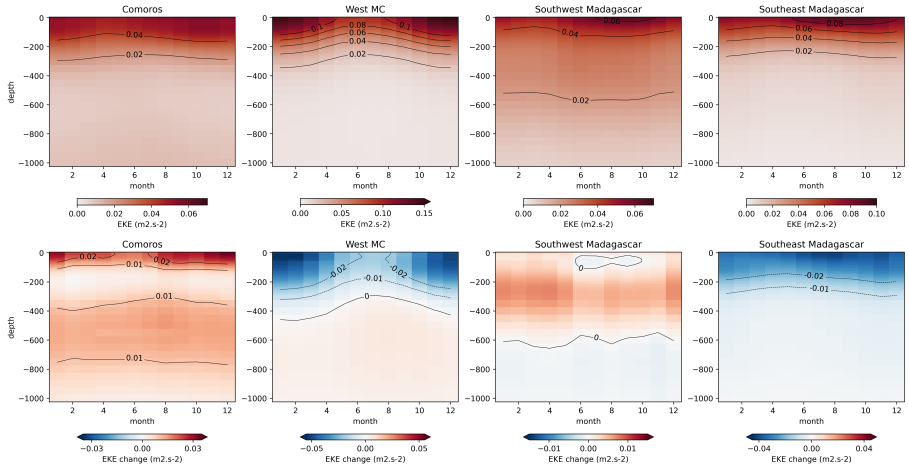

Figure 4.6.: Hövmoller diagrams representing baselines (MOZ36_CR, top) and changes in (MOZ36_F minus MOZ36_CR, bottom) seasonal EKE variations as a function of depth for four regions of interest (same regions as in Fig. 4.5). The colormaps are from cmocean (Thyng et al., 2016).

(Fig. 4.7). TG changes are positive in the Comoros Basin where the difference between pseudo global warming and baseline experiments exceeds 0.02°C/km at surface and even exceeds 0.05°C/km at -150 m (Fig. 4.7, left and center panels). TG are also much stronger in the pseudo global warming experiment east of Madagascar, along the path of the SEMC and at the cyclonic eddies wake documented in Siedler et al. (2009). Within the MC, changes in TG are negative, reaching up to 0.05°C/km at 150 m along the Mozambican shelf south of 16°S.

Mean TG changes between pseudo global warming and baseline experiments extend deep in the water column (Fig. 4.7, right panel), up to 1000 m deep in the southern MC. Mean changes are most dramatic in the Comoros Basin with a local maxima at approximately 100 m (approx. + 0.03°C/km mean change) and 500 m (approx. -0.015 °C/km mean change). Southwest of Madagascar, in the cyclonic SEMC wake, changes are neutral at surface but become more pronounced below 150 m to reach up to +0.01°C/km at 500 m. Within the Channel, south of 17°S, the negative changes in mean TG peak around 200 m at -0.02°C/km and hover at -0.01°C/km even at 1000 m.

Baseline climatologies show that TG are higher at the limit between surface mixed layer and the ocean interior and just below it (Fig. 4.8, top row). TG local maxima go deeper in the water column as the mixed layer thicken in austral winter (de Boyer Montégut et al., 2004). Changes in seasonal variation of TG are concentrated around the position of the mixed layer depth, while they're less intense (although not negligible) in the ocean interior (Fig. 4.8, bottom row). The pattern of positive change just above negative change at the approximate mixed layer depth indicates that thermal fronts are shallower in the pseudo global warming experiment.

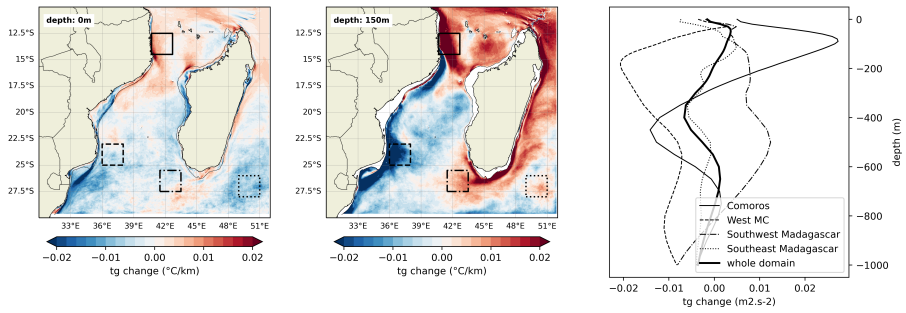

Figure 4.7.: Changes in TG (MOZ36_F minus MOZ36_CR) at surface (left panel) and subsurface (center panel) as well as vertical profiles of the same TG changes for four regions of interest, whose areas are represented in the left panel. The colormaps are from cmocean (Thyng et al., 2016).

4.5.3. Changes in thermal front frequency

Thermal fronts positions and occurrences are estimated by thresholding the thermal gradient field, and keeping only the top 30% thermal gradient values as thermal fronts, as in Sudre et al. (2023a, 2023b). Surprisingly, both baseline and pseudo global warming experiments yield the same 0.05°C/km threshold value at the surface, which is also the same as in Sudre et al. (2023a). The mean thermal front frequency maps shown in Fig. 4.9 (a., c.) closely resemble those of the mean TG in Fig. 4.7, except along the Mozambican shelf where the changes in front frequency are less marked than those in thermal gradients. This suggests that if thermal gradients are much weaker in the projection they still occur at a comparable frequency. Annual mean thermal front frequency distributions across the 22 modeling years display fairly similar medians in the 2 experiments: they both indicate a mean 30% yearly front occurrence at surface and 53% at -150 m (Fig. 4.9 b., d.). However the larger standard deviation of annual mean thermal front frequency in MOZ36_F seems to indicate greater interannual variability in the pseudo global warming experiment.

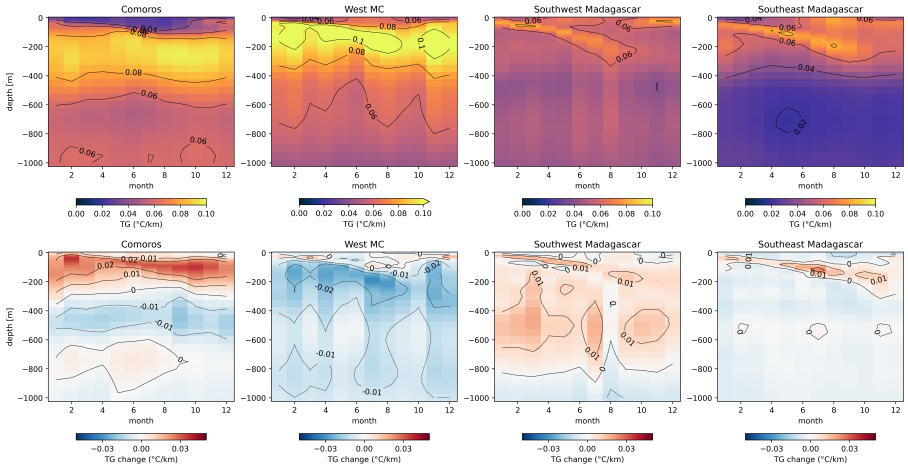

Figure 4.8.: Hövmoller diagrams representing baselines (MOZ36_CR, top) and changes in (MOZ36_F - MOZ36_CR, bottom) seasonal TG variations as a function of depth for four regions of interest (same regions as in Fig. 4.7). The colormaps are from cmocean (Thyng et al., 2016).

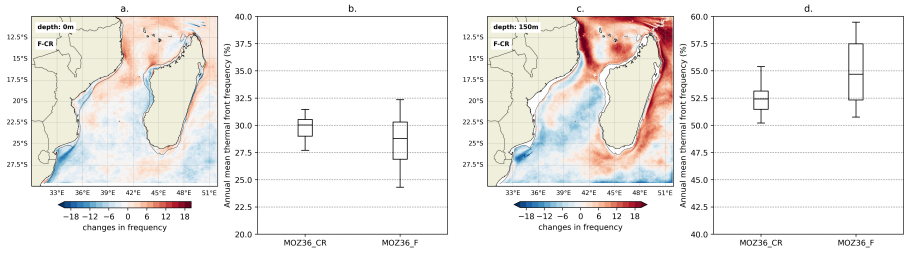

Figure 4.9.: Maps of mean thermal front frequency changes (MOZ36_F minus MOZ36_-CR) at surface (a.) and subsurface (c.) and annual thermal front frequency boxplots at surface (b.) and subsurface (d.) for both experiments. The colormap is from cmocean (Thyng et al., 2016).

4.6. Discussion

4.6.1. Changes in mean currents

The slow down of the SEC, NEMC, SEMC and SICC in the regional pseudo global warming experiment is consistent with the global CESM-LENS member projection (Fig. 4.13). Additionally, Stellema et al. (2019) and Sen Gupta et al. (2021) have also reported a seasonally consistent weakening of the SEC, NEMC and SEMC between mean historical (1900-2000) and "business-as-usual" (2050-2100) experiment in the CMIP latest two versions, which was linked to a weakening of the Indonesian throughflow (Hu et al., 2015; Sen Gupta et al., 2016).

Within the MC, the global CESM-LENS projection indicates a shallower MZC and a MZUC slightly further away from the Mozambican shelf than in the hindcast period (Fig. 4.13), which differs slightly from what is shown in the regional model. Mean cir-

culation inconsistencies between the regional and global models are not uncommon (Sun et al., 2012; Drenkard et al., 2021) and encourages further downscaling work in the region. Indeed, Stellema et al. (2019) also observed significant model variability in the direction of the flow along the Mozambican shelf. The variability of the Mozambique current/undercurrent in models thus adds to the argument made by Lutjeharms et al. (2012) about the overall discontinuity of the flow along the Mozambican shelf.

4.6.2. Changes in mean EKE

The elevated mean EKE along the Mozambican shelf (Fig. 4.4) has already been widely documented from satellite altimetry (Halo et al., 2014; Martínez-Moreno et al., 2021) as well as from realistic numerical models (Penven et al., 2006; Hermes et al., 2007; Sudre et al., 2023a). This study thus aims at showing the effect of a stabilised warm state corresponding to conditions of the late 21st century upon EKE and TG variability in the MC.

Mean EKE changes between baseline and pseudo global warming experiment (Fig. 4.5) show a distinct separation between the Comoros Basin and the innermost part of the MC, located around 16-17°S. A similar divide (between a negative EKE change in the north and a positive one in the south of the Channel) has been reported in Backeberg et al. (2012) and in Martínez-Moreno et al. (2021). However the boundary between the two opposite regions differs between studies. The observational trends documented in Backeberg et al. (2012) show an increase in EKE in the Comoros basin and as far as 20°S, while in Martínez-Moreno et al. (2021) the positive trend is narrower and extend southeast toward Madagascar shelf up to 21°S. In our study, we suggest that the projected increase in EKE in the Comoros Basin is due to the change in simulated circulation north of 16°S (Fig. 4.13) and an increased generation of anti-cyclonic eddies, as in Collins et al. (2014). Indeed, Collins et al. (2014) used both satellite altimetry and an eddy permitting model to show that the formation of anticyclonic eddies in the Comoros basin is due to barotropic instabilities linked to the NEMC. The broadening of the modelled southward branch of the NEMC in the pseudo global warming experiment and the related increased circulation north of 16°S could thus explain the observed intensification of eddy activity in the projected Comoros Basin. Subsequently, the reduced mean EKE within the MC (between 16 and 25°S) could be explained by a decreased in simulated surface circulation (Fig. 4.13). Southeast of Madagascar, the mean EKE anomalies are coherent with the changes in the SEMC, with an increase of mesoscale activity close to the Madagascar shelf and a negative anomaly out in the open ocean. The SEMC near-shelf southwestward plume has previously been associated with intense cyclonic (clockwise) eddy activity, while its open-ocean counterpart has been linked to anticylconic (counter-clockwise) eddy activity (Siedler et al., 2009). The distribution of mean EKE changes in the pseudo global warming experiment thus points towards a marked increase of cyclonic eddies propagating southwest towards the Agulhas Current and a decrease in anticyclonic eddies propagating northeast along with the retroflecting SICC. Observational trends from Backeberg et al. (2012) and Martínez-Moreno et al. (2021) show a uniformly

positive trend in the region southeast of Madagascar. We argue that it is likely that the spatial resolution of global observational datasets does not yet allow for a distinction between the near-shelf SEMC and the open-ocean retroflecting SICC (Backeberg et al., 2012; Martínez-Moreno et al., 2021). Furthermore, Beech et al. (2022) argue that observational changes in mesoscale eddy activity cannot account for the magnitude and sign of long-term change in eddy-rich regions like the MC yet.

4.6.3. Changes in thermal fronts

The elevated mean TG along continental shelves and in the wake of strong geostrophic currents (NEMC, SEMC), has previously been documented in Sudre et al. (2023a, 2023b) (See Chapters 3 and 5). In this study, we suggest that TG seasonal variation changes are driven by changes in the mixed layer depth (de Boyer Montégut et al., 2004). We could thus explain the shallower thermal fronts in the pseudo global warming experiment by the increase of temperature-driven stratification described in Li et al. (2020).

The changes in TG from our 1/36° pseudo global warming experiment (Fig. 4.7) disagree with the larger scale SST gradient trends computed on a 1/4° grid in Martínez-Moreno et al. (2021) for the period January 1993 to March 2020. Martínez-Moreno et al. (2021) report a (statistically significant) trend in SST gradient of about -0.3 °C.km^{-1} per decade in the Comoros Basin (Martínez-Moreno et al., 2021, Extended Data Fig. 3. d.). The discrepancy between the 1/4° SST gradient trends reported by Martínez-Moreno et al. (2021) and the 1/36° TG anomalies from our baseline and pseudo global warming experiments is likely due to the different spatial scales at which the gradients are computed. The gap between those two results emphasizes the need for regional downscaling to improve future trend estimates of fine scale oceanic features.

Furthermore, the TG differences between the two experiments follow closely the differences in mean EKE, suggesting that the thermal fronts most affected by the climate warming perturbation are likely ephemeral "deformation fronts", i.e. filaments occurring at the edges of mesoscale eddies, as defined in McWilliams (2021). Furthermore, Sudre et al. (2023a) (see Chapter 3) showed that thermal front seasonal variability in the MC is not trivially linked to EKE variations. Here we illustrate this contrast further by comparing climate change variations in EKE and TG (Fig. 4.10). In the inner MC, mean TG changes are spatially correlated to EKE changes, and particularly so between 100 and 200 m, in the vicinity of the mixed layer depth where thermal gradients are maximum. Spatial correlation coefficients between changes in TG and EKE then taper down with depth. Outside of the MC, east of Madagascar Island, the same spatial correlation coefficients are highest at surface, with a second maximum at -350 m and a marked drop at approximately -25 m.

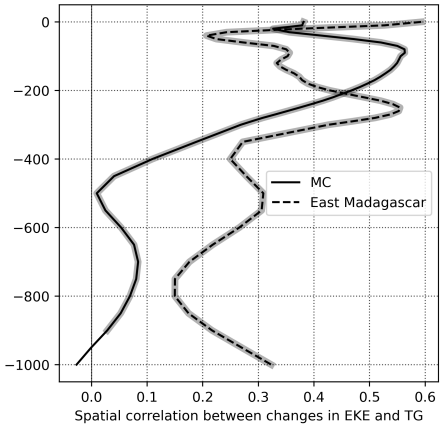

Figure 4.10.: Vertical profiles of the spatial correlation coefficient between EKE and TG inside of the MC and East of Madagascar. The grey shading indicate where the correlation is significant.

4.7. Conclusion

This study's objective is to explore the nature and magnitude of projected regional changes in EKE and thermal fronts in the MC. For this, we compare a regional hindcast simulation (1993-2014) to a pseudo global warming experiment forced similarly to the baseline, but with added seasonal forcings at the surface and lateral boundaries reflecting a stable warm state corresponding to conditions of the late 21st century (2071-2100). The regional projection shows a marked increase of EKE in the Comoros Basin and southwest of Madagascar, and a decrease within the MC (south of 16°S) and southeast of Madagascar, at the SEMC retroflection. Vertically, the EKE changes seem to be restricted to the top 400 m. Similarly to the EKE, TG are projected to increase in the Comoros Basin and southwest Madagascar, and to decrease within the MC (south of 16°S) and southeast Madagascar. The fact that changes in thermal gradients follow closely those of the EKE, suggests that the thermal fronts most affected by the climate warming perturbation correspond to ephemeral "deformation fronts" as defined by McWilliams (2021). Modelled thermal fronts are shallower in the pseudo global warming experiment but changes in TG can reach as deep as 1000 m in some regions. Annual thermal front frequencies averaged over the whole domain do not reveal a significant difference between the medians of the two experiments, but show an increased interannual variability in the projection.

The pseudo global warming downscaling procedure presented in this Chapter 4 allows us to identify changes in finer scale processes such as ocean fronts and filaments in the MC, which would otherwise be missing from coarser global ensemble model projections. However, dynamically downscaled projections are still inherently dependent of their large scale atmospheric and boundary forcings. The delta addition does correct climatological biases found in global models but it also assumes that this bias will not change over time. Additional bias corrections to the monthly deltas,

adapted from Bruyère et al. (2014) and Drenkard et al. (2021), may be considered in future work.

Another limit to this study is that we did not use a regional ocean-atmosphere model in our downscaling procedure due to the additional computational cost. We also chose to use ERA-interim daily means to force our model at surface instead of the most recent ERA5 hourly means in order to stay as close as possible to the original MOZ36 configuration. This means that fine-scale air-sea interactions (Small et al., 2008; Seo et al., 2023) have not been taken into account and could potentially hinder the reproduction of the regional mesoscale eddy activity (Renault et al., 2017, 2020) and related frontogenesis (Thomas & Lee, 2005). We thus expect a slight overestimation of the mesoscale eddy activity in our simulations.

Additionally from improving air-sea interactions in the model, another next step to this study would be to downscale several global models and/or to consider a range of scenarios to account for the full range of climate change uncertainties (Alexander et al., 2020) in the southwest Indian Ocean. To this end, the regional simulations presented in this work could be used to train a climate emulator. Climate emulators are tools built with machine learning techniques and designed to mimic partly (or entirely) climate models but at a much lesser computational cost (Reichstein et al., 2019; Tebaldi et al., 2022; Doury et al., 2023). An emulator model would enable us to derive future changes in key ocean health variables from an ensemble of scenarios, at a fraction of the full dynamical downscaling computational cost.

Finally, because fronts and filaments in the MC are supporting entire ecosystems (Tew Kai et al., 2009; Tew Kai & Marsac, 2010), the projected changes in EKE and thermal fronts South of Madagascar and in the Comoros Basin suggest that key pelagic and benthic habitats might be affected (Weimerskirch et al., 2010; Le Corre et al., 2012; Diamant et al., 2018). Given the climate risks for marine ecosystems also projected from the latest CMIP6 (Tittensor et al., 2021), it would make a lot of sense to couple our regional model to a biogeochemical one. A regional investigation of nitrogen and carbon cycles responses to a global warming scenario would help support spatial planning in the region.

KEY POINTS

. Our pseudo global warming experiment reveals an increase in EKE in the Comoros Basin and southwest of Madagascar, and a decrease in the southern MC and southeast of Madagascar.

. Changes in EKE are confined to the upper 400 m of the water column.

. The projected changes in thermal fronts follow closely those of the EKE: TG are projected to increase in the northern MC and southwest of Madagascar, and to decrease in the southern MC and southeast of Madagascar.

. The thermal fronts most affected by the climate warming perturbation are likely those forming in between eddies.

. Thermal fronts are projected to be shallower in the pseudo global warming experiment, while changes in TG extend as deep as 1000 m in some regions.

. The pseudo global warming experiment shows greater interannual variability in front frequency.

4.8. APPENDIX: Contrasting mean temperature and circulation between baseline and pseudo global warming experiments

Changes in mean temperature

End of the century pseudo global warming sea surface temperatures are 2-3°C warmer than for the hindcast period and particularly so in the southern regions of the MC (Fig. 4.11). This temperature range is consistent with the forcing CESM-LENS member (Fig. 4.11 d.) and with CESM2-LE (Danabasoglu et al., 2020) ensemble mean-state changes of ocean temperature between 1980-2000 and 2080-2100 periods reported by Sharma et al. (2023). Vertically, the anomaly between projected and hindcast mean states from the regional model (Fig. 4.12, left column) and the global model (Fig. 4.12, right column) decreases with depth to about less than 1°C at -1000 m.

Changes in mean currents

East of Madagascar at about 12-16°S, the westward South Equatorial Current (SEC) is slightly weaker and narrower in the pseudo global warming experiment than in the baseline experiment (Fig. 4.13, second column). North of Madagascar, the North East Madagascar Current (NEMC) flows westwards between Madagascar and the Mozambican shelf and is projected to slow down in the pseudo global warming experiment (Fig. 4.13, second column). The NEMC seems to broaden when turning southward along the Mozambique coast and its transport to the MC appears to be impaired by the changes in bathymetry at about 16°S (Fig. 4.1, Fig. 4.13). The seemingly blocked NEMC circulation north of 16°S results in increased current speed in the Comoros Basin. Along the eastern coast of Madagascar, the poleward South East Madagascar Current (SEMC) appears to slow down and narrow closer to the shelf, which explains the positive anomaly near the island and negative one further out in the open ocean (Fig. 4.13, second column). The SEMC retroflection or South Indian Ocean Countercurrent (SICC, Siedler et al., 2009) appears to be significantly reduced in the pseudo global warming experiment.

Within the MC, the discontinuous poleward Mozambique Current (MZC) which flows along the Mozambican shelf (de Ruijter et al., 2002; Lutjeharms et al., 2012) also appears weaker in the pseudo global warming experiment (Fig. 4.13, second column: b., f.). However, the equatorward Mozambique Under Current (MZUC) (de Ruijter et al., 2002; Biastoch et al., 2009; Lutjeharms et al., 2012) is projected to be stronger in the pseudo global warming experiment (Fig. 4.13, second column: j., n.).

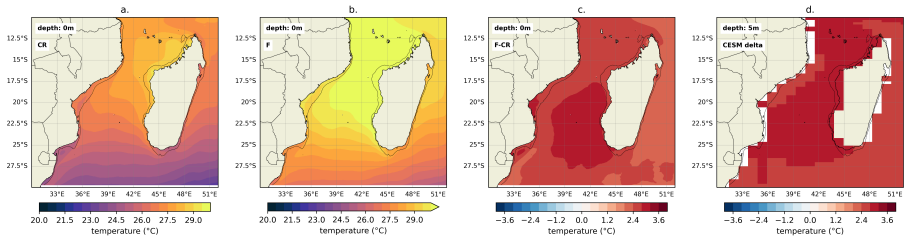

Figure 4.11.: Mean surface temperature from MOZ36_CR (a.), MOZ36_F (b.) and changes in mean surface temperature in the regional model (MOZ36_F - MOZ36_CR, c.) and in the global model (CESM_member$|_{2071\text{-}2100}$ minus CESM_member$|_{1993\text{-}2014}$, d.). The colormaps are from cmocean (Thyng et al., 2016).

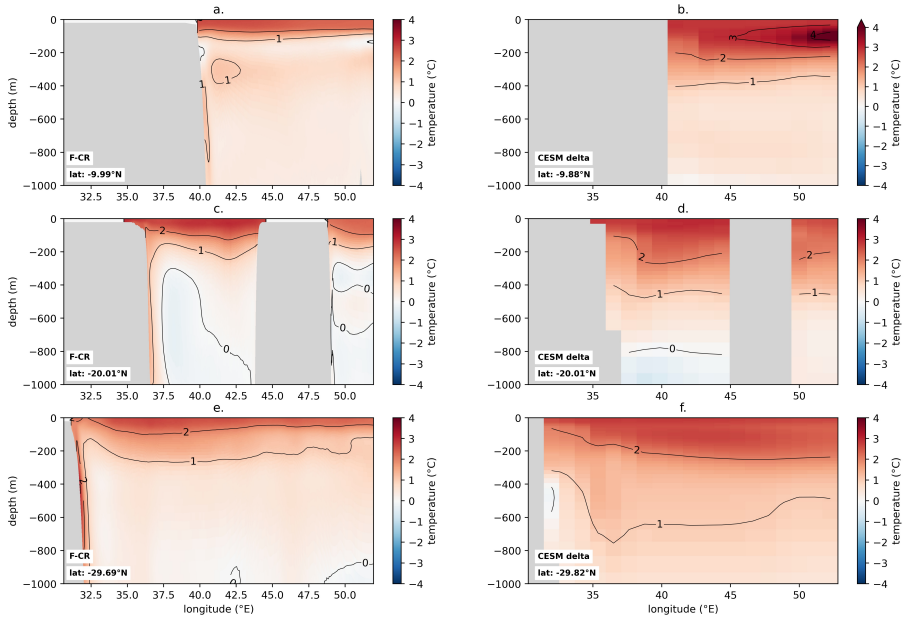

Figure 4.12.: Sections of mean temperature changes (projection minus baseline) in the regional (left column) and global (CESM_member$|_{2071\text{-}2100}$ minus CESM_member$|_{1993\text{-}2014}$, right column) models for several latitudes: 10°S (top row), 20°S (center row) and 30°S (bottom row). The colormaps are from cmocean (Thyng et al., 2016).

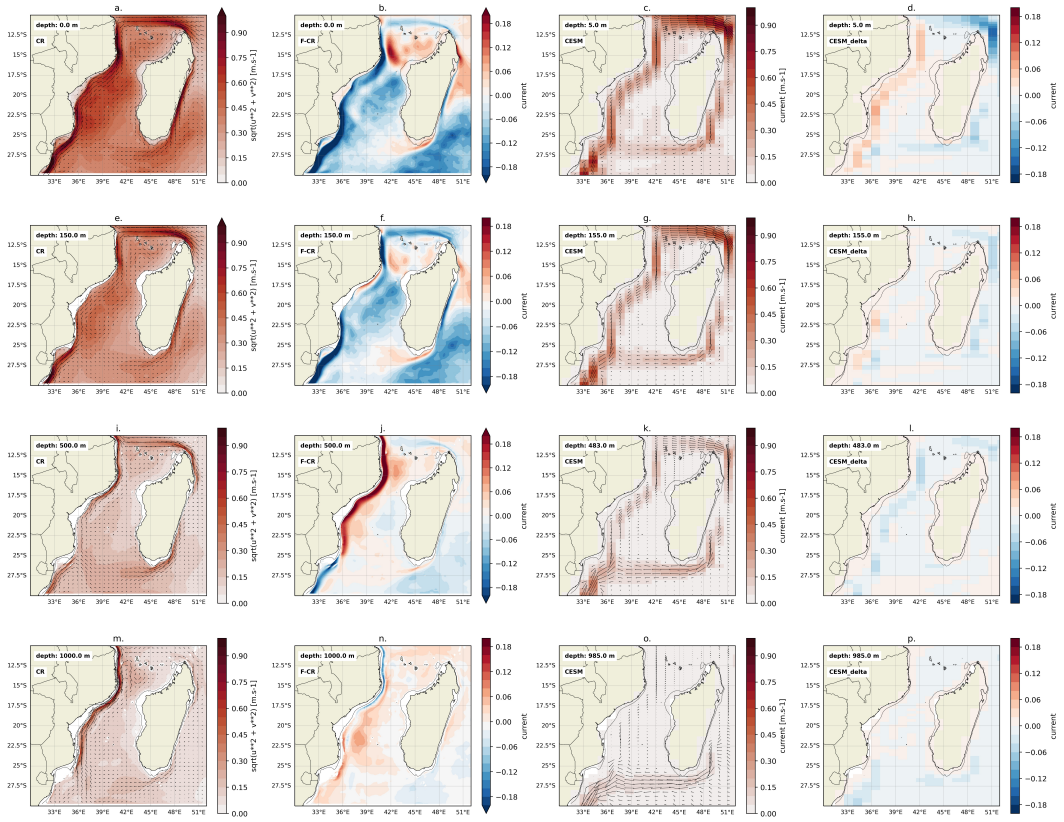

Figure 4.13.: Mean current modulus from MOZ36_CR (1st column), changes in mean current modulus between MOZ36_F and MOZ36_CR (2nd column), mean current modulus from the global model (CESM_member$|_{1993\text{-}2014}$, 3rd column) and changes in mean current modulus in the global model (CESM_member$|_{2071\text{-}2100}$ minus CESM_member$|_{1993\text{-}2014}$, 4th column). The means and mean changes are shown for several depths: 0 m (1st row), -150 m (2nd row), -500 m (3rd row), -1000 m (last row). The colormaps are from cmocean (Thyng et al., 2016).

5. An ocean front dataset for the Mediterranean Sea and Southwest Indian Ocean

Content

5.1. Summary 118
5.2. Résumé en français 119
5.3. NOMAD dataset 122
5.4. Data descriptor 122

5.1. Summary

Ocean fronts are transition zones between water patches of distinct properties. Those transient boundaries are pivotal for marine life, since the associated vertical velocities can bring nutrients up to the sun-lit upper ocean (Klein & Lapeyre, 2009; Mahadevan, 2016). The nutrient injections occurring at ocean fronts sustain higher productivity, which in turn provides abundant food resources for marine organisms: from plankton, and all the way up the trophic chain, to top predators and fisheries.

In Chapter 3, we used modelled and remotely sensed data to show that fronts are ubiquitous in the Mozambique Channel (MC). Persistent fronts form at the Mozambican and Madagascar shelf-breaks and along the NEMC and SEMC. Ephemeral fronts are generated in between MC eddies or at meanders of both NEMC and SEMC. In Chapter 4, we have investigated the response of those fronts to a global warming perturbation akin to a "business-as-usual" scenario for the end of this century. We found that the areas most affected in the pseudo global warming experiment overlap key habitats for seabirds and megafauna: south of Madagascar, along the Mozambican shelf and in the Comoros Basin.

Persistent ocean fronts can be fundamental to the functioning of marine ecosystems and the management of subsequent marine resources. Maps of climatologically persistent fronts can help identify priority marine protection areas (Scales et al., 2014b, 2018). However, marine megafauna – which are considered to be ecosystem sentinels (Hazen et al., 2019) – have also been associated with ephemeral fronts in several instances (e.g. Tew Kai et al., 2009; Siegelman et al., 2020a).

Given the abundance of ephemeral fronts in the MC (Chapter 3), projected changes in front (Chapter 4) and eddy (Martínez-Moreno et al., 2021) activity and the presence

of marine megafauna in the area (e.g., Le Corre et al., 2012; Laran et al., 2017), we posit that ephemeral ocean fronts play a pivotal role in shaping ecosystems in the SWIO. A direct corollary of this hypothesis is that the projected ocean front changes in the SWIO would impact significantly the structure and functioning of those ecosystems. Investigating the interactions between marine megafauna and ephemeral ocean fronts would thus assist marine spatial planning in the region.

The exploration of how marine megafauna makes use of ephemeral fronts in the SWIO requires both multi-species tracking data and fine-scale ocean front maps. In Chapter 5, we contribute to this effort by providing a multi-decadal high-resolution observational front dataset for the SWIO (and the Mediterranean Sea), that we call the NOMAD.

To build the NOMAD, we use satellite sea surface temperature from MUR SST and total currents from CMEMS (see section 2.2). *Thermal fronts* are detected using the same method as the one employed in previous Chapters: we estimate thermal gradient fields with the BOA and apply a statistical threshold to isolate gradient edges. The Eulerian perspective introduced by thermal gradients effectively captures the spatial characteristics of the flow at a specific moment. However, a Lagrangian dynamical approach offers the advantage of incorporating both spatial and temporal current variability, while being independent of cloud cover. We thus complement thermal gradients by computing backward FSLE to identify attracting LCS. *Dynamical fronts* are then identified as ridges of backward FSLE values. The resulting thermal gradients are mapped from 2003 to 2020 on a 1 km grid while the backward FSLE cover 1994 to 2020 on a 1.56 km grid. For both diagnostics, we provide region-appropriate thresholds to highlight thermal (resp. dynamical) fronts, based on thermal gradient (resp. backward FSLE) distributions in each Longhurst province (Longhurst, 2007) and Spalding's ecoregion (Spalding et al., 2007) falling into the Mediterranean Sea and SWIO.

Our NOMAD dataset stands out from existing front datasets (e.g. Belkin et al., 2009; AVISO, 2021) by its higher spatial and temporal resolution and extensive coverage. NOMAD is well-suited for a wide range of applications requiring the detection of fine-scale thermal fronts and LCS in the Mediterranean Sea and the SWIO. We made NOMAD with a view to explore interactions between ocean fronts and megafauna in the SWIO. But NOMAD could also be used to explore the dynamics between fine-scale thermal fronts and low-level winds from Radar Scatterometer data, as it has mostly been done at the mesoscale (O'Neill et al., 2012; Seo et al., 2023) ; or to monitor the spread of marine pollutants along ocean fronts (e.g. Pattiaratchi et al., 2022; Fifani et al., 2021).

5.2. Résumé en français

Les fronts océaniques sont des zones de transition entre des étendues d'eau aux propriétés distinctes. Ces frontières éphémères sont cruciales pour la vie marine, surtout lorsqu'elles sont associées à des vitesses verticales augmentant les flux de nutriments

dans la couche supérieure de l'océan (Klein & Lapeyre, 2009; Mahadevan, 2016). Les injections de nutriments qui se produisent aux fronts océaniques soutiennent une productivité biologique accrue, fournissant ainsi des ressources alimentaires abondantes pour les organismes marins sur toute la chaine trophique : du plus petit plancton jusqu'aux plus grands mammifères marins.

Dans le chapitre 3, nous avons montré à partir de données modélisées et satellitaires que les fronts sont omniprésents dans le canal du Mozambique (MC). Des fronts persistants se forment au niveau des plateaux continentaux du Mozambique et de Madagascar et le long du NEMC et du SEMC. Les fronts éphémères, quant à eux, sont générés entre les tourbillons du MC ou au niveau des méandres du NEMC et du SEMC. Dans le chapitre 4, nous avons étudié la réaction de ces fronts à une perturbation de réchauffement climatique similaire à un scénario "business-as-usual" pour la fin du siècle. Nous avons constaté que les zones les plus affectées par la perturbation de réchauffement climatique chevauchent des habitats clés pour les oiseaux de mer et la mégafaune : au sud de Madagascar, le long du plateau continental du Mozambique et dans le bassin des Comores.

Les fronts océaniques persistants sont essentiels pour le fonctionnement des écosystèmes marins et la gestion de leurs ressources. Des cartes de fronts persistants peuvent ainsi aider à identifier les zones prioritaires de protection marine (Scales et al., 2014b, 2018). Cependant, la mégafaune marine, considérée comme sentinelle des écosystèmes marins (Hazen et al., 2019), a également été associée à des fronts éphémères dans plusieurs études (par exemple Tew Kai et al., 2009; Siegelman et al., 2020a).

Étant donné l'abondance de fronts éphémères dans le MC (Chapitre 3), des changements potentiels de l'activité des fronts et des tourbillons dûs au réchauffement climatique (Chapitre 4, Martínez-Moreno et al., 2021), ainsi que la présence de mégafaune marine dans la région (par exemple, Le Corre et al., 2012; Laran et al., 2017), nous postulons que les fronts océaniques éphémères jouent un rôle central dans la formation des écosystèmes dans le sud-ouest de l'Océan Indien (SWIO). Le corollaire directe de cette hypothèse est qu'un changement dans l'activité des fronts dû au réchauffement climatique aurait un impact significatif sur la structure et le fonctionnement de ces écosystèmes. Mieux comprendre les interactions entre la mégafaune marine et les fronts océaniques éphémères permetrait ainsi d'améliorer la gestion des écosystemes et des resources dans le SWIO.

Pour étudier la manière dont la mégafaune marine utilise les fronts éphémères dans le SWIO, il faut réunir à la fois des données d'observations multi-espèces et des cartes de fronts océaniques à fine échelle. Dans le Chapitre 5, nous contribuons à cet effort en fournissant une base de données de fronts à haute résolution et sur plusieurs décennies pour le SWIO (et la mer Méditerranée): le "oceaN frOnt dataset for the Mediterranean seA and southwest inDian ocean" ou NOMAD.

Pour construire le NOMAD, nous utilisons des données satellitaires de temperature de surface de la mer provenant de MUR SST et les courants totaux du CMEMS (voir la section 2.2). Les fronts thermiques sont détectés en utilisant la même méthode que celle employée dans les chapitres précédents : nous estimons les gradients thermiques avec le BOA et appliquons un seuil statistique pour isoler les gradients les

plus prononcés. La perspective Eulérienne introduite par les gradients thermiques capture efficacement les caractéristiques spatiales du flux à un moment spécifique. Cependant, l'approche dynamique Lagrangienne présente l'avantage d'incorporer à la fois la variabilité spatiale et temporelle des courants, tout en étant indépendante de la couverture nuageuse. Nous complétons donc les gradients thermiques par un calcul de FSLE anti-chronologiques pour identifier des structures Lagrangiennes cohérentes (LCS) convergentes. Les fronts dynamiques sont ensuite identifiés en imposant un seuil statistique sur les valeurs de FSLE anti-chronologiques. Les gradients thermiques de NOMAD sont cartographiés pour la période de 2003 à 2020 sur une grille de 1 km, tandis que les FSLE anti-chronologiques couvrent la période de 1994 à 2020 sur une grille de 1,56 km. Pour ces deux diagnostics, nous fournissons les seuils statistiques permettant de mettre en évidence les fronts thermiques (resp. dynamiques), basés sur les distributions de gradients thermiques (resp. FSLE anti-chronologiques) et pour chaque province de Longhurst (Longhurst, 2007) et écorégions de Spalding (Spalding et al., 2007) de la mer Méditerranée et du SWIO.

Le NOMAD se distingue des bases de données de fronts existantes (par exemple, Belkin et al., 2009; AVISO, 2021) par sa couverture spatiale et ses fines résolutions spatiale et temporelle. Le NOMAD se prete ainsi à une large gamme d'applications nécessitant la détection de fronts thermiques à petite échelle et de structures Lagrangiennes cohérentes dans la mer Méditerranée et le SWIO. Nous avons créé NOMAD dans l'optique d'explorer les interactions entre les fronts océaniques et la mégafaune dans le SWIO. Cependant, NOMAD pourrait également être utilisé pour examiner la dynamique entre les fronts thermiques à fine échelle et les vents de basse altitude à partir de données de radars scatteromètres (e.g. O'Neill et al., 2012; Seo et al., 2023), ou encore pour surveiller la propagation des polluants marins le long des fronts océaniques (e.g. Fifani et al., 2021; Pattiaratchi et al., 2022).

5.3. NOMAD dataset

Sudre, F., Hernández-Carrasco, I., Mazoyer, C., Sudre, J., Dewitte, B., Garçon, V., & Rossi, V. (2023). Nomad: the ocean front dataset for the mediterranean sea and southwest indian ocean. https://doi.org/10.12770/3ea321a1-d9d4-49e5-a592-605b80dec240

5.4. Data descriptor

Sudre, F., Hernández-Carrasco, I., Mazoyer, C., Sudre, J., Dewitte, B., Garçon, V., & Rossi, V. (2023b). An ocean front dataset for the mediterranean sea and southwest indian ocean. *Scientific data, 10*(730). https://doi.org/10.1038/s41597-023-02615-z

www.nature.com/scientificdata

scientific data

Check for updates

OPEN

DATA DESCRIPTOR

An ocean front dataset for the Mediterranean sea and southwest Indian ocean

Floriane Sudre[1]✉, Ismael Hernández-Carrasco[2], Camille Mazoyer[1], Joel Sudre[3], Boris Dewitte[4,5,6,7], Véronique Garçon[8] & Vincent Rossi[1]✉

Fronts are ubiquitous discrete features of the global ocean often associated with enhanced vertical velocities, in turn boosting primary production. Fronts thus form dynamical and ephemeral ecosystems where numerous species meet across all trophic levels. Fronts are also targeted by fisheries. Capturing ocean fronts and studying their long-term variability in relation with climate change is thus key for marine resource management and spatial planning. The Mediterranean Sea and the Southwest Indian Ocean are natural laboratories to study front-marine life interactions due to their energetic flow at sub-to-mesoscales, high biodiversity (including endemic and endangered species) and numerous conservation initiatives. Based on remotely-sensed Sea Surface Temperature and Height, we compute thermal fronts (2003–2020) and attracting Lagrangian coherent structures (1994–2020), in both regions over several decades. We advocate for the combined use of both thermal fronts and attracting Lagrangian coherent structures to study front-marine life interactions. The resulting front dataset differs from other alternatives by its high spatio-temporal resolution, long time coverage, and relevant thresholds defined for ecological provinces.

Background & Summary

Fronts are ubiquitous dynamical features of both coastal and open ocean. This is where water masses of different properties converge, thereby enhancing nutrient availability and local primary productivity[1–3]. Ocean fronts thus form ephemeral ecosystems where numerous species gather[4–6]: from phytoplankton communities[7,8], all the way up the food chain to top predators such as sea birds[9,10], tuna[11,12] and marine mammals[13,14].

Numerous techniques have been developed to define and identify ocean fronts. Front detection methods most commonly used by the scientific community rely on the horizontal distribution of oceanic tracers (temperature, salinity, nutrients, etc.) and are either gradient-based[15,16] or histogram-based[17,18], while others make use of entropy[19], neural networks[20] or singularity exponents[21,22]. While remotely-sensed chlorophyll-a and salinity could be studied, satellite observations of sea surface temperature (SST) provide the most easily-accessible and longest input dataset for front detection[23,24]. Additionally thermal fronts are usually highly spatially correlated to density and chlorophyll-a fronts as well[11,25,26]. Subsequently, SST observations are well-suited to Eulerian front diagnostics and to study front-marine life interactions. Histogram-based front detection, such as the Cayulla and Cornillon algorithm[17] which was further improved by Nieto *et al.*[18], is the most widely used method to detect persistent front edges on large spatial scales from satellite SST observations[11,12,23]. However, gradient-based methods present significant advantages to the study of regional fronts dynamics compared to histogram-based methods[6]. They detect local fronts when the gradient of a specific property (temperature, salinity, nutrient, sea surface height, etc.) exceeds a pre-defined threshold. Gradient-based methods, such as the Belkin and O'Reilly Algorithm (BOA)[16] used in this study, thus provide a gradient magnitude instead of a simple binary edge,

[1]Aix Marseille Université, Université de Toulon, CNRS, IRD, MIO, Marseille, France. [2]Mediterranean Institute for Advanced Studies (UIB-CSIC), Miquel Marques, 21, Esporles, 07190, Balearic Islands, Spain. [3]UAR 2013 CPST, IR DATA TERRA, Z.P. de Brégaillon - CS 20330, 83507, Montpellier, La Seyne Sur Mer, France. [4]Centro de Estudios Avanzados en Zonas Aridas, Facultad de Ciencias del Mar, Universidad Catolica del Norte, Coquimbo, Chile. [5]Departamento de Biología Marina, Universidad Católica del Norte, Coquimbo, Chile. [6]Center for Ecology and Sustainable Management of Oceanic Islands (ESMOI), Faculty of Marine Sciences, Catholic University of the North, Coquimbo, Chile. [7]UMR5318 Climat, Environnement, Couplages et Incertitudes (CECI), Toulouse, France. [8]University of Liège, Liège, Belgium. ✉e-mail: floriane.sudre@mio.osupytheas.fr; vincent.rossi@mio.osupytheas.fr

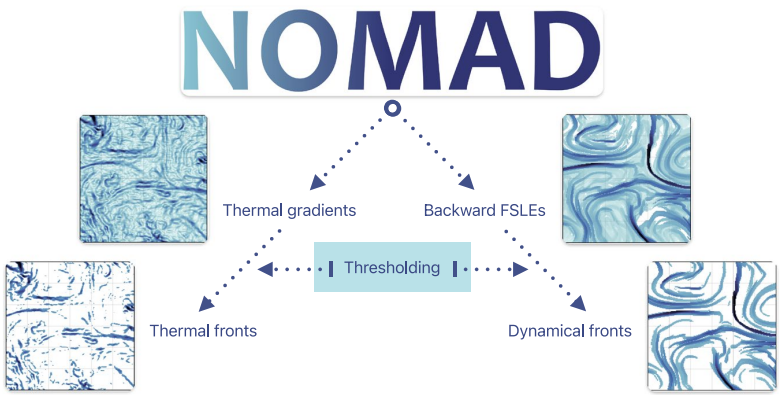

Fig. 1 Illustration showing how NOMAD[51] users can go from thermal gradients (resp. backward FSLEs) to thermal (resp. dynamical) fronts via region-specific thresholding, with example of fields before and after thresholding. All fields were taken on July 1st, 2020. The colormap is from cmocean[80] and with the same range as in Fig. 2.

require less parameter fine-tuning, and thus better reveal region-specific dynamics and variability[6,27]. The BOA improves on the original Canny Algorithm[15] by reducing gradient-generated noise while preserving the shape of frontal structures[16] and it has been successfully applied to the South China Sea[28], the East China Sea[29], the Kuroshio current[30] and the Mozambique Channel[27].

While the Eulerian perspective brought by thermal gradients describes well the spatial features of the flow at a given time, the Lagrangian dynamical approach has the added benefit of integrating both spatial and temporal current variability and brings additional information about transport and mixing properties of the fluid. In particular, Finite-size Lyapunov exponents (FSLEs)[31] used in this study are well-suited to evaluate horizontal mixing and transport in geophysical flows[7,32,33]. High FSLE values reveal lines acting as transport barriers, also expressed as hyperbolic Lagrangian coherent structures (LCS), which help to identify filaments, fronts or eddy boundaries. Ridges of backward-in-time FSLE (also referred to as "backward FSLEs") fields characterize regions of locally high convergence of particle trajectories (attracting LCS) while forward-in-time FSLEs identify regions of locally high divergence (repelling LCS). These dynamical structures greatly organize the fluid motion around them, providing a flow mapping with the main routes of transport[34,35]. Here we provide backward FSLEs to unveil attracting LCS. Tracers (such as temperature, nutrients, pollutants, etc.) converge and spread along attracting LCS, creating filament-like structures of high tracer concentration. This property offers a direct and clear physical interpretation of the attracting LCS.

FSLEs are complementary to thermal gradients because they are not vulnerable to cloud cover, they are able to reveal dynamics at a smaller scale than the resolution of the velocity field[34], and they provide useful transport diagnosis of tracers[7,36]. Additionally, FSLEs are especially useful to study marine bio-physical interactions. Indeed, the LCS revealed by the FSLE field separate regions with different dynamics and often coincide with sharp tracer gradients[37] so that they can be interpreted as dynamical fronts. FSLEs have been used to understand the dynamics of tracers like SST and chlorophyll-a[7,8,38,39], which have direct implications on the behavior of marine life across all trophic levels[5,10,13,14,40–42].

The present dataset offers the synergy of both Eulerian and Lagrangian perspectives by providing a multi-decadal record of both thermal gradient and backward FSLE fields at high resolution. Thermal gradients (resp. backward FSLEs) fields are computed on a 1 km (resp. 1.56 km) grid, covering the period 2003–2020 (resp. 1994–2020), for two oceanic regions characterized by high biodiversity under conservation concerns: the Mediterranean Sea (MedSea) and the Southwest Indian Ocean (SWIO). Thermal gradients (resp. backward FSLEs) lead to thermal (resp. dynamical) fronts after region-appropriate thresholding, as illustrated in Fig. 1.

Other data products informing on ocean fronts have been developed. Belkin *et al.*[23] produced a 9 km-resolution persistent front database for major Large Marine Ecosystems[43]. Additionally, daily backward FSLEs[44] (accessed on Jan 20th 2023) have been computed from altimetry derived daily velocities on a 4 km global grid since 1994 following the method of d'Ovidio *et al.*[32]. Finally, the BOA has been used by the National Oceanic and Atmospheric Administration (NOAA) since 2013 to produce near real-time chlorophyll-a frontal maps (accessed on Jan 20th, 2023) for the U.S. coastal areas only. Those existing datasets target analyses of much larger spatial scales, their resolution being 2.5 to 9 time coarser than the dataset presented here, and/or do not cover the present geographical domains of interest. Our front dataset differs to those existing by being specifically designed for multidisciplinary research, especially topics linking ocean weather and marine ecology[45]. It is dedicated to researchers who investigate front dynamics at space and time scales that relate to the highly patchy distribution of biological production and the rapidly evolving behavior (for foraging, mating, socializing, migrating, etc.) of marine species, especially top marine predators. Additionally, the greater length of the provided time series allows for analyzing long-term variability and trends. Our ocean front dataset for the Mediterranean Sea and the Southwest Indian Ocean aims to

bridge the gap between advances in the identification of physical oceanic features and the search of general rules governing how marine life across trophic levels exploits the highly heterogeneous seascape.

Methods

Thermal gradients. We use the BOA[16], and more specifically Benjamin Galuardi's pseudo-code written in R (available on https://github.com/galuardi/boaR, accessed on May 19th, 2022) to compute thermal gradient magnitudes. We apply the BOA on daily satellite Sea Surface Temperatures (SST) from the Multi-scale Ultra-high Resolution sea-surface temperature analysis (MUR SST, accessed on Jan 10th, 2023)[46], the resulting field is a thermal gradient expressed in °C/km. The resulting Southwestern Indian Ocean (SWIO) thermal gradient dataset covers latitudes between 5°S and 35°S and longitudes between 30°E to 80°E, and the Mediterranean Sea (MedSea) dataset covers latitudes between 30°N and 46°N and longitudes between −6°E to 37°E. The outputs for both geographical domains are produced daily from 2003 to 2020 and at the same spatial resolution of 1/100° which is about 1 km.

Each daily thermal gradient map includes a flag variable indicating whether a given pixel is located on land (flag = 2), or if it is "suitable" (flag = 0) or "unsuitable" (flag = 1) for thermal front analysis. Pixels are deemed "unsuitable" based on MUR SST standard deviation of the formal estimation error, which is considered to be a good estimate on MUR analysis uncertainty[46]. When the MUR SST standard deviation of the estimation error is high, the thermal gradient field is smoothed out and possible front or eddy structures are obfuscated. We thus recommend applying the flag before any further analysis of the thermal gradient field. We set the MUR SST standard deviation of the estimation error threshold, i.e. threshold above which a pixel is deemed "unsuitable" for front analysis, at 0.0384 °C. The choice of threshold is based on a preliminary comparison between MUR SST standard deviation and our thermal gradient dataset.

Finite-size Lyapunov exponents. In this work, backward-in-time FSLEs in the SWIO are computed from remotely-sensed Sea Surface Height (SSH) at 1/4° spatial resolution from Global Total Surface and 15 m Current (CLS, 2018, COPERNICUS-GLOBCURRENT, accessed on Jan 10th, 2023) from Altimetric absolute geostrophic velocities and Modeled Ekman Current Reprocessing[47]. In the MedSea, backward FSLEs are computed from daily absolute geostrophic surface currents derived from Sea Level Anomalies (SLA) at 1/8° spatial resolution from a SSALTO/DUACS multimission altimeter regional L4 product released in 2016 by AVISO + and based on regional mean dynamic topography[47] (https://data.marine.copernicus.eu, accessed on Feb 10th, 2023).

Backward FSLEs were obtained following the algorithm described by Hernandez-Carrasco *et al.*[34]. Essentially, the algorithm computes backward FSLEs by integrating backward in time two neighbouring particle trajectories advected in a two-dimensional flow using a fourth order Runge-Kutta scheme with a bilinear interpolation in space and linear in time. The total period of integration is 90 days. The Runge Kutta time step was set at 6 hours to reduce numerical diffusion. As we are interested in simulating fluid particles, we computed trajectories of infinitesimal passive particles. The FSLE value at a given position and time (x, y, t) can be expressed as:

$$\mathrm{FSLE}(x,\, y,\, t,\, \delta_f,\, \delta_0) \,=\, \frac{1}{\tau}\log\left(\frac{\delta_f}{\delta_0}\right).$$

δ_0 is the initial distance between a particle at (x, y, t) and its 4 closest neighbors. δ_0 corresponds to the spatial resolution of the FSLE grid, which is here 1/64° or approximately 1.56 km. δ_f is the final distance between particles, here it is set so that $\delta_f = 10\delta_0$. τ is the minimum time (among the 4 particle pairs) that it takes for the particles to reach the distance δ_f. FSLEs are thus expressed in day^{-1}. Similarly to the thermal front dataset, the SWIO FSLE dataset covers latitudes between 5°S and 35°S and longitude between 30°E to 80°E, and the MedSea dataset covers latitudes between 30°N and 46°N and longitudes between −6°E to 37°E. Both geographical domains have a spatial resolution of 1/64° which is about 1.56 km, and the output is produced daily from 1994 to 2020. Each daily FSLE dataset includes a flag variable indicating whether pixels are located on land (flag = 2), or if they are "suitable" (flag = 0) or "unsuitable" (flag = 1) for front analysis. Pixels are deemed "unsuitable" based on their FSLE value. Pixels whose FSLE value is 0 day^{-1} correspond to particles which have not reached the final distance δ_f after the integration time, i.e. after 90 days. Pixels whose FSLE value is above 900 day^{-1} correspond to beached particles. We thus recommend applying the flag before any further analysis of the FSLE field. Figure 2 is an example snapshot of the thermal gradient and backward FSLE fields in the MedSea and the SWIO.

Thresholds. One of the advantages of using the BOA and backward FSLEs to detect fronts is that both outputs are continuous fields. Users can then determine the threshold above which thermal gradients or FSLE values belong to a meaningful front, as illustrated in Fig. 1. Since different regions present different ranges of front intensity, that are somehow non-trivially linked to contrasting levels of Eddy-Kinetic Energy[27], it is relevant to define region-specific thresholds. Moreover, it is very likely that marine organisms aggregate actively along the most adequate fronts for foraging not based on their absolute characteristics but rather on their relative properties (i.e. targeting the most advantageous fronts as compared to all those found in the surroundings). As such, and to adapt our dataset to users interested in the interaction between fronts and marine life at both basin and eco-region scales, we provide thresholds for the MedSea and the SWIO basins but also for each Longhurst's provinces[48,49] and Spalding's ecoregions[50] falling into each geographical domain (Fig. 3). For both levels of analysis, we set the regional and subregional thresholds at the value of the 70th percentile computed over all the "suitable" pixels in the multidecadal dataset.

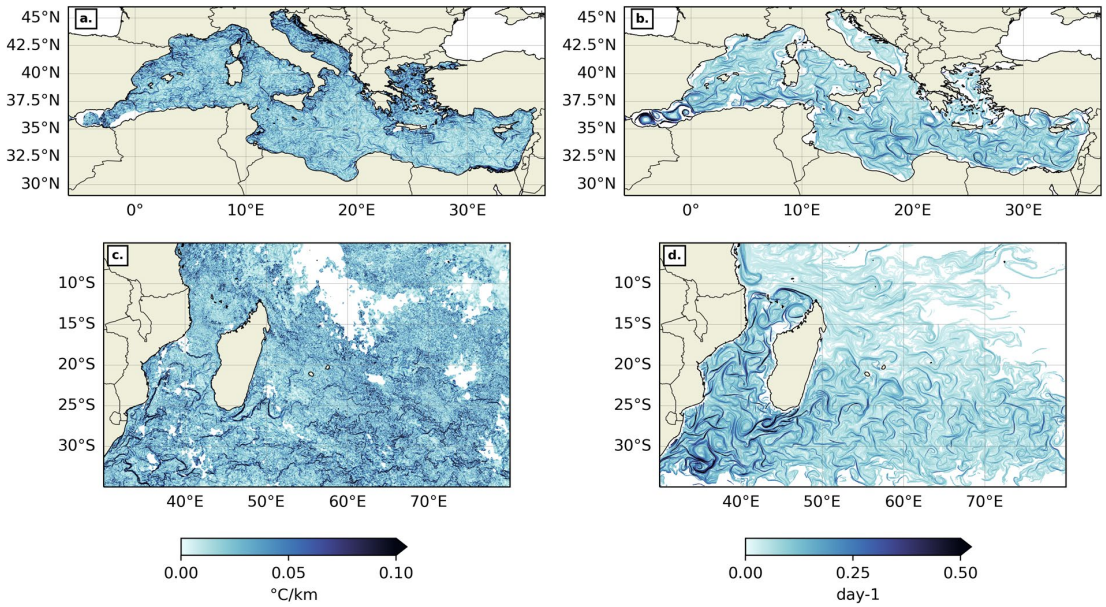

Fig. 2 Example snapshots of thermal gradient (**a,c**) and FSLE (**b,d**) fields in the MedSea (**a,b**) and SWIO (**c,d**), for "suitable" pixels only, on July 1st, 2020. The colormap is from cmocean[80].

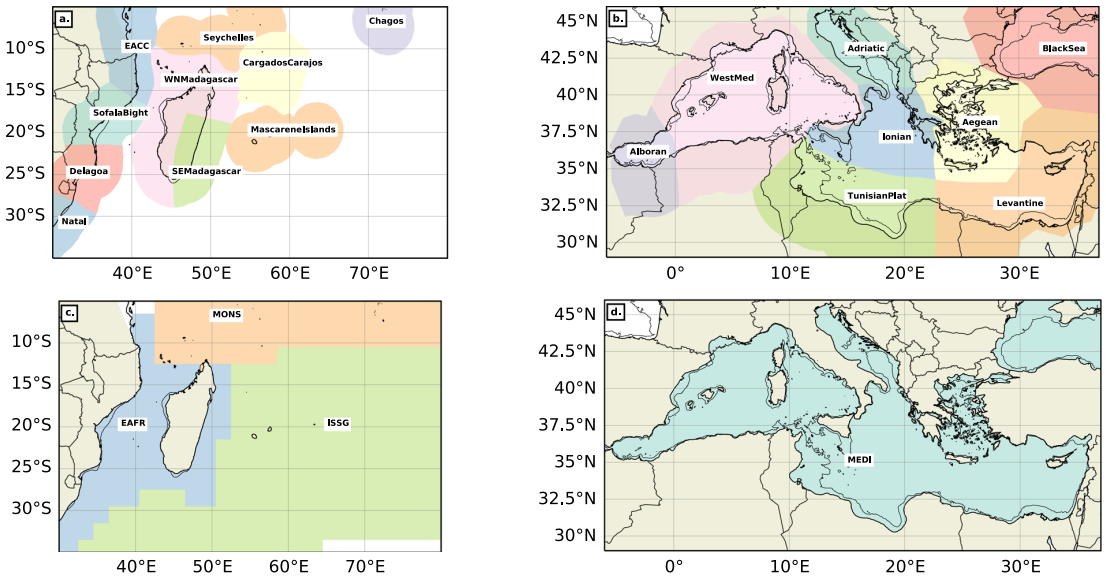

Fig. 3 Spalding's ecoregions[50] (**a,b**) and Longhurst's provinces[48,49] (**c,d**) in the SWIO (**a,c**) and in the MedSea (**b,d**).

Percentage of "suitable" pixels. The percentage of "suitable" pixels in each region of interest (SPP) is given by:

$$\mathrm{SPP(region)} = \frac{\mathrm{SPC(region)}}{\mathrm{OPC(region)}} * 100.$$

Where SPC is the number of "suitable" pixels in the region of interest and OPC is the total number of ocean pixels in the same region. Thresholds and SPP are provided for each region and subregion in Table 2 and as attributes in each netcdf file.

Folder name	Region	Variable	size	time period	temporal resolution	spatial resolution
TG_MedSea	MedSea	thermal gradient	128 Gb	2003–2020	daily	1/100° (approx. 1 km)
FSLE_MedSea	MedSea	backward FSLE	61 Gb	1994–2020	daily	1/64° (approx. 1.56 km)
TG_SWIO	SWIO	thermal gradient	507 Gb	2003–2020	daily	1/100° (approx. 1 km)
FSLE_SWIO	SWIO	backward FSLE	244 Gb	1994–2020	daily	1/64° (approx. 1.56 km)

Table 1. Dataset subfolders details.

Region	Classification	Subregion	Thermal Gradients (°C/km)		FSLEs (day^{-1})	
			Threshold	SPP	Threshold	SPP
MedSea	WHOLE	n/a	0.033	83.8%	0.123	57.3%
MedSea	LH	MEDI	0.033	83.6%	0.123	59.8%
MedSea	MEOW	Adriatic Sea	0.039	78.0%	0.086	44.0%
MedSea	MEOW	Aegean Sea	0.039	78.9%	0.135	49.0%
MedSea	MEOW	Alboran Sea	0.039	75.9%	0.254	41.3%
MedSea	MEOW	Ionian Sea	0.031	84.4%	0.113	73.3%
MedSea	MEOW	Levantine Sea	0.032	86.4%	0.142	75.6%
MedSea	MEOW	Tunisian Plateau	0.030	85.9%	0.111	76.4%
MedSea	MEOW	Western Mediterranean	0.033	85.6%	0.119	69.3%
SWIO	WHOLE	n/a	0.035	74.1%	0.105	73.3%
SWIO	LH	EAFR	0.036	78.5%	0.166	89.3%
SWIO	LH	ISSG	0.036	77.1%	0.094	74.7%
SWIO	LH	MONS	0.034	60.3%	0.083	56.3%
SWIO	MEOW	Bight of Sofala	0.033	79.2%	0.190	90.4%
SWIO	MEOW	Cargados Carajos	0.034	68.3%	0.077	77.0%
SWIO	MEOW	Chagos	0.036	49.7%	0.075	42.7%
SWIO	MEOW	Delagoa	0.038	83.3%	0.179	95.2%
SWIO	MEOW	East African Coral Coast	0.032	71.7%	0.128	79.0%
SWIO	MEOW	Mascarene Islands	0.033	81.1%	0.089	88.0%
SWIO	MEOW	Natal	0.041	76.5%	0.210	89.0%
SWIO	MEOW	Seychelles	0.034	67.5%	0.083	66.3%
SWIO	MEOW	Southeast Madagascar	0.037	76.6%	0.142	93.7%
SWIO	MEOW	Western and Northern Madagascar	0.034	75.8%	0.146	86.6%

Table 2. Thresholds and SPP for each region, Longhurst's provinces (LH)[48,49] and Spalding's Marine Ecoregions of the World (MEOW)[50].

Data Records

The oceaN frOnt dataset for the Mediterranean seA and southwest inDian ocean (NOMAD)[51] can be accessed through Ifremer online data repository. Figure 2 is a sample snapshot of the thermal gradient and backward-in-time FSLE field in the MedSea and the SWIO. The front dataset is 940 Gb in total, and is separated into 4 folders as detailed in Table 1. Each folder contains yearly subfolders, consisting of daily netcdf files. Each netcdf file provides: thermal gradient or backward FSLE values, pixel quality flags, but also front threshold values specific to each Longhurst's province and Spalding's ecoregion found in the MedSea or SWIO, as well as the corresponding percentage of "suitable" pixels found in those same ecologically-relevant subregions of the MedSea and the SWIO. Each netcdf file contains variables as shown below:

Thermal gradient netcdf files (TG_*region*_*date*.nc)

(1) time: date in seconds since 1950-01-01 in the proleptic gregorian calendar.
(2) lat: latitude, in decimal degree north.
(3) lon: longitude, in decimal degree east.
(4) tg: thermal gradient, in °C/km.
(5) flag: quality flag, which options are 0 = suitable, 1 = unsuitable, 2 = land.
(6) threshold_*subregion*: value of the 70th percentile of the thermal gradient field in a specific subregion, in °C/km.
(7) SPP_*subregion*: percentage of pixels deemed suitable in a specific subregion, in %.

Backward FSLE netcdf files **(FSLE_*region*_*date*.nc)**

(1) time: date in seconds since 1950-01-01 in the proleptic gregorian calendar.
(2) lat: latitude, in decimal degree north.

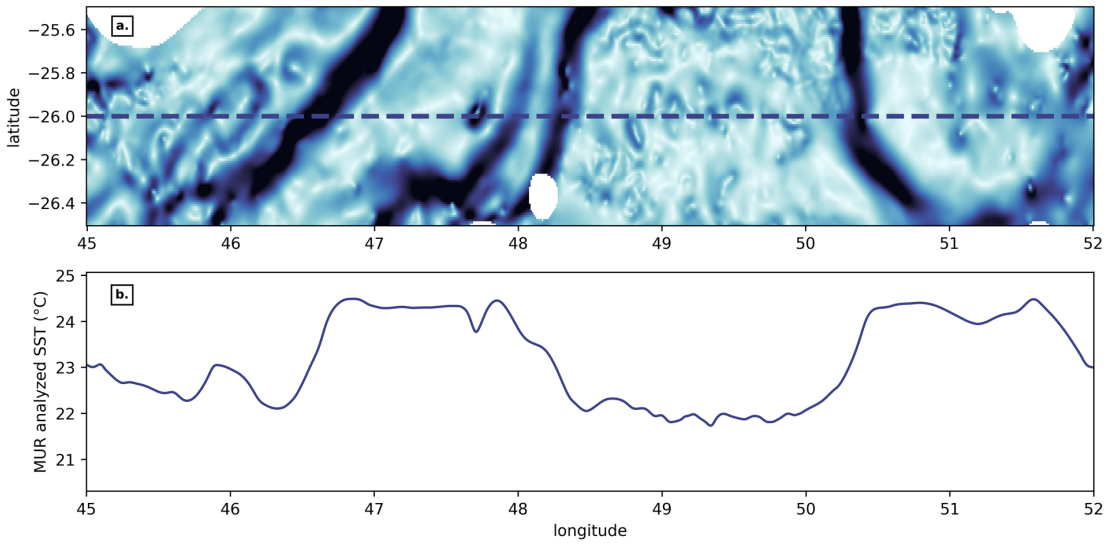

Fig. 4 Example of thermal gradient magnitude from the BOA (**a**) and corresponding MUR analysed SST value (**b**) for a section at 26°S in the SWIO, for July 1st, 2020. The colormap of Fig. 4a is from cmocean[80] and with the same range in °C/km as in Fig. 2.

(3) lon: longitude, in decimal degree east.
(4) fsle: backward finite-size Lyapunov exponents, in day^{-1}.
(5) flag: quality flag, which options are 0 = suitable, 1 = unsuitable, 2 = land.
(6) threshold_*subregion*: value of the 70th percentile of the FSLE field in a specific subregion, in day^{-1}.
(7) SPP_*subregion*: percentage of pixels deemed suitable in a specific subregion, in %.

Technical Validation

About thermal fronts. NOMAD[51] provides a multidecadal record of thermal gradients, which can be translated into thermal fronts via region-specific thresholding (Fig. 1). The BOA[16], which we used to compute NOMAD[51] thermal gradients, has been successfully employed multiple times: in physical oceanography[27,28], marine ecology[30,52], as well as by the National Oceanic and Atmospheric Administration (NOAA) since 2013[24]; and can thus be considered as an established method recognized by the research community. Figure 4 illustrates the BOA performance by putting side by side the horizontal thermal gradient issued from the BOA (top panel) and its corresponding MUR SST variation on a section at 26°S. Sharp changes of temperature (ranging approximately from 0.25 to 2 °C in this particular example) coincide with high values of thermal gradients (occurring at spatial scales ranging 10 to 50 km, in this example). High thermal gradient values thus are of the order of several degrees Celsius per 100 km.

Choice of SST data. When choosing a suitable SST product, we compromised spatial and temporal resolutions, cloud-contamination, time coverage and public availability. Cloud contamination is a real issue, especially when high spatial resolution is needed: infra-red radiometers cannot sense through cloud cover but micro-wave sensors do not have a sufficient spatial resolution yet to access small-scales dynamics. We thus opted for the Multi-scale Ultra-high Resolution (MUR) SST analysis[46], which combines 1 km resolution Moderate Resolution Imaging Spectroradiometer (MODIS) images, to 5–9 km resolution Advanced Very High Resolution Radiometer (AVHRR) products, 25 km resolution micro-wave data, and point-wise *in-situ* SST data. The integration and interpolation of those different satellite products is done by the Multi-Resolution Variational Analysis (MRVA) method, which uses scale-dependent time windows to adjust for various spatial resolutions[46]. MUR analysis thus provides improved spatial coverage and resolution of its SST product compared to conventional L3 data. However, such interpolation procedure also tends to blur oceanic features of interest such as eddies and fronts. It is thus necessary to find a way to identify pixels which have been blurred beyond a certain limit. The MUR SST product comes with a standard deviation of the estimation error (in °C) at each grid point[46]. We use this estimate of MUR analysis uncertainty to identify a suitable threshold above which the multidecadal dataset is considered too blurred for front analysis. The MUR analysis product also provides the time lag to most recent 1 km data, which would help the filtering, but the variable is only included after July 2016. Figure 8 of Sudre *et al.* work[27] further illustrates the relationship between thermal front detection and the two quality flags available in the MUR dataset. We finally opted for using only the standard deviation of the estimation error to provide a uniform and consistent multidecadal database. Visual comparisons between MUR standard deviation of the estimation error and our thermal gradient dataset were performed to find an arbitrary threshold that would return well-defined frontal structures without too much gaps. A too high estimation error limit would

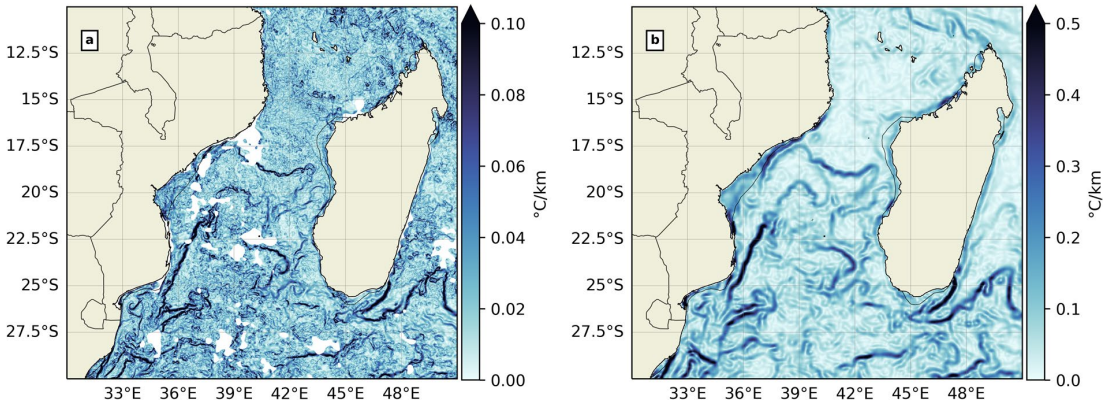

Fig. 5 (**a**) thermal gradient output from MUR SST and (**b**) thermal gradient output from SST CCI analysis, in the Mozambique Channel for July 1st, 2020. The colormap is from cmocean[80].

not filter out pixels where the MUR fusion and interpolation procedure blurred fronts and eddies. Yet a too low estimation error limit would lead to many pixels being filtered out, and some front features being hidden despite looking sharp enough to be exploitable. An additional difficulty resides in the fact that the standard deviation of the estimation error is a discrete variable in the MUR SST netcdf files. We found a good compromise for a standard deviation of the estimation error equal to 0.0384 °C.

The European Space Agency Sea Surface Temperature Climate Change Initiative: Analysis product[53] (SST CCI analysis) could be an attractive alternative to the MUR SST due to its climate-readiness. However, the SST CCI analysis is offered on a 1/20° grid (about 5 km), which is 5 times coarser than that of MUR SST. When pairing with biological observations such as GPS tracks, aerial surveys or sightings, the SST CCI may return spurious and artificial correlations. In designing NOMAD[51], the authors favored the grid resolution over the climate readiness of the final product to better fit typical scales of marine animal trajectories in the SWIO[54–56], hence the final choice of SST MUR over the SST CCI analysis. The comparison between both MUR SST and SST CCI analysis is illustrated in Fig. 5 over the front-rich Mozambique Channel[27]. The larger thermal gradient magnitudes from SST CCI could be explained by the contextual median filtering step in the BOA[16]. We hope future ocean front datasets will be able to combine the advantage of both fine-grid resolution and climate-readiness without much compromise.

About dynamical fronts. NOMAD[51] provides a multidecadal record of backward-in-time FSLEs, which can be interpreted as dynamical fronts through region-specific thresholding (Fig. 1). In the past 20 years, FSLEs have been recognized by the ocean science community as a reliable way to identify Lagrangian coherent structures[32,34,57–59]. Indeed, FSLEs tend to be better-suited to transport barrier detection than other diagnostics such as the Okubo-Weiss parameter and finite-time Lyapunov exponents[33,59,60]. Additionally, FSLEs perform well in the presence of noise and unresolved scales[34]. Finally FSLEs pairs well with tracer-based front indicators, such as sea-surface temperature[37,61] and phytoplankton communities[8,42].

Choice of velocity data. The choice of suitable velocity products for the MedSea and the SWIO was motivated by their spatial and temporal resolutions but also the extent of the datasets. The velocity products chosen for the MedSea and SWIO are different because we opted to select the best available product for each domain. Globcurrent 1/4° total velocities[47] are optimal for the SWIO because of the integration of the Ekman component to the velocity field, its spatial and temporal resolutions and coverage. To the authors knowledge, there is no available operational product providing total velocities (geostrophic + Ekman components) for the MedSea. While the ageostrophic components of the circulation may become relevant in a few rare instances, such as during short-living storms in the Northwestern MedSea[62], geostrophic currents resolved well the main surface dynamics. We thus opted for the next best: 1/8° geostrophic velocities derived from a SSALTO/DUACS multimission altimeter regional L4 product[47] for the MedSea. Although both velocity datasets perform well at the mesoscale (typical horizontal scales of 100 km), it is worth noting that they are not climate-ready. The choice of a uniform global climate-ready alternative, such as DUACS geostrophy-only currents distributed by the Copernicus Climate Change Service (C3S) (https://data.marine.copernicus.eu, accessed on Feb 10th, 2023), would have been uniform between both domains but would also have resulted in the loss of the Ekman component in the SWIO and led to a spatial resolution downgrade from 1/8° to 1/4° in the MedSea. The comparison between FSLEs derived from Globcurrent total velocities[47] and FSLEs derived from geostrophy-only currents from the C3S[63] in the SWIO is illustrated in Fig. 6. The difference between FSLEs computed from total and geostrophy-only currents reveals small changes in their magnitude and overall pattern, but also show some variations in the positions of the LCS (in the approximate range of 0.5–1°or 50–100 km). These displacements are especially strong in front-rich regions such as the Mozambique Channel and South East of Madagascar. We thus chose to let go of uniformity and climate-readiness to ensure the best rendering of front structures with available

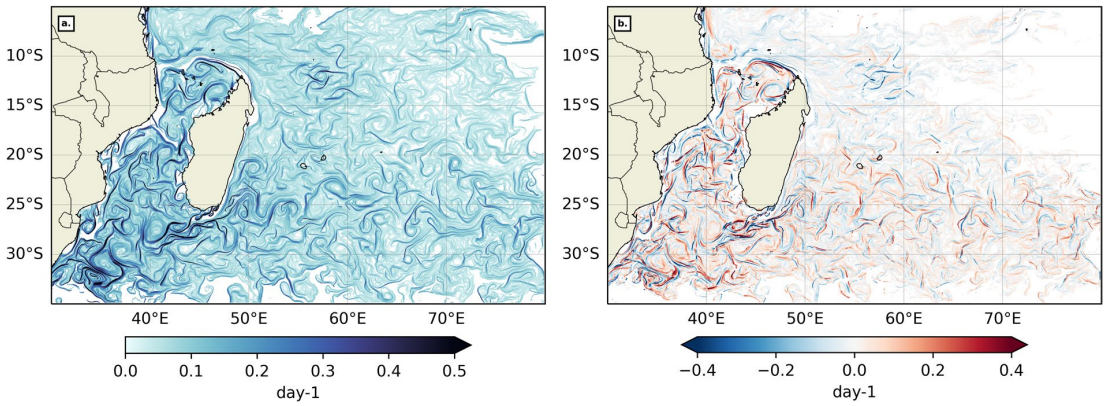

Fig. 6 (**a**) Snapshot of FSLEs computed from geostrophy-only currents from the Copernicus Climate Change Service and (**b**) its difference from FSLEs computed from total currents (shown in Fig. 2d), in the SWIO for July 1st, 2020. The colormaps are from cmocean[80].

altimetry products. Should climate-readiness be of interest to end-users, future front data products could use newer climate-ready products with our proposed methodology.

Added-value of spatial resolution. The NOMAD[51] dataset distinguishes itself from existing front databases by its higher spatial and temporal resolutions. A great advantage of FSLEs is that they are robust to small changes in the velocity field, and they also exhibit typical multifractal properties[34]. These properties ensure that FSLEs produced on a finer-grid than the original velocity grid are indeed meaningful and not artificial. They cannot resolve all the small scales processes, but they render well the dynamics driven by the coarser velocity field. We argue that spatial resolution is critical when investigating fronts-marine life interactions. To illustrate this statement, we compare NOMAD[51] backward FSLE dataset to the AVISO FSLE product[44] in the SWIO. The AVISO FSLE field is computed from 1/4° SSALTO/Duacs delayed-time global ocean absolute geostrophic currents (DUACS2018 DT MADT UV products) on a 4 km grid. The AVISO FSLE product[44] differs from NOMAD[51] FSLEs in several parameters including velocity field, spatial resolution, times of integration, δ_0 and δ_f. We have already contrasted the difference between total and geostrophy-only currents in FSLE computations in the previous paragraph. Additionally, we assume that the AVISO FSLE product time of integration, δ_0 and δ_f have been optimized for the flow field. We will thus only focus here on why we think the higher spatial resolution of the NOMAD[51] FSLE field is a significant added-value for biological use. We generated 1000 series of 100 to 200 points. Each point is separated from the next by a random direction and a distance of the order of 50–100 km, consistent with typical scales of marine animal presence/absence data (including sightings, GPS tracks, aerial survey, etc.), like those of whale sharks[54], sea turtles[55] or the great frigatebirds[56] in the SWIO. The next step is to collocate each series of points with both NOMAD and AVISO FSLE fields[44], taken on the same date. For each series the date was picked randomly in the year 2020 to avoid any bias brought on by seasonality. Figure 7 is an example snapshot of NOMAD[51] and AVISO[44] FSLE fields overlapped by a sample series of randomly-generated points in the South Mozambique Channel. Lastly, for each of the 1000 series, and relating to both finer NOMAD[51] FSLE (1.56 km resolution) and coarser AVISO[44] FSLE (4 km resolution) fields, we extracted 3 metrics:

- the mean FSLE value located under each randomly-generated point,
- the percentage of points collocated with FSLE front pixels (defined by subregional thresholds as in Table 2),
- and the mean distance between each point and its nearest FSLE front (defined by subregional thresholds as in Table 2)

We thus obtain, for each series of randomly-generated points, a difference (between NOMAD[51] and AVISO[44] FSLE) for each metrics described above. These analyses were performed for both the EAFR and ISSG Longhurst subregions[48,49] (Fig. 3) to illustrate the region-specific sensitivity to spatial resolution. The mean difference in FSLE values located under each randomly-generated point in the EAFR (resp. ISSG) subregion is of the order of 0.028 day^{-1} (resp. 0.016 day^{-1}), and reaching up to 0.202 day^{-1} (resp. 0.096 day^{-1}) (Fig. 8). The difference in collocation percentage is on average 8.03% in the EAFR and 6.5% in the ISSG subregions (Fig. 8), and going up to 35.55% and 24.04% respectively. Finally, the mean difference in distance to nearest front is smaller in EAFR at 4.3 km compared to 16.3 km in ISSG, likely due to the higher concentration of fronts in the Mozambique Channel[27]. Overall, the mean and maximum differences between fine and coarse FSLEs for those three metrics are non-negligible, especially in front-rich regions such as the Mozambique Channel and southeast of Madagascar, which will then reflect into any statistical comparison between biological observations and front occurrence. NOMAD's[51] finer spatial resolution is thus a significant added-value for high-resolution tracking of marine life-front interactions.

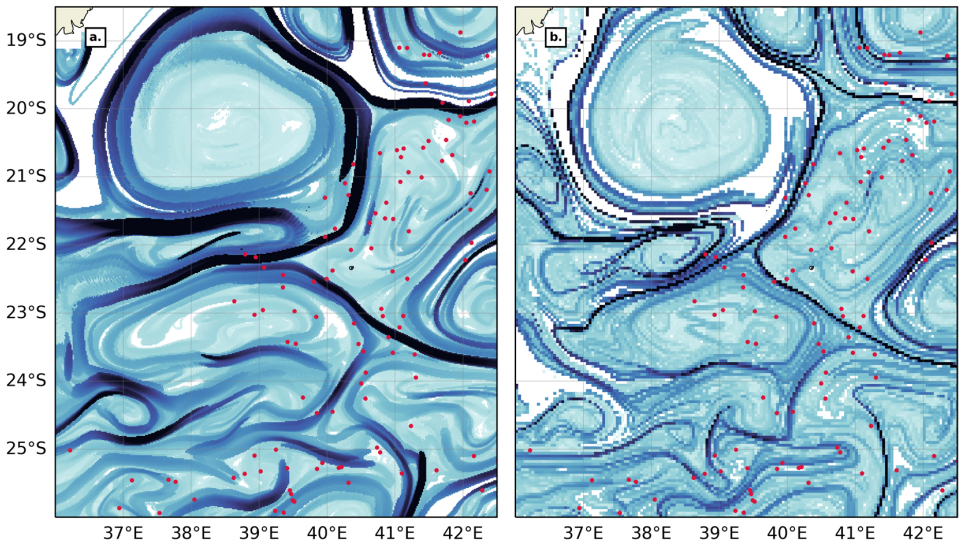

Fig. 7 Example of the collocation between randomly-generated points (in red) and FSLE fields for (**a**) NOMAD[51] backward FSLEs on a 1.5 km grid and for (**b**) AVISO backward near-real-time FSLEs[44] on a 4 km grid, for Jan 15th, 2020. The colormap is from cmocean[80] and with the same range as in Fig. 2.

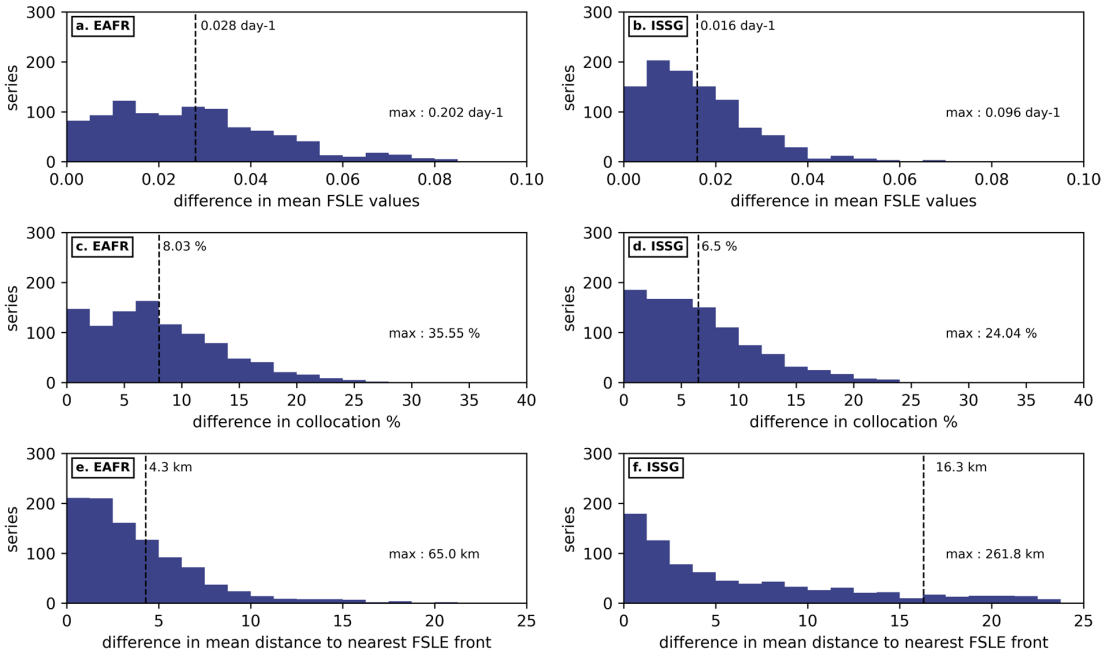

Fig. 8 Distributions of the differences in mean FSLE values (**a, b**), collocation percentage (**c, d**) and distance to nearest front (**e, f**) between NOMAD[51] and AVISO[44] FSLE front fields for 1000 series of 100–200 randomly-generated points. We chose 2 Longhurst[48,49] subregions to illustrate the region-specific sensitivity to spatial resolution: EAFR (**b**), ISSG (**c**). The vertical dotted lines mark the mean difference for all 1000 trajectories, weighted on the number of points per trajectory.

Finally, the backward FSLEs described in this paper were previously studied to analyze transport processes in the MedSea and were validated with trajectories of real drifters, as shown in Figs. 2b, 3. of Hernández-Carrasco and Orfila's work[64]. Similar validation has been performed in the SWIO and is available upon request.

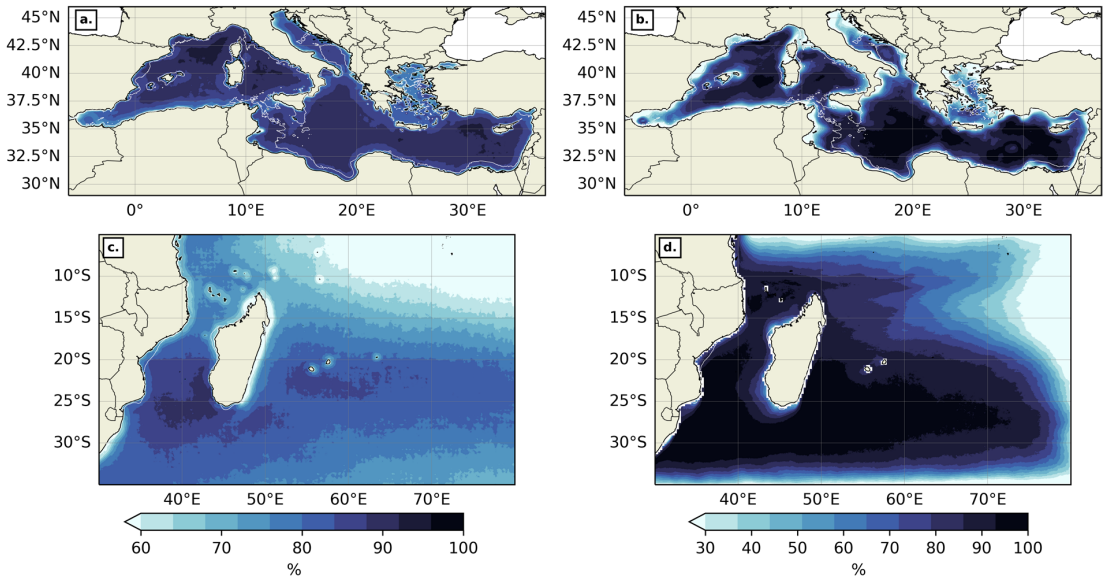

Fig. 9 Frequency of suitable days for thermal gradients (**a, c**) and FSLEs (**b, d**) in the MedSea (**a, b**) and the SWIO (**c, d**). The background white contour shows the 200 m isobath. The colormap is from cmocean[80].

Numerical diagnostics. *Suitable day frequency.* For each position in space (x, y) the frequency of "suitable" days (FSD) has been computed as follow:

$$\mathrm{FSD(x,\,y)} = \frac{\mathrm{NSD(x,\,y)}}{\mathrm{TND}} * 100.$$

Where NSD (x,y) is the number of "suitable" days at (x, y), i.e. when the flag is equal to 0, and TND is the total number of days in the whole dataset. The FSD for thermal gradients reveals which regions are more prone to cloudiness between 2003 and 2020 (Fig. 9a,c). In the MedSea, most of the open ocean presents a FSD above 85% thanks to the dominant clear sky typical of Mediterranean climate. The Mediterranean regions most covered by clouds are the western Alboran Sea, the northern Aegean Sea and more generally coastal areas. In the SWIO, most of the open ocean in the Mozambique Channel and east of Madagascar has a FSD above 80%. Continental shelves, Islands (the Comoros archipelago, Mayotte, La Réunion and Mauricius islands) and northeast of the South Equatorial Current are marked by a reduced FSD, but rarely fall below 50%. The FSD for the backward FSLE dataset reveals regions most accessible to advected ocean particles between 1994 and 2020 (Fig. 9b,d). In the MedSea, the FSD is lowest on continental shelves and western Alboran Sea but above 90% for most of the open ocean. In the SWIO, the FSD is above 90% in the Mozambique Channel and most of the western Indian Ocean. Lesser FSD can be found along the path of the South Equatorial Current, along the west Madagascar continental shelves and more generally at the border of the geographical domain. Overall both datasets and both geographical domains present a very good ratio of suitable pixel for front analysis.

Mean fields. Time average maps have been produced for both thermal gradients (Fig. 10a,c) and backward FSLE fields (Fig. 10b,d) in both geographical domains over their respective time period (2003–2020 for thermal gradients and 1994–2020 for backward FSLEs). Only the "suitable" pixels were counted when time-averaging. In the MedSea, thermal gradients are stronger on average along continental shelves and highlight specific regional features, such as the quasi-permanent eddies of the Alboran Sea, the Almeria-Oran front[65], the Cartagena-Tenes Front[64], and the Liguro-Catalan current. Time-averaged backward FSLE values are higher in the Alboran Sea, South of Sardinia, along the Liguro-Catalan current and in the Levantine Sea. In the SWIO, mean thermal gradients are most intense on continental shelves as well, but also in the wake of both Northeast and Southeast Madagascar currents (NEMC and SEMC) and more generally south of 25°S. These results were also shown from a 1/36° resolution realistic CROCO simulation of the Mozambique Channel[27] and from Level 3 National Oceanic and Atmospheric Administration (NOAA) Advanced Very High Resolution Radiometer (AVHRR) SST data[11]. Time-averaged backward FSLE values are also stronger in the path of the NEMC and SEMC, but also at the side edges of the eddy train that characterizes the Mozambique Channel circulation[66,67], and towards the Agulhas current[68]. These results are consistent with previous works on time-averaged thermal gradients[58] and FSLEs in the MedSea[32,69], but also in the SWIO[11,27], thus validating our dataset for large time scales.

Front frequency. Another helpful metric to assess our dataset is the front frequency (FF), i.e. frequency of front days (amongst suitable days only) at a position (x, y), computed as follow:

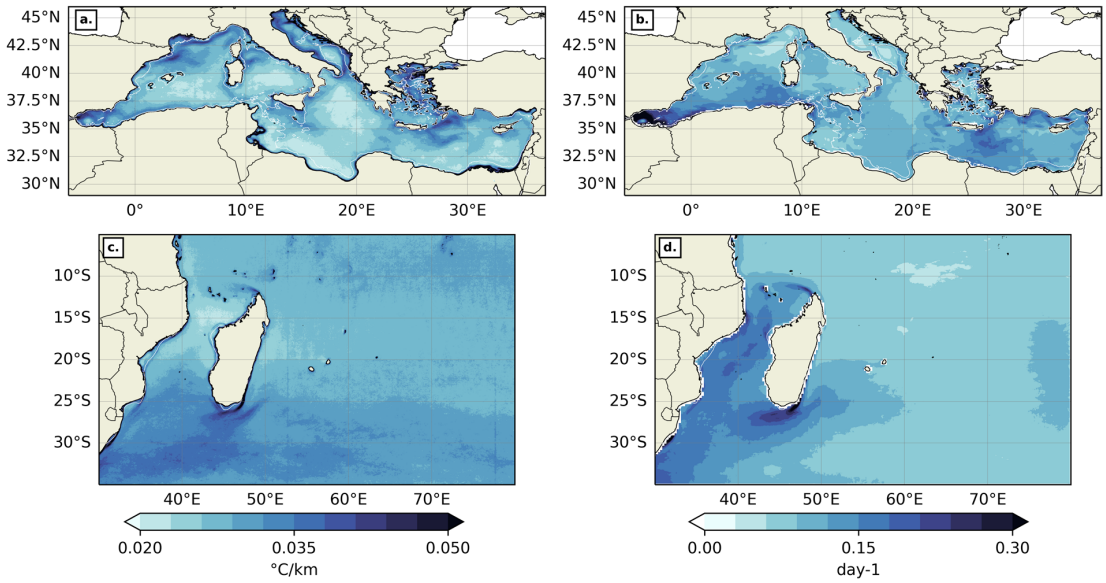

Fig. 10 Time average for thermal gradients (**a, c**) and FSLEs (**b, d**) in the MedSea (**a, b**) and the SWIO (**c, d**). The background white contour shows the 200 m isobath. The colormap is from cmocean[80].

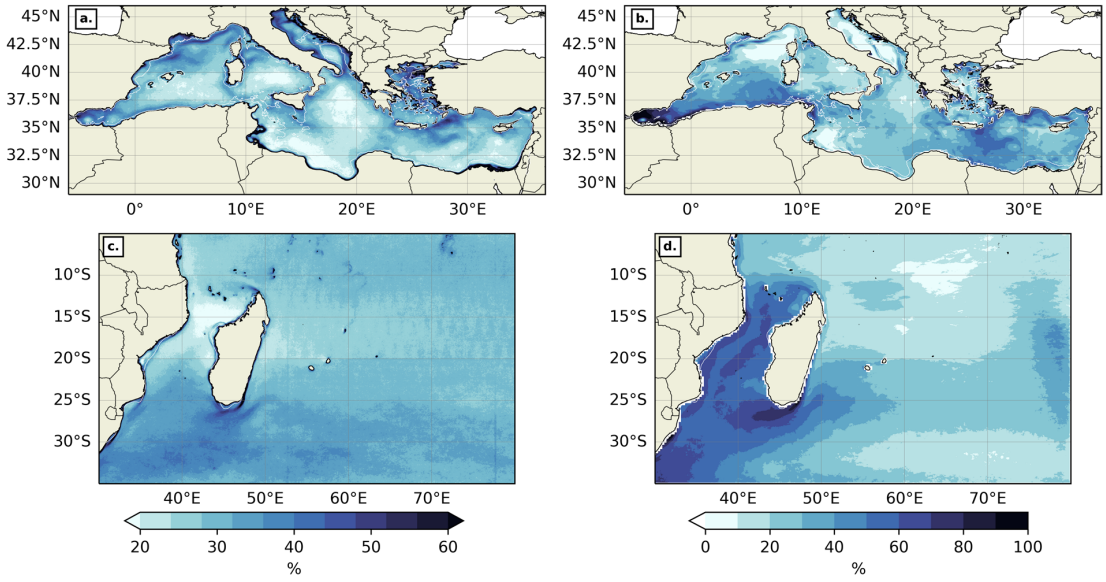

Fig. 11 Front frequency for thermal gradients (**a, c**) and FSLEs (**b, d**) in the MedSea (**a, b**) and the SWIO (**c, d**). The background white contour shows the 200 m isobath. The colormap is from cmocean[80].

$$FF(x, y) = \frac{SNFD(x, y)}{TNSD(x, y)} * 100.$$

Where SNFD (x, y) is the number of front days (amongst "suitable" days only) at (x, y), and TNSD (x, y) is the total number of "suitable" days at the same position. "Front days" correspond to days when thermal gradient of FSLE values at (x, y) are above a pre-determined 70th percentile threshold. We chose to take whole region thresholds for both geographic domains. In the MedSea (resp. SWIO), the thermal gradient threshold was taken at 0.033 °C/km (resp. 0.035 °C/km), and the backward FSLE threshold at 0.123 day^{-1} (resp. 0.105 day^{-1}). In both the MedSea and the SWIO, the spatial patterns of thermal (Fig. 11a,c) and FSLE-derived (Fig. 11b,d) front frequencies tend to overlap with the mean intensity maps of the same variables (Fig. 10). These results are consistent with the works of

Nieblas *et al.*[11] which used a different front detection method and a different SST product, and Sudre *et al.* when applying the BOA to numerically simulated temperature at different depths in the Mozambique Channel[27].

About MUR SST analysis artefacts. Some artefacts are visible on thermal gradient mean and frequency figures (Figs. 9a,c, 10a,c, 11a,c). They are most visible in the SWIO, but can also be found in the MedSea. These criss-cross and square-like patterns are characteristics of satellite fingerprints and enhanced by MUR MRVA interpolations[46]. Similar satellite-SST-derived artefacts are also seen in Nieblas *et al.* Figure 8.D[11]. And indeed, the artefacts do not appear when the BOA[16] is applied on numerical simulations instead of remotely-sensed SST[27]. More importantly, they are not visible in NOMAD[51] thermal gradient snapshots (Fig. 2a,c) and therefore will not affect front-marine life interaction analysis. To conclude, since the artefacts are only produced after aggregating thermal gradients on long time-scales, the authors are confident they should not alter the reliability of the NOMAD[51] thermal gradient product for biological use.

Usage Notes

The oceaN frOnt for the Mediterranean seA and southwest inDian ocean dataset (NOMAD[51]) is a multi-decadal record of thermal gradients and backward FSLEs in the Southwest Indian Ocean and the Mediterranean Sea. The NOMAD[51] distinguishes itself from existing alternatives[23,44] by its higher temporal and spatial resolution and extent. NOMAD[51] is suitable for a broad variety of applications where the detection of thermal fronts and attracting Lagrangian coherent structures in the MedSea and the SWIO is needed. These include the identification of spatial and temporal dynamics of thermal and dynamic fronts, along with multidecadal variability analyses. Additionally, the release of our front dataset makes the investigation of the relationship between fronts and marine life possible thanks to a high temporal and spatial resolution.

The provided dataset is divided into 4 folders as described in Table 1. Each folder contains yearly subfolders with daily netcdf files. The netcdf files can be read as is, as they directly provide direct thermal gradient or backward-in-time FSLE fields. We suggest to use Python language software with xarray and dask packages, which are best suited to handle large datasets and High Power Computing. NOMAD[51] will be updated on a yearly basis.

NOMAD visualization. The authors suggest using the quality flag provided in each dataset to select "suitable" pixels (i.e. flag = 0) before further front analysis. Then front detection is a simple thresholding of the field of interest as illustrated in Fig. 1. Subregion-specific thresholds are added as attributes of each netcdf file, but custom thresholding is also possible. Python xarray package makes filtering and thresholding of the data very intuitive with the function xarray.where. An example Jupyter Notebook for visualization of NOMAD[51] data and the reproduction of Fig. 2 is available on Github: https://github.com/FlorianeSudre/NOMAD_notebooks/.

Front collocation with biological data. NOMAD[51] is primarily designed to study front-marine life interactions. To this end, the authors recommend using both thermal gradients and FSLE fields, and to interpolate them on the same grid, whose temporal and spatial scale is congruent with the behavior of the specie of interest. Temporal degradation of the dataset is easily performed by xarray.Dataset.resample while spatial regridding can be done with tools such as the Climate Data Operator (CDO) or with the Python package xgcm used in tandem with xarray). The authors recommend comparing quantitatively and qualitatively BOA outputs solely between same-grid products. For example, one can compare thermal gradient magnitudes and patterns within the entire NOMAD[51] thermal gradient dataset, as the SST field comes from a single product. However, while qualitative comparison (i.e. spatial patterns) is possible among thermal gradients originating from different SST fields, a quantitative comparison would require to determine a suitable threshold for each product since BOA algorithm is sensitive to the grid resolution of the input data. Attention should also be brought to the fact that thermal gradients and FSLEs do not have NaNs (where the pixel is deemed "unsuitable", i.e. where the quality flag is not equal to 0) at the same time and place. NaNs appear in FSLE fields near domain boundaries and in coastal areas, while NaNs in thermal gradient fields depend on cloud cover (Fig. 9). The difference in NaN coverage in both dataset should be taken into account when pairing with biological data to avoid any additional bias due to suitable day frequency.

Other possible uses for NOMAD. Beside the study of front-marine life interactions[10], investigating trophic relationships[70] and the accumulation of fish larvae[71], NOMAD[51] could also be employed to monitor marine pollutants such as microplastics[72,73] and oil spills[74] along fronts. One could also examine relationships between surface thermal fronts and low-level winds at submesoscales from Radar Scatterometer data; as it has only been done at mesoscales so far[75–77]. Finally, following the recent work of Roman-Stork *et al.*[78], it would be interesting to explore new blended metrics based on both SST fronts and FSLEs and their co-variability with key biogeochemical elements (such as Chl-a, pH, nitrates, phosphates) to inform on where oceanic fronts are more likely to impact nutrient cycling in the upper and interior ocean[79].

Code availability

The code we used to produce thermal gradients with the BOA is available in R on Github thanks to Benjamin Galuardi (available on https://github.com/galuardi/boaR, accessed on May 19th, 2022). The code to produce the backward FSLEs belongs to Ismael Hernández-Carrasco, was extensively described in Hernández-Carrasco *et al.*[34], and is available upon request. An example jupyter notebook for front visualization is available on a github repository (https://github.com/FlorianeSudre/NOMAD_notebooks).

Received: 12 July 2023; Accepted: 3 October 2023;
Published online: 21 October 2023

References

1. Mahadevan, A. & Archer, D. Modeling the impact of fronts and mesoscale circulation on the nutrient supply and biogeochemistry of the upper ocean. *Journal of Geophysical Research* **105**, 1209–1225, https://doi.org/10.1029/1999jc900216 (2000).
2. Taylor, J. R. & Ferrari, R. Ocean fronts trigger high latitude phytoplankton blooms. *Geophysical Research Letters* **38**, https://doi.org/10.1029/2011gl049312 (2011).
3. Lévy, M., Ferrari, R., Franks, P. J. S., Martin, A. P. & Rivière, P. Bringing physics to life at the submesoscale. *Geophysical Research Letters* **39**, https://doi.org/10.1029/2012gl052756 (2012).
4. Bakun, A. Fronts and eddies as key structures in the habitat of marine fish larvae: opportunity, adaptive response and competitive advantage. *Scientia marina* **70**, 105–122, https://doi.org/10.3989/scimar.2006.70s2105 (2006).
5. Lévy, M., Franks, P. J. S. & Smith, K. S. The role of submesoscale currents in structuring marine ecosystems. *Nature Communications* **9**, 4758, https://doi.org/10.1038/s41467-018-07059-3 (2018).
6. Chapman, C. C., Lea, M.-A., Meyer, A., Sallée, J.-B. & Hindell, M. Defining southern ocean fronts and their influence on biological and physical processes in a changing climate. *Nature Climate Change* **10**, 209–219, https://doi.org/10.1038/s41558-020-0705-4 (2020).
7. Lehahn, Y., d'Ovidio, F., Lévy, M. & Heifetz, E. Stirring of the northeast atlantic spring bloom: A lagrangian analysis based on multisatellite data. *Journal of Geophysical Research* **112**, https://doi.org/10.1029/2006jc003927 (2007).
8. Tzortzis, R. *et al*. Impact of moderately energetic fine-scale dynamics on the phytoplankton community structure in the western mediterranean sea. *Biogeosciences* **18**, 6455–6477, https://doi.org/10.5194/bg-18-6455-2021 (2021).
9. Weimerskirch, H., Le Corre, M., Jaquemet, S., Potier, M. & Marsac, F. Foraging strategy of a top predator in tropical waters: great frigatebirds in the mozambique channel. *Marine Ecology Progress Series* **275**, 297–308, https://doi.org/10.3354/meps275297 (2004).
10. Tew Kai, E. *et al*. Top marine predators track lagrangian coherent structures. *Proceedings of the National Academy of Sciences of the United States of America* **106**, 8245–8250, https://doi.org/10.1073/pnas.0811034106 (2009).
11. Nieblas, A.-E., Demarcq, H., Drushka, K., Sloyan, B. & Bonhommeau, S. Front variability and surface ocean features of the presumed southern bluefin tuna spawning grounds in the tropical southeast indian ocean. *Deep-sea Research. Part II, Topical Studies in Oceanography* **107**, 64–76, https://doi.org/10.1016/j.dsr2.2013.11.007 (2014).
12. Nieto, K., Xu, Y., Teo, S. L. H., McClatchie, S. & Holmes, J. How important are coastal fronts to albacore tuna (thunnus alalunga) habitat in the northeast pacific ocean. *Progress in Oceanography* **150**, 62–71, https://doi.org/10.1016/j.pocean.2015.05.004 (2017).
13. Scales, K. L. *et al*. Mesoscale fronts as foraging habitats: composite front mapping reveals oceanographic drivers of habitat use for a pelagic seabird. *Journal of the Royal Society, Interface* **11**, 20140679, https://doi.org/10.1098/rsif.2014.0679 (2014).
14. Siegelman, L. *et al*. Enhanced upward heat transport at deep submesoscale ocean fronts. *Nature Geoscience* **13**, 50–55, https://doi.org/10.1038/s41561-019-0489-1 (2020).
15. Canny, J. A computational approach to edge detection. *IEEE transactions on pattern analysis and machine intelligence* **8**, 679–698 (1986).
16. Belkin, I. M. & O'Reilly, J. E. An algorithm for oceanic front detection in chlorophyll and sst satellite imagery. *Journal of marine systems: journal of the European Association of Marine Sciences and Techniques* **78**, 319–326, https://doi.org/10.1016/j.jmarsys.2008.11.018 (2009).
17. Cayula, J.-F. & Cornillon, P. Multi-image edge detection for sst images. *Journal of Atmospheric and Oceanic Technology* **12**, 821–829, 10.1175/1520-0426(1995)012<0821:miedfs>2.0.co;2 (1995).
18. Nieto, K., Demarcq, H. & McClatchie, S. Mesoscale frontal structures in the canary upwelling system: New front and filament detection algorithms applied to spatial and temporal patterns. *Remote Sensing of Environment* **123**, 339–346, https://doi.org/10.1016/j.rse.2012.03.028 (2012).
19. Shimada, T., Sakaida, F., Kawamura, H. & Okumura, T. Application of an edge detection method to satellite images for distinguishing sea surface temperature fronts near the japanese coast. *Remote Sensing of Environment* **98**, 21–34, https://doi.org/10.1016/j.rse.2005.05.018 (2005).
20. Torres Arriaza, J. A., Guindos Rojas, F., Peralta Lopez, M. & Canton, M. Competitive neural-net-based system for the automatic detection of oceanic mesoscalar structures on avhrr scenes. *IEEE transactions on geoscience and remote sensing: a publication of the IEEE Geoscience and Remote Sensing Society* **41**, 845–852, https://doi.org/10.1109/tgrs.2003.809929 (2003).
21. Turiel, A., Solé, J., Nieves, V., Ballabrera-Poy, J. & García-Ladona, E. Tracking oceanic currents by singularity analysis of microwave sea surface temperature images. *Remote Sensing of Environment* **112**, 2246–2260, https://doi.org/10.1016/j.rse.2007.10.007 (2008).
22. Tamim, A. *et al*. Detection of moroccan coastal upwelling fronts in sst images using the microcanonical multiscale formalism. *Pattern Recognition Letters* **55**, 28–33, https://doi.org/10.1016/j.patrec.2014.12.006 (2015).
23. Belkin, I. M., Cornillon, P. C. & Sherman, K. Fronts in large marine ecosystems. *Progress in Oceanography* **81**, 223–236, https://doi.org/10.1016/j.pocean.2009.04.015 (2009).
24. Belkin, I. M. Remote sensing of ocean fronts in marine ecology and fisheries. *Remote sensing* **13**, 883, https://doi.org/10.3390/rs13050883 (2021).
25. Park, S. & Chu, P. C. Thermal and haline fronts in the yellow/east china seas: Surface and subsurface seasonality comparison. *Journal of Oceanography* **62**, 617–638, https://doi.org/10.1007/s10872-006-0081-3 (2006).
26. McWilliams, J. C. Oceanic frontogenesis. *Annual Review of Marine Science* **13**, 227–253, https://doi.org/10.1146/annurev-marine-032320-120725 (2021).
27. Sudre, F. *et al*. Spatial and seasonal variability of horizontal temperature fronts in the mozambique channel for both epipelagic and mesopelagic realms. *Frontiers in Marine Science* **9**, https://doi.org/10.3389/fmars.2022.1045136 (2023).
28. Wang, D., Liu, Y., Qi, Y. & Shi, P. Seasonal variability of thermal fronts in the northern south china sea from satellite data. *Geophysical Research Letters* **28**, 3963–3966, https://doi.org/10.1029/2001gl013306 (2001).
29. Lin, L., Liu, D., Luo, C. & Xie, L. Double fronts in the yellow sea in summertime identified using sea surface temperature data of multi-scale ultra-high resolution analysis. *Continental Shelf Research* **175**, 76–86, https://doi.org/10.1016/j.csr.2019.02.004 (2019).
30. Liu, D., Wang, Y., Wang, Y. & Keesing, J. K. Ocean fronts construct spatial zonation in microfossil assemblages. *Global Ecology and Biogeography: a Journal of Macroecology* **27**, 1225–1237, https://doi.org/10.1111/geb.12779 (2018).
31. Aurell, E., Boffetta, G., Crisanti, A., Paladin, G. & Vulpiani, A. Predictability in the large: an extension of the concept of lyapunov exponent. *Journal of physics A: Mathematical and general* **30**, 1–26, https://doi.org/10.1088/0305-4470/30/1/003 (1997).
32. d'Ovidio, F., Fernández, V., Hernández-García, E. & López, C. Mixing structures in the mediterranean sea from finite-size lyapunov exponents. *Geophysical Research Letters* **31**, https://doi.org/10.1029/2004gl020328 (2004).
33. Hernández-Carrasco, I., López, C., Hernández-García, E. & Turiel, A. Seasonal and regional characterization of horizontal stirring in the global ocean. *Journal of Geophysical Research* **117**, https://doi.org/10.1029/2012jc008222 (2012).
34. Hernández-Carrasco, I., López, C., Hernández-García, E. & Turiel, A. How reliable are finite-size lyapunov exponents for the assessment of ocean dynamics. *Ocean Modelling* **36**, 208–218, https://doi.org/10.1016/j.ocemod.2010.12.006 (2011).
35. Bettencourt, J. H., López, C. & Hernández-García, E. Oceanic three-dimensional lagrangian coherent structures: A study of a mesoscale eddy in the benguela upwelling region. *Ocean Modelling* **51**, 73–83, https://doi.org/10.1016/j.ocemod.2012.04.004 (2012).
36. d'Ovidio, F., Isern-Fontanet, J., López, C., Hernández-García, E. & García-Ladona, E. Comparison between eulerian diagnostics and finite-size lyapunov exponents computed from altimetry in the algerian basin. *Deep-sea Research. Part I, Oceanographic Research Papers* **56**, 15–31, https://doi.org/10.1016/j.dsr.2008.07.014 (2009).

37. Bettencourt, J. H., Rossi, V., Hernández-García, E., Marta-Almeida, M. & López, C. Characterization of the structure and cross-shore transport properties of a coastal upwelling filament using three-dimensional finite-size lyapunov exponents. *Journal of Geophysical Research. Oceans* **122**, 7433–7448, https://doi.org/10.1002/2017jc012700 (2017).
38. Hernández-Carrasco, I., Orfila, A. & Rossi, V. & Garçon, V. Effect of small scale transport processes on phytoplankton distribution in coastal seas. *Scientific Reports* **8**, 8613, https://doi.org/10.1038/s41598-018-26857-9 (2018).
39. Mathur, M., David, M. J., Sharma, R. & Agarwal, N. Thermal fronts and attracting lagrangian coherent structures in the north bay of bengal during december 2015–march 2016. *Deep-sea Research. Part II, Topical Studies in Oceanography* **168**, 104636, https://doi.org/10.1016/j.dsr2.2019.104636 (2019).
40. Scales, K. L. *et al*. Fisheries bycatch risk to marine megafauna is intensified in lagrangian coherent structures. *Proceedings of the National Academy of Sciences of the United States of America* **115**, 7362–7367, https://doi.org/10.1073/pnas.1801270115 (2018).
41. Abrahms, B. *et al*. Mesoscale activity facilitates energy gain in a top predator. *Proceedings. Biological sciences* **285**, 20181101, https://doi.org/10.1098/rspb.2018.1101 (2018).
42. Hernández-Carrasco, I. *et al*. Lagrangian flow effects on phytoplankton abundance and composition along filament-like structures. *Progress in Oceanography* **189**, 102469, https://doi.org/10.1016/j.pocean.2020.102469 (2020).
43. Sherman, K. *The large marine ecosystem approach for assessment and management of ocean coastal waters*, 3–16 (Elsevier, 2005).
44. LOCEAN/CLS/CTOH/CNES. Fsle - finite-size lyapunov exponents and orientations of the associated eigenvectors, https://doi.org/10.24400/527896/A01-2022.002 (2021).
45. Bates, A. E. *et al*. Biologists ignore ocean weather at their peril. *Nature* **560**, 299–301, https://doi.org/10.1038/d41586-018-05869-5 (2018).
46. Chin, T. M., Vazquez-Cuervo, J. & Armstrong, E. M. A multi-scale high-resolution analysis of global sea surface temperature. *Remote Sensing of Environment* **200**, 154–169, https://doi.org/10.1016/j.rse.2017.07.029 (2017).
47. Rio, M.-H., Mulet, S. & Picot, N. Beyond goce for the ocean circulation estimate: Synergetic use of altimetry, gravimetry, and *in situ* data provides new insight into geostrophic and ekman currents: Ocean circulation beyond goce. *Geophysical Research Letters* **41**, 8918–8925, https://doi.org/10.1002/2014gl061773 (2014).
48. Longhurst, A. Seasonal cycles of pelagic production and consumption. *Progress in oceanography* **36**, 77–167, https://doi.org/10.1016/0079-6611(95)00015-1 (1995).
49. Longhurst, A. *Ecological geography of the sea*, 2 edn (Academic Press, 2007).
50. Spalding, M. D. *et al*. Marine ecoregions of the world: A bioregionalization of coastal and shelf areas. *BioScience* **57**, 573–583, https://doi.org/10.1641/b570707 (2007).
51. Sudre, F. *et al*. Nomad: the ocean front dataset for the mediterranean sea and southwest indian ocean. *Sextant* https://doi.org/10.12770/3ea321a1-d9d4-49e5-a592-605b80dec240 (2023).
52. Dodge, K. L., Galuardi, B., Miller, T. J. & Lutcavage, M. E. Leatherback turtle movements, dive behavior, and habitat characteristics in ecoregions of the northwest atlantic ocean. *PloS one* **9**, e91726, https://doi.org/10.1371/journal.pone.0091726 (2014).
53. Merchant, C. J. *et al*. Satellite-based time-series of sea-surface temperature since 1981 for climate applications. *Nature Scientific Data* **6**, 223, https://doi.org/10.1038/s41597-019-0236-x (2019).
54. Rohner, C. A. *et al*. Satellite tagging highlights the importance of productive mozambican coastal waters to the ecology and conservation of whale sharks. *PeerJ* **6**, e4161, https://doi.org/10.7717/peerj.4161 (2018).
55. Luschi, P. *et al*. Marine turtles use geomagnetic cues during open-sea homing. *Current Biology* **17**, 126–133, https://doi.org/10.1016/j.cub.2006.11.062 (2007).
56. Weimerskirch, H., Corre, M. L., Kai, E. T. & Marsac, F. Foraging movements of great frigatebirds from aldabra island: Relationship with environmental variables and interactions with fisheries. *Progress in Oceanography* **86**, 204–213, https://doi.org/10.1016/j.pocean.2010.04.003 (2010).
57. Artale, V., Boffetta, G., Celani, A., Cencini, M. & Vulpiani, A. Dispersion of passive tracers in closed basins: Beyond the diffusion coefficient. *Physics of fluids (Woodbury, N.Y.: 1994)* **9**, 3162–3171, https://doi.org/10.1063/1.869433 (1997).
58. Nieblas, A.-E. *et al*. Defining mediterranean and black sea biogeochemical subprovinces and synthetic ocean indicators using mesoscale oceanographic features. *PloS one* **9**, e111251, https://doi.org/10.1371/journal.pone.0111251 (2014).
59. Haller, G. Lagrangian coherent structures. *Annual Review of Fluid Mechanics* **47**, 137–162, https://doi.org/10.1146/annurev-fluid-010313-141322 (2015).
60. Boffetta, G., Lacorata, G., Redaelli, G. & Vulpiani, A. Detecting barriers to transport: a review of different techniques. *Physica D. Nonlinear Phenomena* **159**, 58–70, https://doi.org/10.1016/s0167-2789(01)00330-x (2001).
61. Rousselet, L. *et al*. Large- to submesoscale surface circulation and its implications on biogeochemical/biological horizontal distributions during the outpace cruise (southwest pacific. *Biogeosciences* **15**, 2411–2431, https://doi.org/10.5194/bg-15-2411-2018 (2018).
62. Morales-Márquez, V., Hernández-Carrasco, I., Simarro, G., Rossi, V. & Orfila, A. Regionalizing the impacts of wind- and wave-induced currents on surface ocean dynamics: A long-term variability analysis in the mediterranean sea. *Journal of Geophysical Research. Oceans* **126**, https://doi.org/10.1029/2020jc017104 (2021).
63. Global ocean gridded l4 sea surface heights and derived variables reprocessed. copernicus climate change service (c3s). [dataset], https://doi.org/10.48670/MOI-00145 (2023).
64. Hernández-Carrasco, I. & Orfila, A. The role of an intense front on the connectivity of the western mediterranean sea: The cartagena-tenes front. *Journal of Geophysical Research. Oceans* **123**, 4398–4422, https://doi.org/10.1029/2017jc013613 (2018).
65. Tintore, J., La Violette, P. E., Blade, I. & Cruzado, A. A study of an intense density front in the eastern alboran sea: The almeria–oran front. *Journal of Physical Oceanography* **18**, 1384–1397, 10.1175/1520-0485(1988)018<1384:asoaid>2.0.co;2 (1988).
66. de Ruijter, W. P. M., Ridderinkhof, H., Lutjeharms, J. R. E., Schouten, M. W. & Veth, C. Observations of the flow in the mozambique channel. *Geophysical Research Letters* **29**, 140–1–140–3, https://doi.org/10.1029/2001gl013714 (2002).
67. Halo, I. *et al*. Eddy properties in the mozambique channel: A comparison between observations and two numerical ocean circulation models. *Deep-sea Research. Part II, Topical Studies in Oceanography* **100**, 38–53, https://doi.org/10.1016/j.dsr2.2013.10.015 (2014).
68. Lutjeharms, J. R. E. Three decades of research on the greater agulhas current. *Ocean Sci. Discuss.* **3**, 939–995, https://doi.org/10.5194/osd-3-939-2006 (2006).
69. García-Olivares, A., Isern-Fontanet, J. & García-Ladona, E. Dispersion of passive tracers and finite-scale lyapunov exponents in the western mediterranean sea. *Deep-sea Research. Part I, Oceanographic Research Papers* **54**, 253–268, https://doi.org/10.1016/j.dsr.2006.10.009 (2007).
70. Mangolte, I., Lévy, M., Haëck, C. & Ohman, M. D. Sub-frontal niches of plankton communities driven by transport and trophic interactions at ocean fronts. *Biogeosciences* **20**, 3273–3299, https://doi.org/10.5194/bg-20-3273-2023 (2023).
71. Harrison, C. S., Siegel, D. A. & Mitarai, S. Filamentation and eddy eddy interactions in marine larval accumulation and transport. *Marine ecology progress series* **472**, 27–44, https://doi.org/10.3354/meps10061 (2013).
72. Suaria, G. *et al*. *Dynamics of transport, accumulation, and export of plastics at oceanic fronts*, 1–51 (Springer Berlin Heidelberg, Berlin, Heidelberg, 2021).
73. Pattiaratchi, C. *et al*. Plastics in the indian ocean – sources, transport, distribution, and impacts. *Ocean science* **18**, 1–28, https://doi.org/10.5194/os-18-1-2022 (2022).
74. Fifani, G. *et al*. Drifting speed of lagrangian fronts and oil spill dispersal at the ocean surface. *Remote sensing* **13**, 4499, https://doi.org/10.3390/rs13224499 (2021).

75. O'Neill, L. W., Chelton, D. B. & Esbensen, S. K. Covariability of surface wind and stress responses to sea surface temperature fronts. *Journal of climate* **25**, 5916–5942, https://doi.org/10.1175/jcli-d-11-00230.1 (2012).
76. Renault, L., McWilliams, J. C. & Masson, S. Satellite observations of imprint of oceanic current on wind stress by air-sea coupling. *Scientific reports* **7**, https://doi.org/10.1038/s41598-017-17939-1 (2017).
77. Seo, H. *et al*. Ocean mesoscale and frontal-scale ocean–atmosphere interactions and influence on large-scale climate: A review. *Journal of climate* **36**, 1981–2013, https://doi.org/10.1175/jcli-d-21-0982.1 (2023).
78. Roman-Stork, H. L., Byrne, D. A. & Leuliette, E. W. Mesi: A multiparameter eddy significance index. *Earth and space science (Hoboken, N.J.)* **10**, https://doi.org/10.1029/2022ea002583 (2023).
79. McKee, D. C. *et al*. Biophysical dynamics at ocean fronts revealed by bio-argo floats. *Journal of geophysical research. Oceans* **128**, https://doi.org/10.1029/2022jc019226 (2023).
80. Thyng, K., Greene, C., Hetland, R., Zimmerle, H. & DiMarco, S. True colors of oceanography: Guidelines for effective and accurate colormap selection. *Oceanography* **29**, 9–13, https://doi.org/10.5670/oceanog.2016.66 (2016).

Acknowledgements

This work was supported by the Mediterranean Institute of Oceanography (MIO) and the French National Institute for Sustainable Development (IRD). The authors wish to thank J. Lecubin, C. Yohia and C. Quentin for general technical assistance as well as J. Meillon, C. Pertuisot and M. Dequidt from Ifremer for setting up the online data repository. The authors acknowledge funding from the "Ocean Front Change" project, funded by the Belmont Forum and implemented through the French National Research Agency (ANR-20-BFOC-0006-04). The project leading to this publication has received funding from European FEDER Fund (1166-39417) and from Excellence Initiative of AMU - A*MIDEX ("Investissements d'Avenir"). BD acknowledges support from ANID (Concurso de Fortalecimiento al Desarrollo Cientifico de Centros Regionales 2020-R20F0008-CEAZA and Centro de Investigación Oceanográfica en el Pacífico Sur-Oriental COPAS COASTAL FB210021).

Author contributions

F.S. with I.H.C. and V.R. designed the dataset. I.H.C. provided the FSLE code, and guidance for its execution and further analyses of FSLEs. J.S. retrieved the remotely sensed MUR SST data. F.S. produced the front dataset and subsequent analysis of the results. C.M. assisted with the High Performance Computing. V.R., B.D. and V.G. supervised the execution of this work and provided critical feedbacks. F.S. produced the figures and wrote the manuscript with input from all authors. All authors contributed to the article and approved the submitted version.

Competing interests

The authors declare that the research was conducted in the absence of any commercial or financial relationships that could be construed as a potential conflict of interest.

Additional information

Correspondence and requests for materials should be addressed to F.S. or V.R.

Reprints and permissions information is available at www.nature.com/reprints.

Publisher's note Springer Nature remains neutral with regard to jurisdictional claims in published maps and institutional affiliations.

Open Access This article is licensed under a Creative Commons Attribution 4.0 International License, which permits use, sharing, adaptation, distribution and reproduction in any medium or format, as long as you give appropriate credit to the original author(s) and the source, provide a link to the Creative Commons licence, and indicate if changes were made. The images or other third party material in this article are included in the article's Creative Commons licence, unless indicated otherwise in a credit line to the material. If material is not included in the article's Creative Commons licence and your intended use is not permitted by statutory regulation or exceeds the permitted use, you will need to obtain permission directly from the copyright holder. To view a copy of this licence, visit http://creativecommons.org/licenses/by/4.0/.

© The Author(s) 2023

6. Conclusion

Content

6.1. Summary 138
6.2. Key results 140

6.1. Summary

Ocean fronts are sharp gradients contrasting a relatively homogeneous background in tracers such as temperature, chlorophyll or density. They are characterised by an along-front jet, toward which the flow converge. At the submesoscale, ocean fronts often exhibit a vertical overturning circulation, which is key to biogeochemical exchanges between the nutrient-rich ocean interior and the well-lit but nutrient-poor surface layer (Klein & Lapeyre, 2009; Mahadevan, 2016; Lévy et al., 2018). Fronts are ubiquitous in the oceans, cover a wide range of spatial and temporal scales, and originate from complex combinations of ocean processes (Belkin, 2021; McWilliams, 2021). Fronts are particularly relevant to study in a changing climate because they are major actors of climate variability and can form hotspots of biodiversity (Seo et al., 2023; Scales et al., 2014b; Lévy et al., 2018).

Despite the cross-disciplinary interest stirred by those fine-scale ephemeral structures, they are still difficult to study over time scales greater than a few years. Their unpredictability makes them elusive to sample from ocean cruises and their fine temporal and spatial scales implies high computational and storage costs for their simulations. The Mozambique Channel (MC) is an ideal laboratory to study ocean fronts thanks to its high biodiversity and turbulent flow (Schott & McCreary, 2001; Marsac et al., 2014; Obura et al., 2019), but also because the size of the Channel allows for sensible simulation costs (although not small). In this thesis we use the MC as a test-bed to study fine-scale ocean fronts in the past decades and in a pseudo global warming experiment. As this thesis is part of the cross-disciplinary Ocean Front Change Project, financed by the Belmont Forum, special attention is paid to produce knowledge that can be re-usable by marine ecologists or within a conservation framework.

The present research is guided by the following questions:

1. where are ocean fronts more frequent in the MC?
2. how deep do they extend in the water column?

3. what is driving their seasonal variability in the MC?

4. how will fronts change in response to global warming?

In Chapter 3, we tackle the first three questions and propose a description of where, when and how thermal fronts occur in the MC from two decades of high-resolution satellite and modelled temperature and velocity data. Thermal fronts are identified from thresholded thermal gradient fields, estimated from the BOA. They are defined as the top 30% of the thermal gradient distribution for each dataset. The eddy activity is inferred from intra-seasonal EKE. We find that persistent fronts form along the Mozambican and Madagascar continental shelves and along the mean NEMC and SEMC flows. Ephemeral fronts are generated most frequently in between MC eddies and at the transitory meanders related to the NEMC and SEMC. Vertically, thermal gradients peak where the stratification is maximum, between -80 and -150 m. We find that the seasonal variations in frontal activity can be interpreted as resulting from the variations in eddy activity and regional upwelling cells.

In the last decades, observational trends have shown that the mesoscale eddy activity in the MC is shifting in response to climate change (Backeberg et al., 2012; Martínez-Moreno et al., 2021). In Chapter 4, we hypothesize that if climate warming can lead to changes in the eddy regime within the Channel, it would also have significant impacts on ocean front variability. To test this hypothesis and answer the fourth research question, we use a dynamical downscaling procedure to investigate the impact of a warming climate on front and eddy activity in the MC. We compare two regional CROCO simulations on the same 3 km grid centered on the MC. One is a hindcast covering the period 1993-2014. The other is a pseudo global warming experiment whose boundary and atmospheric forcings reflect a pessimistic "business as usual" scenario for the end of this century. We find that eddy and front activity are projected to increase by the end of the century in the Comoros basin and southwest of Madagascar. They are projected to decrease however, in the southern MC (south of 17°S) and southeast of Madagascar. The pattern of thermal gradient changes being so similar to those of the EKE suggests that the thermal fronts most affected by a warming climate are those occurring at the edge of eddies. We also show that if the median annual front frequency remains comparable in both scenarii, there seems to be a greater interannual variability in the future scenario. Overall, we find that the Comoros Basin, South Madagascar and the Mozambican shelf-break regions are the most affected by the projection. These three regions are also key habitats for seabirds and megafauna.

Maps of climatologically persistent fronts, or regions of enhanced front frequency like those identified in Chapters 3 and 4, can help managing marine ecosystems (Scales et al., 2014b, 2018). However, despite marine megafauna having been reported to follow submesoscale fronts in some instances (e.g. Tew Kai et al., 2009; Siegelman et al., 2020a), there is still no long-term study looking at statistical relationships between those sentinel species and fine-scale fronts. Considering the prevalence of ephemeral fronts in the MC (Chapter 3), their potential for enhanced primary productivity (Mahadevan, 2016) and given the abundant megafauna in the region

(Le Corre et al., 2012; Laran et al., 2017), we hypothesize that fine-scale fronts are indeed actively sought after by marine megafauna in the SWIO. Given future changes in eddy and frontal activity discussed in Chapter 4 and in the work of Martínez-Moreno et al. (2021), a direct consequence of the above hypothesis is that a change in frontal activity would impact the population of these sentinel species, with consequences for the whole ecosystem and their dependent fisheries. To understand how marine megafauna uses ephemeral ocean fronts, we need to compare animal tracking data to maps of fine-scale fronts. With this objective in mind, we provide a publicly available high-resolution observational dataset of fine-scale ocean fronts for the SWIO (and the Mediterranean Sea). The oceaN frOnt dataset for the Mediterranean seA and south-west inDian ocean (or NOMAD) is described in Chapter 5. The NOMAD offers both observational thermal gradients and attracting LCS. Thermal gradients are mapped on a 1 km grid, for the period 2003-2020. Attracting LCS complement thermal gradient fields with a Lagrangian perspective on the definition of fronts. They add information about mixing and transport characteristics of the flow, while also being independent of cloud cover. Attracting LCS are identified as ridges of backward FSLE, derived from satellite altimetry, and provided on a 1.56 km grid, from 1994 to 2020. The NOMAD is originally built to investigate the relationship between marine megafauna and ocean fronts but could also be used to examine finer-scale air-sea feedbacks or pollutant dispersion at fronts.

6.2. Key results

KEY RESULTS

. Thermal gradients are elevated in the whole mesopelagic realm, in particular along continental shelves, in the wake of both NEMC and SEMC, and more generally South of the Channel.

. Thermal front peaks at subsurface, concomitantly to vertical stratification maxima.

. The seasonal variability of thermal gradients is regionally marked in the Mozambique Channel and possesses a rich vertical structure.

. Thermal fronts changes are most prominent in the Comoros Basin and South of Madagascar Island and those changes are felt in the entire mesopelagic realm.

. There is a higher interannual variability of thermal fronts frequency in the future, which is solely due to changes in mean statistics.

7. Discussion and perspectives

Content

7.1. Beyond surface front detection 141
7.2. On the relationship between thermal and dynamical front diagnostics 142
7.3. Modeling considerations 145
7.4. Beyond physical diagnostics 148

7.1. Beyond surface front detection

In Chapter 3 and 4, we showed that horizontal thermal gradients are maximum between -80 and -150 m, indicating that thermal fronts are likely driven by aspects of the ocean dynamics rather than surface mixed-layer processes. One direct implication of this is that thermal fronts derived from satellite SST products might not inform on thermal fronts below the mixed layer. To illustrate this with the original MOZ36 (see section 2.3.1), we can consider the probability of finding a horizontal thermal front at surface given one at -100 m (Fig. 7.1, left) or at -500 m (Fig. 7.1, right).

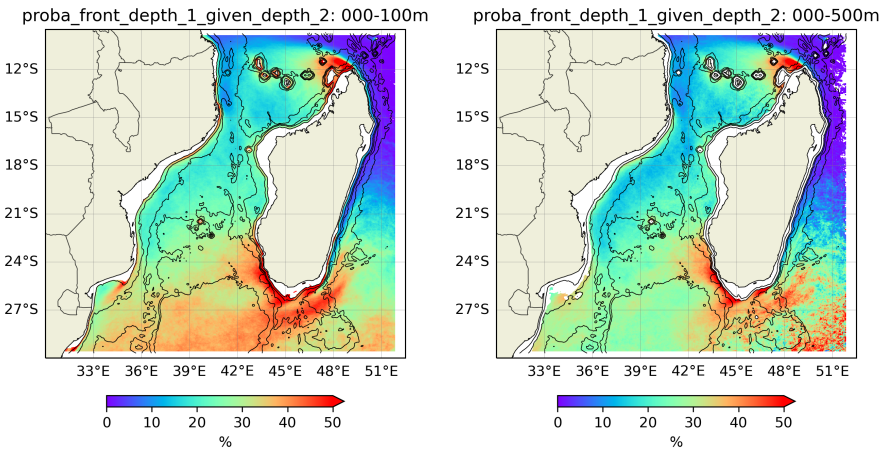

Figure 7.1.: Probability of finding a thermal front at surface given one at -100 m (left) or at -500 m (right).

Given a horizontal thermal front at -100 m, the probability of also detecting it from surface temperature data ranges between 40 and 50% along the NEMC, SEMC, and South Magagascar shelf-break (Fig. 7.1). The same probability nears 40% in the

southern MC, south of 22°S but barely reaches 30% everywhere else in the Channel, even where the eddy activity is most intense, around 16-17°S. The probability of detecting a thermal fronts at -500 m from surface data has a similar distribution than for -100 m, but on lower ranges.

The discrepancy illustrated in Fig. 7.1 between thermal fronts at surface and subsurface could have several origins. The first likely possibility is that thermal fronts detected at surface might be vertically sloped, so that they are not seen at the same position on deeper layers. This could be tested from models, such as MOZ36 or MOZ36_CR (see section 2.3), by considering a spatial window for the probability calculation instead of looking at the exact same position for different depths. From this computation, and assuming we are tracking the same front at surface and below, one could also infer the vertical slope of the front. Another likely possibility would be that most mixed layer frontal dynamics are decoupled from the deeper ocean interior.

This thesis thus highlights the need to go beyond the present descriptive analyses of thermal front variability (Chapter 3) to disentangle the mechanisms acting behind the formation of fronts in the MC, in the mixed layer and in the ocean interior. For instance, it would be interesting to quantify the influence of the main drivers of frontogenesis with eddy kinetic (Martínez-Moreno et al., 2019; Conejero et al., 2020; Martínez-Moreno et al., 2022) or frontogenesis (Koseki et al., 2019) function decomposition. Such exercises could provide insights on dynamical links between surface satellite observations (SST or altimetry) and subsurface circulation features of ecological interest.

7.2. On the relationship between thermal and dynamical front diagnostics

The focus of Chapter 3 and 4 is on thermal fronts, derived from temperature gradients. In Chapter 1, we describe fronts as high tracer gradients but also as area of flow convergence. This is why in Chapter 5 we also include backward FSLE to complement thermal gradients in the NOMAD dataset. In Chapter 3, we argue that the mesoscale eddy activity in the MC does not fully explain the thermal front variability on seasonal time scales. While it seems logical that thermal gradients can be intensified by coastal upwelling pulses, we hypothesize that the influence of upwellings is much smaller for backward FSLE computed from horizontal velocities. And indeed, seasonal Hovmöller diagrams of surface NOMAD TG (Fig. 7.2 left) and FSLE (Fig. 7.2 right), and EKE (derived from CMEMS total currents, see section 2.2, Fig. 7.2 center) for the zonally averaged MC open-ocean reveal a much closer seasonal pattern between backward FSLE and EKE than between TG and EKE. The spatial correlation — in the (latitude, month) space — between backward FSLE and EKE is 0.7 (with p-value < 0.01), while the same correlation between TG and EKE is near zero and not significant (p-value >0.05). This suggests that, given the computational cost involved with FSLE, the intra-seasonal EKE could be an acceptable proxy to evaluate open-ocean dynamical front activity on time scales larger than several years. Backward FSLE would be best suited

to studies requiring fine time and spatial scales on shorter periods as mentioned in Chapter 5, and also shown in Tew Kai et al. (2009), Tzortzis et al. (2021) and Mangolte et al. (Mangolte et al.).

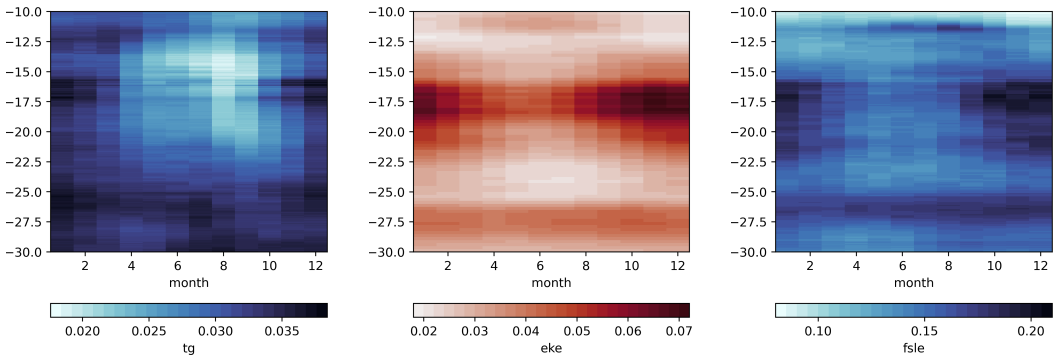

Figure 7.2.: Seasonal Hovmöller diagrams in the zonally averaged MC open-ocean (bathymetry > 200 m) for NOMAD TG (left, in °C.km^{-1}), EKE (center, in m^2.s^{-2}) and NOMAD FSLE (right, in day^{-1}). The y-axis corresponds to latitudes in degree north. The colormaps are from cmocean (Thyng et al., 2016).

Dewitte et al. and Amos and Castelao document another example of potential non-direct relationship between EKE and thermal fronts off the Peru-Chile coast. On one hand, Amos and Castelao show that during El Niño events, thermal fronts are less frequent. They explain this lesser thermal front occurrence by linking it to a reduction in upwelling favorable winds (Amos & Castelao, 2022), although upwelling favourable winds were shown to increase during El Niño events in other studies (Kessler, 2006; Dewitte & Takahashi, 2019). On the other hand, Conejero et al. 2020 show a marked increased in EKE during El Niño events in the same region, underlining a potential interannual discrepancy between EKE and thermal front variability in the Peru-Chile region. Similarly to the previous seasonal Hovmöller diagrams (Fig. 7.2), interannual diagrams of surface anomalies in EKE (derived from CMEMS total currents, Fig. 7.3 top), NOMAD backward FSLE (Fig. 7.3 center) and TG (Fig. 7.3 bottom) for the zonally averaged MC exhibit a much closer relationship between backward FSLE and EKE (spatial correlation in the (latitude, year) space: 0.45, p-value<0.01) than between TG and EKE (spatial correlation in the (latitude, year) space: 0.07, p-value<0.01). So there seem to be a non-trivial relationship between EKE and thermal front variability on interannual time scales as well in the MC.

The MC is connected to broader dynamics — internal and external to the Indian Ocean — via SEC transport, Kelvin and Rossby wave propagation, and biannual monsoon circulation (Vinayachandran et al., 2002; Phillips et al., 2021). The MC is thus expected to show natural variability on interannual timescales as well (Fig. 7.5). For instance, circulation and mesoscale eddy activity in the Channel are influenced

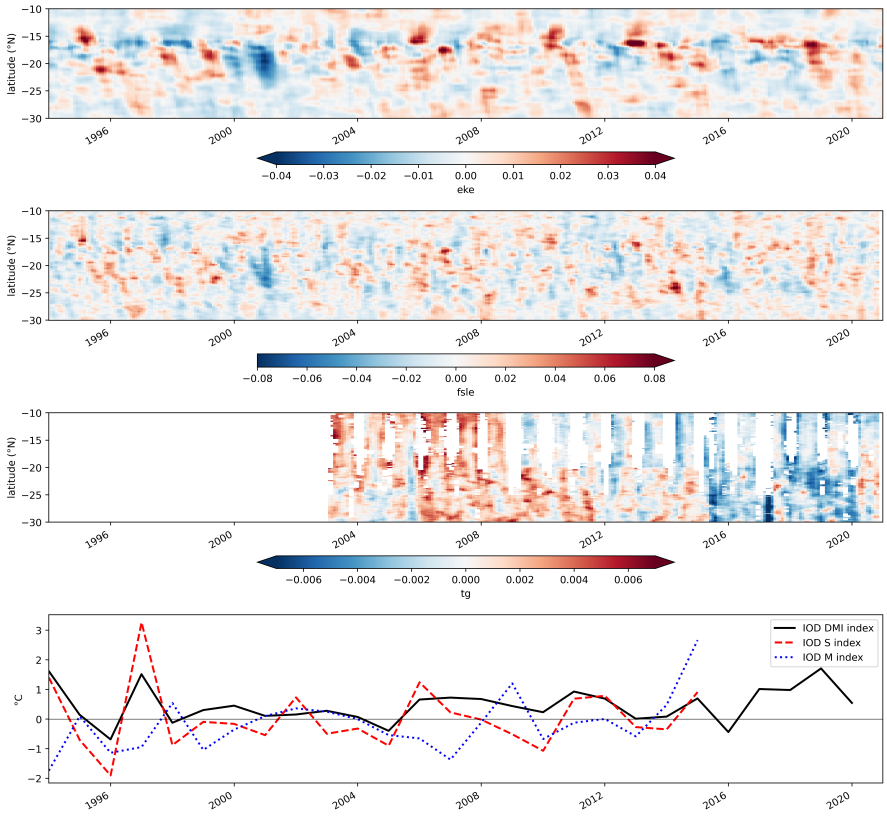

Figure 7.3.: Interannual Hovmöller diagrams in the zonally averaged MC open-ocean (bathymetry > 200 m) for anomalies of EKE (top, in $m^2.s^{-2}$) and NOMAD FSLE (2nd row, in day^{-1}) and TG (3rd row, in °C.km^{-1}). The y-axis corresponds to latitudes in degree north. The blank areas in the TG hovmöller diagram represent flagged pixels due to cloud cover. The bottom panel represents the time series of the IOD dipole mode indices following the method presented in Saji et al. (1999) and Cai et al. (2021) from HadISST 1.1 monthly average sea surface temperature (Rayner et al., 2003). Note that the indices derived from the method presented in Cai et al. (2021) only go up to 2015. The colormap is from cmocean (Thyng et al., 2016).

by IOD events. Negative (positive) IOD anomalies are correlated to stronger (weaker) NEMC and SEMC, whose subsequent instabilities could enhance (dampen) frontal and eddy activity within the Channel (Saji et al., 1999; Webster et al., 1999; Palastanga et al., 2006; Ridderinkhof et al., 2010). IOD modes have been linked to ENSO events, but can also emerge from internal variability (Saji et al., 1999; Huang & Kinter, 2002; Yang et al., 2015). Looking into the next decades, strong and moderate positive IOD events are projected to have opposite responses to global warming (Cai et al., 2013, 2021). In light of this work, and the influence of the aforementioned interannual climatic drivers on the Indian Ocean variability (and correlations shown in Fig. 4.10), we recommend that further studies explore the impact of large-scale lower-frequency

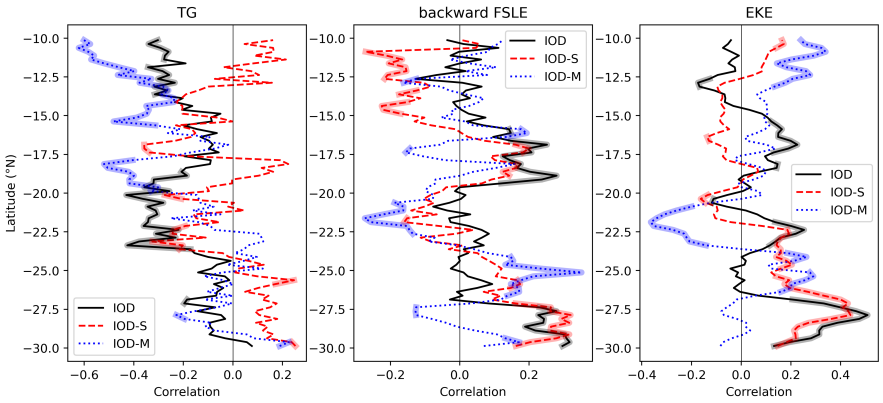

Figure 7.4.: Correlation coefficients per latitude between TG (left), backward FSLE (center) and EKE (right) and IOD indices as per Saji et al. (1999) (in black) and Cai et al. (2021) (strong IOD in red and moderate IOD in blue). The interannual anomalies in TG, FSLE and EKE are the same as for the Hövmoller diagram in Fig. 7.3. Significant correlations (p-values<0.05) are marked by thicker shaded lines.

modes of variability on fine-scale thermal fronts and mesoscale eddy activity in the MC as well as the interplay between them.

7.3. Modeling considerations

Rivers & ocean-atmosphere feedbacks

The CROCO configurations used in this thesis (detailed in 2.3) do not include river runoff from Mozambique and Madagascar. This is why we mostly focused our attention on thermal fronts, instead of density fronts in Chapter 3 and 4. The most prominent river in the MC area is the Zambezi river, at 18°S on the Mozambique Sofala bank. We thus expect thermal gradients over the Sofala Bank to be slightly underestimated from our simulations. Our CROCO configurations did not include a coupled ocean-atmosphere component either. Thermal feedbacks mentioned in Chapter 1, detailed in Renault et al. (2019) and reviewed in Seo et al. (2023) are not resolved potentially leading to an overestimation of the mesoscale eddy activity in our regional simulations. We chose not to use a regional ocean-atmosphere model to avoid additional computational cost and reduce biases in mean state that would have influence the EKE regionally (Li & Xie, 2014; Chowdary et al., 2016).

Bias propagation in downscaling procedures

The downscaling procedure – employed in Chapter 4 – enables us to examine smaller-scale eddies and fronts within the MC that would not be discernible in coarser global projections. However, our regional projection still relies on larger-scale atmospheric

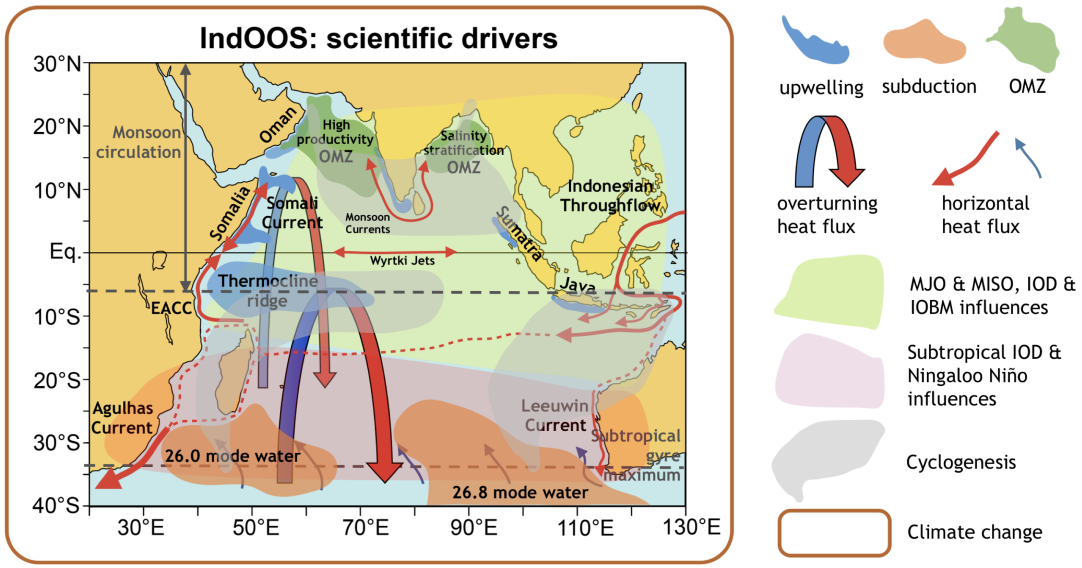

Figure 7.5.: Key drivers of climate and ocean variability in the Indian Ocean region. This schematic is from CLIVAR's IndOOS-2 report (Indian Ocean Observing System, Beal et al., 2019). The schematic includes oxygen minimum zones (OMZs), upwelling and subduction zones, main heat flux components. On intraseasonal time scales: Madden–Julian Oscillations (MJO) and Monsoon Intra-Seasonal Oscillations (MISO). On interannual time scales: the Indian Ocean Dipole (IOD) and Indian Ocean Basin Mode (IOBM), the subtropical modes of Ningaloo Niño and subtropical IOD, cyclogenesis, and climate change.

and boundary forcings derived from the global projection, and thus also inherits their associated biases (Liang et al., 2008). The delta method – consisting in applying the difference between mean future and historical states to base forcings – has the advantage of correcting climatological biases, but only if we assume that these biases are stationary (Drenkard et al., 2021). Moreover, there seems to be no linear relationship between climatological biases seen in hindcast global models and their projected trends (Liang et al., 2008; Drenkard et al., 2021). This means that the various biases propagated from global model projections to regional ones cannot easily be disentangled and are likely dependent on regions of interest.

Uncertainties in future projections

The projected regional simulation described in Chapter 4 offers the first insight on fine-scale eddy and front responses to one scenario of climate warming downscaled around the MC. However, this regional projection inherits biases from the global model through boundary and atmospheric forcings, despite the use of the pseudo global warming method that by construction corrects the mean state bias. First, global products used as boundary conditions are contaminated by 3 sources of uncertainties:

model uncertainty due to different model physics and parametrisation, uncertainty associated to internal variability, and those associated with scenario uncertainty. Given the same initial conditions and forcings, different models will yield different results due to their distinct modules and parametrization schemes. The range of difference between multi-model results makes the *model uncertainty*. Now, if instead of considering several models, we take a single one and run it several times with the same initial and boundary conditions, the resulting outputs will still differ due to stochastic processes, this is the *internal climate variability* (e.g. Tebaldi et al., 2011; Hogg et al., 2022). The *scenario uncertainty* does not depend on models but rather on emission policy prescription (IPCC, 2023).

These uncertainties are transmitted to regional models, such as the one presented in Chapter 4, through boundary forcings, which adds to uncertainties associated to the regional model itself (i.e. model physics, parametrisation, and internal variability). The relative contributions of these uncertainties is difficult to assess and would require numerous experiments. Still, ensemble simulations can offer a way to circumvent uncertainties associated with internal variability (Kay et al., 2015; Frölicher et al., 2016). The challenge of determining regional marine impacts from global projections consists in minimizing or quantifying biases and uncertainties coming from the use of models, while keeping sensible computational costs. Applying the same dynamical downscaling procedure to all of the 40 CESM-LENS ensemble members was beyond the scope of this thesis but it would have helped quantifying internal climate variability on the regional scale. Similarly, looking at a range of multi-model responses as in Alexander et al. (2020) would have accounted for model uncertainties. One way to bypass the hefty computational cost related to dynamical downscaling of global simulations would be to train a climate emulator for the Southwest Indian Ocean.

Climate emulators

Climate emulators work by capturing the essential relationships and patterns observed in global climate models and then applying this knowledge to make predictions at a finer, regional scale (Reichstein et al., 2019; Tebaldi et al., 2022; Doury et al., 2023).

The first step to build such tool involves the collection of data from ocean or climate models during a training phase. Statistical techniques are then applied to identify essential relationships within the data. Based on these patterns, a so-called emulator model is developed and parameterized to replicate the key responses of the climate system observed in the training data. The parametrization could include ocean-atmosphere feedback mechanisms for instance. The emulator should then be validated against independent real-world observational datasets to ensure accuracy (Doury et al., 2023). The validation step is important to ensure that the emulator model is capable of identifying patterns in the training data but also capable of producing realistic simulations from new climate data. Once validated, the emulator model can be applied to downscale global climate information at the regional scale, at a fraction of the computational cost involved with traditional dynamical downscaling techniques (Drenkard et al., 2021; Sonnewald et al., 2021). One could then imagine

using a climate emulator for the Southwest Indian Ocean to produce an ensemble of regional simulations quantifying the marine impacts and uncertainties of a warming climate in the MC.

Climate emulators are promising tools — although mostly applied in atmospheric research so far — but they come with their own set of assumptions and uncertainties. For instance, the identified statistical patterns might dampen the complexity of the most intricate or fine-scale processes which would be better resolved in high-resolution ocean models. They also assume that present statistical patterns detected in the training data are also applicable in the future (this stationarity assumption is also present in ocean models, Dixon et al., 2016; Trapp et al., 2021) which might lead to uncertainties in long-term simulations. Additionally, emulators are dependent on their training data and associated biases, implying that emulators might not predict accurately unprecedented climate shifts.

It would thus be interesting to combine physics-based ocean models and climate emulators in a hybrid approach. For example, with a nested configuration in which a higher-resolution regional emulator is nested inside a coarser ocean model, we could minimize run-time and computational costs while modelling large and regional scale processes with acceptable accuracy.

7.4. Beyond physical diagnostics

The anticipated shifts in EKE and thermal fronts to the south of Madagascar and in the Comoros Basin raise concerns about potential impacts on key pelagic and benthic habitats (Kiszka & Ridoux, 2007; Weimerskirch et al., 2010; Le Corre et al., 2012; McClanahan et al., 2014; Laran et al., 2017; Diamant et al., 2018). Given the climate-related risks projected for marine ecosystems by the latest Coupled Model Intercomparison Project (CMIP6) (Tittensor et al., 2021), there is a compelling case for integrating a biological component to our physical analyses.

Satellite chlorophyll

In this thesis, gradient-based front detection methods are applied on remotely-sensed and modelled temperature data. Following the work of Haëck et al., it would be interesting to also study ocean front variability in the MC from remotely-sensed estimates of chlorophyll-a (Haëck et al., 2023). Indeed the BOA is well-suited to the identification of chlorophyll-a fronts (Belkin & O'Reilly, 2009). There have been several theoretical and in-situ studies investigating the processes affecting plankton communities at fronts (e.g. Tzortzis et al., 2021, also see section 1.5.3.1), but very few of them offer a synoptic view of primary productivity at ephemeral fronts over large areas and on multi-decadal time scales (e.g. Haëck et al., 2023). Abrupt gradients in estimates of chlorophyll-a – marked as chlorophyll-a fronts – may indicate areas where nutrient-rich waters are upwelled to the surface, supporting the growth of plankton and other marine organisms. Chlorophyll-a front maps would thus complement the

NOMAD and analyses from Chapter 3 by bridging the gap between physical diagnostic and marine productivity.

Furthermore, chlorophyll-a trends for the period 1997-2021 provided by the CMEMS (Fig. 7.6) display a similar pattern of change in the MC compared to EKE and thermal front changes highlighted in the pseudo global warming scenario (see Chapter 4). However, the sign of those changes seems to be opposite within the Channel. Chlorophyll-a concentrations are observed to decrease in the Channel north of 20°S – where we show an increase in both EKE and thermal fronts in the pseudo global warming experiment – and increase south of 20°S. Given that numerous studies have highlighted the enhanced primary productivity of fine-scale turbulence (see section 1.5.3.1), we would expect that higher EKE and thermal front activity in the Channel would result in increased chlorophyll-a concentration. Subsequently, this comparison (although tenuous since we compare present-day observational trends on a 4 km grid to one hypothetical end-of-century projection on a 3 km grid) brings forward the need for adding a biogeochemical component to our pseudo global warming modeling experiment.

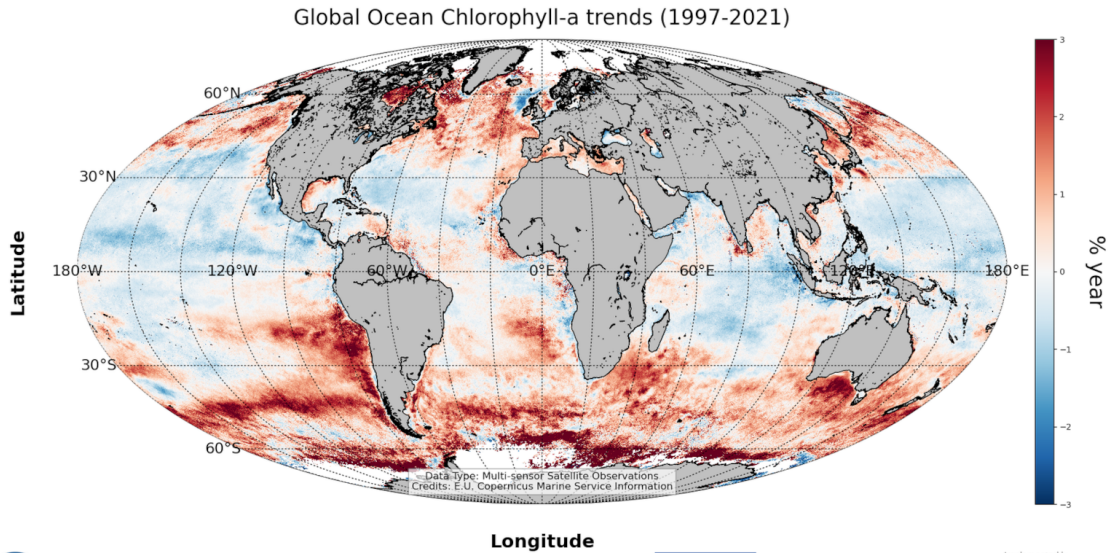

Figure 7.6.: Chlorophyll-a trend map (1997-2021) from CMEMS Observations Reprocessing. The trend comes from the 5th version of global climate-quality chlorophyll time series from the ESA Ocean Colour Climate Change Initiative (ESA OC-CCI, Sathyendranath et al., 2019) on a 4 km grid. Image credits: E.U. Copernicus Marine Service Information.

Biogeochemical modeling

Following the work of José et al. (2014), the high-resolution simulations produced for this thesis (see section 2.3) could be paired with a biogeochemical model to improve our understanding of the complex interactions between biological, chemical, and

physical processes in marine ecosystems of the MC. José et al. 2014 coupled a regional ocean model (Regional Ocean Modeling System (ROMS), Shchepetkin and McWilliams, 2005) to a biogeochemical one (PISCES, Aumont and Bopp, 2006) to investigate how the MC eddies affect the biogeochemistry of the Channel at the mesoscale. They used an eddy-permitting configuration on a 1/6° grid (approx. 19 km). While this resolution is sufficient to capture the effect of mesoscale eddies, it does not allow for the identification of finer-scale fronts and filaments. Future research could thus couple our 1/36° child simulations to a biogeochemical model to evaluate the impact of climate warming on key marine ecosystem properties (e.g. nutrients, pH, dissolved oxygen, plankton biomass) similarly to what has been done in the California Current System by Howard et al. (2020).

Coral reef connectivity

The SWIO contains critical coral reef habitats (McClanahan et al., 2014; Obura et al., 2019; Obura et al., 2021), which were found to be highly vulnerable to climate warming by Obura et al. (Fig. 7.7, Obura et al., 2021). Besides, Vogt-Vincent et al. (2023) showed that the variability of remote coral reef connectivity in the region operate mostly on daily time scales. It would thus be interesting to use the daily output of our fine-scale simulations to investigate coral larvae dispersal and reef connectivity in a warming MC by comparing connectivity matrices derived from baseline and future scenarii. If coupled to a biogeochemical module, the same simulations could also provide projections of key coral reef health indicators such as pH or dissolved oxygen. Recognizing the interconnected nature of ecoregions in the SWIO is essential for effective conservation planning. This study would help developing conservation strategies that protect entire ecosystems rather than isolated components.

Interactions between top predators and fronts

The enhanced primary productivity observed at ocean fronts attracts a wide range of marine organisms from all trophic levels (see section 1.5.3). Many of these organisms are top predators relying on frontal areas for their abundant food resources (e.g. Tew Kai et al., 2009; Arostegui et al., 2022). Ocean fronts are critical to the functioning and health of marine ecosystems but their interaction with megafauna remains speculative, and especially so for finer scale ephemeral fronts (Lévy et al., 2018). Considering the MC's intense frontal activity (see Chapter 3 and 5) and abundance of marine megafauna (section 1.5.3), we suggest that ocean fronts play a key role in influencing the abundance and behaviour of top predators in the region. To test this hypothesis, and in collaboration with Isaac Brito-Morales and Lee Hannah from Conservation International, we compare ocean front occurrences from NOMAD to historical tracks of whale sharks, seabirds and turtles in the MC. The animal data were gathered during a Workshop organized by Conservation International, in November 2022. The contributors are: Christoph Rohner, Matthieu Le Corre, Audrey Jaeger, Sophie Laran, Olivier

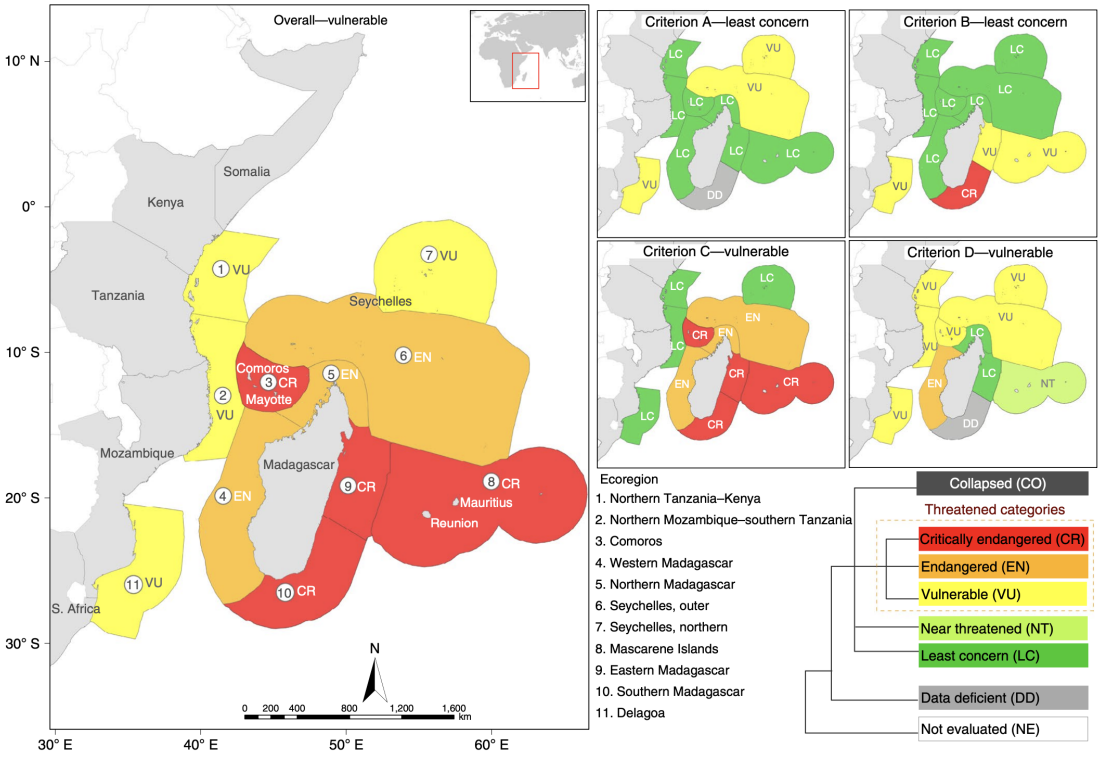

Figure 7.7.: Evaluation of the vulnerability of SWIO coral reefs and ecoregions following the Red List Ecosystem method from the IUCN, figure extracted from Obura et al. (2021).

Bousquet, Ana Sequeira, Kylie Scales, Elliott Hazen, Salvatore Cerchio, Tammy Davies and Daniel Dunn.

Although this work is still ongoing, preliminary results are promising (Brito-Morales et al., in preparation). Whale sharks and seabirds seem to follow ocean fronts in the MC (Fig. 7.8). Random walk distributions show that these results are robust for both FSLE and thermal fronts. Whale sharks seem to have a preference for thermal fronts over FSLE, while seabirds react similarly to the two front diagnostics. However, turtles do not seem to follow fronts at all. The turtles followed in this study are mostly late juveniles journeying toward the Oman Gulf for reproduction. We suspect they are guided by geomagnetic cues (Benhamou et al., 2011) and that their feeding strategy shifts to a more opportunistic mode while migrating toward the Oman Gulf (Brito-Morales et al., in preparation).

Overall, we hope to highlight robust, multi-decadal relationships between pelagic predators and fine-scale fronts. This work is particularly timely as scientists are considering dynamic marine conservation strategies to protect highly mobile species and face the challenges of global warming on biodiversity (Maxwell et al., 2020).

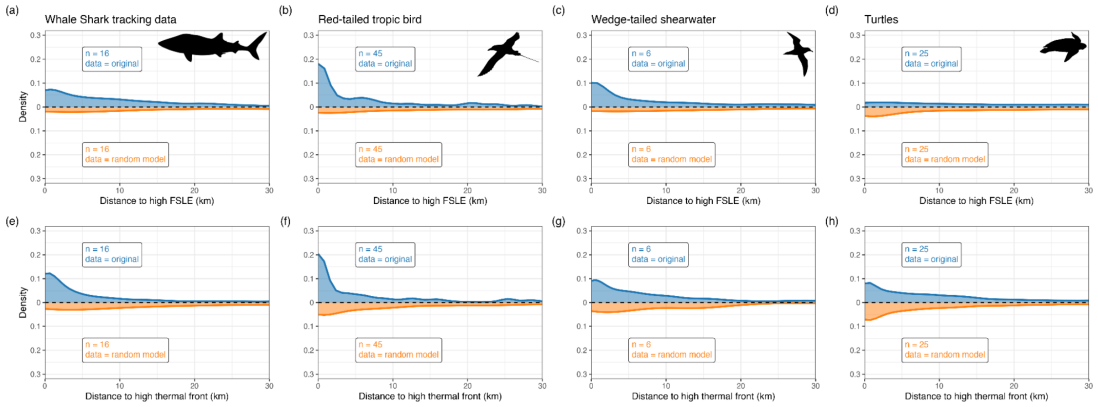

Figure 7.8.: Preliminary figure of kernel density estimations between whale sharks (a, e), red-tailed tropic birds (b, f), wedge-tailed shearwater (c, g), turtles (d, h) and distance to high FSLE values (top) and thermal fronts (bottom) in blue. Orange kernel density estimations correspond to random walks. Figure extracted from Brito-Morales et al., in preparation.

Bibliography

Abraham, E. R. (1998). The generation of plankton patchiness by turbulent stirring. *Nature*, *391*(6667), 577–580. https://doi.org/10.1038/35361 (cit. on p. 41).

Acha, E. M., Mianzan, H. W., Guerrero, R. A., Favero, M., & Bava, J. (2004). Marine fronts at the continental shelves of austral south america. *Journal of marine systems: journal of the European Association of Marine Sciences and Techniques*, *44*(1–2), 83–105. https://doi.org/10.1016/j.jmarsys.2003.09.005 (cit. on p. 30).

Akan, Ç., McWilliams, J. C., Moghimi, S., & Özkan-Haller, H. T. (2018). Frontal dynamics at the edge of the columbia river plume. *Ocean modelling*, *122*, 1–12. https://doi.org/10.1016/j.ocemod.2017.12.001 (cit. on p. 30).

Alemany, D., Acha, E. M., & Iribarne, O. (2009). The relationship between marine fronts and fish diversity in the patagonian shelf large marine ecosystem. *Journal of biogeography*, *36*(11), 2111–2124. https://doi.org/10.1111/j.1365-2699.2009.02148.x (cit. on p. 42).

Alemany, D., Acha, E. M., & Iribarne, O. O. (2014). Marine fronts are important fishing areas for demersal species at the argentine sea (southwest atlantic ocean). *Journal of sea research*, *87*, 56–67. https://doi.org/10.1016/j.seares.2013.12.006 (cit. on p. 42).

Alexander, M. A., Shin, S.-I., Scott, J. D., Curchitser, E., & Stock, C. (2020). The response of the northwest atlantic ocean to climate change. *Journal of climate*, *33*(2), 405–428. https://doi.org/10.1175/jcli-d-19-0117.1 (cit. on pp. 101, 113, 147).

Allen, J. T., Brown, L., Sanders, R., Moore, C. M., Mustard, A., Fielding, S., Lucas, M., Rixen, M., Savidge, G., Henson, S., & Mayor, D. (2005). Diatom carbon export enhanced by silicate upwelling in the northeast atlantic. *Nature*, *437*(7059), 728–732. https://doi.org/10.1038/nature03948 (cit. on p. 41).

Amos, C. M., & Castelao, R. M. (2022). Influence of the el niño-southern oscillation on sst fronts along the west coasts of north and south america. *Journal of geophysical research. Oceans*, *127*(10), e2022JC018479. https://doi.org/10.1029/2022JC018479 (cit. on pp. 59, 61, 143).

Annasawmy, P., Ternon, J. F., Marsac, F., Cherel, Y., Béhagle, N., Roudaut, G., Lebourges-Dhaussy, A., Demarcq, H., Moloney, C. L., Jaquemet, S., & Ménard, F. (2018). Micronekton diel migration, community composition and trophic position within two biogeochemical provinces of the south west indian ocean: insight from acoustics and stable isotopes. *Deep-sea research. Part I, Oceanographic research papers*, *138*, 85–97. https://doi.org/10.1016/j.dsr.2018.07.002 (cit. on pp. 47, 100).

Arostegui, M. C., Gaube, P., Woodworth-Jefcoats, P. A., Kobayashi, D. R., & Braun, C. D. (2022). Anticyclonic eddies aggregate pelagic predators in a subtropical gyre.

Nature, *609*(7927), 535–540. https://doi.org/10.1038/s41586-022-05162-6 (cit. on p. 150).

Auclair, F., Benshila, R., Bordois, L., Boutet, M., Brémond, M., Caillaud, M., Cambon, G., Capet, X., Debreu, L., Ducousso, N., Dufois, F., Dumas, F., Ethé, C., Gula, J., Hourdin, C., Illig, S., Jullien, S., Corre, M. L., Gac, S. L., … Theetten, S. (2022, November). *Coastal and regional ocean community model* (Version 1.3). Zenodo. https://doi.org/10.5281/zenodo.7415343 (cit. on pp. 53, 58, 101).

Aumont, O., & Bopp, L. (2006). Globalizing results from ocean in situ iron fertilization studies. *Global biogeochemical cycles*, *20*(2). https://doi.org/10.1029/2005gb002591 (cit. on p. 150).

Aurell, E., Boffetta, G., Crisanti, A., Paladin, G., & Vulpiani, A. (1997). Predictability in the large: an extension of the concept of lyapunov exponent. *Journal of physics A: Mathematical and general*, *30*(1), 1–26. https://doi.org/10.1088/0305-4470/30/1/003 (cit. on pp. 35, 36).

AVISO. (2021). Fsle - finite-size lyapunov exponents and orientations of the associated eigenvectors. https://doi.org/10.24400/527896/A01-2022.002 (cit. on pp. 119, 121).

Backeberg, B. C., & Reason, C. J. C. (2010). A connection between the south equatorial current north of madagascar and mozambique channel eddies. *Geophysical research letters*, *37*(4). https://doi.org/10.1029/2009gl041950 (cit. on p. 100).

Backeberg, B. C., Penven, P., & Rouault, M. (2012). Impact of intensified indian ocean winds on mesoscale variability in the agulhas system. *Nature climate change*, *2*(8), 608–612. https://doi.org/10.1038/nclimate1587 (cit. on pp. 38, 95, 96, 98, 110, 111, 139).

Bakhoday-Paskyabi, M. (2020). Ocean surface hidden structures in the lofoten area of the norwegian sea. *Dynamics of atmospheres and oceans*, *92*(101173), 101173. https://doi.org/10.1016/j.dynatmoce.2020.101173 (cit. on p. 36).

Bakun, A. (2006). Fronts and eddies as key structures in the habitat of marine fish larvae: opportunity, adaptive response and competitive advantage. *Scientia marina*, *70*(S2). https://doi.org/10.3989/scimar.2006.70s2105 (cit. on p. 100).

Barlow, R., Lamont, T., Morris, T., Sessions, H., & van den Berg, M. (2014). Adaptation of phytoplankton communities to mesoscale eddies in the mozambique channel. *Deep-sea research. Part II, Topical studies in oceanography*, *100*, 106–118. https://doi.org/10.1016/j.dsr2.2013.10.020 (cit. on p. 47).

Barrillon, S., Fuchs, R., Petrenko, A. A., Comby, C., Bosse, A., Yohia, C., Fuda, J.-L., Bhairy, N., Cyr, F., Doglioli, A. M., Grégori, G., Tzortzis, R., d'Ovidio, F., & Thyssen, M. (2023). Phytoplankton reaction to an intense storm in the northwestern mediterranean sea. *Biogeosciences*, *20*(1), 141–161. https://doi.org/10.5194/bg-20-141-2023 (cit. on p. 40).

Bates, A. E., Helmuth, B., Burrows, M. T., Duncan, M. I., Garrabou, J., Guy-Haim, T., Lima, F., Queiros, A. M., Seabra, R., Marsh, R., Belmaker, J., Bensoussan, N., Dong, Y., Mazaris, A. D., Smale, D., Wahl, M., & Rilov, G. (2018). Biologists ignore ocean weather at their peril. *Nature*, *560*(7718), 299–301. https://doi.org/10.1038/d41586-018-05869-5 (cit. on p. 41).

Baudena, A., Ser-Giacomi, E., D'Onofrio, D., Capet, X., Cotté, C., Cherel, Y., & D'Ovidio, F. (2021). Fine-scale structures as spots of increased fish concentration in the open ocean. *Scientific reports*, *11*(1). https://doi.org/10.1038/s41598-021-94368-1 (cit. on pp. 29, 35, 42).

Beal, L. M., Vialard, J., Roxy, M. K., Ravichandran, M., Mcphaden, M. J., Feng, M., Lumpkin, R., Unnikrishnan, A. S., Lee, T., Sloyan, B., Andres, M., Subramanian, A. C., Yu, L., Lengaigne, M., Shinoda, T., Hariharasubramanian, A. M., C, C., Strutton, P., Masumoto, Y., … Hood, R. (2019). A roadmap to sustained observations of the indian ocean for 2020-2030. https://www.clivar.org/sites/default/files/documents/IndOOS_report_small.pdf (cit. on p. 146).

Beech, N., Rackow, T., Semmler, T., Danilov, S., Wang, Q., & Jung, T. (2022). Long-term evolution of ocean eddy activity in a warming world. *Nature climate change*, *12*(10), 910–917. https://doi.org/10.1038/s41558-022-01478-3 (cit. on p. 111).

Béhagle, N., du Buisson, L., Josse, E., Lebourges-Dhaussy, A., Roudaut, G., & Ménard, F. (2014). Mesoscale features and micronekton in the mozambique channel: an acoustic approach. *Deep-sea research. Part II, Topical studies in oceanography*, *100*, 164–173. https://doi.org/10.1016/j.dsr2.2013.10.024 (cit. on pp. 47, 100).

Belkin, I. M. (2021). Remote sensing of ocean fronts in marine ecology and fisheries. *Remote sensing*, *13*(5), 883. https://doi.org/10.3390/rs13050883 (cit. on pp. 29, 30, 34, 37, 138).

Belkin, I. M., Cornillon, P. C., & Sherman, K. (2009). Fronts in large marine ecosystems. *Progress in oceanography*, *81*(1–4), 223–236. https://doi.org/10.1016/j.pocean.2009.04.015 (cit. on pp. 29, 30, 59, 61, 119, 121).

Belkin, I. M., & O'Reilly, J. E. (2009). An algorithm for oceanic front detection in chlorophyll and sst satellite imagery. *Journal of marine systems: journal of the European Association of Marine Sciences and Techniques*, *78*(3), 319–326. https://doi.org/10.1016/j.jmarsys.2008.11.018 (cit. on pp. 33, 56, 103, 148).

Benavides, M., Conradt, L., Bonnet, S., Berman-Frank, I., Barrillon, S., Petrenko, A., & Doglioli, A. (2021). Fine-scale sampling unveils diazotroph patchiness in the south pacific ocean. *ISME communications*, *1*(1). https://doi.org/10.1038/s43705-021-00006-2 (cit. on p. 41).

Benhamou, S., Sudre, J., Bourjea, J., Ciccione, S., De Santis, A., & Luschi, P. (2011). The role of geomagnetic cues in green turtle open sea navigation. *PloS one*, *6*(10), e26672. https://doi.org/10.1371/journal.pone.0026672 (cit. on pp. 48, 152).

Beron-Vera, F. J., Olascoaga, M. J., & Goni, G. J. (2008). Oceanic mesoscale eddies as revealed by lagrangian coherent structures. *Geophysical Research Letters*, *35*(12). https://doi.org/10.1029/2008gl033957 (cit. on p. 35).

Bertrand, A., Grados, D., Colas, F., Bertrand, S., Capet, X., Chaigneau, A., Vargas, G., Mousseigne, A., & Fablet, R. (2014). Broad impacts of fine-scale dynamics on seascape structure from zooplankton to seabirds. *Nature communications*, *5*(1). https://doi.org/10.1038/ncomms6239 (cit. on pp. 41, 42).

Bettencourt, J. H., López, C., & Hernández-García, E. (2012). Oceanic three-dimensional lagrangian coherent structures: a study of a mesoscale eddy in the benguela

upwelling region. *Ocean modelling*, *51*, 73–83. https://doi.org/10.1016/j.ocemod.2012.04.004 (cit. on p. 36).

Bettencourt, J. H., Rossi, V., Hernández-García, E., Marta-Almeida, M., & López, C. (2017). Characterization of the structure and cross-shore transport properties of a coastal upwelling filament using three-dimensional finite-size lyapunov exponents. *Journal of geophysical research. Oceans*, *122*(9), 7433–7448. https://doi.org/10.1002/2017jc012700 (cit. on p. 36).

Biastoch, A., Beal, L. M., Lutjeharms, J. R. E., & Casal, T. G. D. (2009). Variability and coherence of the agulhas undercurrent in a high-resolution ocean general circulation model. *Journal of physical oceanography*, *39*(10), 2417–2435. https://doi.org/10.1175/2009jpo4184.1 (cit. on pp. 45, 115).

Boffetta, G., Lacorata, G., Redaelli, G., & Vulpiani, A. (2001). Detecting barriers to transport: a review of different techniques. *Physica D. Nonlinear Phenomena*, *159*(1–2), 58–70. https://doi.org/10.1016/s0167-2789(01)00330-x (cit. on pp. 35, 37).

Bost, C. A., Cotté, C., Bailleul, F., Cherel, Y., Charrassin, J. B., Guinet, C., Ainley, D. G., & Weimerskirch, H. (2009). The importance of oceanographic fronts to marine birds and mammals of the southern oceans. *Journal of marine systems: journal of the European Association of Marine Sciences and Techniques*, *78*(3), 363–376. https://doi.org/10.1016/j.jmarsys.2008.11.022 (cit. on p. 42).

Bourjea, J., Lapègue, S., Gagnevin, L., Broderick, D., Mortimer, J. A., Ciccione, S., Roos, D., Taquet, C., & Grizel, H. (2007). Phylogeography of the green turtle, chelonia mydas, in the southwest indian ocean. *Molecular ecology*, *16*(1), 175–186. https://doi.org/10.1111/j.1365-294X.2006.03122.x (cit. on p. 48).

Bower, A. S., Rossby, H. T., & Lillibridge, J. L. (1985). The gulf stream—barrier or blender? *Journal of physical oceanography*, *15*(1), 24–32. https://doi.org/10.1175/1520-0485(1985)015<0024:tgsob>2.0.co;2 (cit. on pp. 31, 41).

Boyd, P. W., Claustre, H., Levy, M., Siegel, D. A., & Weber, T. (2019). Multi-faceted particle pumps drive carbon sequestration in the ocean. *Nature*, *568*(7752), 327–335. https://doi.org/10.1038/s41586-019-1098-2 (cit. on p. 39).

Brito-Morales, I., Schoeman, D. S., Everett, J. D., Klein, C. J., Dunn, D. C., García Molinos, J., Burrows, M. T., Buenafe, K. C. V., Dominguez, R. M., Possingham, H. P., & Richardson, A. J. (2022). Towards climate-smart, three-dimensional protected areas for biodiversity conservation in the high seas. *Nature climate change*, *12*(4), 402–407. https://doi.org/10.1038/s41558-022-01323-7 (cit. on p. 42).

Brito-Morales, I., Sudre, F., Rossi, V., Rohner, C., Le Corre, M., Jaeger, A., Laran, S., Bousquet, O., Sequeira, A., Scales, K., Hazen, E., Cerchio, S., Davies, T., Dunn, D., & Hannah, L. (in preparation). Ocean fronts aggregates marine megafauna in the southwest indian ocean (cit. on p. 152).

Bruyère, C. L., Done, J. M., Holland, G. J., & Fredrick, S. (2014). Bias corrections of global models for regional climate simulations of high-impact weather. *Climate dynamics*, *43*(7–8), 1847–1856. https://doi.org/10.1007/s00382-013-2011-6 (cit. on p. 113).

Cai, W., Yang, K., Wu, L., Huang, G., Santoso, A., Ng, B., Wang, G., & Yamagata, T. (2021). Opposite response of strong and moderate positive indian ocean dipole to global warming. *Nature climate change*, *11*(1), 27–32. https://doi.org/10.1038/s41558-020-00943-1 (cit. on pp. 54, 144, 145).

Cai, W., Zheng, X.-T., Weller, E., Collins, M., Cowan, T., Lengaigne, M., Yu, W., & Yamagata, T. (2013). Projected response of the indian ocean dipole to greenhouse warming. *Nature geoscience*, *6*(12), 999–1007. https://doi.org/10.1038/ngeo2009 (cit. on p. 144).

Calil, P. H. R., Suzuki, N., Baschek, B., & da Silveira, I. C. A. (2021). Filaments, fronts and eddies in the cabo frio coastal upwelling system, brazil. *Fluids*, *6*(2), 54. https://doi.org/10.3390/fluids6020054 (cit. on p. 31).

Canny, J. (1986). A computational approach to edge detection. *IEEE transactions on pattern analysis and machine intelligence*, *8*(6), 679–698 (cit. on p. 33).

Capet, X., McWilliams, J. C., Molemaker, M. J., & Shchepetkin, A. F. (2008a). Mesoscale to submesoscale transition in the california current system. part i: flow structure, eddy flux, and observational tests. *Journal of physical oceanography*, *38*(1), 29–43. https://doi.org/10.1175/2007jpo3671.1 (cit. on p. 26).

Capet, X., McWilliams, J. C., Molemaker, M. J., & Shchepetkin, A. F. (2008b). Mesoscale to submesoscale transition in the california current system. part ii: frontal processes. *Journal of physical oceanography*, *38*(1), 44–64. https://doi.org/10.1175/2007jpo3672.1 (cit. on pp. 26, 28, 29, 31).

Capotondi, A., Alexander, M. A., Bond, N. A., Curchitser, E. N., & Scott, J. D. (2012). Enhanced upper ocean stratification with climate change in the cmip3 models. *Journal of geophysical research*, *117*(C4). https://doi.org/10.1029/2011jc007409 (cit. on p. 100).

Castelao, R. M., Barth, J. A., & Mavor, T. P. (2005). Flow-topography interactions in the northern california current system observed from geostationary satellite data. *Geophysical research letters*, *32*(24). https://doi.org/10.1029/2005gl024401 (cit. on p. 31).

Cayula, J.-F., & Cornillon, P. (1992). Edge detection algorithm for sst images. *Journal of atmospheric and oceanic technology*, *9*(1), 67–80. https://doi.org/10.1175/1520-0426(1992)009<0067:edafsi>2.0.co;2 (cit. on p. 34).

Cayula, J.-F., & Cornillon, P. (1995). Multi-image edge detection for sst images. *Journal of atmospheric and oceanic technology*, *12*(4), 821–829. https://doi.org/10.1175/1520-0426(1995)012<0821:miedfs>2.0.co;2 (cit. on p. 34).

Chang, P., Xu, G., Kurian, J., Small, R. J., Danabasoglu, G., Yeager, S., Castruccio, F., Zhang, Q., Rosenbloom, N., & Chapman, P. (2023). Uncertain future of sustainable fisheries environment in eastern boundary upwelling zones under climate change. *Communications earth environment*, *4*(1). https://doi.org/10.1038/s43247-023-00681-0 (cit. on p. 100).

Chapman, C. C., Lea, M.-A., Meyer, A., Sallée, J.-B., & Hindell, M. (2020). Defining southern ocean fronts and their influence on biological and physical processes in a changing climate. *Nature Climate Change*, *10*(3), 209–219. https://doi.org/10.1038/s41558-020-0705-4 (cit. on p. 100).

Chassot, E., Bodin, N., Sardenne, F., & Obura, D. (2019). The key role of the northern mozambique channel for indian ocean tropical tuna fisheries. *Reviews in fish biology and fisheries*, *29*(3), 613–638. https://doi.org/10.1007/s11160-019-09569-9 (cit. on pp. 48, 59, 61, 100).

Chelton, D. B., deSzoeke, R. A., Schlax, M. G., El Naggar, K., & Siwertz, N. (1998). Geographical variability of the first baroclinic rossby radius of deformation. *Journal of physical oceanography*, *28*(3), 433–460. https://doi.org/10.1175/1520-0485(1998)028<0433:gvotfb>2.0.co;2 (cit. on p. 29).

Chin, T. M., Vazquez-Cuervo, J., & Armstrong, E. M. (2017). A multi-scale high-resolution analysis of global sea surface temperature. *Remote sensing of environment*, *200*, 154–169. https://doi.org/10.1016/j.rse.2017.07.029 (cit. on pp. 52, 104, 105).

Chowdary, J. S., Parekh, A., Srinivas, G., Gnanaseelan, C., Fousiya, T. S., Khandekar, R., & Roxy, M. K. (2016). Processes associated with the tropical indian ocean sub-surface temperature bias in a coupled model. *Journal of physical oceanography*, *46*(9), 2863–2875. https://doi.org/10.1175/jpo-d-15-0245.1 (cit. on p. 145).

Clayton, S., Nagai, T., & Follows, M. J. (2014). Fine scale phytoplankton community structure across the kuroshio front. *Journal of plankton research*, *36*(4), 1017–1030. https://doi.org/10.1093/plankt/fbu020 (cit. on p. 41).

Collins, C., Hermes, J. C., & Reason, C. J. C. (2014). Mesoscale activity in the comoros basin from satellite altimetry and a high-resolution ocean circulation model. *Journal of geophysical research. Oceans*, *119*(8), 4745–4760. https://doi.org/10.1002/2014jc010008 (cit. on pp. 45, 110).

Conejero, C., Dewitte, B., Garçon, V., Sudre, J., & Montes, I. (2020). Enso diversity driving low-frequency change in mesoscale activity off peru and chile. *Scientific reports*, *10*(1), 17902. https://doi.org/10.1038/s41598-020-74762-x (cit. on pp. 54, 55, 142, 143).

Cotte, C., d'Ovidio, F., Chaigneau, A., Lèvy, M., Taupier-Letage, I., Mate, B., & Guinet, C. (2011). Scale-dependent interactions of mediterranean whales with marine dynamics. *Limnology and oceanography*, *56*(1), 219–232. https://doi.org/10.4319/lo.2011.56.1.0219 (cit. on p. 42).

Cotté, C., d'Ovidio, F., Dragon, A.-C., Guinet, C., & Lévy, M. (2015). Flexible preference of southern elephant seals for distinct mesoscale features within the antarctic circumpolar current. *Progress in oceanography*, *131*, 46–58. https://doi.org/10.1016/j.pocean.2014.11.011 (cit. on p. 42).

Dall'Olmo, G., Dingle, J., Polimene, L., Brewin, R. J. W., & Claustre, H. (2016). Substantial energy input to the mesopelagic ecosystem from the seasonal mixed-layer pump. *Nature geoscience*, *9*(11), 820–823. https://doi.org/10.1038/ngeo2818 (cit. on p. 39).

Danabasoglu, G., Lamarque, J.-F., Bacmeister, J., Bailey, D. A., DuVivier, A. K., Edwards, J., Emmons, L. K., Fasullo, J., Garcia, R., Gettelman, A., Hannay, C., Holland, M. M., Large, W. G., Lauritzen, P. H., Lawrence, D. M., Lenaerts, J. T. M., Lindsay, K., Lipscomb, W. H., Mills, M. J., … Strand, W. G. (2020). The community earth system model version 2 (cesm2). *Journal of advances in modeling earth systems*, *12*(2). https://doi.org/10.1029/2019ms001916 (cit. on p. 115).

De Falco, C., Desbiolles, F., Bracco, A., & Pasquero, C. (2022). Island mass effect: a review of oceanic physical processes. *Frontiers in marine science, 9*. https://doi.org/10.3389/fmars.2022.894860 (cit. on p. 31).

de Boyer Montégut, C., Madec, G., Fischer, A. S., Lazar, A., & Iudicone, D. (2004). Mixed layer depth over the global ocean: an examination of profile data and a profile-based climatology. *Journal of geophysical research, 109*(C12). https://doi.org/10.1029/2004jc002378 (cit. on pp. 107, 111).

Debreu, L., Marchesiello, P., Penven, P., & Cambon, G. (2012). Two-way nesting in split-explicit ocean models: algorithms, implementation and validation. *Ocean modelling, 49–50*, 1–21. https://doi.org/10.1016/j.ocemod.2012.03.003 (cit. on p. 53).

Dee, D. P., Uppala, S. M., Simmons, A. J., Berrisford, P., Poli, P., Kobayashi, S., Andrae, U., Balmaseda, M. A., Balsamo, G., Bauer, P., Bechtold, P., Beljaars, A. C. M., van de Berg, L., Bidlot, J., Bormann, N., Delsol, C., Dragani, R., Fuentes, M., Geer, A. J., … Vitart, F. (2011). The era-interim reanalysis: configuration and performance of the data assimilation system. *Quarterly journal of the Royal Meteorological Society. Royal Meteorological Society (Great Britain), 137*(656), 553–597. https://doi.org/10.1002/qj.828 (cit. on pp. 53, 54, 101).

Delworth, T. L., Rosati, A., Anderson, W., Adcroft, A. J., Balaji, V., Benson, R., Dixon, K., Griffies, S. M., Lee, H.-C., Pacanowski, R. C., Vecchi, G. A., Wittenberg, A. T., Zeng, F., & Zhang, R. (2012). Simulated climate and climate change in the gfdl cm2.5 high-resolution coupled climate model. *Journal of climate, 25*(8), 2755–2781. https://doi.org/10.1175/jcli-d-11-00316.1 (cit. on p. 100).

de Ruijter, W. P. M., Ridderinkhof, H., Lutjeharms, J. R. E., Schouten, M. W., & Veth, C. (2002). Observations of the flow in the mozambique channel. *Geophysical research letters, 29*(10), 140-1-140–3. https://doi.org/10.1029/2001gl013714 (cit. on pp. 45, 115).

Dewitte, B., Conejero, C., Ramos, M., Bravo, L., Garçon, V., Parada, C., Sellanes, J., Mecho, A., Muñoz, P., & Gaymer, C. F. (2021). Understanding the impact of climate change on the oceanic circulation in the chilean island ecoregions. *Aquatic conservation: marine and freshwater ecosystems, 31*(2), 232–252. https://doi.org/10.1002/aqc.3506 (cit. on pp. 103, 143).

Dewitte, B., & Takahashi, K. (2019). Diversity of moderate el niño events evolution: role of air–sea interactions in the eastern tropical pacific. *Climate dynamics, 52*(12), 7455–7476. https://doi.org/10.1007/s00382-017-4051-9 (cit. on p. 143).

Diamant, S., Rohner, C. A., Kiszka, J. J., Guillemain d'Echon, A., Guillemain d'Echon, T., Sourisseau, E., & Pierce, S. J. (2018). Movements and habitat use of satellite-tagged whale sharks off western madagascar. *Endangered species research, 36*, 49–58. https://doi.org/10.3354/esr00889 (cit. on pp. 48, 96, 99, 100, 113, 148).

DiMarco, S. F., Chapman, P., Nowlin, J., Worth D., Hacker, P., Donohue, K., Luther, M., Johnson, G. C., & Toole, J. (2002). Volume transport and property distributions of the mozambique channel. *Deep-sea research. Part II, Topical studies in oceanography, 49*(7–8), 1481–1511. https://doi.org/10.1016/s0967-0645(01)00159-x (cit. on p. 45).

Dixon, K. W., Lanzante, J. R., Nath, M. J., Hayhoe, K., Stoner, A., Radhakrishnan, A., Balaji, V., & Gaitán, C. F. (2016). Evaluating the stationarity assumption in statistically downscaled climate projections: is past performance an indicator of future results? *Climatic change*, *135*(3–4), 395–408. https://doi.org/10.1007/s10584-016-1598-0 (cit. on pp. 104, 148).

Doniol-Valcroze, T., Berteaux, D., Larouche, P., & Sears, R. (2007). Influence of thermal fronts on habitat selection by four rorqual whale species in the gulf of st. lawrence. *Marine ecology progress series*, *335*, 207–216. https://doi.org/10.3354/meps335207 (cit. on p. 42).

Doury, A., Somot, S., Gadat, S., Ribes, A., & Corre, L. (2023). Regional climate model emulator based on deep learning: concept and first evaluation of a novel hybrid downscaling approach. *Climate dynamics*, *60*(5–6), 1751–1779. https://doi.org/10.1007/s00382-022-06343-9 (cit. on pp. 113, 147).

d'Ovidio, F., De Monte, S., Alvain, S., Dandonneau, Y., & Lévy, M. (2010). Fluid dynamical niches of phytoplankton types. *Proceedings of the National Academy of Sciences of the United States of America*, *107*(43), 18366–18370. https://doi.org/10.1073/pnas.1004620107 (cit. on p. 41).

d'Ovidio, F., Fernández, V., Hernández-García, E., & López, C. (2004). Mixing structures in the mediterranean sea from finite-size lyapunov exponents. *Geophysical Research Letters*, *31*(17). https://doi.org/10.1029/2004gl020328 (cit. on p. 36).

Drenkard, E. J., Stock, C., Ross, A. C., Dixon, K. W., Adcroft, A., Alexander, M., Balaji, V., Bograd, S. J., Butenschön, M., Cheng, W., Curchitser, E., Lorenzo, E. D., Dussin, R., Haynie, A. C., Harrison, M., Hermann, A., Hollowed, A., Holsman, K., Holt, J., … Wang, M. (2021). Next-generation regional ocean projections for living marine resource management in a changing climate. *ICES journal of marine science: journal du conseil*, *78*(6), 1969–1987. https://doi.org/10.1093/icesjms/fsab100 (cit. on pp. 96, 98, 100, 101, 110, 113, 146, 147).

Fairall, C. W., Bradley, E. F., Rogers, D. P., Edson, J. B., & Young, G. S. (1996). Bulk parameterization of air-sea fluxes for tropical ocean-global atmosphere coupled-ocean atmosphere response experiment. *Journal of geophysical research*, *101*(C2), 3747–3764. https://doi.org/10.1029/95jc03205 (cit. on p. 102).

Fiedler, P. C., & Bernard, H. J. (1987). Tuna aggregation and feeding near fronts observed in satellite imagery. *Continental shelf research*, *7*(8), 871–881. https://doi.org/10.1016/0278-4343(87)90003-3 (cit. on p. 42).

Fifani, G., Baudena, A., Fakhri, M., Baaklini, G., Faugère, Y., Morrow, R., Mortier, L., & d'Ovidio, F. (2021). Drifting speed of lagrangian fronts and oil spill dispersal at the ocean surface. *Remote sensing*, *13*(22), 4499. https://doi.org/10.3390/rs13224499 (cit. on pp. 119, 121).

Findlay, K., Meyer, M., Elwen, S., Kotze, D., Johnson, R., Truter, P., Uamasse, C., Sitoe, S., Wilke, C., Kerwath, S., & et al. (2020). Distribution and abundance of humpback whales, megaptera novaeangliae, off the coast of mozambique, 2003. *J. Cetacean Res. Manage.*, (3), 163–174. https://journal.iwc.int/index.php/jcrm/article/view/327 (cit. on p. 48).

Flament, P., & Armi, L. (2000). The shear, convergence, and thermohaline structure of a front. *Journal of physical oceanography*, *30*(1), 51–66. https://doi.org/10.1175/1520-0485(2000)030<0051:tscats>2.0.co;2 (cit. on p. 28).

Fonvieille, N., Guinet, C., Saraceno, M., Picard, B., Tournier, M., Goulet, P., Campagna, C., Campagna, J., & Nerini, D. (2023). Swimming in an ocean of curves: a functional approach to understanding elephant seal habitat use in the argentine basin. *Progress in oceanography*, *218*(103120), 103120. https://doi.org/10.1016/j.pocean.2023.103120 (cit. on pp. 42, 50).

Fossette, S., Heide-Jørgensen, M.-P., Jensen, M. V., Kiszka, J., Bérubé, M., Bertrand, N., & Vély, M. (2014). Humpback whale (megaptera novaeangliae) post breeding dispersal and southward migration in the western indian ocean. *Journal of experimental marine biology and ecology*, *450*, 6–14. https://doi.org/10.1016/j.jembe.2013.10.014 (cit. on p. 48).

Frankignoul, C., Sennéchael, N., Kwon, Y.-O., & Alexander, M. A. (2011). Influence of the meridional shifts of the kuroshio and the oyashio extensions on the atmospheric circulation. *Journal of climate*, *24*(3), 762–777. https://doi.org/10.1175/2010jcli3731.1 (cit. on p. 38).

Franks, P. J. S. (1992). Sink or swim, accumulation of biomass at fronts. *Marine ecology progress series*, *82*, 1–12. https://doi.org/10.3354/meps082001 (cit. on p. 41).

Freeman, N. M., Lovenduski, N. S., Munro, D. R., Krumhardt, K. M., Lindsay, K., Long, M. C., & Maclennan, M. (2018). The variable and changing southern ocean silicate front: insights from the cesm large ensemble. *Global biogeochemical cycles*, *32*(5), 752–768. https://doi.org/10.1029/2017gb005816 (cit. on p. 40).

Frenger, I., Gruber, N., Knutti, R., & Münnich, M. (2013). Imprint of southern ocean eddies on winds, clouds and rainfall. *Nature geoscience*, *6*(8), 608–612. https://doi.org/10.1038/ngeo1863 (cit. on p. 38).

Frölicher, T. L., Rodgers, K. B., Stock, C. A., & Cheung, W. W. L. (2016). Sources of uncertainties in 21st century projections of potential ocean ecosystem stressors. *Global biogeochemical cycles*, *30*(8), 1224–1243. https://doi.org/10.1002/2015gb005338 (cit. on p. 147).

Fu, L.-L. (1983). Recent progress in the application of satellite altimetry to observing the mesoscale variability and general circulation of the oceans. *Reviews of geophysics (Washington, D.C.: 1985)*, *21*(8), 1657–1666. https://doi.org/10.1029/rg021i008p01657 (cit. on p. 25).

Galarza, J. A., Carreras-Carbonell, J., Macpherson, E., Pascual, M., Roques, S., Turner, G. F., & Rico, C. (2009). The influence of oceanographic fronts and early-life-history traits on connectivity among littoral fish species. *Proceedings of the National Academy of Sciences of the United States of America*, *106*(5), 1473–1478. https://doi.org/10.1073/pnas.0806804106 (cit. on p. 42).

Gao, W., Zhang, X., Yang, L., & Liu, H. (2010). An improved sobel edge detection. *2010 3rd International Conference on Computer Science and Information Technology* (cit. on pp. 33, 103).

Garvine, R. W., & Monk, J. D. (1974). Frontal structure of a river plume. *Journal of geophysical research*, *79*(15), 2251–2259. https://doi.org/10.1029/jc079i015p02251 (cit. on p. 30).

Gaube, P., Chelton, D. B., Samelson, R. M., Schlax, M. G., & O'Neill, L. W. (2015). Satellite observations of mesoscale eddy-induced ekman pumping. *Journal of physical oceanography*, *45*(1), 104–132. https://doi.org/10.1175/jpo-d-14-0032.1 (cit. on p. 38).

Gawarkiewicz, G., & Chapman, D. C. (1992). The role of stratification in the formation and maintenance of shelf-break fronts. *Journal of physical oceanography*, *22*(7), 753–772. https://doi.org/10.1175/1520-0485(1992)022<0753:trosit>2.0.co;2 (cit. on p. 30).

Gill, A. E., Green, J. S. A., & Simmons, A. J. (1974). Energy partition in the large-scale ocean circulation and the production of mid-ocean eddies. *Deep sea research and oceanographic abstracts*, *21*(7), 499–528. https://doi.org/10.1016/0011-7471(74)90010-2 (cit. on p. 26).

Gough, M. K., Reniers, A., Olascoaga, M. J., Haus, B. K., MacMahan, J., Paduan, J., & Halle, C. (2016). Lagrangian coherent structures in a coastal upwelling environment. *Continental shelf research*, *128*, 36–50. https://doi.org/10.1016/j.csr.2016.09.007 (cit. on p. 36).

Gower, J. F. R., Denman, K. L., & Holyer, R. J. (1980). Phytoplankton patchiness indicates the fluctuation spectrum of mesoscale oceanic structure. *Nature*, *288*(5787), 157–159. https://doi.org/10.1038/288157a0 (cit. on p. 26).

Gross, A., Kiszka, J., Van Canneyt, O., Richard, P., & Ridoux, V. (2009). A preliminary study of habitat and resource partitioning among co-occurring tropical dolphins around mayotte, southwest indian ocean. *Estuarine, coastal and shelf science*, *84*(3), 367–374. https://doi.org/10.1016/j.ecss.2009.05.017 (cit. on p. 48).

Gula, J., Molemaker, M. J., & McWilliams, J. C. (2014). Submesoscale cold filaments in the gulf stream. *Journal of physical oceanography*, *44*(10), 2617–2643. https://doi.org/10.1175/jpo-d-14-0029.1 (cit. on pp. 29, 31).

Haëck, C., Lévy, M., Mangolte, I., & Bopp, L. (2023). Satellite data reveal earlier and stronger phytoplankton blooms over fronts in the gulf stream region. *Biogeosciences*, *20*(9), 1741–1758. https://doi.org/10.5194/bg-20-1741-2023 (cit. on pp. 34, 41, 59, 61, 148).

Haller, G. (2015). Lagrangian coherent structures. *Annual Review of Fluid Mechanics*, *47*(1), 137–162. https://doi.org/10.1146/annurev-fluid-010313-141322 (cit. on pp. 35–37).

Hallier, J. P., & Fonteneau, A. (2015). Tuna aggregation and movement from tagging data: a tuna "hub" in the indian ocean. *Fisheries research*, *163*, 34–43. https://doi.org/10.1016/j.fishres.2014.06.003 (cit. on p. 48).

Halo, I., Backeberg, B., Penven, P., Ansorge, I., Reason, C., & Ullgren, J. E. (2014). Eddy properties in the mozambique channel: a comparison between observations and two numerical ocean circulation models. *Deep-sea research. Part II, Topical*

studies in oceanography, 100, 38–53. https://doi.org/10.1016/j.dsr2.2013.10.015 (cit. on pp. 45, 100, 110).

Hansen, J., Johnson, D., Lacis, A., Lebedeff, S., Lee, P., Rind, D., & Russell, G. (1981). Climate impact of increasing atmospheric carbon dioxide. *Science (New York, N.Y.), 213*(4511), 957–966. https://doi.org/10.1126/science.213.4511.957 (cit. on p. 39).

Hazen, E. L., Abrahms, B., Brodie, S., Carroll, G., Jacox, M. G., Savoca, M. S., Scales, K. L., Sydeman, W. J., & Bograd, S. J. (2019). Marine top predators as climate and ecosystem sentinels. *Frontiers in ecology and the environment, 17*(10), 565–574. https://doi.org/10.1002/fee.2125 (cit. on pp. 97, 99, 118, 120).

Hermes, J. C., Reason, C. J. C., & Lutjeharms, J. R. E. (2007). Modeling the variability of the greater agulhas current system. *Journal of climate, 20*(13), 3131–3146. https://doi.org/10.1175/jcli4154.1 (cit. on p. 110).

Hernández-Carrasco, I., Alou-Font, E., Dumont, P.-A., Cabornero, A., Allen, J., & Orfila, A. (2020). Lagrangian flow effects on phytoplankton abundance and composition along filament-like structures. *Progress in Oceanography, 189*(102469), 102469. https://doi.org/10.1016/j.pocean.2020.102469 (cit. on pp. 36, 41).

Hernández-Carrasco, I., & Orfila, A. (2018). The role of an intense front on the connectivity of the western mediterranean sea: the cartagena-tenes front. *Journal of Geophysical Research. Oceans, 123*(6), 4398–4422. https://doi.org/10.1029/2017jc013613 (cit. on p. 42).

Hernández-Carrasco, I., Orfila, A., Rossi, V., & Garçon, V. (2018). Effect of small scale transport processes on phytoplankton distribution in coastal seas. *Scientific Reports, 8*(1), 8613. https://doi.org/10.1038/s41598-018-26857-9 (cit. on pp. 36, 41).

Hernández-Carrasco, I., López, C., Hernández-García, E., & Turiel, A. (2011). How reliable are finite-size lyapunov exponents for the assessment of ocean dynamics? *Ocean Modelling, 36*(3–4), 208–218. https://doi.org/10.1016/j.ocemod.2010.12.006 (cit. on pp. 35–37, 56).

Hernández-Carrasco, I., Rossi, V., Navarro, G., Turiel, A., Bracco, A., & Orfila, A. (2023). Flow structures with high lagrangian coherence rate promote diatom blooms in oligotrophic waters. *Geophysical research letters, 50*(15). https://doi.org/10.1029/2023gl103688 (cit. on p. 36).

Ho, C.-R., Zheng, Q., & Kuo, N.-J. (2004). Seawifs observations of upwelling south of madagascar: long-term variability and interaction with east madagascar current. *Deep-sea research. Part II, Topical studies in oceanography, 51*(1–3), 59–67. https://doi.org/10.1016/j.dsr2.2003.05.001 (cit. on p. 47).

Hogg, A., Dewar, W. K., Berloff, P., Kravtsov, S., & Hutchinson, D. K. (2009). The effects of mesoscale ocean–atmosphere coupling on the large-scale ocean circulation. *Journal of climate, 22*(15), 4066–4082. https://doi.org/10.1175/2009jcli2629.1 (cit. on p. 38).

Hogg, A., Meredith, M. P., Chambers, D. P., Abrahamsen, E. P., Hughes, C. W., & Morrison, A. K. (2015). Recent trends in the southern ocean eddy field. *Journal*

of geophysical research. Oceans, *120*(1), 257–267. https://doi.org/10.1002/2014jc010470 (cit. on p. 38).

Hogg, A. M., Penduff, T., Close, S. E., Dewar, W. K., Constantinou, N. C., & Martínez-Moreno, J. (2022). Circumpolar variations in the chaotic nature of southern ocean eddy dynamics. *Journal of geophysical research. Oceans*, *127*(5). https://doi.org/10.1029/2022jc018440 (cit. on p. 147).

Holyer, R. J., & Peckinpaugh, S. H. (1989). Edge detection applied to satellite imagery of the oceans. *IEEE transactions on geoscience and remote sensing: a publication of the IEEE Geoscience and Remote Sensing Society*, *27*(1), 46–56. https://doi.org/10.1109/36.20274 (cit. on p. 33).

Howard, E. M., Frenzel, H., Kessouri, F., Renault, L., Bianchi, D., McWilliams, J. C., & Deutsch, C. (2020). Attributing causes of future climate change in the california current system with multimodel downscaling. *Global biogeochemical cycles*, *34*(11). https://doi.org/10.1029/2020gb006646 (cit. on pp. 100, 150).

Hu, D., Wu, L., Cai, W., Gupta, A. S., Ganachaud, A., Qiu, B., Gordon, A. L., Lin, X., Chen, Z., Hu, S., Wang, G., Wang, Q., Sprintall, J., Qu, T., Kashino, Y., Wang, F., & Kessler, W. S. (2015). Pacific western boundary currents and their roles in climate. *Nature*, *522*(7556), 299–308. https://doi.org/10.1038/nature14504 (cit. on p. 109).

Huang, B., & Kinter, I., James L. (2002). Interannual variability in the tropical indian ocean. *Journal of geophysical research*, *107*(C11). https://doi.org/10.1029/2001jc001278 (cit. on p. 144).

Huggett, J. A. (2014). Mesoscale distribution and community composition of zooplankton in the mozambique channel. *Deep-sea research. Part II, Topical studies in oceanography*, *100*, 119–135. https://doi.org/10.1016/j.dsr2.2013.10.021 (cit. on p. 47).

Hunt, B. P. V., & Hosie, G. W. (2005). Zonal structure of zooplankton communities in the southern ocean south of australia: results from a 2150km continuous plankton recorder transect. *Deep-sea research. Part I, Oceanographic research papers*, *52*(7), 1241–1271. https://doi.org/10.1016/j.dsr.2004.11.019 (cit. on p. 41).

IPCC. (2023). Ipcc, 2023: sections. in: climate change 2023: synthesis report. contribution of working groups i, ii and iii to the sixth assessment report of the intergovernmental panel on climate change [core writing team, h. lee and j. romero (eds.)], 35–115. https://doi.org/10.59327/IPCC/AR6-9789291691647 (cit. on pp. 39, 147).

Jo, H.-S., Ham, Y.-G., Kug, J.-S., Li, T., Kim, J.-H., Kim, J.-G., & Kim, H. (2022). Southern indian ocean dipole as a trigger for central pacific el niño since the 2000s. *Nature communications*, *13*(1). https://doi.org/10.1038/s41467-022-34721-8 (cit. on pp. 54, 55).

Jochum, M., & Murtugudde, R. (2006). *Physical oceanography: developments since 1950*. Springer Science Business Media. (Cit. on p. 25).

José, Y. S., Aumont, O., Machu, E., Penven, P., Moloney, C. L., & Maury, O. (2014). Influence of mesoscale eddies on biological production in the mozambique channel: several contrasted examples from a coupled ocean-biogeochemistry

model. *Deep-sea research. Part II, Topical studies in oceanography*, *100*, 79–93. https://doi.org/10.1016/j.dsr2.2013.10.018 (cit. on pp. 47, 100, 149, 150).

Kaplan, D. M., Chassot, E., Amandé, J. M., Dueri, S., Demarcq, H., Dagorn, L., & Fonteneau, A. (2014). Spatial management of indian ocean tropical tuna fisheries: potential and perspectives. *ICES journal of marine science: journal du conseil*, *71*(7), 1728–1749. https://doi.org/10.1093/icesjms/fst233 (cit. on p. 48).

Kay, J. E., Deser, C., Phillips, A., Mai, A., Hannay, C., Strand, G., Arblaster, J. M., Bates, S. C., Danabasoglu, G., Edwards, J., Holland, M., Kushner, P., Lamarque, J.-F., Lawrence, D., Lindsay, K., Middleton, A., Munoz, E., Neale, R., Oleson, K., … Vertenstein, M. (2015). The community earth system model (cesm) large ensemble project: a community resource for studying climate change in the presence of internal climate variability. *Bulletin of the American Meteorological Society*, *96*(8), 1333–1349. https://doi.org/10.1175/bams-d-13-00255.1 (cit. on pp. 54, 96, 98, 102, 147).

Kazmin, A. S., & Rienecker, M. M. (1996). Variability and frontogenesis in the large-scale oceanic frontal zones. *Journal of geophysical research*, *101*(C1), 907–921. https://doi.org/10.1029/95jc02992 (cit. on p. 33).

Kessler, W. S. (2006). The circulation of the eastern tropical pacific: a review. *Progress in oceanography*, *69*(2–4), 181–217. https://doi.org/10.1016/j.pocean.2006.03.009 (cit. on p. 143).

Kirby, D. S., Fiksen, Ø., & Hart, P. J. B. (2000). A dynamic optimisation model for the behaviour of tunas at ocean fronts. *Fisheries oceanography*, *9*(4), 328–342. https://doi.org/10.1046/j.1365-2419.2000.00144.x (cit. on p. 42).

Kirches, G., Paperin, M., Klein, H., Brockmann, C., & Stelzer, K. (2016). Gradhist — a method for detection and analysis of oceanic fronts from remote sensing data. *Remote sensing of environment*, *181*, 264–280. https://doi.org/10.1016/j.rse.2016.04.009 (cit. on p. 34).

Kiszka, J., Muir, C., & Amon, A. (2009). Status of a marginal dugong (dugong dugon) population in the lagoon of mayotte (mozambique channel), in the western indian ocean. *Western Indian Ocean journal of marine science*, *6*(1). https://doi.org/10.4314/wiojms.v6i1.48230 (cit. on p. 48).

Kiszka, J., & Ridoux, V. (2007). Cetacean diversity around the mozambique channel island of mayotte (comoros archipelago). *Journal of cetacean resource management*, *2*, 105–109 (cit. on pp. 48, 148).

Klein, P., & Lapeyre, G. (2009). The oceanic vertical pump induced by mesoscale and submesoscale turbulence. *Annual review of marine science*, *1*(1), 351–375. https://doi.org/10.1146/annurev.marine.010908.163704 (cit. on pp. 29, 40, 43, 118, 120, 138).

Koseki, S., Giordani, H., & Goubanova, K. (2019). Frontogenesis of the angola–benguela frontal zone. *Ocean science*, *15*(1), 83–96. https://doi.org/10.5194/os-15-83-2019 (cit. on p. 142).

Kuwano-Yoshida, A., & Minobe, S. (2017). Storm-track response to sst fronts in the northwestern pacific region in an agcm. *Journal of climate*, *30*(3), 1081–1102. https://doi.org/10.1175/jcli-d-16-0331.1 (cit. on p. 38).

Landry, M. R., Ohman, M. D., Goericke, R., Stukel, M. R., Barbeau, K. A., Bundy, R., & Kahru, M. (2012). Pelagic community responses to a deep-water front in the california current ecosystem: overview of the a-front study. *Journal of plankton research*, *34*(9), 739–748. https://doi.org/10.1093/plankt/fbs025 (cit. on p. 31).

Laran, S., Authier, M., Van Canneyt, O., Dorémus, G., Watremez, P., & Ridoux, V. (2017). A comprehensive survey of pelagic megafauna: their distribution, densities, and taxonomic richness in the tropical southwest indian ocean. *Frontiers in marine science*, *4*. https://doi.org/10.3389/fmars.2017.00139 (cit. on pp. 48, 59, 61, 96, 99, 100, 119, 120, 140, 148).

Large, W. G., McWilliams, J. C., & Doney, S. C. (1994). Oceanic vertical mixing: a review and a model with a nonlocal boundary layer parameterization. *Reviews of geophysics (Washington, D.C.: 1985)*, *32*(4), 363–403. https://doi.org/10.1029/94rg01872 (cit. on p. 101).

Le Corre, M., Jaeger, A., Pinet, P., Kappes, M. A., Weimerskirch, H., Catry, T., Ramos, J. A., Russell, J. C., Shah, N., & Jaquemet, S. (2012). Tracking seabirds to identify potential marine protected areas in the tropical western indian ocean. *Biological conservation*, *156*, 83–93. https://doi.org/10.1016/j.biocon.2011.11.015 (cit. on pp. 48, 96, 99, 113, 119, 120, 140, 148).

Legeckis, R. (1978). A survey of worldwide sea surface temperature fronts detected by environmental satellites. *Journal of geophysical research*, *83*(C9), 4501. https://doi.org/10.1029/jc083ic09p04501 (cit. on pp. 33, 59, 61).

Lehahn, Y., d'Ovidio, F., & Koren, I. (2018). A satellite-based lagrangian view on phytoplankton dynamics. *Annual review of marine science*, *10*(1), 99–119. https://doi.org/10.1146/annurev-marine-121916-063204 (cit. on pp. 35–37).

Letelier, J., Pizarro, O., & Nuñez, S. (2009). Seasonal variability of coastal upwelling and the upwelling front off central chile. *Journal of geophysical research*, *114*(C12). https://doi.org/10.1029/2008jc005171 (cit. on p. 31).

Lévy, M., Ferrari, R., Franks, P. J. S., Martin, A. P., & Rivière, P. (2012). Bringing physics to life at the submesoscale. *Geophysical research letters*, *39*(14). https://doi.org/10.1029/2012gl052756 (cit. on p. 100).

Lévy, M., Franks, P. J. S., & Smith, K. S. (2018). The role of submesoscale currents in structuring marine ecosystems. *Nature communications*, *9*(1), 4758. https://doi.org/10.1038/s41467-018-07059-3 (cit. on pp. 26, 29, 32, 41, 43, 50, 59, 61, 138, 150).

Lévy, M., Jahn, O., Dutkiewicz, S., Follows, M. J., & d'Ovidio, F. (2015). The dynamical landscape of marine phytoplankton diversity. *Journal of the Royal Society, Interface*, *12*(111), 20150481. https://doi.org/10.1098/rsif.2015.0481 (cit. on p. 41).

Lévy, M., Klein, P., & Treguier, A.-M. (2001). Impact of sub-mesoscale physics on production and subduction of phytoplankton in an oligotrophic regime. *Journal of marine research*, *59*(4), 535–565. https://doi.org/10.1357/002224001762842181 (cit. on pp. 40, 41).

Lewison, R. L., Crowder, L. B., Wallace, B. P., Moore, J. E., Cox, T., Zydelis, R., McDonald, S., DiMatteo, A., Dunn, D. C., Kot, C. Y., Bjorkland, R., Kelez, S., Soykan, C.,

Stewart, K. R., Sims, M., Boustany, A., Read, A. J., Halpin, P., Nichols, W. J., & Safina, C. (2014). Global patterns of marine mammal, seabird, and sea turtle bycatch reveal taxa-specific and cumulative megafauna hotspots. *Proceedings of the National Academy of Sciences of the United States of America*, *111*(14), 5271–5276. https://doi.org/10.1073/pnas.1318960111 (cit. on p. 48).

Li, G., & Xie, S.-P. (2014). Tropical biases in cmip5 multimodel ensemble: the excessive equatorial pacific cold tongue and double itcz problems. *Journal of climate*, *27*(4), 1765–1780. https://doi.org/10.1175/jcli-d-13-00337.1 (cit. on p. 145).

Li, G., Cheng, L., Zhu, J., Trenberth, K. E., Mann, M. E., & Abraham, J. P. (2020). Increasing ocean stratification over the past half-century. *Nature climate change*, *10*(12), 1116–1123. https://doi.org/10.1038/s41558-020-00918-2 (cit. on pp. 100, 111).

Li, Q. P., Franks, P. J. S., Ohman, M. D., & Landry, M. R. (2012). Enhanced nitrate fluxes and biological processes at a frontal zone in the southern california current system. *Journal of plankton research*, *34*(9), 790–801. https://doi.org/10.1093/plankt/fbs006 (cit. on p. 40).

Liang, X.-Z., Kunkel, K. E., Meehl, G. A., Jones, R. G., & Wang, J. X. L. (2008). Regional climate models downscaling analysis of general circulation models present climate biases propagation into future change projections. *Geophysical research letters*, *35*(8). https://doi.org/10.1029/2007gl032849 (cit. on p. 146).

Lima, I. D., Olson, D. B., & Doney, S. C. (2002). Biological response to frontal dynamics and mesoscale variability in oligotrophic environments: biological production and community structure. *Journal of geophysical research*, *107*(C8). https://doi.org/10.1029/2000jc000393 (cit. on p. 41).

Lin, L., Liu, D., Luo, C., & Xie, L. (2019). Double fronts in the yellow sea in summertime identified using sea surface temperature data of multi-scale ultra-high resolution analysis. *Continental shelf research*, *175*, 76–86. https://doi.org/10.1016/j.csr.2019.02.004 (cit. on p. 33).

Liu, D., Wang, Y., Wang, Y., & Keesing, J. K. (2018). Ocean fronts construct spatial zonation in microfossil assemblages. *Global ecology and biogeography: a journal of macroecology*, *27*(10), 1225–1237. https://doi.org/10.1111/geb.12779 (cit. on p. 33).

Liu, X., & Levine, N. (2016). Enhancement of phytoplankton chlorophyll by submesoscale frontal dynamics in the north pacific subtropical gyre. *Geophysical research letters*, *43*(4), 1651–1659. https://doi.org/10.1002/2015gl066996 (cit. on pp. 34, 41).

Locarnini, R. A., Mishonov, A. V., Baranova, O. K., Boyer, T. P., Zweng, M. M., Garcia, H. E., Reagan, J. R., Seidov, D., Weathers, K. W., Paver, C. R., & Smolyar, I. V. (2018). World ocean atlas. *Temperature. A. Mishonov, Technical Editor. NOAA Atlas NESDIS*, *1* (cit. on p. 104).

Longhurst, A. (2007). *Ecological geography of the sea* (2nd ed.). Academic Press. https://doi.org/https://doi.org/10.1016/B978-0-12-455521-1.X5000-1 (cit. on pp. 119, 121).

Lozier, M. S., & Reed, M. S. C. (2005). The influence of topography on the stability of shelfbreak fronts. *Journal of physical oceanography*, *35*(6), 1023–1036. https://doi.org/10.1175/jpo2717.1 (cit. on p. 30).

Luo, J. Y., Grassian, B., Tang, D., Irisson, J. O., Greer, A. T., Guigand, C. M., McClatchie, S., & Cowen, R. K. (2014). Environmental drivers of the fine-scale distribution of a gelatinous zooplankton community across a mesoscale front. *Marine ecology progress series*, *510*, 129–149. https://doi.org/10.3354/meps10908 (cit. on p. 41).

Lutjeharms, J. R. E. (2006). *Three decades of research on the greater agulhas current*. https://doi.org/10.5194/osd-3-939-2006 (cit. on p. 44).

Lutjeharms, J. R. E., & Stockton, P. L. (1987). Kinematics of the upwelling front off southern africa. *South African Journal of Marine Science/Suid-Afrikaanse Tydskrif vir Seewetenskap*, *5*(1), 35–49. https://doi.org/10.2989/025776187784522612 (cit. on p. 31).

Lutjeharms, J. R. E., Biastoch, A., Van der Werf, P. M., Ridderinkhof, H., & De Ruijter, W. P. M. (2012). On the discontinuous nature of the mozambique current. *South African journal of science*, *108*(1/2). https://doi.org/10.4102/sajs.v108i1/2.428 (cit. on pp. 45, 100, 110, 115).

Ma, X., Chang, P., Saravanan, R., Montuoro, R., Hsieh, J.-S., Wu, D., Lin, X., Wu, L., & Jing, Z. (2015). Distant influence of kuroshio eddies on north pacific weather patterns? *Scientific reports*, *5*(1). https://doi.org/10.1038/srep17785 (cit. on p. 38).

Ma, X., Jing, Z., Chang, P., Liu, X., Montuoro, R., Small, R. J., Bryan, F. O., Greatbatch, R. J., Brandt, P., Wu, D., Lin, X., & Wu, L. (2016). Western boundary currents regulated by interaction between ocean eddies and the atmosphere. *Nature*, *535*(7613), 533–537. https://doi.org/10.1038/nature18640 (cit. on p. 38).

Mahadevan, A. (2016). The impact of submesoscale physics on primary productivity of plankton. *Annual review of marine science*, *8*(1), 161–184. https://doi.org/10.1146/annurev-marine-010814-015912 (cit. on pp. 28, 29, 32, 40, 41, 43, 118, 120, 138, 139).

Mahadevan, A., & Archer, D. (2000). Modeling the impact of fronts and mesoscale circulation on the nutrient supply and biogeochemistry of the upper ocean. *Journal of Geophysical Research*, *105*(C1), 1209–1225. https://doi.org/10.1029/1999jc900216 (cit. on p. 40).

Malauene, B. S., Shillington, F. A., Roberts, M. J., & Moloney, C. L. (2014). Cool, elevated chlorophyll-a waters off northern mozambique. *Deep-sea research. Part II, Topical studies in oceanography*, *100*, 68–78. https://doi.org/10.1016/j.dsr2.2013.10.017 (cit. on p. 47).

Mangolte, I., Lévy, M., Dutkiewicz, S., Clayton, S., & Jahn, O. (2022). Plankton community response to fronts: winners and losers. *Journal of plankton research*, *44*(2), 241–258. https://doi.org/10.1093/plankt/fbac010 (cit. on p. 41).

Mangolte, I., Lévy, M., Haëck, C., & Ohman, M. D. (2023). Sub-frontal niches of plankton communities driven by transport and trophic interactions at ocean fronts.

Biogeosciences, *20*(15), 3273–3299. https://doi.org/10.5194/bg-20-3273-2023 (cit. on pp. 29, 41, 100, 143).

Mannocci, L., Laran, S., Monestiez, P., Dorémus, G., Van Canneyt, O., Watremez, P., & Ridoux, V. (2014). Predicting top predator habitats in the southwest indian ocean. *Ecography*, *37*(3), 261–278. https://doi.org/10.1111/j.1600-0587.2013.00317.x (cit. on p. 48).

Marathe, S., Terray, P., & Karumuri, A. (2021). Tropical indian ocean and enso relationships in a changed climate. *Climate dynamics*, *56*(9–10), 3255–3276. https://doi.org/10.1007/s00382-021-05641-y (cit. on p. 54).

Marchesiello, P., McWilliams, J. C., & Shchepetkin, A. (2001). Open boundary conditions for long-term integration of regional oceanic models. *Ocean modelling*, *3*(1–2), 1–20. https://doi.org/10.1016/s1463-5003(00)00013-5 (cit. on pp. 53, 101).

Mariani, P., MacKenzie, B. R., Iudicone, D., & Bozec, A. (2010). Modelling retention and dispersion mechanisms of bluefin tuna eggs and larvae in the northwest mediterranean sea. *Progress in oceanography*, *86*(1–2), 45–58. https://doi.org/10.1016/j.pocean.2010.04.027 (cit. on p. 42).

Marsac, F., Barlow, R., Ternon, J. F., Ménard, F., & Roberts, M. (2014). Ecosystem functioning in the mozambique channel: synthesis and future research. *Deep-sea research. Part II, Topical studies in oceanography*, *100*, 212–220. https://doi.org/10.1016/j.dsr2.2013.10.028 (cit. on pp. 46, 49, 59, 61, 138).

Martínez-Moreno, J., Hogg, A. M., & England, M. H. (2022). Climatology, seasonality, and trends of spatially coherent ocean eddies. *Journal of geophysical research. Oceans*, *127*(7). https://doi.org/10.1029/2021jc017453 (cit. on pp. 100, 142).

Martínez-Moreno, J., Hogg, A. M., England, M. H., Constantinou, N. C., Kiss, A. E., & Morrison, A. K. (2021). Global changes in oceanic mesoscale currents over the satellite altimetry record. *Nature climate change*, *11*(5), 397–403. https://doi.org/10.1038/s41558-021-01006-9 (cit. on pp. 95, 96, 98, 100, 110, 111, 118, 120, 139, 140).

Martínez-Moreno, J., Hogg, A. M., Kiss, A. E., Constantinou, N. C., & Morrison, A. K. (2019). Kinetic energy of eddy-like features from sea surface altimetry. *Journal of advances in modeling earth systems*, *11*(10), 3090–3105. https://doi.org/10.1029/2019ms001769 (cit. on p. 142).

Mathur, M., David, M. J., Sharma, R., & Agarwal, N. (2019). Thermal fronts and attracting lagrangian coherent structures in the north bay of bengal during december 2015–march 2016. *Deep-sea Research. Part II, Topical Studies in Oceanography*, *168*(104636), 104636. https://doi.org/10.1016/j.dsr2.2019.104636 (cit. on pp. 59, 61).

Mauzole, Y. L. (2022). Objective delineation of persistent sst fronts based on global satellite observations. *Remote sensing of environment*, *269*(112798), 112798. https://doi.org/10.1016/j.rse.2021.112798 (cit. on pp. 29–31, 59, 61).

Maxwell, S. M., Gjerde, K. M., Conners, M. G., & Crowder, L. B. (2020). Mobile protected areas for biodiversity on the high seas. *Science (New York, N.Y.)*, *367*(6475), 252–254. https://doi.org/10.1126/science.aaz9327 (cit. on p. 152).

Maxwell, S. M., Hazen, E. L., Lewison, R. L., Dunn, D. C., Bailey, H., Bograd, S. J., Briscoe, D. K., Fossette, S., Hobday, A. J., Bennett, M., Benson, S., Caldwell, M. R., Costa, D. P., Dewar, H., Eguchi, T., Hazen, L., Kohin, S., Sippel, T., & Crowder, L. B. (2015). Dynamic ocean management: defining and conceptualizing real-time management of the ocean. *Marine policy*, *58*, 42–50. https://doi.org/10.1016/j.marpol.2015.03.014 (cit. on pp. 41, 42).

McClanahan, T. R., Ateweberhan, M., Darling, E. S., Graham, N. A. J., & Muthiga, N. A. (2014). Biogeography and change among regional coral communities across the western indian ocean. *PloS one*, *9*(4), e93385. https://doi.org/10.1371/journal.pone.0093385 (cit. on pp. 148, 150).

McGillicuddy, J., D. J., Anderson, L. A., Doney, S. C., & Maltrud, M. E. (2003). Eddy-driven sources and sinks of nutrients in the upper ocean: results from a 0.1° resolution model of the north atlantic. *Global biogeochemical cycles*, *17*(2). https://doi.org/10.1029/2002gb001987 (cit. on p. 41).

McGillicuddy, J., Dennis J. (2016). Mechanisms of physical-biological-biogeochemical interaction at the oceanic mesoscale. *Annual review of marine science*, *8*(1), 125–159. https://doi.org/10.1146/annurev-marine-010814-015606 (cit. on p. 43).

McKee, D. C., Doney, S. C., Della Penna, A., Boss, E. S., Gaube, P., & Behrenfeld, M. J. (2023). Biophysical dynamics at ocean fronts revealed by bio-argo floats. *Journal of geophysical research. Oceans*, *128*(3). https://doi.org/10.1029/2022jc019226 (cit. on p. 40).

McWilliams, J. C. (2016). Submesoscale currents in the ocean. *Proceedings. Mathematical, physical, and engineering sciences*, *472*(2189), 20160117. https://doi.org/10.1098/rspa.2016.0117 (cit. on pp. 29, 31, 32, 43).

McWilliams, J. C. (2021). Oceanic frontogenesis. *Annual review of marine science*, *13*(1), 227–253. https://doi.org/10.1146/annurev-marine-032320-120725 (cit. on pp. 28–32, 43, 111, 112, 138).

Mecking, J. V., & Drijfhout, S. S. (2023). The decrease in ocean heat transport in response to global warming. *Nature climate change*. https://doi.org/10.1038/s41558-023-01829-8 (cit. on p. 100).

Miller, P. (2009). Composite front maps for improved visibility of dynamic sea-surface features on cloudy seawifs and avhrr data. *Journal of marine systems: journal of the European Association of Marine Sciences and Techniques*, *78*(3), 327–336. https://doi.org/10.1016/j.jmarsys.2008.11.019 (cit. on p. 34).

Miller, P., Xu, W., & Carruthers, M. (2015). Seasonal shelf-sea front mapping using satellite ocean colour and temperature to support development of a marine protected area network. *Deep-sea research. Part II, Topical studies in oceanography*, *119*, 3–19. https://doi.org/10.1016/j.dsr2.2014.05.013 (cit. on p. 34).

Minobe, S., Kuwano-Yoshida, A., Komori, N., Xie, S.-P., & Small, R. J. (2008). Influence of the gulf stream on the troposphere. *Nature*, *452*(7184), 206–209. https://doi.org/10.1038/nature06690 (cit. on p. 38).

Miramontes, E., Penven, P., Fierens, R., Droz, L., Toucanne, S., Jorry, S. J., Jouet, G., Pastor, L., Silva Jacinto, R., Gaillot, A., Giraudeau, J., & Raisson, F. (2019). The

influence of bottom currents on the zambezi valley morphology (mozambique channel, sw indian ocean): in situ current observations and hydrodynamic modelling. *Marine geology*, *410*, 42–55. https://doi.org/10.1016/j.margeo.2019.01.002 (cit. on p. 102).

Moore, K., Abbott, M., & Richman, J. (1997). Variability in the location of the antarctic polar front (90°–20°w) from satellite sea surface temperature data. *Journal of geophysical research*, *102*(C13), 27825–27833. https://doi.org/10.1029/97jc01705 (cit. on p. 33).

Morato, T., Miller, P. I., Dunn, D. C., Nicol, S. J., Bowcott, J., & Halpin, P. N. (2016). A perspective on the importance of oceanic fronts in promoting aggregation of visitors to seamounts. *Fish and fisheries (Oxford, England)*, *17*(4), 1227–1233. https://doi.org/10.1111/faf.12126 (cit. on p. 42).

Moreton, S. M., Ferreira, D., Roberts, M. J., & Hewitt, H. T. (2020). Evaluating surface eddy properties in coupled climate simulations with 'eddy-present' and 'eddy-rich' ocean resolution. *Ocean modelling*, *147*(101567), 101567. https://doi.org/10.1016/j.ocemod.2020.101567 (cit. on p. 100).

Munday, D. R., & Zhai, X. (2015). Sensitivity of southern ocean circulation to wind stress changes: role of relative wind stress. *Ocean modelling*, *95*, 15–24. https://doi.org/10.1016/j.ocemod.2015.08.004 (cit. on p. 38).

Munk, W., & Wunsch, C. (1982). Observing the ocean in the 1990s. *Philosophical transactions of the Royal Society of London*, *307*(1499), 439–464. https://doi.org/10.1098/rsta.1982.0120 (cit. on p. 25).

Munk, W., Armi, L., Fischer, K., & Zachariasen, F. (2000). Spirals on the sea. *Proceedings. Mathematical, physical, and engineering sciences*, *456*(1997), 1217–1280. https://doi.org/10.1098/rspa.2000.0560 (cit. on pp. 25, 26, 33).

Murase, H., Hakamada, T., Matsuoka, K., Nishiwaki, S., Inagake, D., Okazaki, M., Tojo, N., & Kitakado, T. (2014). Distribution of sei whales (balaenoptera borealis) in the subarctic–subtropical transition area of the western north pacific in relation to oceanic fronts. *Deep-sea research. Part II, Topical studies in oceanography*, *107*, 22–28. https://doi.org/10.1016/j.dsr2.2014.05.002 (cit. on p. 42).

Nagai, T., Tandon, A., & Rudnick, D. L. (2006). Two-dimensional ageostrophic secondary circulation at ocean fronts due to vertical mixing and large-scale deformation. *Journal of geophysical research*, *111*(C9). https://doi.org/10.1029/2005jc002964 (cit. on p. 29).

Nagai, T., & Clayton, S. (2017). Nutrient interleaving below the mixed layer of the kuroshio extension front. *Ocean dynamics*, *67*(8), 1027–1046. https://doi.org/10.1007/s10236-017-1070-3 (cit. on p. 40).

Nagata, Y., Yoshida, J., & Shin, H.-R. (1986). Detailed structure of the kuroshio front and the origin of the water in warm-core rings. *Deep-sea research. Part A, Oceanographic research papers*, *33*(11–12), 1509–1526. https://doi.org/10.1016/0198-0149(86)90065-8 (cit. on p. 31).

Nakamura, H., Sampe, T., Tanimoto, Y., & Shimpo, A. (2013). Observed associations among storm tracks, jet streams and midlatitude oceanic fronts. In *Earth's climate* (pp. 329–345). American Geophysical Union. (Cit. on p. 38).

Nataniel, A., Pennino, M. G., Lopez, J., & Soto, M. (2022). Modelling the impacts of climate change on skipjack tuna (katsuwonus pelamis) in the mozambique channel. *Fisheries oceanography*, *31*(2), 149–163. https://doi.org/10.1111/fog.12568 (cit. on pp. 48, 59, 61, 100).

Netburn, A. N., & Koslow, J. A. (2018). Mesopelagic fish assemblages across oceanic fronts: a comparison of three frontal systems in the southern california current ecosystem. *Deep-sea research. Part I, Oceanographic research papers*, *134*, 80–91. https://doi.org/10.1016/j.dsr.2018.03.005 (cit. on p. 42).

Nieblas, A.-E., Demarcq, H., Drushka, K., Sloyan, B., & Bonhommeau, S. (2014). Front variability and surface ocean features of the presumed southern bluefin tuna spawning grounds in the tropical southeast indian ocean. *Deep-sea research. Part II, Topical studies in oceanography*, *107*, 64–76. https://doi.org/10.1016/j.dsr2.2013.11.007 (cit. on pp. 34, 42).

Nieto, K., Demarcq, H., & McClatchie, S. (2012). Mesoscale frontal structures in the canary upwelling system: new front and filament detection algorithms applied to spatial and temporal patterns. *Remote sensing of environment*, *123*, 339–346. https://doi.org/10.1016/j.rse.2012.03.028 (cit. on p. 34).

Nieto, K., Xu, Y., Teo, S. L. H., McClatchie, S., & Holmes, J. (2017). How important are coastal fronts to albacore tuna (thunnus alalunga) habitat in the northeast pacific ocean? *Progress in oceanography*, *150*, 62–71. https://doi.org/10.1016/j.pocean.2015.05.004 (cit. on pp. 34, 42).

Obura, D., Bandeira, S. O., Bodin, N., Burgener, V., Braulik, G., Chassot, E., Gullström, M., Kochzius, M., Nicoll, M., Osuka, K., Ralison, H. O., Richmond, M., Samoilys, M. A., Scheren, P., & Ternon, J.-F. (2019). The northern mozambique channel. In *World seas: an environmental evaluation* (pp. 75–99). Elsevier. (Cit. on pp. 45, 47–49, 59, 61, 100, 138, 150).

Obura, D. (2012). The diversity and biogeography of western indian ocean reef-building corals. *PloS one*, *7*(9), e45013. https://doi.org/10.1371/journal.pone.0045013 (cit. on p. 47).

Obura, D., Gudka, M., Samoilys, M., Osuka, K., Mbugua, J., Keith, D. A., Porter, S., Roche, R., van Hooidonk, R., Ahamada, S., Araman, A., Karisa, J., Komakoma, J., Madi, M., Ravinia, I., Razafindrainibe, H., Yahya, S., & Zivane, F. (2021). Vulnerability to collapse of coral reef ecosystems in the western indian ocean. *Nature sustainability*, *5*(2), 104–113. https://doi.org/10.1038/s41893-021-00817-0 (cit. on pp. 150, 151).

Oh, Y., Kim, D.-W., Jo, Y.-H., Hwang, J.-D., & Chung, C.-Y. (2020). Spatial variability of fishing grounds in response to oceanic front changes detected by multiple satellite measurements in the east (japan) sea. *International journal of remote sensing*, *41*(15), 5884–5904. https://doi.org/10.1080/01431161.2019.1685722 (cit. on p. 42).

Ohman, M. D., Powell, J. R., Picheral, M., & Jensen, D. W. (2012). Mesozooplankton and particulate matter responses to a deep-water frontal system in the southern california current system. *Journal of plankton research*, *34*(9), 815–827. https://doi.org/10.1093/plankt/fbs028 (cit. on p. 41).

Omand, M. M., D'Asaro, E. A., Lee, C. M., Perry, M. J., Briggs, N., Cetinić, I., & Mahadevan, A. (2015). Eddy-driven subduction exports particulate organic carbon from the spring bloom. *Science*, *348*(6231), 222–225. https://doi.org/10.1126/science.1260062 (cit. on p. 39).

O'Neill, L. W., Chelton, D. B., & Esbensen, S. K. (2012). Covariability of surface wind and stress responses to sea surface temperature fronts. *Journal of climate*, *25*(17), 5916–5942. https://doi.org/10.1175/jcli-d-11-00230.1 (cit. on pp. 38, 119, 121).

O'Reilly, C. H., & Czaja, A. (2015). The response of the pacific storm track and atmospheric circulation to kuroshio extension variability: response of storm tracks to kuroshio extension variability. *Quarterly journal of the Royal Meteorological Society. Royal Meteorological Society (Great Britain)*, *141*(686), 52–66. https://doi.org/10.1002/qj.2334 (cit. on p. 38).

Orsi, A. H., Whitworth, I., Thomas, & Nowlin, J., Worth D. (1995). On the meridional extent and fronts of the antarctic circumpolar current. *Deep-sea research. Part I, Oceanographic research papers*, *42*(5), 641–673. https://doi.org/10.1016/0967-0637(95)00021-w (cit. on p. 31).

Oschlies, A., & Garçon, V. (1998). Eddy-induced enhancement of primary production in a model of the north atlantic ocean. *Nature*, *394*(6690), 266–269. https://doi.org/10.1038/28373 (cit. on p. 40).

Palastanga, V., van Leeuwen, P. J., & de Ruijter, W. P. M. (2006). A link between low-frequency mesoscale eddy variability around madagascar and the large-scale indian ocean variability. *Journal of geophysical research*, *111*(C9). https://doi.org/10.1029/2005jc003081 (cit. on p. 144).

Pattiaratchi, C., van der Mheen, M., Schlundt, C., Narayanaswamy, B. E., Sura, A., Hajbane, S., White, R., Kumar, N., Fernandes, M., & Wijeratne, S. (2022). Plastics in the indian ocean – sources, transport, distribution, and impacts. *Ocean science*, *18*(1), 1–28. https://doi.org/10.5194/os-18-1-2022 (cit. on pp. 119, 121).

Pedlosky, J. (1979). *Geophysical fluid dynamics*. Springer-Verlag. (Cit. on pp. 28, 38, 45).

Penven, P., Lutjeharms, J. R. E., & Florenchie, P. (2006). Madagascar: a pacemaker for the agulhas current system? *Geophysical research letters*, *33*(17). https://doi.org/10.1029/2006gl026854 (cit. on pp. 45, 100, 110).

Phillips, H. E., Tandon, A., Furue, R., Hood, R., Ummenhofer, C. C., Benthuysen, J. A., Menezes, V., Hu, S., Webber, B., Sanchez-Franks, A., Cherian, D., Shroyer, E., Feng, M., Wijesekera, H., Chatterjee, A., Yu, L., Hermes, J., Murtugudde, R., Tozuka, T., … Wiggert, J. (2021). Progress in understanding of indian ocean circulation, variability, air–sea exchange, and impacts on biogeochemistry. *Ocean science*, *17*(6), 1677–1751. https://doi.org/10.5194/os-17-1677-2021 (cit. on pp. 44, 45, 49, 59, 61, 143).

Pingree, R. D., & Griffiths, D. K. (1978). Tidal fronts on the shelf seas around the british isles. *Journal of geophysical research*, *83*(C9), 4615–4622. https://doi.org/10.1029/jc083ic09p04615 (cit. on p. 30).

Pingree, R. D., Pugh, P. R., Holligan, P. M., & Forster, G. R. (1975). Summer phytoplankton blooms and red tides along tidal fronts in the approaches to the english channel. *Nature*, *258*(5537), 672–677. https://doi.org/10.1038/258672a0 (cit. on pp. 29, 30).

Pollard, R. T., Lucas, M. I., & Read, J. F. (2002). Physical controls on biogeochemical zonation in the southern ocean. *Deep-sea research. Part II, Topical studies in oceanography*, *49*(16), 3289–3305. https://doi.org/10.1016/s0967-0645(02)00084-x (cit. on p. 40).

Polovina, J. J., Howell, E., Kobayashi, D. R., & Seki, M. P. (2001). The transition zone chlorophyll front, a dynamic global feature defining migration and forage habitat for marine resources. *Progress in oceanography*, *49*(1–4), 469–483. https://doi.org/10.1016/s0079-6611(01)00036-2 (cit. on p. 42).

Polovina, J. J., Kobayashi, D. R., Parker, D. M., Seki, M. P., & Balazs, G. H. (2000). Turtles on the edge: movement of loggerhead turtles (caretta caretta) along oceanic fronts, spanning longline fishing grounds in the central north pacific, 1997–1998. *Fisheries oceanography*, *9*(1), 71–82. https://doi.org/10.1046/j.1365-2419.2000.00123.x (cit. on p. 42).

Potier, M., Bach, P., Ménard, F., & Marsac, F. (2014). Influence of mesoscale features on micronekton and large pelagic fish communities in the mozambique channel. *Deep-sea research. Part II, Topical studies in oceanography*, *100*, 184–199. https://doi.org/10.1016/j.dsr2.2013.10.026 (cit. on p. 100).

Pozo Buil, M., Jacox, M. G., Fiechter, J., Alexander, M. A., Bograd, S. J., Curchitser, E. N., Edwards, C. A., Rykaczewski, R. R., & Stock, C. A. (2021). A dynamically downscaled ensemble of future projections for the california current system. *Frontiers in marine science*, *8*. https://doi.org/10.3389/fmars.2021.612874 (cit. on pp. 101, 103).

Prants, S. V., Budyansky, M. V., & Uleysky, M. Y. (2014). Identifying lagrangian fronts with favourable fishery conditions. *Deep-sea research. Part I, Oceanographic research papers*, *90*, 27–35. https://doi.org/10.1016/j.dsr.2014.04.012 (cit. on p. 42).

Prants, S. (2023). Transport barriers in geophysical flows: a review. *Symmetry*, *15*(10), 1942. https://doi.org/10.3390/sym15101942 (cit. on pp. 35–37).

Pripp, T., Gammelsrød, T., & Krakstad, J. O. (2014). Physical influence on biological production along the western shelf of madagascar. *Deep-sea research. Part II, Topical studies in oceanography*, *100*, 174–183. https://doi.org/10.1016/j.dsr2.2013.10.025 (cit. on p. 47).

Qiu, B., & Chen, S. (2010). Eddy-mean flow interaction in the decadally modulating kuroshio extension system. *Deep-sea research. Part II, Topical studies in oceanography*, *57*(13–14), 1098–1110. https://doi.org/10.1016/j.dsr2.2008.11.036 (cit. on p. 31).

Quartly, G. D., Buck, J. J. H., Srokosz, M. A., & Coward, A. C. (2006). Eddies around madagascar — the retroflection re-considered. *Journal of marine systems: journal of the European Association of Marine Sciences and Techniques*, *63*(3–4), 115–129. https://doi.org/10.1016/j.jmarsys.2006.06.001 (cit. on p. 45).

Queiroz, N., Humphries, N. E., Mucientes, G., Hammerschlag, N., Lima, F. P., Scales, K. L., Miller, P. I., Sousa, L. L., Seabra, R., & Sims, D. W. (2016). Ocean-wide tracking of pelagic sharks reveals extent of overlap with longline fishing hotspots. *Proceedings of the National Academy of Sciences of the United States of America*, *113*(6), 1582–1587. https://doi.org/10.1073/pnas.1510090113 (cit. on p. 42).

Queiroz, N., Humphries, N. E., Noble, L. R., Santos, A. M., & Sims, D. W. (2012). Spatial dynamics and expanded vertical niche of blue sharks in oceanographic fronts reveal habitat targets for conservation. *PloS one*, *7*(2), e32374. https://doi.org/10.1371/journal.pone.0032374 (cit. on p. 42).

Ramanantsoa, J. D., Krug, M., Penven, P., Rouault, M., & Gula, J. (2018). Coastal upwelling south of madagascar: temporal and spatial variability. *Journal of marine systems: journal of the European Association of Marine Sciences and Techniques*, *178*, 29–37. https://doi.org/10.1016/j.jmarsys.2017.10.005 (cit. on p. 47).

Ramanantsoa, J. D., Penven, P., Raj, R. P., Renault, L., Ponsoni, L., Ostrowski, M., Dilmahamod, A. F., & Rouault, M. (2021). Where and how the east madagascar current retroflection originates? *Journal of geophysical research. Oceans*, *126*(11). https://doi.org/10.1029/2020jc016203 (cit. on p. 45).

Rayner, N. A., Parker, D. E., Horton, E. B., Folland, C. K., Alexander, L. V., Rowell, D. P., Kent, E. C., & Kaplan, A. (2003). Global analyses of sea surface temperature, sea ice, and night marine air temperature since the late nineteenth century. *Journal of geophysical research*, *108*(D14). https://doi.org/10.1029/2002jd002670 (cit. on pp. 54, 144).

Reichstein, M., Camps-Valls, G., Stevens, B., Jung, M., Denzler, J., Carvalhais, N., & Prabhat. (2019). Deep learning and process understanding for data-driven earth system science. *Nature*, *566*(7743), 195–204. https://doi.org/10.1038/s41586-019-0912-1 (cit. on pp. 113, 147).

Renault, L., Masson, S., Oerder, V., Jullien, S., & Colas, F. (2019). Disentangling the mesoscale ocean-atmosphere interactions. *Journal of geophysical research. Oceans*, *124*(3), 2164–2178. https://doi.org/10.1029/2018jc014628 (cit. on pp. 38, 145).

Renault, L., Deutsch, C., McWilliams, J. C., Frenzel, H., Liang, J.-H., & Colas, F. (2016a). Partial decoupling of primary productivity from upwelling in the california current system. *Nature geoscience*, *9*(7), 505–508. https://doi.org/10.1038/ngeo2722 (cit. on p. 38).

Renault, L., Masson, S., Arsouze, T., Madec, G., & McWilliams, J. C. (2020). Recipes for how to force oceanic model dynamics. *Journal of advances in modeling earth systems*, *12*(2). https://doi.org/10.1029/2019ms001715 (cit. on p. 113).

Renault, L., McWilliams, J. C., & Gula, J. (2018). Dampening of submesoscale currents by air-sea stress coupling in the californian upwelling system. *Scientific reports*, *8*(1). https://doi.org/10.1038/s41598-018-31602-3 (cit. on p. 38).

Renault, L., McWilliams, J. C., & Masson, S. (2017). Satellite observations of imprint of oceanic current on wind stress by air-sea coupling. *Scientific reports*, *7*(1). https://doi.org/10.1038/s41598-017-17939-1 (cit. on p. 113).

Renault, L., Molemaker, M. J., McWilliams, J. C., Shchepetkin, A. F., Lemarié, F., Chelton, D., Illig, S., & Hall, A. (2016b). Modulation of wind work by oceanic current interaction with the atmosphere. *Journal of physical oceanography*, *46*(6), 1685–1704. https://doi.org/10.1175/jpo-d-15-0232.1 (cit. on p. 38).

Ridderinkhof, H., & de Ruijter, W. P. M. (2003). Moored current observations in the mozambique channel. *Deep-sea research. Part II, Topical studies in oceanography*, *50*(12–13), 1933–1955. https://doi.org/10.1016/s0967-0645(03)00041-9 (cit. on p. 45).

Ridderinkhof, H., van der Werf, P. M., Ullgren, J. E., van Aken, H. M., van Leeuwen, P. J., & de Ruijter, W. P. M. (2010). Seasonal and interannual variability in the mozambique channel from moored current observations. *Journal of geophysical research*, *115*(C6). https://doi.org/10.1029/2009jc005619 (cit. on pp. 45, 144).

Rio, M.-H., Mulet, S., & Picot, N. (2014). Beyond goce for the ocean circulation estimate: synergetic use of altimetry, gravimetry, and in situ data provides new insight into geostrophic and ekman currents: ocean circulation beyond goce. *Geophysical research letters*, *41*(24), 8918–8925. https://doi.org/10.1002/2014gl061773 (cit. on pp. 52, 104, 105).

Roberts, M. J., Ternon, J.-F., & Morris, T. (2014). Interaction of dipole eddies with the western continental slope of the mozambique channel. *Deep-sea research. Part II, Topical studies in oceanography*, *100*, 54–67. https://doi.org/10.1016/j.dsr2.2013.10.016 (cit. on pp. 31, 45–47).

Robinson, N. J., Morreale, S. J., Nel, R., & Paladino, F. V. (2016). Coastal leatherback turtles reveal conservation hotspot. *Scientific reports*, *6*(1). https://doi.org/10.1038/srep37851 (cit. on p. 48).

Roden, G. I. (1991). Effects of the hawaiian ridge upon oceanic flow and thermohaline structure. *Deep-sea research. Part A, Oceanographic research papers*, *38*, S623–S654. https://doi.org/10.1016/s0198-0149(12)80026-4 (cit. on p. 31).

Rohner, C. A., Pierce, S. J., Marshall, A. D., Weeks, S. J., Bennett, M. B., & Richardson, A. J. (2013). Trends in sightings and environmental influences on a coastal aggregation of manta rays and whale sharks. *Marine ecology progress series*, *482*, 153–168. https://doi.org/10.3354/meps10290 (cit. on pp. 48, 96, 99).

Rohner, C. A., Richardson, A. J., Jaine, F. R. A., Bennett, M. B., Weeks, S. J., Cliff, G., Robinson, D. P., Reeve-Arnold, K. E., & Pierce, S. J. (2018). Satellite tagging highlights the importance of productive mozambican coastal waters to the ecology and conservation of whale sharks. *PeerJ*, *6*(e4161), e4161. https://doi.org/10.7717/peerj.4161 (cit. on pp. 48, 96, 99).

Rossi, V., Morel, Y., & Garçon, V. (2010). Effect of the wind on the shelf dynamics: formation of a secondary upwelling along the continental margin. *Ocean modelling*, *31*(3–4), 51–79. https://doi.org/10.1016/j.ocemod.2009.10.002 (cit. on p. 31).

Rousselet, L., de Verneil, A., Doglioli, A. M., Petrenko, A. A., Duhamel, S., Maes, C., & Blanke, B. (2018). Large to submesoscale surface circulation and its implications on biogeochemical/biological horizontal distributions during the

outpace cruise (southwest pacific). *Biogeosciences*, *15*(8), 2411–2431. https://doi.org/10.5194/bg-15-2411-2018 (cit. on p. 36).

Roxy, M. K., Ritika, K., Terray, P., & Masson, S. (2014). The curious case of indian ocean warming. *Journal of climate*, *27*(22), 8501–8509. https://doi.org/10.1175/jcli-d-14-00471.1 (cit. on p. 100).

Ryan, J. P., Green, J. R., Espinoza, E., & Hearn, A. R. (2017). Association of whale sharks (rhincodon typus) with thermo-biological frontal systems of the eastern tropical pacific. *PloS one*, *12*(8), e0182599. https://doi.org/10.1371/journal.pone.0182599 (cit. on p. 42).

Saba, V. S., Griffies, S. M., Anderson, W. G., Winton, M., Alexander, M. A., Delworth, T. L., Hare, J. A., Harrison, M. J., Rosati, A., Vecchi, G. A., & Zhang, R. (2016). Enhanced warming of the northwest atlantic ocean under climate change. *Journal of geophysical research. Oceans*, *121*(1), 118–132. https://doi.org/10.1002/2015jc011346 (cit. on pp. 96, 98, 100).

Sabarros, P. S., Grémillet, D., Demarcq, H., Moseley, C., Pichegru, L., Mullers, R. H. E., Stenseth, N. C., & Machu, E. (2014). Fine-scale recognition and use of mesoscale fronts by foraging cape gannets in the benguela upwelling region. *Deep-sea research. Part II, Topical studies in oceanography*, *107*, 77–84. https://doi.org/10.1016/j.dsr2.2013.06.023 (cit. on p. 42).

Sabarros, P. S., Ménard, F., Lévénez, J. J., Tew-Kai, E., & Ternon, J. F. (2009). Mesoscale eddies influence distribution and aggregation patterns of micronekton in the mozambique channel. *Marine ecology progress series*, *395*, 101–107. https://doi.org/10.3354/meps08087 (cit. on pp. 48, 59, 61, 100).

Sætre, R., & Da Silva, A. J. (1984). The circulation of the mozambique channel. *Deep-sea research. Part A, Oceanographic research papers*, *31*(5), 485–508. https://doi.org/10.1016/0198-0149(84)90098-0 (cit. on p. 45).

Saji, N. H., Goswami, B. N., Vinayachandran, P. N., & Yamagata, T. (1999). A dipole mode in the tropical indian ocean. *Nature*, *401*(6751), 360–363. https://doi.org/10.1038/43854 (cit. on pp. 54, 55, 144, 145).

Sathyendranath, S., Brewin, R., Brockmann, C., Brotas, V., Calton, B., Chuprin, A., Cipollini, P., Couto, A., Dingle, J., Doerffer, R., Donlon, C., Dowell, M., Farman, A., Grant, M., Groom, S., Horseman, A., Jackson, T., Krasemann, H., Lavender, S., … Platt, T. (2019). An ocean-colour time series for use in climate studies: the experience of the ocean-colour climate change initiative (oc-cci). *Sensors*, *19*(19), 4285. https://doi.org/10.3390/s19194285 (cit. on p. 149).

Sato, M., Barth, J. A., Benoit-Bird, K. J., Pierce, S. D., Cowles, T. J., Brodeur, R. D., & Peterson, W. T. (2018). Coastal upwelling fronts as a boundary for planktivorous fish distributions. *Marine ecology progress series*, *595*, 171–186. https://doi.org/10.3354/meps12553 (cit. on pp. 42, 54).

Sato, T., Kimura, F., & Kitoh, A. (2007). Projection of global warming onto regional precipitation over mongolia using a regional climate model. *Journal of hydrology*, *333*(1), 144–154. https://doi.org/10.1016/j.jhydrol.2006.07.023 (cit. on pp. 96, 98, 102).

Scales, K. L., Hazen, E. L., Jacox, M. G., Castruccio, F., Maxwell, S. M., Lewison, R. L., & Bograd, S. J. (2018). Fisheries bycatch risk to marine megafauna is intensified in lagrangian coherent structures. *Proceedings of the National Academy of Sciences of the United States of America*, *115*(28), 7362–7367. https://doi.org/10.1073/pnas.1801270115 (cit. on pp. 42, 100, 118, 120, 139).

Scales, K. L., Miller, P. I., Embling, C. B., Ingram, S. N., Pirotta, E., & Votier, S. C. (2014a). Mesoscale fronts as foraging habitats: composite front mapping reveals oceanographic drivers of habitat use for a pelagic seabird. *Journal of the Royal Society, Interface*, *11*(100), 20140679. https://doi.org/10.1098/rsif.2014.0679 (cit. on p. 42).

Scales, K. L., Miller, P. I., Hawkes, L. A., Ingram, S. N., Sims, D. W., & Votier, S. C. (2014b). On the front line: frontal zones as priority at-sea conservation areas for mobile marine vertebrates. *The journal of applied ecology*, *51*(6), 1575–1583. https://doi.org/10.1111/1365-2664.12330 (cit. on pp. 30, 42, 43, 59, 61, 100, 118, 120, 138, 139).

Scales, K. L., Moore, I., Thomas S., Sloyan, B., Spillman, C. M., Eveson, J. P., Patterson, T. A., Williams, A. J., Hobday, A. J., & Hartog, J. R. (2023). Forecast-ready models to support fisheries' adaptation to global variability and change. *Fisheries oceanography*, *32*(4), 405–417. https://doi.org/10.1111/fog.12636 (cit. on p. 41).

Schär, C., Frei, C., Lüthi, D., & Davies, H. C. (1996). Surrogate climate-change scenarios for regional climate models. *Geophysical research letters*, *23*(6), 669–672. https://doi.org/10.1029/96gl00265 (cit. on pp. 54, 102).

Scheffer, A., Bost, C. A., & Trathan, P. N. (2012). Frontal zones, temperature gradient and depth characterize the foraging habitat of king penguins at south georgia. *Marine ecology progress series*, *465*, 281–297. https://doi.org/10.3354/meps09884 (cit. on p. 42).

Scheffer, A., Trathan, P. N., & Collins, M. (2010). Foraging behaviour of king penguins (aptenodytes patagonicus) in relation to predictable mesoscale oceanographic features in the polar front zone to the north of south georgia. *Progress in oceanography*, *86*(1–2), 232–245. https://doi.org/10.1016/j.pocean.2010.04.008 (cit. on p. 42).

Schneider, D. C. (1990). Seabirds and fronts: a brief overview. *Polar research*, *8*(1), 17–21. https://doi.org/10.1111/j.1751-8369.1990.tb00370.x (cit. on p. 42).

Schott, F. A., & McCreary, J., Julian P. (2001). The monsoon circulation of the indian ocean. *Progress in oceanography*, *51*(1), 1–123. https://doi.org/10.1016/s0079-6611(01)00083-0 (cit. on pp. 44, 45, 49, 138).

Schott, F. A., Xie, S.-P., & McCreary, J., Julian P. (2009). Indian ocean circulation and climate variability. *Reviews of geophysics (Washington, D.C.: 1985)*, *47*(1). https://doi.org/10.1029/2007rg000245 (cit. on p. 45).

Schouten, M. W., de Ruijter, W. P. M., van Leeuwen, P. J., & Ridderinkhof, H. (2003). Eddies and variability in the mozambique channel. *Deep-sea research. Part II, Topical studies in oceanography*, *50*(12–13), 1987–2003. https://doi.org/10.1016/s0967-0645(03)00042-0 (cit. on p. 45).

Sen Gupta, A., McGregor, S., van Sebille, E., Ganachaud, A., Brown, J. N., & Santoso, A. (2016). Future changes to the indonesian throughflow and pacific circulation: the differing role of wind and deep circulation changes. *Geophysical research letters*, *43*(4), 1669–1678. https://doi.org/10.1002/2016gl067757 (cit. on p. 109).

Sen Gupta, A., Stellema, A., Pontes, G. M., Taschetto, A. S., Vergés, A., & Rossi, V. (2021). Future changes to the upper ocean western boundary currents across two generations of climate models. *Scientific reports*, *11*(1), 9538. https://doi.org/10.1038/s41598-021-88934-w (cit. on pp. 100, 109).

Seo, H., Jochum, M., Murtugudde, R., & Miller, A. J. (2006). Effect of ocean mesoscale variability on the mean state of tropical atlantic climate. *Geophysical research letters*, *33*(9). https://doi.org/10.1029/2005gl025651 (cit. on p. 38).

Seo, H., Miller, A. J., & Norris, J. R. (2016). Eddy–wind interaction in the california current system: dynamics and impacts. *Journal of physical oceanography*, *46*(2), 439–459. https://doi.org/10.1175/jpo-d-15-0086.1 (cit. on p. 38).

Seo, H., O'Neill, L. W., Bourassa, M. A., Czaja, A., Drushka, K., Edson, J. B., Fox-Kemper, B., Frenger, I., Gille, S. T., Kirtman, B. P., Minobe, S., Pendergrass, A. G., Renault, L., Roberts, M. J., Schneider, N., Small, R. J., Stoffelen, A., & Wang, Q. (2023). Ocean mesoscale and frontal-scale ocean–atmosphere interactions and influence on large-scale climate: a review. *Journal of climate*, *36*(7), 1981–2013. https://doi.org/10.1175/jcli-d-21-0982.1 (cit. on pp. 43, 113, 119, 121, 138, 145).

Sequeira, A., Mellin, C., Delean, S., Meekan, M. G., & Bradshaw, C. J. A. (2013). Spatial and temporal predictions of inter-decadal trends in indian ocean whale sharks. *Marine ecology progress series*, *478*, 185–195. https://doi.org/10.3354/meps10166 (cit. on p. 48).

Sequeira, A., Mellin, C., Fordham, D. A., Meekan, M. G., & Bradshaw, C. J. A. (2014). Predicting current and future global distributions of whale sharks. *Global change biology*, *20*(3), 778–789. https://doi.org/10.1111/gcb.12343 (cit. on p. 48).

Sequeira, A., Mellin, C., Rowat, D., Meekan, M. G., & Bradshaw, C. J. A. (2012). Ocean-scale prediction of whale shark distribution: environmental drivers of whale shark distribution. *Diversity distributions*, *18*(5), 504–518. https://doi.org/10.1111/j.1472-4642.2011.00853.x (cit. on pp. 48, 59, 61).

Ser-Giacomi, E., Legrand, T., Hernández-Carrasco, I., & Rossi, V. (2021). Explicit and implicit network connectivity: analytical formulation and application to transport processes. *Physical review. E*, *103*(4–1), 042309. https://doi.org/10.1103/PhysRevE.103.042309 (cit. on p. 42).

Sharma, S., Ha, K.-J., Yamaguchi, R., Rodgers, K. B., Timmermann, A., & Chung, E.-S. (2023). Future indian ocean warming patterns. *Nature communications*, *14*(1), 1–11. https://doi.org/10.1038/s41467-023-37435-7 (cit. on p. 115).

Shchepetkin, A. F., & McWilliams, J. C. (2005). The regional oceanic modeling system (roms): a split-explicit, free-surface, topography-following-coordinate oceanic model. *Ocean modelling*, *9*(4), 347–404. https://doi.org/10.1016/j.ocemod.2004.08.002 (cit. on pp. 53, 101, 150).

Shimada, T., Sakaida, F., Kawamura, H., & Okumura, T. (2005). Application of an edge detection method to satellite images for distinguishing sea surface temperature fronts near the japanese coast. *Remote sensing of environment*, *98*(1), 21–34. https://doi.org/10.1016/j.rse.2005.05.018 (cit. on p. 34).

Siedler, G., Rouault, M., Biastoch, A., Backeberg, B., Reason, C. J. C., & Lutjeharms, J. R. E. (2009). Modes of the southern extension of the east madagascar current. *Journal of geophysical research*, *114*(C1). https://doi.org/10.1029/2008jc004921 (cit. on pp. 45, 98, 107, 110, 115).

Siedler, G., Rouault, M., & Lutjeharms, J. R. E. (2006). Structure and origin of the subtropical south indian ocean countercurrent. *Geophysical research letters*, *33*(24). https://doi.org/10.1029/2006gl027399 (cit. on p. 45).

Siegelman, L., Klein, P., Rivière, P., Thompson, A. F., Torres, H. S., Flexas, M., & Menemenlis, D. (2020a). Enhanced upward heat transport at deep submesoscale ocean fronts. *Nature geoscience*, *13*(1), 50–55. https://doi.org/10.1038/s41561-019-0489-1 (cit. on pp. 31, 118, 120, 139).

Siegelman, L., Klein, P., Thompson, A. F., Torres, H. S., & Menemenlis, D. (2020b). Altimetry-based diagnosis of deep-reaching sub-mesoscale ocean fronts. *Fluids*, *5*(3), 145. https://doi.org/10.3390/fluids5030145 (cit. on p. 36).

Siegelman, L., O'Toole, M., Flexas, M., Rivière, P., & Klein, P. (2019). Submesoscale ocean fronts act as biological hotspot for southern elephant seal. *Scientific reports*, *9*(1). https://doi.org/10.1038/s41598-019-42117-w (cit. on pp. 29, 42, 50).

Sims, D. W., & Quayle, V. A. (1998). Selective foraging behaviour of basking sharks on zooplankton in a small-scale front. *Nature*, *393*(6684), 460–464. https://doi.org/10.1038/30959 (cit. on p. 42).

Small, R. J., deSzoeke, S. P., Xie, S. P., O'Neill, L., Seo, H., Song, Q., Cornillon, P., Spall, M., & Minobe, S. (2008). Air–sea interaction over ocean fronts and eddies. *Dynamics of atmospheres and oceans*, *45*(3–4), 274–319. https://doi.org/10.1016/j.dynatmoce.2008.01.001 (cit. on pp. 38, 43, 113).

Small, R. J., Tomas, R. A., & Bryan, F. O. (2014). Storm track response to ocean fronts in a global high-resolution climate model. *Climate dynamics*, *43*(3–4), 805–828. https://doi.org/10.1007/s00382-013-1980-9 (cit. on p. 38).

Small, R. J., Xie, S.-P., & Hafner, J. (2005). Satellite observations of mesoscale ocean features and copropagating atmospheric surface fields in the tropical belt. *Journal of geophysical research*, *110*(C2). https://doi.org/10.1029/2004jc002598 (cit. on p. 38).

Snyder, S., Franks, P. J. S., Talley, L. D., Xu, Y., & Kohin, S. (2017). Crossing the line: tunas actively exploit submesoscale fronts to enhance foraging success. *Limnology and oceanography letters*, *2*(5), 187–194. https://doi.org/10.1002/lol2.10049 (cit. on p. 42).

Sonnewald, M., Lguensat, R., Jones, D. C., Dueben, P. D., Brajard, J., & Balaji, V. (2021). Bridging observations, theory and numerical simulation of the ocean using machine learning. *Environmental research letters*, *16*(7), 073008. https://doi.org/10.1088/1748-9326/ac0eb0 (cit. on p. 147).

Spalding, M. D., Fox, H. E., Allen, G. R., Davidson, N., Ferdaña, Z. A., Finlayson, M., Halpern, B. S., Jorge, M. A., Lombana, A., Lourie, S. A., Martin, K. D., McManus, E., Molnar, J., Recchia, C. A., & Robertson, J. (2007). Marine ecoregions of the world: a bioregionalization of coastal and shelf areas. *BioScience*, *57*(7), 573–583. https://doi.org/10.1641/b570707 (cit. on pp. 119, 121).

Stellema, A., Sen Gupta, A., & Taschetto, A. S. (2019). Projected slow down of south indian ocean circulation. *Scientific reports*, *9*(1). https://doi.org/10.1038/s41598-019-54092-3 (cit. on pp. 109, 110).

Stommel, H. (1961). Thermohaline convection with two stable regimes of flow. *Tellus*, *13*(2), 224–230. https://doi.org/10.3402/tellusa.v13i2.9491 (cit. on p. 25).

Strub, P. T., Kosro, P. M., & Huyer, A. (1991). The nature of the cold filaments in the california current system. *Journal of geophysical research*, *96*(C8), 14743–14768. https://doi.org/10.1029/91jc01024 (cit. on p. 31).

Stukel, M. R., Aluwihare, L. I., Barbeau, K. A., Chekalyuk, A. M., Goericke, R., Miller, A. J., Ohman, M. D., Ruacho, A., Song, H., Stephens, B. M., & Landry, M. R. (2017). Mesoscale ocean fronts enhance carbon export due to gravitational sinking and subduction. *Proceedings of the National Academy of Sciences of the United States of America*, *114*(6), 1252–1257. https://doi.org/10.1073/pnas.1609435114 (cit. on p. 39).

Sudre, F., Dewitte, B., Mazoyer, C., Garçon, V., Sudre, J., Penven, P., & Rossi, V. (2023a). Spatial and seasonal variability of horizontal temperature fronts in the mozambique channel for both epipelagic and mesopelagic realms. *Frontiers in Marine Science*, *9*. https://doi.org/10.3389/fmars.2022.1045136 (cit. on pp. 63, 100, 102–104, 106, 108, 110, 111).

Sudre, F., Hernández-Carrasco, I., Mazoyer, C., Sudre, J., Dewitte, B., Garçon, V., & Rossi, V. (2023b). An ocean front dataset for the mediterranean sea and southwest indian ocean. *Scientific data*, *10*(730). https://doi.org/10.1038/s41597-023-02615-z (cit. on pp. 100, 103, 108, 111, 122).

Sudre, F., Hernández-Carrasco, I., Mazoyer, C., Sudre, J., Dewitte, B., Garçon, V., & Rossi, V. (2023). Nomad: the ocean front dataset for the mediterranean sea and southwest indian ocean. https://doi.org/10.12770/3ea321a1-d9d4-49e5-a592-605b80dec240 (cit. on p. 122).

Sun, C., Feng, M., Matear, R. J., Chamberlain, M. A., Craig, P., Ridgway, K. R., & Schiller, A. (2012). Marine downscaling of a future climate scenario for australian boundary currents. *Journal of climate*, *25*(8), 2947–2962. https://doi.org/10.1175/jcli-d-11-00159.1 (cit. on pp. 101, 110).

Sverdrup, H. U. (1947). Wind-driven currents in a baroclinic ocean; with application to the equatorial currents of the eastern pacific. *Proceedings of the National Academy of Sciences of the United States of America*, *33*(11), 318–326. https://doi.org/10.1073/pnas.33.11.318 (cit. on pp. 25, 38).

Sverdrup, H. U. (1953). On conditions for the vernal blooming of phytoplankton. *ICES journal of marine science: journal du conseil*, *18*(3), 287–295. https://doi.org/10.1093/icesjms/18.3.287 (cit. on p. 40).

Takahashi, K., Montecinos, A., Goubanova, K., & Dewitte, B. (2011). Enso regimes: reinterpreting the canonical and modoki el niño. *Geophysical research letters*, *38*(10). https://doi.org/10.1029/2011gl047364 (cit. on p. 54).

Taylor, J. R., & Ferrari, R. (2011a). Ocean fronts trigger high latitude phytoplankton blooms. *Geophysical Research Letters*, *38*(23). https://doi.org/10.1029/2011gl049312 (cit. on p. 40).

Taylor, J. R., & Ferrari, R. (2011b). Shutdown of turbulent convection as a new criterion for the onset of spring phytoplankton blooms. *Limnology and oceanography*, *56*(6), 2293–2307. https://doi.org/10.4319/lo.2011.56.6.2293 (cit. on p. 40).

Taylor, J. R., & Thompson, A. F. (2023). Submesoscale dynamics in the upper ocean. *Annual review of fluid mechanics*, *55*(1), 103–127. https://doi.org/10.1146/annurev-fluid-031422-095147 (cit. on pp. 26, 28–30, 32).

Tebaldi, C., Arblaster, J. M., & Knutti, R. (2011). Mapping model agreement on future climate projections: mapping model agreement. *Geophysical research letters*, *38*(23). https://doi.org/10.1029/2011gl049863 (cit. on p. 147).

Tebaldi, C., Snyder, A., & Dorheim, K. (2022). Stitches: creating new scenarios of climate model output by stitching together pieces of existing simulations. *Earth system dynamics*, *13*(4), 1557–1609. https://doi.org/10.5194/esd-13-1557-2022 (cit. on pp. 113, 147).

Tedesco, P., Gula, J., Ménesguen, C., Penven, P., & Krug, M. (2019). Generation of submesoscale frontal eddies in the agulhas current. *Journal of geophysical research. Oceans*, *124*(11), 7606–7625. https://doi.org/10.1029/2019jc015229 (cit. on p. 31).

Ternon, J. F., Bach, P., Barlow, R., Huggett, J., Jaquemet, S., Marsac, F., Ménard, F., Penven, P., Potier, M., & Roberts, M. J. (2014a). The mozambique channel: from physics to upper trophic levels. *Deep-sea research. Part II, Topical studies in oceanography*, *100*, 1–9. https://doi.org/10.1016/j.dsr2.2013.10.012 (cit. on p. 100).

Ternon, J. F., Roberts, M. J., Morris, T., Hancke, L., & Backeberg, B. (2014b). In situ measured current structures of the eddy field in the mozambique channel. *Deep-sea research. Part II, Topical studies in oceanography*, *100*, 10–26. https://doi.org/10.1016/j.dsr2.2013.10.013 (cit. on p. 100).

Tew Kai, E., & Marsac, F. (2010). Influence of mesoscale eddies on spatial structuring of top predators' communities in the mozambique channel. *Progress in oceanography*, *86*(1–2), 214–223. https://doi.org/10.1016/j.pocean.2010.04.010 (cit. on pp. 48, 96, 99, 100, 113).

Tew Kai, E., Rossi, V., Sudre, J., Weimerskirch, H., Lopez, C., Hernandez-Garcia, E., Marsac, F., & Garçon, V. (2009). Top marine predators track lagrangian coherent structures. *Proceedings of the National Academy of Sciences of the United States of America*, *106*(20), 8245–8250. https://doi.org/10.1073/pnas.0811034106 (cit. on pp. 35, 42, 48, 96, 99, 100, 113, 118, 120, 139, 143, 150).

Tew-Kai, E., & Marsac, F. (2009). Patterns of variability of sea surface chlorophyll in the mozambique channel: a quantitative approach. *Journal of marine systems:*

journal of the European Association of Marine Sciences and Techniques, *77*(1–2), 77–88. https://doi.org/10.1016/j.jmarsys.2008.11.007 (cit. on pp. 46, 47, 100).

Thibault, D., Gaudy, R., & Le Fèvre, J. (1994). Zooplankton biomass, feeding and metabolism in a geostrophic frontal area (almeria-oran front, western mediterranean). significance to pelagic food webs. *Journal of marine systems: journal of the European Association of Marine Sciences and Techniques*, *5*(3–5), 297–311. https://doi.org/10.1016/0924-7963(94)90052-3 (cit. on p. 41).

Thomas, L., & Ferrari, R. (2008). Friction, frontogenesis, and the stratification of the surface mixed layer. *Journal of physical oceanography*, *38*(11), 2501–2518. https://doi.org/10.1175/2008jpo3797.1 (cit. on pp. 29, 38).

Thomas, L., & Lee, C. (2005). Intensification of ocean fronts by down-front winds. *Journal of physical oceanography*, *35*(6), 1086–1102. https://doi.org/10.1175/jpo2737.1 (cit. on pp. 38, 113).

Thyng, K., Greene, C., Hetland, R., Zimmerle, H., & DiMarco, S. (2016). True colors of oceanography: guidelines for effective and accurate colormap selection. *Oceanography*, *29*(3), 9–13. https://doi.org/10.5670/oceanog.2016.66 (cit. on pp. 46, 102, 104–109, 116, 117, 143, 144).

Tittensor, D. P., Mora, C., Jetz, W., Lotze, H. K., Ricard, D., Berghe, E. V., & Worm, B. (2010). Global patterns and predictors of marine biodiversity across taxa. *Nature*, *466*(7310), 1098–1101. https://doi.org/10.1038/nature09329 (cit. on p. 47).

Tittensor, D. P., Novaglio, C., Harrison, C. S., Heneghan, R. F., Barrier, N., Bianchi, D., Bopp, L., Bryndum-Buchholz, A., Britten, G. L., Büchner, M., Cheung, W. W. L., Christensen, V., Coll, M., Dunne, J. P., Eddy, T. D., Everett, J. D., Fernandes-Salvador, J. A., Fulton, E. A., Galbraith, E. D., … Blanchard, J. L. (2021). Next-generation ensemble projections reveal higher climate risks for marine ecosystems. *Nature climate change*, *11*(11), 973–981. https://doi.org/10.1038/s41558-021-01173-9 (cit. on pp. 100, 113, 148).

Tixier, P., Lea, M.-A., Hindell, M. A., Welsford, D., Mazé, C., Gourguet, S., & Arnould, J. P. Y. (2021). When large marine predators feed on fisheries catches: global patterns of the depredation conflict and directions for coexistence. *Fish and fisheries (Oxford, England)*, *22*(1), 31–53. https://doi.org/10.1111/faf.12504 (cit. on p. 42).

Tozuka, T., & Cronin, M. F. (2014). Role of mixed layer depth in surface frontogenesis: the agulhas return current front. *Geophysical research letters*, *41*(7), 2447–2453. https://doi.org/10.1002/2014gl059624 (cit. on p. 31).

Trapp, R. J., Woods, M. J., Lasher-Trapp, S. G., & Grover, M. A. (2021). Alternative implementations of the "pseudo-global-warming" methodology for event-based simulations. *Journal of Geophysical Research Atmospheres*, *126*(24). https://doi.org/10.1029/2021jd035017 (cit. on pp. 103, 104, 148).

Tseng, C.-T., Sun, C.-L., Belkin, I. M., Yeh, S.-Z., Kuo, C.-L., & Liu, D.-C. (2014). Sea surface temperature fronts affect distribution of pacific saury (cololabis saira) in the northwestern pacific ocean. *Deep-sea research. Part II, Topical studies in*

oceanography, *107*, 15–21. https://doi.org/10.1016/j.dsr2.2014.06.001 (cit. on p. 42).

Tzortzis, R., Doglioli, A. M., Barrillon, S., Petrenko, A. A., d'Ovidio, F., Izard, L., Thyssen, M., Pascual, A., Barceló-Llull, B., Cyr, F., Tedetti, M., Bhairy, N., Garreau, P., Dumas, F., & Gregori, G. (2021). Impact of moderately energetic fine-scale dynamics on the phytoplankton community structure in the western mediterranean sea. *Biogeosciences*, *18*(24), 6455–6477. https://doi.org/10.5194/bg-18-6455-2021 (cit. on pp. 41, 143, 148).

Unep-Nairobi Convention, W. (2015). *The regional state of the coast report: western indian ocean (546 pp)*. UNEP; WIOMSA. (Cit. on pp. 47, 59, 61, 100).

Vázquez, D. P., Atae-Allah, C., & Escamilla, P. L. L. (1999). Entropic approach to edge detection for sst images. *Journal of atmospheric and oceanic technology*, *16*(7), 970–979. https://doi.org/10.1175/1520-0426(1999)016<0970:eatedf>2.0.co;2 (cit. on p. 34).

Venables, S. K., van Duinkerken, D. I., Rohner, C. A., & Marshall, A. D. (2020). Habitat use and movement patterns of reef manta rays mobula alfredi in southern mozambique. *Marine ecology progress series*, *634*, 99–114. https://doi.org/10.3354/meps13178 (cit. on p. 48).

Vinayachandran, P., Masumoto, Y., Roberts, M. J., Huggett, J. A., Halo, I., Chatterjee, A., Amol, P., Gupta, G. V. M., Singh, A., Mukherjee, A., Prakash, S., Beckley, L. E., Raes, E. J., & Hood, R. (2021). Reviews and syntheses: physical and biogeochemical processes associated with upwelling in the indian ocean. *Biogeosciences*, *18*(22), 5967–6029. https://doi.org/10.5194/bg-18-5967-2021 (cit. on p. 47).

Vinayachandran, P. N., Iizuka, S., & Yamagata, T. (2002). Indian ocean dipole mode events in an ocean general circulation model. *Deep-sea research. Part II, Topical studies in oceanography*, *49*(7–8), 1573–1596. https://doi.org/10.1016/s0967-0645(01)00157-6 (cit. on p. 143).

Vogt-Vincent, N., Mitarai, S., & Johnson, H. L. (2023). *High-frequency variability dominates potential connectivity between remote coral reefs*. https://doi.org/10.5194/egusphere-2023-778 (cit. on p. 150).

Wang, D., Liu, Y., Qi, Y., & Shi, P. (2001). Seasonal variability of thermal fronts in the northern south china sea from satellite data. *Geophysical research letters*, *28*(20), 3963–3966. https://doi.org/10.1029/2001gl013306 (cit. on p. 33).

Wang, S., Jing, Z., Wu, L., Cai, W., Chang, P., Wang, H., Geng, T., Danabasoglu, G., Chen, Z., Ma, X., Gan, B., & Yang, H. (2022). El niño/southern oscillation inhibited by submesoscale ocean eddies. *Nature geoscience*, *15*(2), 112–117. https://doi.org/10.1038/s41561-021-00890-2 (cit. on p. 100).

Wang, X., Matear, R. J., & Trull, T. W. (2003). Nutrient utilization ratios in the polar frontal zone in the australian sector of the southern ocean: a model. *Global biogeochemical cycles*, *17*(1). https://doi.org/10.1029/2002gb001938 (cit. on p. 40).

Weatherall, P., Marks, K. M., Jakobsson, M., Schmitt, T., Tani, S., Arndt, J. E., Rovere, M., Chayes, D., Ferrini, V., & Wigley, R. (2015). A new digital bathymetric model

of the world's oceans. *Earth and space science (Hoboken, N.J.)*, *2*(8), 331–345. https://doi.org/10.1002/2015ea000107 (cit. on pp. 53, 101).

Webster, P. J., Moore, A. M., Loschnigg, J. P., & Leben, R. R. (1999). Coupled ocean-atmosphere dynamics in the indian ocean during 1997-98. *Nature*, *401*(6751), 356–360. https://doi.org/10.1038/43848 (cit. on pp. 54, 144).

Weimerskirch, H., Le Corre, M., Jaquemet, S., Potier, M., & Marsac, F. (2004). Foraging strategy of a top predator in tropical waters: great frigatebirds in the mozambique channel. *Marine Ecology Progress Series*, *275*, 297–308. https://doi.org/10.3354/meps275297 (cit. on pp. 42, 48, 96, 99).

Weimerskirch, H., Corre, M. L., Kai, E. T., & Marsac, F. (2010). Foraging movements of great frigatebirds from aldabra island: relationship with environmental variables and interactions with fisheries. *Progress in Oceanography*, *86*(1–2), 204–213. https://doi.org/10.1016/j.pocean.2010.04.003 (cit. on pp. 48, 100, 113, 148).

Wenegrat, J. O., Thomas, L. N., Sundermeyer, M. A., Taylor, J. R., D'Asaro, E. A., Klymak, J. M., Shearman, R. K., & Lee, C. M. (2020). Enhanced mixing across the gyre boundary at the gulf stream front. *Proceedings of the National Academy of Sciences of the United States of America*, *117*(30), 17607–17614. https://doi.org/10.1073/pnas.2005558117 (cit. on p. 40).

Wengel, C., Lee, S.-S., Stuecker, M. F., Timmermann, A., Chu, J.-E., & Schloesser, F. (2021). Future high-resolution el niño/southern oscillation dynamics. *Nature climate change*, *11*(9), 758–765. https://doi.org/10.1038/s41558-021-01132-4 (cit. on p. 100).

Whitt, D. B., Lévy, M., & Taylor, J. R. (2019). Submesoscales enhance storm-driven vertical mixing of nutrients: insights from a biogeochemical large eddy simulation. *Journal of geophysical research. Oceans*, *124*(11), 8140–8165. https://doi.org/10.1029/2019jc015370 (cit. on p. 40).

Williams, R. G., & Follows, M. J. (2003). Physical transport of nutrients and the maintenance of biological production. In *Ocean biogeochemistry* (pp. 19–51). Springer Berlin Heidelberg. (Cit. on p. 40).

Williams, R. G., & Follows, M. J. (2012). *Ocean dynamics and the carbon cycle: principles and mechanisms*. Cambridge University Press. https://doi.org/10.1017/cbo9780511977817 (cit. on pp. 39, 40).

Woodson, C. B., & Litvin, S. Y. (2015). Ocean fronts drive marine fishery production and biogeochemical cycling. *Proceedings of the National Academy of Sciences of the United States of America*, *112*(6), 1710–1715. https://doi.org/10.1073/pnas.1417143112 (cit. on p. 42).

Xi, J., Wang, Y., Feng, Z., Liu, Y., & Guo, X. (2022). Variability and intensity of the sea surface temperature front associated with the kuroshio extension. *Frontiers in marine science*, *9*. https://doi.org/10.3389/fmars.2022.836469 (cit. on p. 31).

Xu, Y., Nieto, K., Teo, S. L. H., McClatchie, S., & Holmes, J. (2017). Influence of fronts on the spatial distribution of albacore tuna (thunnus alalunga) in the northeast pacific over the past 30 years (1982–2011). *Progress in oceanography*, *150*, 72–78. https://doi.org/10.1016/j.pocean.2015.04.013 (cit. on p. 42).

Yanagi, T., & Tamaru, H. (1990). Temporal and spatial variations in a tidal front. *Continental shelf research*, *10*(7), 615–627. https://doi.org/10.1016/0278-4343(90)90041-j (cit. on p. 30).

Yang, Y., Xie, S.-P., Wu, L., Kosaka, Y., Lau, N.-C., & Vecchi, G. A. (2015). Seasonality and predictability of the indian ocean dipole mode: enso forcing and internal variability. *Journal of climate*, *28*(20), 8021–8036. https://doi.org/10.1175/jcli-d-15-0078.1 (cit. on pp. 54, 144).

Yoder, J. A., Ackleson, S. G., Barber, R. T., Flament, P., & Balch, W. M. (1994). A line in the sea. *Nature*, *371*(6499), 689–692. https://doi.org/10.1038/371689a0 (cit. on p. 33).

Zhang, L., Han, W., & Sienz, F. (2018). Unraveling causes for the changing behavior of the tropical indian ocean in the past few decades. *Journal of climate*, *31*(6), 2377–2388. https://doi.org/10.1175/jcli-d-17-0445.1 (cit. on p. 100).

Zweng, M. M., Reagan, J. R., Seidov, D., Boyer, T. P., Locarnini, R. A., Garcia, H. E., Mishonov, A. V., Baranova, O. K., Weathers, K., Paver, C. R., & Smolyar, I. (2018). *World ocean atlas: salinity*. (Cit. on p. 104).

A. Other collaborative works

1. Transport patterns and hydrodynamic context of the MERITE-HIPPOCAMPE cruise: Implications for contaminants distribution and origin. Rwawi C., Hernández-Carrasco I., **Sudre F.**, Tedetti M. and Rossi V. **2024**. *Marine Pollution Bulletin 198, 115743*.
DOI : http://dx.doi.org/10.1016/j.marpolbul.2023.115743.

2. Diazotrophy in two contrasted sub-basins of the northern Indian Ocean. Chowdhury S., Ahmed N., **Sudre F.**, ..., Rossi V., Singh A., and Benavides M. **(In preparation)**.

3. Central structure of a Mozambique Channel mesoscale eddy-ring dipole. Penven P., Ternon J-F., Noyon M., Herbette S., Cambon G., Comby C., Fuda J-L., Le Bot P., L'Hegaret P., Malauene B., Menage O., Menesguen C., Nehama F., Quemener L., Rauntenbach G., Rufino Y. and **Sudre F. (in preparation)**.

Abstract

Fronts are ubiquitous ocean structures delineating waters of distinct properties. They are major actors of climate variability and attract a wide range of marine organisms. Fine-scale fronts in particular are difficult to study on multidecadal timescales due to their short life-cycle, unpredictability and small size, thereby involving high computational costs. In this work, we use the turbulent Mozambique Channel as a natural laboratory to explore present-day variability of fine-scale fronts from multidecadal satellite and modelled data. We then extend our analyses by downscaling global climate projections to investigate how warming would impact fronts in the region. We find that the areas most affected by the warming overlap key megafauna habitats. We thus developed a high-resolution front dataset to investigate the interactions between front and megafauna, in view to contribute to the development of conservation areas that are aware of front variability and resilient to changes.

Keywords: mesoscale, fine-scale, eddies, ocean fronts, Indian Ocean, Mozambique Channel

Résumé

Les fronts sont des structures océaniques délimitant des eaux aux propriétés distinctes. Ils jouent un rôle majeur dans la variabilité climatique et attirent une grande diversité d'organismes marins. Les fronts éphémères de fine échelle sont difficiles à étudier sur des échelles multidécennales en raison de leur imprévisibilité et petite taille. Dans cette thèse, nous explorons la variabilité des fronts de petite échelle dans le Canal du Mozambique à partir de données satellitaires et modélisées. Nous étendons ensuite nos analyses en régionalisant des projections climatiques globales pour étudier l'impact du réchauffement sur les fronts. Les zones les plus impactées chevauchent des habitats clés de la mégafaune. Nous avons donc élaboré une base de données de fronts à haute résolution pour étudier les interactions entre les fronts et la mégafaune et contribuer au développement de zones de conservation adaptées à la variabilité des fronts et aux projections climatiques dans la région.

Mots clés: méso-échelle, fine-échelle, tourbillons, fronts océaniques, océan indien, Canal du Mozambique